Determining the U-Pb emplacement age of lamproites and kimberlites in Southeastern Kansas

by

Isabella Lupini

B.S., George Mason University, 2019

A THESIS

submitted in partial fulfillment of the requirements for the degree

MASTER OF SCIENCE

Department of Geology
College of Arts and Sciences

KANSAS STATE UNIVERSITY
Manhattan, Kansas

2024

Approved by:

Major Professor
Dr. Pamela Kempton

Copyright

Abstract

In eastern Kansas, twelve kimberlites and two lamproites constitute the southern portion of a ~5000 km stretch of Mid-Cretaceous-age alkali magmatism in central North America. Four main geodynamic models have been proposed to explain the formation of this alkaline igneous corridor including entrainment by mantle plumes, subduction of the Farallon plate, large low shear velocity provinces, and edge-driven mantle convection cells. Each of these models has temporal constraints that can be used to evaluate their viability. The emplacement ages for the Kansas kimberlites were previously reported by Blackburn et al. (2008) as 110-85 Ma, with a younger hydrothermal reheating event recorded at ~65 Ma. K-Ar geochronology conducted on the Kansas lamproites by Zartman et al. (1967) suggest they are younger than most of the kimberlites, with an age of ~90-88 Ma. However, the limited amount of data and their uncertainty make it difficult to assess the relationship between the two magmatic events. To better constrain the timing of emplacement, we conducted in situ U-Pb perovskite geochronology on the Hills Pond and Rose Dome lamproites, along with reanalysis of the Tuttle and Bala kimberlites. Perovskite was chosen for analysis because it is one of the few primary phases that occurs in both rock types AND has survived the pervasive alteration observed. Our age data for the Kansas kimberlites and lamproites are consistent with previous studies. The Tuttle perovskites yield an age of 105.6 ± 1.9 Ma, which agrees well with the 106.6 ± 1 Ma age determined by Blackburn et al. (2008) using Rb-Sr on megacrystic phlogopite and clinopyroxene. In contrast, the Bala kimberlite yields two arrays on the Tera-Wasserburg concordia diagram, one with an age of 59.6 ± 7.4 Ma and the other 81.7 ± 8.6 Ma. Blackburn et al. (2008) also report two ages for this kimberlite. Their younger age of 64.3 ± 7.5 Ma, based on

(U-Th)/He in apatite, is within error of our new perovskite age. However, their older age of 103.0 ± 7.5 Ma, based on (U-Th)/He in magnetite separated from a calcite vein, is more than 20 m.y. older than our older perovskite age. Our petrologic data, in combination with the two perovskite age populations, suggest in contrast to Blackburn et al. (2008), that the Bala kimberlite site sustained reoccurring magmatism for at least ~22 m.y., and possibly longer.

The Hills Pond and Rose Dome perovskites yield ages of 86.8 ± 3.5 and 97.1 ± 12.6 Ma, respectively. Thus, the emplacement of the Kansas kimberlites and lamproites overlap in time, but with the initiation of kimberlite magmatism preceding that of the lamproites by at least 8 m.y. The significant time span for the kimberlite and lamproite magmatism is most consistent with an edge-driven convection model of formation.

Table of Contents

List of Figures

List of Tables

Acknowledgements

I'd like to thank everyone in both my personal and professional life who has allowed me to make it to where I am today. Thank you to Dr. Giuseppina Mattietti for sparking and nurturing my initial interest in igneous petrology; without you, I would have never thought I could pursue such a subject.

Thank you to Nicole Potter from the Kansas Geological Survey for answering all my niche questions and providing access to the Rose Dome cores. Thank you to Dr. Pieter Berendsen for your advice on which Rose Dome cores would be best to sample. Thank you to everyone at MicroLite, especially Ron May, for not only allowing us to sample your large core collection but for creating such a welcoming environment. Thank you for granting me the opportunity to take a leading role in the 4H field trip hosted at the mine. It was an incredible experience to be able to lead an event that my younger self would have died for.

Thank you to Dr. Pamela Kempton for all your help and support throughout this project. I am immensely grateful to have had such a dedicated and understanding thesis advisor. You and the graduate program as a whole repeatedly pushed me out of my comfort zone and showed me I am capable of much more than my fears would have me believe. Thank you to my committee members, Dr. Andreas Möller and Dr. Claudia Adam, for all their support and feedback. I appreciate their patience in closing the gaps in my knowledge of geophysics and U-Pb geochronology.

I'd also like to thank all my friends, both here at KState and beyond, for repeatedly reminding me that life is better when I am not constantly reading and analyzing data. A bad day can become amazing if only I take the time to reach out. Special thanks to Karl, Morgan, Blaire, and Alex for keeping in touch even when I forget how important a social life is.

Thank you to Matthew for providing constant support and company during my time here in Manhattan. I feel incredibly lucky to have you by my side throughout this part of my life. Thank you for joining me on my adventure to Kansas.

I’d like to thank my family for their unconditional love and support throughout my life. Thank you for always believing in me and only wishing for my happiness. You know I am too hard on myself, and you always try to relieve the pressures, and for that, I am eternally grateful. Thank you for putting up with my radio silence when I get incredibly stressed. Lastly, thank you for allowing me to fill every room in our house with rocks.

Chapter 1 - Introduction

Lamproites and kimberlites are known for providing petrologic and geochemical information on Earth's mantle through the study of the xenoliths they entrain and the nature of their unusual, trace-element-enriched compositions (Kopylova and Caro, 2004; Kjarsgaard et al., 2017; Liu et al., 2018). In addition to their scientific significance, these rocks are of economic importance as they are the primary host of diamonds (Kjarsgaard and Levinson, 2002; Mitchell, 2020). They also contain high concentrations of critical elements such as Ni, Cr, and V, which are used in numerous energy storage technologies, as well as mantle-incompatible elements (Nb, Nd, Ce, La, Y, Ta, Hf, Ti, Sm, Zr, and Rb) (Fig. 1) (Cullers and Berendsen, 2011; Kempton et al., 2019b; Lee et al., 2020) that are vital to numerous modern technologies because of their unique properties of magnetism, oxidation-reduction, and luminescence (Wall et al., 2017). However, lamproite and kimberlite formation is still poorly understood, because the rocks are often intensely and pervasively altered. This also makes them difficult to date, because most of the primary minerals are altered to serpentine, calcite, and/or chlorite (Heaman et al., 2019).

Lamproites are known to form in both intraplate (e.g., Leucite Hills, Wyoming, USA; Baifen, China) and converging plate margins (e.g., most Mediterranean localities), with the two tectonic settings producing rocks that are compositionally distinct (Kononova et al., 2011; Mitchell, 2020). Lamproites from convergent margin settings typically show strong depletion in high field strength elements (e.g., Ti, Nb, and Ta), typical of the subduction environment (e.g., Casalini et al., 2022), whereas the intraplate lamproites commonly contain high SiO_2 and low concentrations of CaO, Al_2O_3, and Na_2O at high K_2O/Al_2O_3 ratios (Kononova et al., 2011). Cratonic (intraplate) lamproites typically form within Proterozoic to early Phanerozoic accreted mobile belts, regions of thick lithosphere (> 150-200 km) (Mitchell and Bergman, 1991; Kononova et al., 2011).

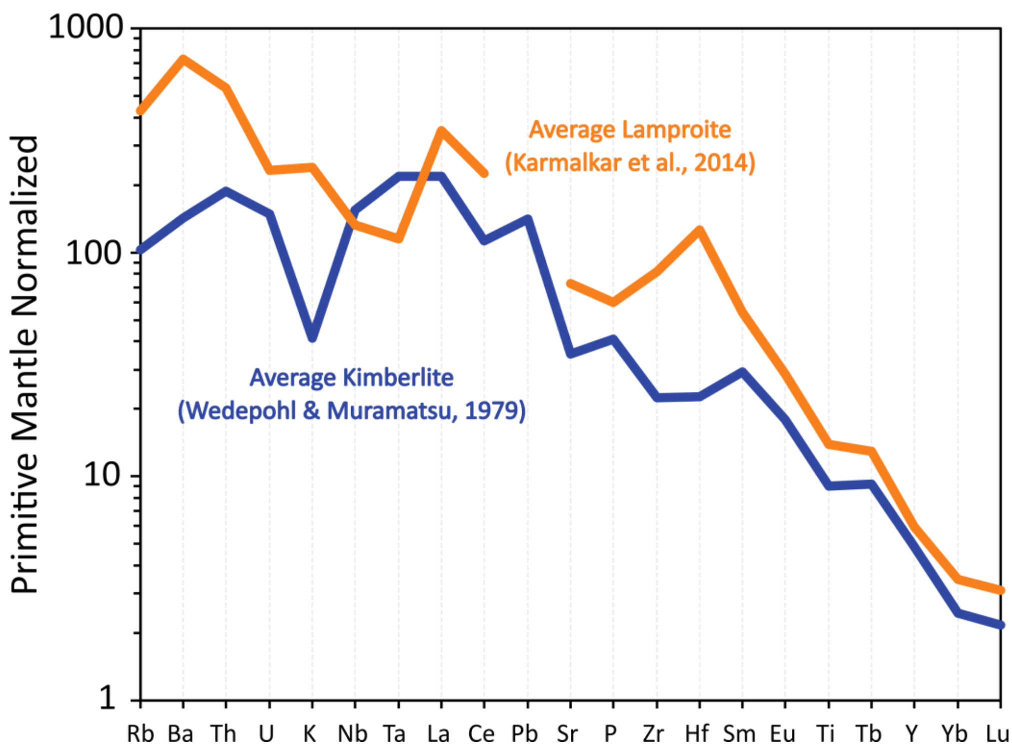

Figure 1. Average Kimberlite and Lamproite Whole Rock Trace Element Diagram
A primitive mantle normalized incompatible element plot displaying the difference between the global average kimberlite in blue (Wedepohl and Muramatsu, 1979), and the global average lamproite in orange (Karlmalkar et al., 2014).

Similarly, kimberlites typically occur within or near Archean cratons, as lithospheric thickness in these localities (> 150-200 km) provides adequate pressure (> 6 GPa) and temperature (> 1,400 ˚C) conditions conducive for the formation of kimberlite melts of varying composition and volatile contents (Fig. 2a) (Gaetani and Grove 1998; Priestly et al. 2006; Sparks, 2013; Tappe et al., 2018). However, the kimberlites in Kansas, USA, are not near an Archean craton but rather within a region of Proterozoic basement rocks accreted to Laurentia approximately 1.6 to 1.7 b.y. ago (Sims et al., 1987; Berendsen, 2011). The atypical location of the Kansas kimberlites, in addition to their association with other North American kimberlites, has led to several research efforts to better understand their formation (Brookins, 1970; Blackburn et al., 2008; Cullers and Berendsen, 2011; Cullers et al., 2012; Kempton et al., 2019a,b; Lee, 2023, and references therein).

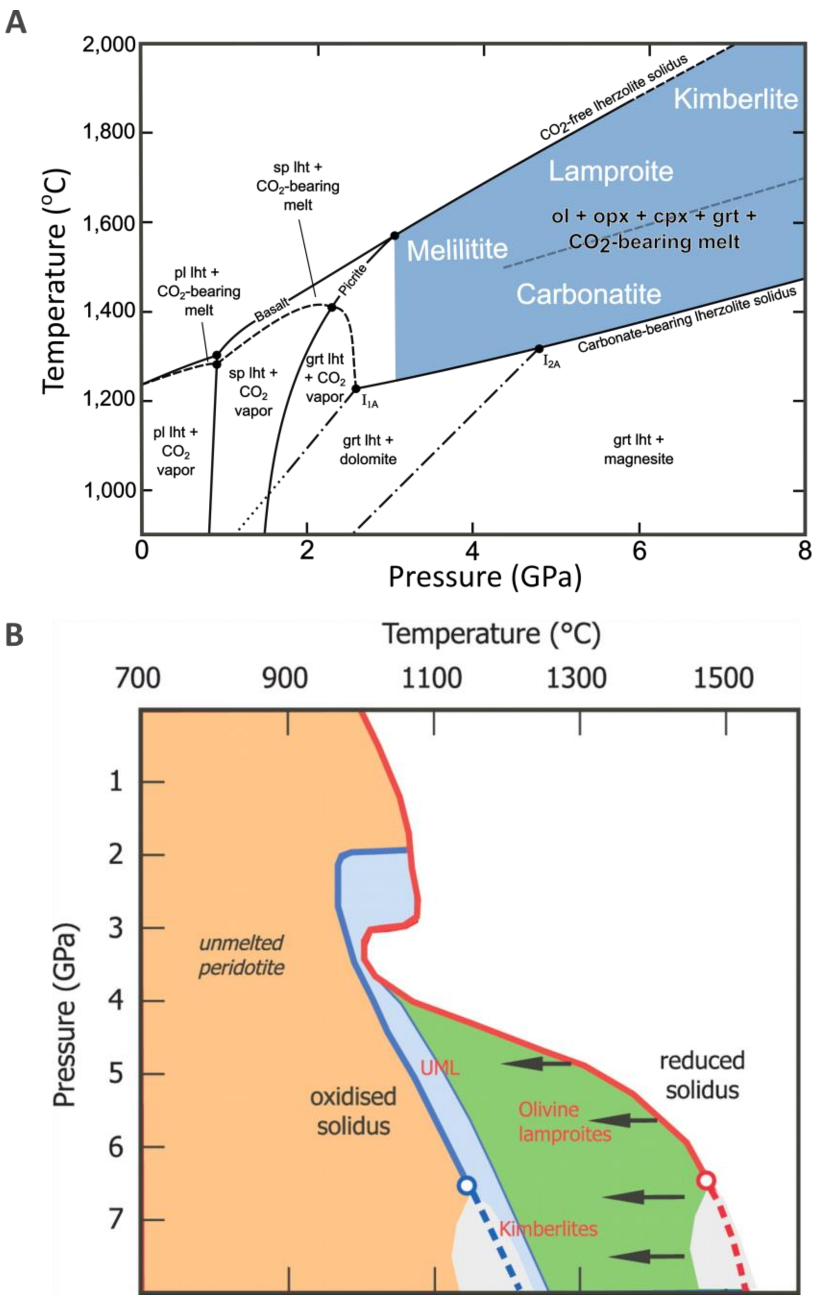

Figure 2. Pressure-Temperature Phase Diagrams

a) Simple pressure-temperature phase diagram of the carbonated mantle (CMAS-CO_2) illustrating conditions necessary for kimberlitic melt formation. Figure modified from Sparks (2013) with the approximate location of lamproite melt generation from Foley (2011). b) A pressure-temperature phase diagram comparing reduced

($CH_4 + H_2O$; after Taylor and Green, 1988; Green and Falloon, 1998) and oxidized ($CO_2 + H_2O$; Foley et al., 2009) melting curves. Arrows indicate an increase in aH_2O, and UML stands for ultramafic lamprophyre. Figure from Foley (2011).

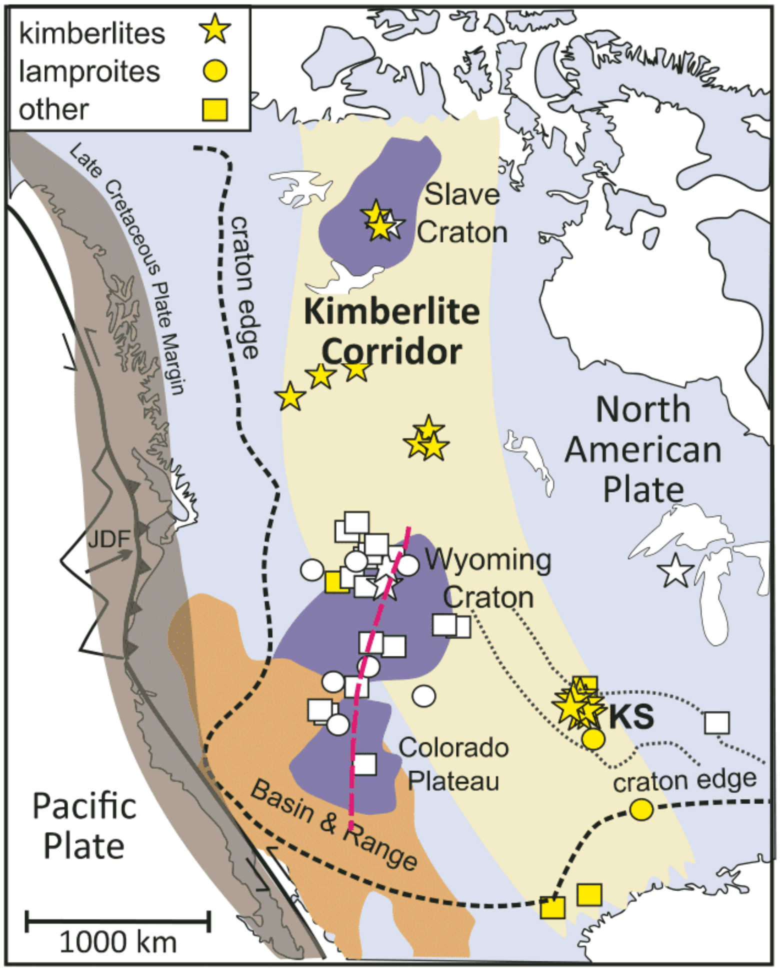

Figure 3. Distribution of Alkaline Igneous Rocks Within North America

A map, adapted by Kempton et al. (2019b) and modified from Currie and Beaumont (2011) and Schaeffer and Lebedev (2014), displaying the location of the alkali igneous corridor also known as the "Kimberlite Corridor" (pale yellow) within North America. The shapes plotted on this diagram represent the locations of known kimberlites (stars), lamproites (circles) and other alkali igneous rocks (squares). The color within these shapes describes whether the rocks are Cretaceous in age (yellow) or not (white). Locations of Archean cratons are dark purple, the Basin and Range in dark orange, and the late Cretaceous plate margin in light brown. Black dashed line represents the location of the North American craton today. The two grey dotted lines denote the approximate location of the border between a deep, sharply defined lithosphere-asthenosphere boundary (LAB) to the east and a shallow, roughly defined LAB to the west. Red dotted line depicts the position of the leading edge of the subducting Farallon around ~100 Ma (after Spasojevic et al., 2009, and Kjarsgaard et al., 2017). The Juan de Fuca plate (JDF) is last remaining (unsubducted) section of the subducted Farallon plate.

In this context, it has been noted that the Kansas lamproites and kimberlites make up the southern end of a north-south trending Mid-Cretaceous 'corridor' of alkaline igneous rocks (Fig. 3) (Kjarsgaard et al., 2017). Various models have been proposed for their formation including association with mantle plumes (Heaman and Kjarsgaard, 2000; Heaman et al., 2003 and 2004; Chu et al., 2013), subduction-related processes (Currie and Beaumont, 2011; Duke et al., 2014), and edge-driven mantle-convection cells (EDC) (Kjarsgaard et al., 2017; Kempton et al., 2019a,b). Each of these models has temporal constraints. As such, accurate information on the age of emplacement is essential for evaluating the viability of each model. Blackburn et al. (2008) determined the emplacement ages of five of the twelve Kansas kimberlites (Tuttle, Stockdale, Baldwin Creek, Bala, and Leonardville) through the (U–Th)/He method applied to the minerals apatite, titanite, zircon, magnetite, and garnet. Their work yielded dates ranging between 110 and 103 Ma for most kimberlites, with one locality (Baldwin Creek) possibly as young as 85 Ma (see detailed review in Section 2.6). However, age constraints for the Kansas lamproites are more limited and less precise, including only three K-Ar analyses of biotite macrocrysts separated from the Hills Pond and Rose Dome localities (Zartman et al., 1967). Therefore, in order to better understand the geodynamic setting responsible for the southern portion of the North American Mid-Cretaceous corridor, better geochronological constraints are needed, particularly for the Kansas lamproites but also for the kimberlites. In this study we present new in situ laser ablation inductively coupled plasma mass spectrometry (LA-ICP-MS) U-Pb ages on perovskites from the Kansas lamproites and kimberlites, focusing primarily on the lamproites as less age data has been published for these localities. We are using perovskites because (a) they are present in both the kimberlites and the lamproites, making age comparison between the two rock types more straightforward; and (b) they are one of the few primary phases to survive the extensive alteration experienced by both rock types. Based on our new data, we have been able to show that (1) the timing of emplacement of Kansas kimberlites and lamproites overlap, but with the earliest kimberlites preceding lamproites by at least 8 m.y., and (2) an edge-driven convection model for the origin of the kimberlites and lamproites is most consistent with available geochronological data. Collectively, these data provide new insights into the origin of alkaline igneous rocks in central North America.

Chapter 2 - Background

2.1 What are Lamproites and Kimberlites?

The name kimberlite was coined by Henry Carver Lewis in 1887 to describe the diamond-bearing rocks mined in Kimberley, South Africa (Dawson, 1980; Mitchell, 1995). Kimberlites are classified as potassic, ultrabasic, volatile-rich (dominantly CO2), silica-undersaturated igneous rocks (Woolley et al., 1996; Blackburn et al., 2008; Kononova et al., 2011; Kjarsgaard et al., 2017). Previously, kimberlites were divided into two groups, based in part on their isotopic compositions (Fig. 4). Group I (archetypal) kimberlites exhibit Sr- and Nd-isotope compositions that suggest contributions from bulk silicate earth (BSE), enriched mantle I (EMI), and/or depleted mantle (DM) reservoirs in their formation, consistent with derivation from asthenospheric mantle (Mitchell and Bergman, 1991; Woolley et al., 1996; Mitchell, 2008; Kononova et al., 2011). Group II kimberlites and orangeites have recently been reclassified as lamproites and lamproite var. Kaapvaal, respectively, due to the similarity in their Sr- and Nd-isotope signatures to bona fide lamproites (Kononova et al., 2011; Scott Smith et al., 2018; Pearson et al., 2019; Mitchell, 2020). The larger range in Sr- and Nd-isotope ratios among lamproites (Fig. 4) suggests derivation from mantle sources that exhibit time-integrated enrichment in Rb relative to Sr (high Sr-isotope ratios) and Nd relative to Sm (low Nd-isotope ratios). Such time-integrated enrichment requires a reservoir that has been isolated from the convecting mantle for long periods of time and is often attributed to lithospheric mantle (Mitchell and Bergman, 1991; Mitchell, 2008; Kononova et al., 2011; Mitchell, 2020).

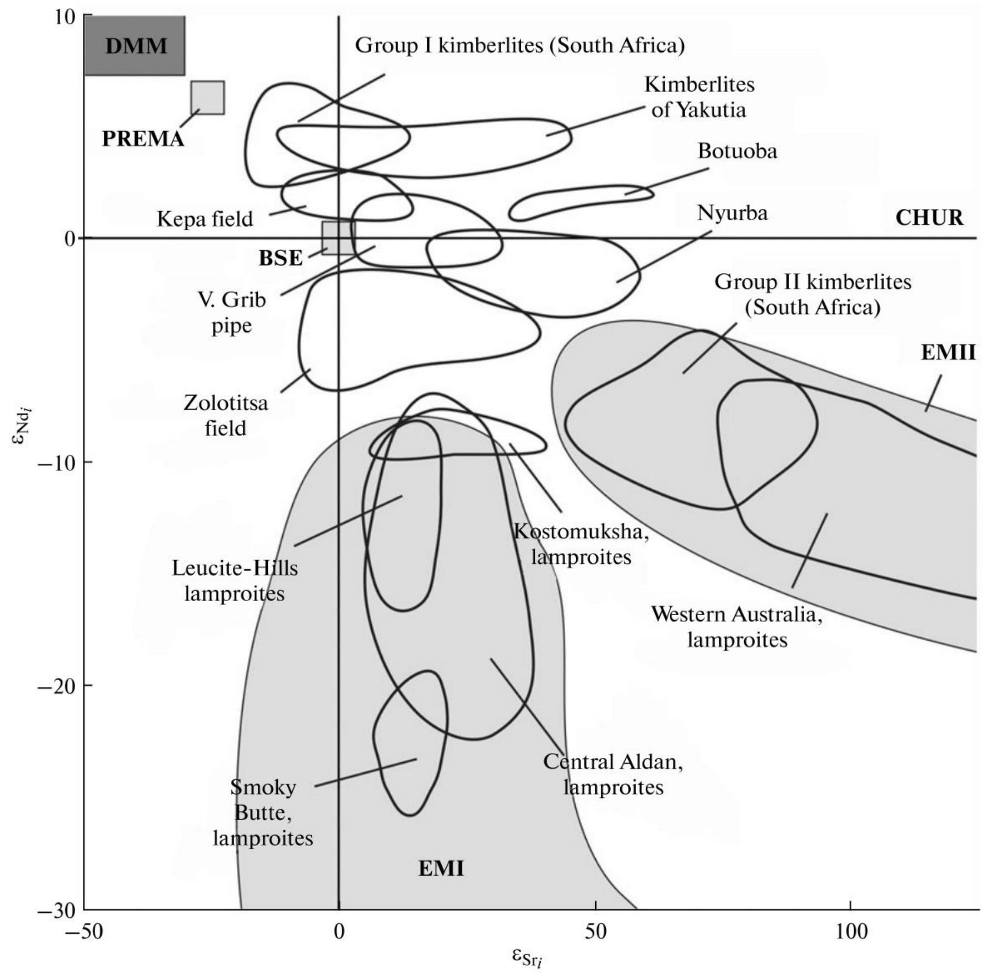

Figure 4. εNd–εSr Diagram

A comparison of lamproite and kimberlite εNd–εSr values by Kononova et al. (2011)

The term 'lamproite' was first introduced into the literature by Niggli (1923). He derived the name from the Greek root, λάμπρος, meaning *glistening*, which refers to the abundance of phlogopite phenocrysts within the rocks (Mitchell and Bergman, 1991; Lustrino et al., 2016; Mitchell, 2020). Despite the definition of lamproite evolving over time, and not every lamproite containing phlogopite, the term has remained in geologic literature (Mitchell and Bergman, 1991; Mitchell, 2020). Today, lamproites are classified as ultrapotassic, peralkaline, undersaturated, and volatile-rich (dominantly H_2O) igneous rocks (Woolley et al., 1996; Mitchell and Chakhmouradian, 1999; Fritschle et al., 2013). Compared to kimberlites, lamproites are a more diverse rock group characterized by wide variations in geochemistry, mineralogy, and texture caused by derivation from a variably metasomatized (lithospheric) mantle source, variations in the depth and extent of partial melting, the differing degrees of fractionation they undergo prior to final crystallization, and the number of phases that crystallize from such diverse melts (Woolley et al., 1996; Kononova et al., 2011; Mitchell, 2020). As mentioned above, the wide variation in Sr- and Nd-isotopic compositions, as well as elevated $^{87}Sr/^{86}Sr$ ratios, indicates they are sourced from the heterogenous non-convecting lithospheric mantle (Fig. 4) (Mitchell and Bergman., 1991; Mitchell, 2008; Kononova et al., 2011). Moreover, lamproite enrichment in potassium and incompatible trace elements suggests derivation from K-Ti-Ba-REE rich veins, or metasomes, within the subcontinental lithospheric mantle (SCLM) (Mitchell and Bergman, 1991; Mitchell, 2020; Sarkar et al., 2022). A singular simple petrogenic model cannot be devised for lamproite formation, as each lamproite's geologic location differs according to its tectonic setting and geochemical evolution. Each lamproite field reflects the age, modification, and variability of the metasomatic source; as well as the variable partial melting processes and contributions of asthenosphere, lithosphere, and/or recently subducted (Tertiary) material (Mitchell, 2020).

Unlike most rocks, lamproites and kimberlites cannot be identified in the traditional sense through simple modal bulk mineralogical assemblages due to their fine-grained textures and complex mineralogy that includes a plethora of xenocrystic and cryptogenic material (Mitchell, 2008; Mitchell, 2020). Instead, these hybrid rock types are discerned via mineralogical-genetic classification schemes (e.g., Scott Smith and Skinner, 1984; Mitchell and Bergman, 1991; Woolley et al., 1996; and Tappe et al., 2005) that focus on the primary mineral assemblages whose compositions reflect their parental magma (Mitchell, 2020). This includes minor, trace, and accessory phases. Due to their complex hybrid nature, propensity for alteration, and history of locality specific names, the identification and distinction between these rock types, in addition to other rare alkaline rocks (leucitite, minette, and lamprophyres), has been, and still remains, difficult (Mitchell, 2020).

2.2 Pressure, Temperature, and Compositional Conditions of Formation for Lamproites and Kimberlites

The pressure and temperature conditions required for formation of kimberlitic and lamproitic melts, as well as the parental compositions of both kimberlites and lamproites, remain subjects of debate. Mitchell and Bergmann (1991) believe that phlogopite lamproites are closest in composition to a lamproite parental magma, whereas Foley (2011) proposed that olivine lamproite represents the most unevolved lamproite composition. Figure 2b suggests that olivine lamproite melts can be produced under reducing conditions at pressures ≥ 4 GPa and temperatures ≥ 1050 ˚C, indicating melting can occur anywhere between 120-300 km (Foley, 2011). In contrast Figure 2a suggests that kimberlitic melts are produced under oxidizing conditions at pressures ≥ 6 GPa and temperatures ≥ 1500 ˚C (Sparks, 2013). However, addition of volatiles, such H2O or F, or mantle compositions that are more Fe, P or alkali (Na, K) rich, can lower the solidus by ~100˚C, simulating conditions more consistent with the base of the continental lithosphere (i.e., depths of about 150 km and temperatures: 1,350-1,450˚ C) (Gaetani and Grove, 1998; Priestly et al., 2006; Sparks, 2013).

2.3 Perovskite

Perovskites with the ABO_3 structure (i.e., oxide single perovskites) are the most abundant naturally occurring species of the perovskite supergroup and are common within undersaturated alkaline rocks (Mitchell et al., 2017; Locock and Mitchell, 2018). Although they are considered a ubiquitous accessory phase within kimberlites, perovskites are only found within the olivine and madupitic lamproite varieties (Mitchell and Reed, 1988; Mitchell and Chakhmouradian, 1999). It typically occurs throughout the crystallization sequence as discrete groundmass grains; however, they can also be found as poikilitic plates or intergrowths with other oxide minerals (Mitchell, 1996; Tappe and Simomnetti, 2012). Within alkaline rocks, perovskite group minerals serve as the primary host for REE, especially LREE. While lamproite and kimberlite perovskites have similar REE distribution patterns, those within lamproites tend to have higher Sr and Ce contents (Mitchell and Bergman, 1991 (Fig.5). The higher Sr contents are due to the preference of Sr to partition into carbonates. Therefore, alkaline silicate rocks which lack primary carbonates, such as lamproites, are able to contain Sr-rich perovskite (Mitchell, 1997; Mitchell and Chakhmouradian, 1999).

As a result of the perovskite structure's tolerance to distortions, extensive solid solution is possible on the A (Ca, Sr, Na, K, REE, Ba, Pb, Th, Y) and B (Ti, Zr, Nb, Sn, Si, Mg, Al, Sc, Cr, Mn, Fe, Hf, Ta, U) cation sites (Mitchell, 1996; Locock and Mitchell, 2018). This results in wide compositional variations, especially within the tausonite-perovskite-lueshite-loparite ($SrTiO_3$-$CaTiO_3$-$NaNbO_3$-$REETi_2O_6$) quaternary system, which serve as sensitive indicators of magmatic differentiation (Fig. 6) (Mitchell and Vladykin, 1993; Mitchell and Chakhmouradian, 1999; Locock and Mitchell, 2018). Perovskite compositions are typically depicted in the following subsystems: (1) lueshite-loparite-perovskite, (2) perovskite-loparite-tausonite, and (3) lueshite-loparite-tausonite (Mitchell, 1996). The latter ternary is rarely used, as there is little to no known solid solution between lueshite and tausonite or lueshite and loparite (Mitchell, 1996).

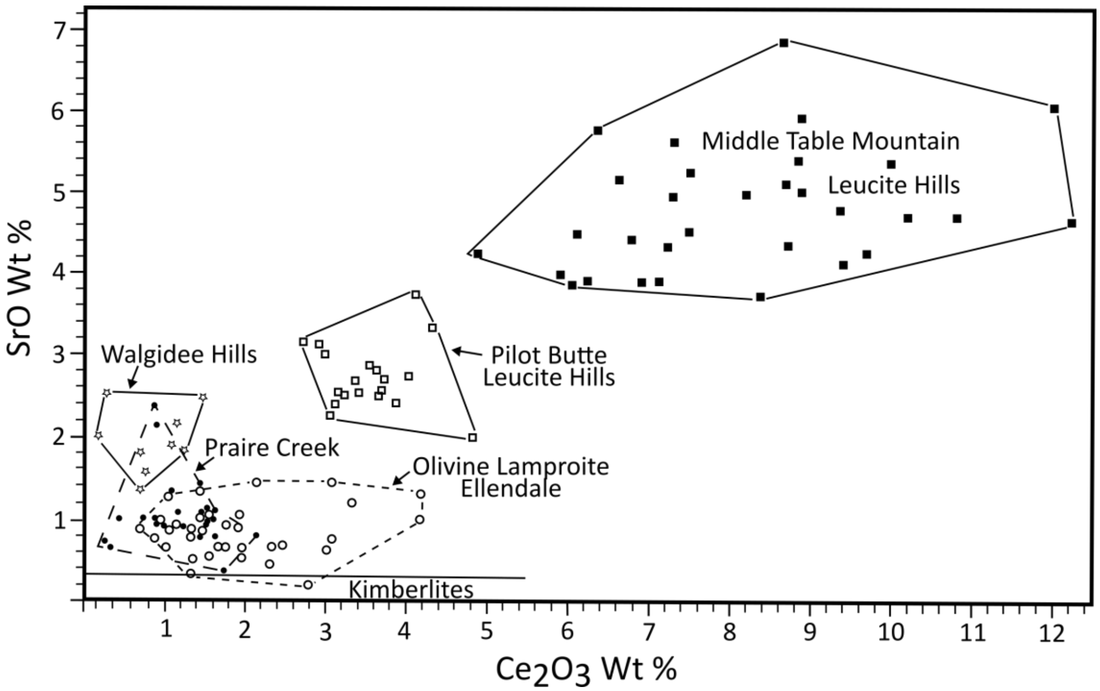

Figure 5. SrO vs Ce_2O_3 Diagram

Variation of SrO vs Ce_2O_3 wt% within perovskites from kimberlites and lamproites, modified from Mitchell and Bergman (1991).

Natural perovskites within the perovskite-tausonite-lueshite ternary system have not yet been found. Figure 6 illustrates that kimberlite perovskites tend to have ≥ 90 mol% $CaTiO_3$ with minor cation substitution, resulting in < 7 mol% of other endmembers, mainly lueshite and loparite (Chakhmouradian and Mitchell, 2000). In contrast, perovskites from more evolved alkaline rocks exhibit extensive solid solution (Fig. 6).

Perovskite has been used for the U-Pb geochronology of kimberlites and other alkaline rocks as (1) it is typically an early crystallizing groundmass phase and, thus, records the primary geochemical and isotopic signature of the alkaline magma (Wu et al., 2010; Tappe and

Simomnetti, 2012); (2) it contains an abundance of U (20–200 ppm) and Th (>500 ppm), ideal for U-Pb dating (Heaman et al., 2019); (3) it is unlikely to originate from entrained crustal material due to its paucity in crustal rocks (Heaman et al., 2019); and (4) its relative abundance in alkaline rocks allows it to be dated *in situ* via LA-ICP-MS (Li et al., 2010).

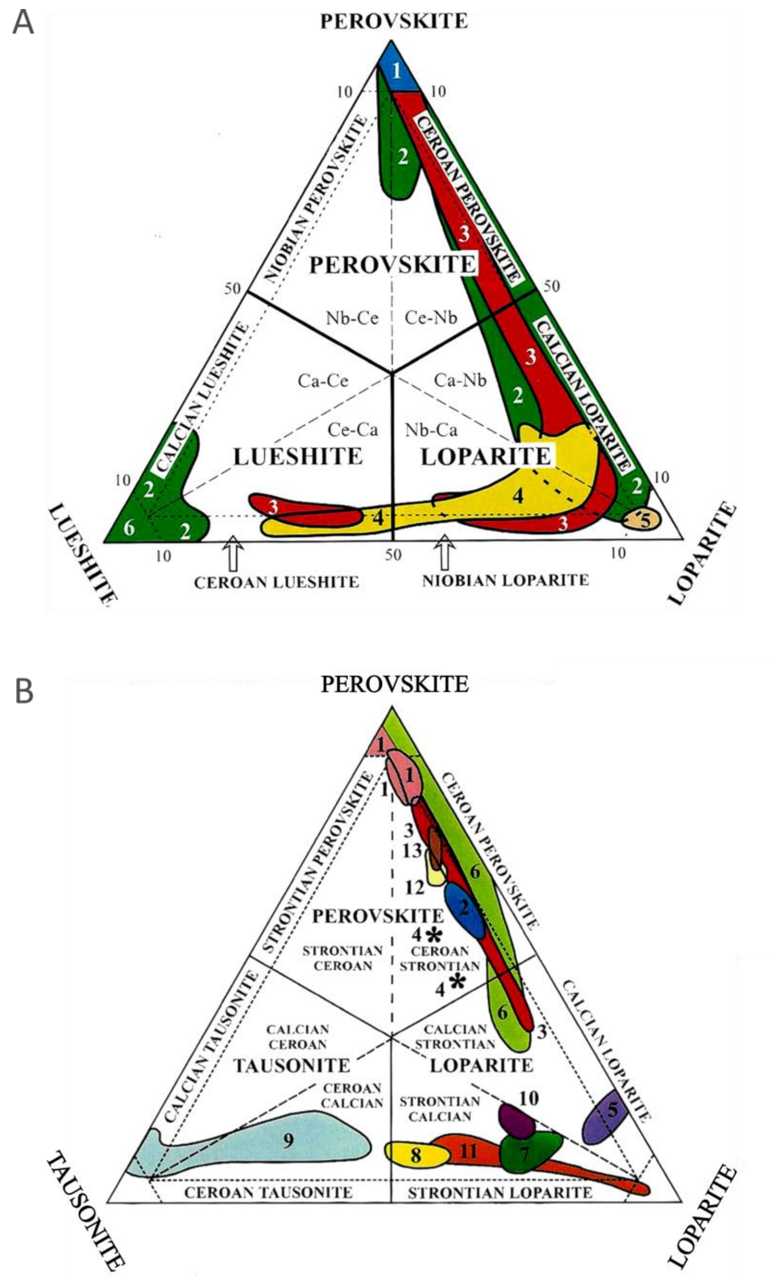

Figure 6. Perovskite Ternary Diagrams

Comparison of the compositional variation (mol. %) of perovskite group minerals from a variety of rock types within the $NaNbO_3$-$NaREETi_2O_6$-$CaTiO_3$ (lueshite-loparite-perovskite) (A) and $SrTiO_3$–$NaREETi_2O_6$–$CaTiO_3$ (tausonite–loparite– perovskite) (B) ternary systems from Mitchell (2017). The numbered fields in figure A are as follows: (1) kimberlites; (2) alkaline ultramafic rocks and carbonates; (3) Khibinia nepheline syneites and ijolites; (4) Lovozero nepheline syneites and urtites; (5) Burpala albitites and aegirinites; (6) Lueshe carbonatite. In figure B: (1) olivine lamproite; (2) Middle Table Mountain; (3) Hills Pond; (4) Oldoinyo Lengai; (5) Lovozero; (6) Khibinia; (7) Salitre; (8) Sarambi; (9) Murun; (10) Gordon Butte; (11) Pegmatite Peak; (12) Sover North; (13) Besterskraal.

U-Pb analysis of perovskite, however, presents two main challenges: (1) the small grain size and (2) the high common Pb (5-80% of total Pb) component, which can result in the age calculations being sensitive to the initial common Pb correction (Wu et al., 2010, Stamm et al.,2018; Heaman et al., 2019).

2.4 Kansas Lamproites and Kimberlites

Numerous kimberlites and lamproites have been identified in eastern Kansas. In the northeast, twelve kimberlite pipes occur in Riley and Marshall counties, whereas to the southeast two lamproite localities occur between Woodson and Wilson counties (Fig. 7). Figure 8 shows that the kimberlites were emplaced between the Mid-Continent Rift System (MCR) (a Proterozoic, failed rift system that appears as a high Bouguer gravity anomaly in the sub-surface) and the crest of the Nemaha uplift (a late Paleozoic fold and reverse fault structure) (Bunker et al., 1988; Berendsen, 1997; Kempton et al., 2019a,b). The kimberlites intruded into limestones and shales of the lower Permian Chase group along the southeastern margin of the Abilene anticline (Brookins, 1970; Mansker et al., 1987; Blackburn et al., 2008). Five of the twelve kimberlites (Bala, Leonardville, Randolph #1 and Randolph #2, and Stockdale) are exposed at the surface while the rest (Tuttle, Winkler, Lonetree, Antioch, Baldwin Creek, Fancy Creek, and Swede Creek) are covered by glacial till and colluvium up to 7.6 m thick (Brookins, 1970;

Blackburn et al., 2008; Kempton et al., 2019b) (Fig. 9).The localities included in this study are Bala and Tuttle (Fig. 9).

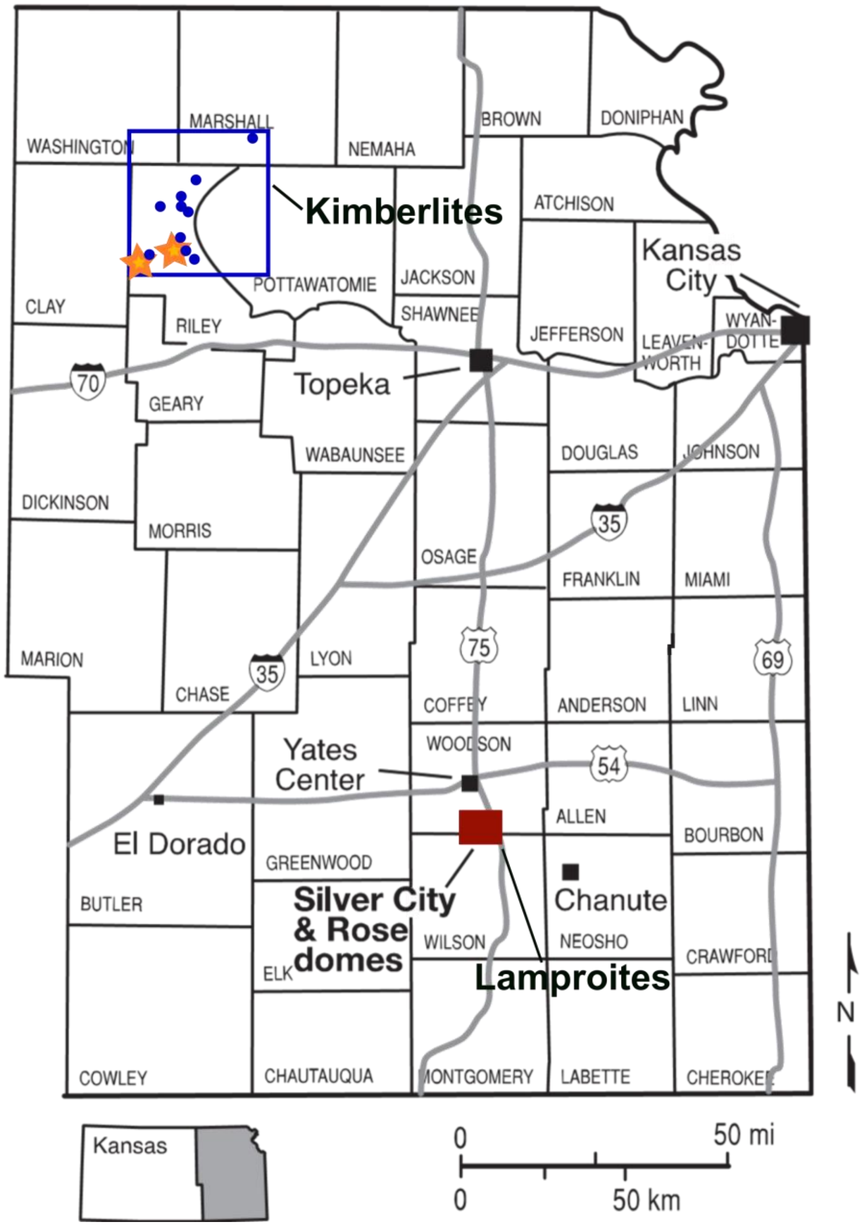

Figure 7. Kansas Kimberlite and Lamproite Location Map

County map of eastern Kansas indicating the locations of the twelve Kansas kimberlites as blue and orange circles and stars within a blue square, and the location of the two lamproites marked by the filled in red square. The two kimberlites marked in orange represent the kimberlite pipes analyzed in this study, Tuttle and Bala. Figure modified from Berendsen (2011).

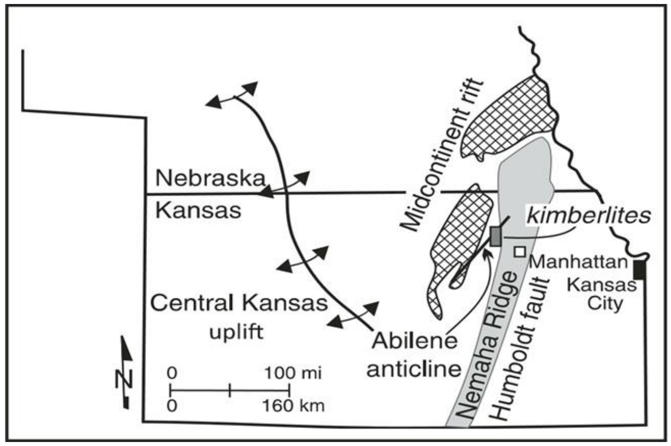

Figure 8. Major Geologic Structures of Kansas and Nebraska

A map of the major structures in Kansas from Kempton et al. (2019b), modified from Steeples and Brozius (2014).

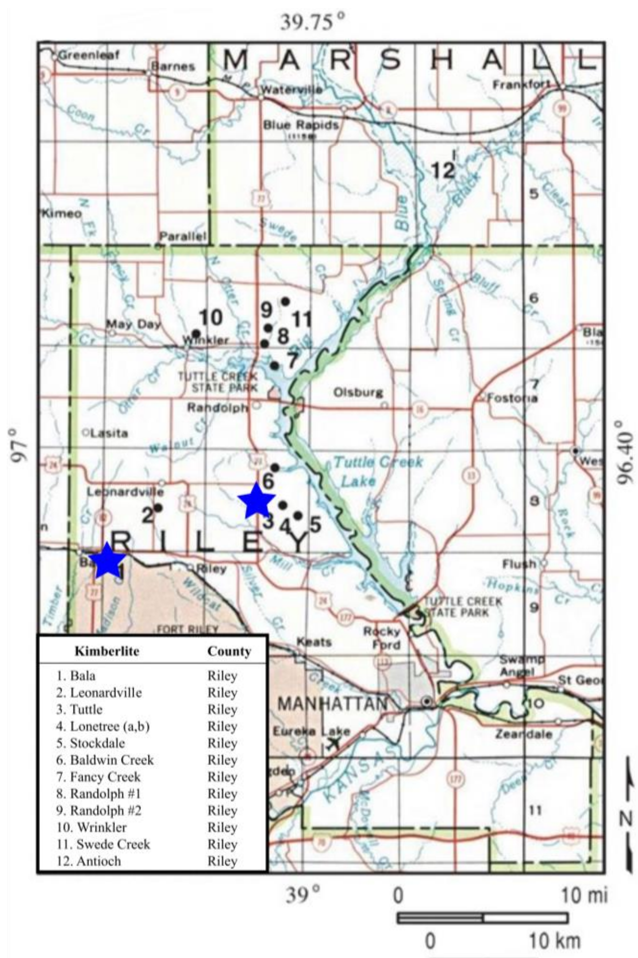

Figure 9. Location of the Bala and Tuttle Kimberlites

Kimberlite location map from Kempton et al. (2019b), modified from Cullers et al. (2012). The Bala and Tuttle localities are marked with a blue star.

The Hills Pond and Rose Dome lamproites occur 200 km to the SE of the kimberlites (Fig. 7). They intruded into and uplifted the local Upper Pennsylvanian limestones, sandstones, and shales, creating domal structures referred to as the Silver City Dome and Rose Dome, respectively (Fig. 10) (Wagner, 1995). Both domes have similar surficial morphology in that they are elliptical in shape (4.8 x3.2 km) and are aligned in a generally northeastern direction, with the major axis of the Silver City Dome trending east-northeast and the major axis of the Rose Dome trending northeast (Berendsen, 2011). The Hills Pond lamproite is exposed at the surface and is currently mined for weathered phlogopite by Micro-Lite LLC for use as Mg, K, and Fe supplements in cattle feed (Benedictis et al., 2008). The Rose Dome lamproite is overlain by ≤ 5.2 m of sedimentary rocks and was discovered through the granite boulders it rafted from the basement to the surface as well as shallow auger and drill holes (Mitchell and Bergman 1991; Berendsen, 2011).

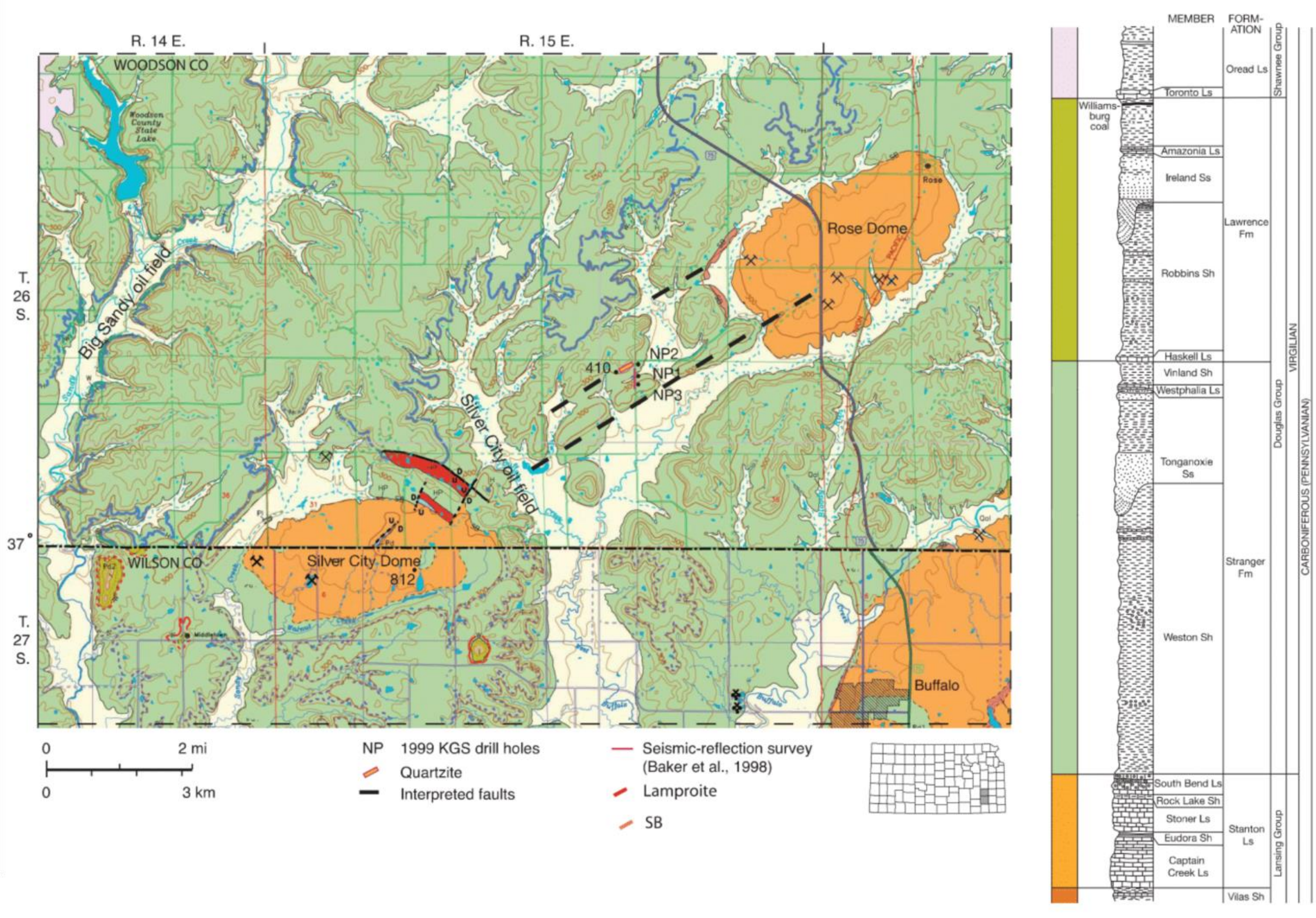

Figure 10. Geology Surrounding the Kansas Lamproites

Topographic map, from Berendsen (2011), showing the general subsurface and surficial geology of the area as well as the location of Silver City and Rose Domes, and Hills Pond lamproite, Kansas. Crossed hammers indicate quarry locations, and SB stands for the Spring Branch Limestone member. On the right is the stratigraphy of the area.

2.5 Comparison of the Kansas Lamproites and Kimberlites

2.5.1 Structure and Facies

Both the Kansas kimberlites and lamproites took advantage of previously established structural features (i.e., NNE and NW trending faults) to facilitate their injection into the crust. Indeed, the proximity of both rock types to the regional NNE and NW trending faults (Fig. 11), and the reactivation of the faults throughout time suggests that both alkaline magmas utilized these faults for access to the surface (Berendsen, 1978; Wilson, 1979; Berendsen and Blair, 1986). Furthermore, the trends of the structural axes of the lamproites and the ESE magmatic trend of the kimberlites parallel the regional fault trends (Dreyer, 1947; Cook 1995; Dowell, 1964; Brookins, 1970; Berendsen 1978; Berendsen, 2011).

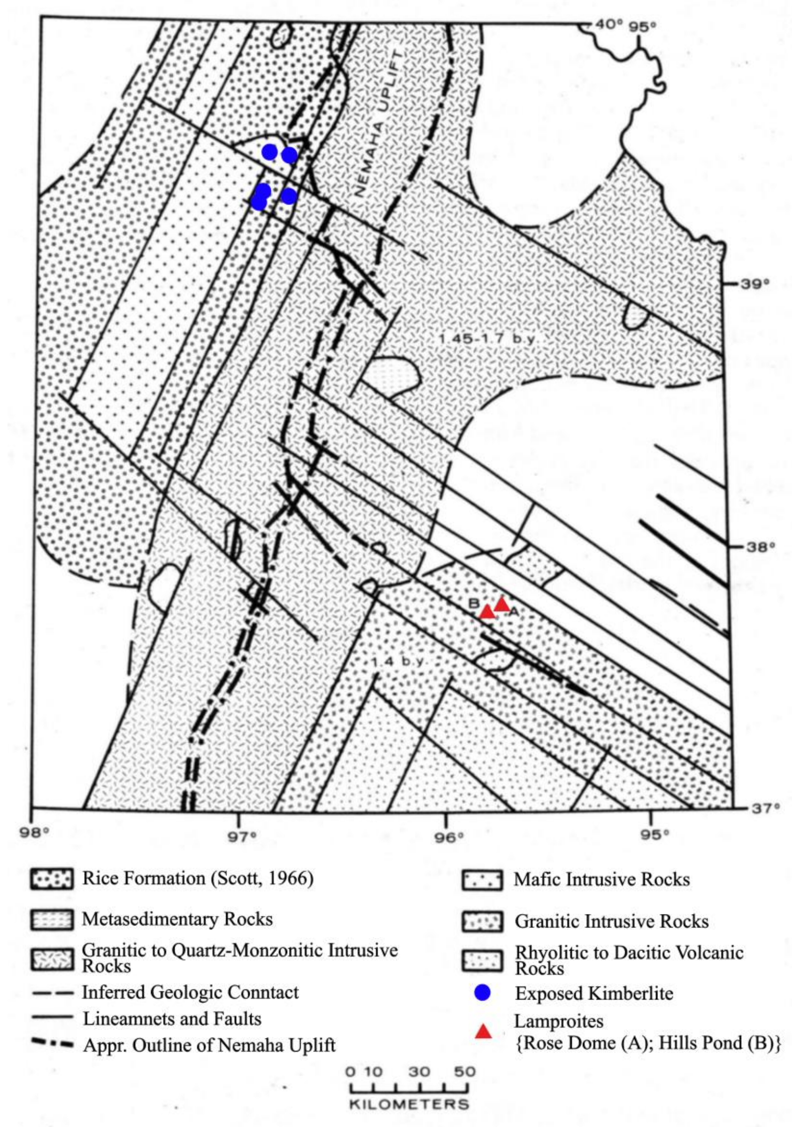

Figure 11. Lineaments and Faults of Eastern Kansas

Interpretation of the structural features, adapted from Berendsen et al. (1978) and modified from Bickford et al. (1979), of the Precambrian basement rocks in eastern Kansas. Blank areas represent areas where the basement rock composition is unknown.

Morphologies of emplacement for the Kansas kimberlites and lamproites differ significantly. In general, kimberlites occur as pipe-like bodies, and the kimberlites of Kansas are no exception. They can be subdivided into three facies or two subgroups (Mitchell 1986; Mitchell 1995; Kjarsgaard 2007; Mitchell et al., 2019) (Fig. 12). The facies approach is a textural-genetic classification scheme devised by Clement and Skinner (1979,1985), and Clement (1982). It divides the kimberlites into (i) the upper *crater facies*, which contains layers of pyroclastic and resedimented volcaniclastic rocks; (ii) the *diatreme facies,* a cone-shaped structure with steeply dipping sides (80-85˚); and (iii) the *hypabyssal facies,* which begins at the root zone where the diatreme extends into a network of sills and dikes (Mitchell 1986; Mitchell 1995). The non-genetic approach subdivides the kimberlite into 2 groups based on the difference in texture and mineralogy: (i) volcaniclastic kimberlite (VK) is characterized by fragmented rocks and (ii) hypabyssal kimberlite (HK) is made up of non-fragmental rocks (Mitchell 1995; Kjarsgaard 2007). The most common facies represented in the Kansas kimberlites is the upper brecciated section of the diatreme facies (Blackburn et al., 2008). The two kimberlite localities analyzed as part of this study, i.e., Bala and Tuttle, have been previously classified as hypabyssal and diatreme facies, respectively (Blackburn et al., 2008). Therefore, the Bala pipe is considered a HK and the Tuttle pipe a VK.

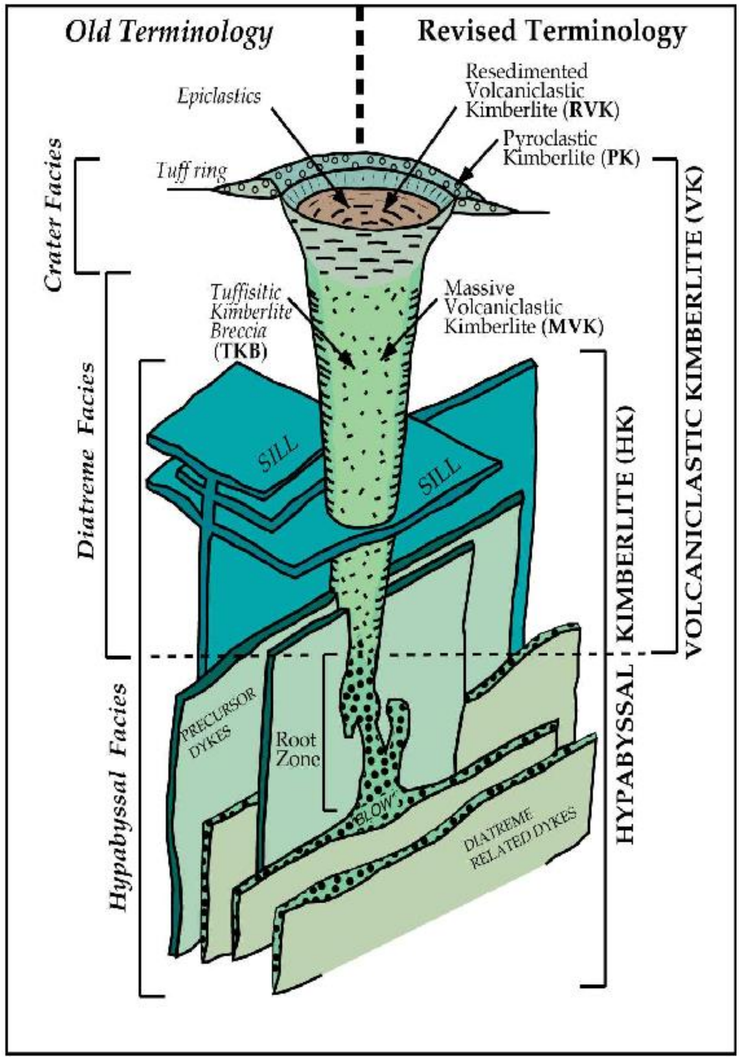

Figure 12. Kimberlite Morphology Model

Kimberlite morphology model divided based on the older facies approach on the left and the more modern non-genetic approach on the right. Diagram from Kjarsgaard (2007) modified from Mitchell (1986)

In contrast to kimberlite vent morphology, which is generally carrot shaped with 2-3 km of vertical flaring and ~ 82˚ dipping margins, lamproites are typically champagne glass or funnel shaped with 0.5-1 km of vertical flaring and gradually dipping margins (25-60˚) (Mitchell 1986; Mitchell and Bergman, 1991). Mitchell and Bergman (1991) created a textural-genetic classification scheme for lamproites similar to the facies classification for kimberlites (Clement and Skinner, 1979; 1985; and Clement, 1982) and basalts (Cas and Wright, 1987) (Fig. 13). The classification scheme divides the lamproites into four facies. The lava facies (1) occurs at the top. It is interlayered with the *crater and pyroclastic facies* (2), which forms early and is intruded by the later-stage hypabyssal facies (3). *The hypabyssal facies* consists of both fragmented and non-fragmented rocks within a network of sills and dikes. The fourth, and rarest, facies is the *plutonic facies* (4); it is deepest and consists of the coarsest grained material. Both the Hills Pond and Rose Dome lamproites represent hypabyssal facies rocks with each locality consisting of multiple, stacked sills (Mitchell and Bergman, 1991).

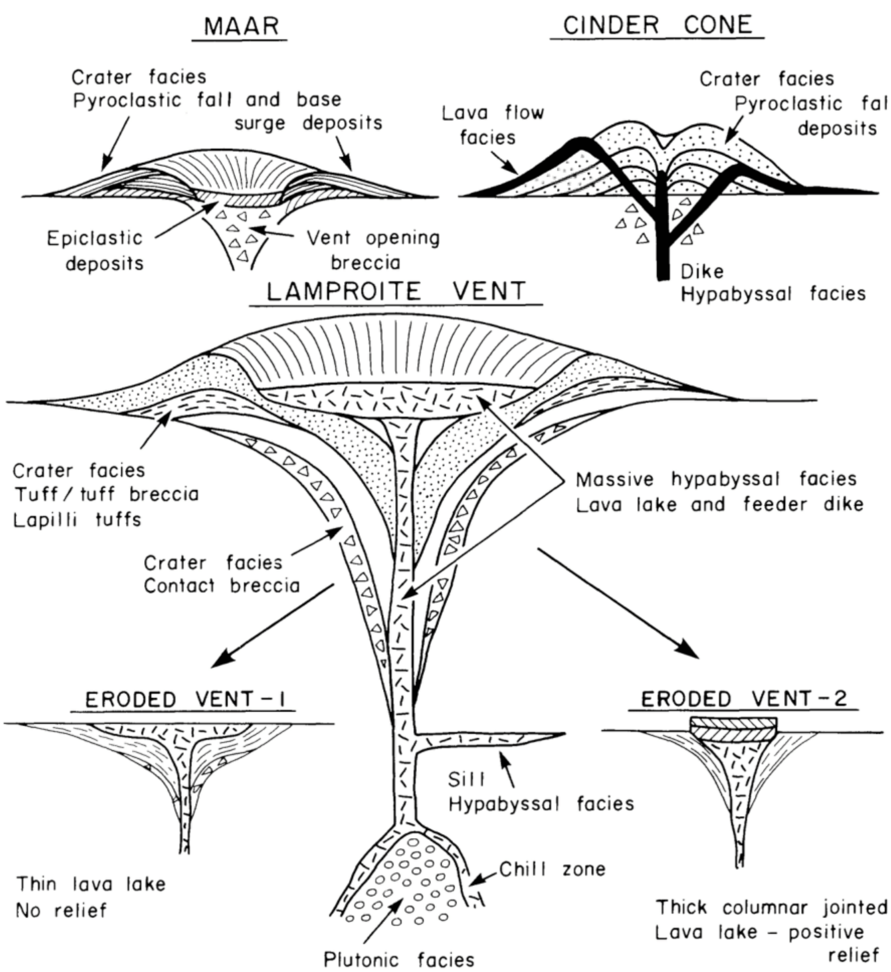

Figure 13. Lamproite Morphology Models

Idealized morphology diagram from Mitchell and Bergman (1991) showing the relationships between the lava, crater and pyroclastic, hypabyssal, and plutonic facies lamproites in a few vent complexes. Also shown are models of lamproite vents after erosion of the maar crater.

Over the years various drilling projects have occurred at the Silver City and Rose Dome localities in order to better understand the petrogenesis of the associated lamproites as well as to prospect for oil. In 1958, the Kansas Geological Survey (KGS) drilled nine holes (1M-7M and 1A-2A, Fig. 14), two of which (1A-2A) were offset, to determine the extent of the Hills Pond lamproite.

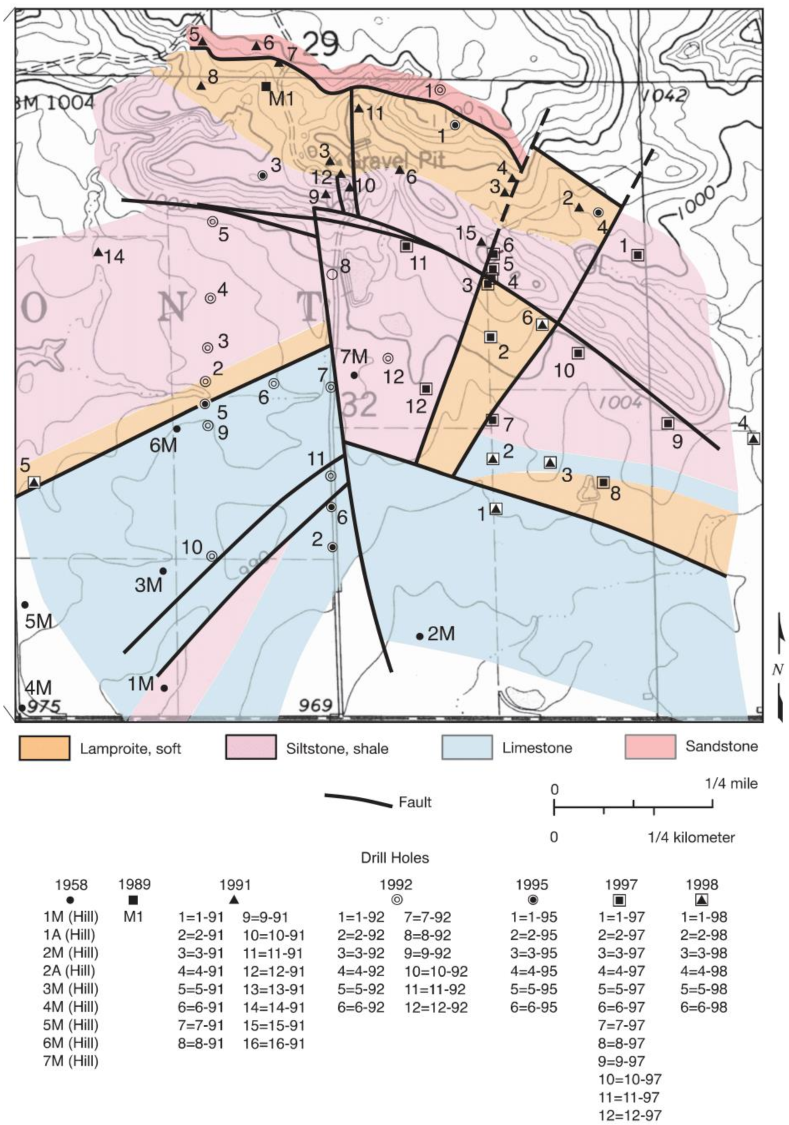

Figure 14. Locations of the Lamproite Cores Drilled Between 1958-1998

Map from Cullers and Berendsen (2011) of the Silver City Dome depicting and listing the Hills Pond lamproite cores drilled between 1958-1998. Drill hole 1A was drilled in the same location as 1M and drill hole 2A was drilled 9m southwest of hole 2M.

An additional five cores were drilled in 1967, one of which, Hase No. 1, encountered the thickest lamproite (58m) sill yet discovered at Silver City (Fig. 15). In the 1980's, due to the discovery of the Silver City oil field four decades earlier, 26 more oil exploration holes, including the Guess and Ecco Ranch cores (Table 1), were drilled along the eastern flank of the Silver City Dome to explore the southern extent of the oil field (Fig. 15)

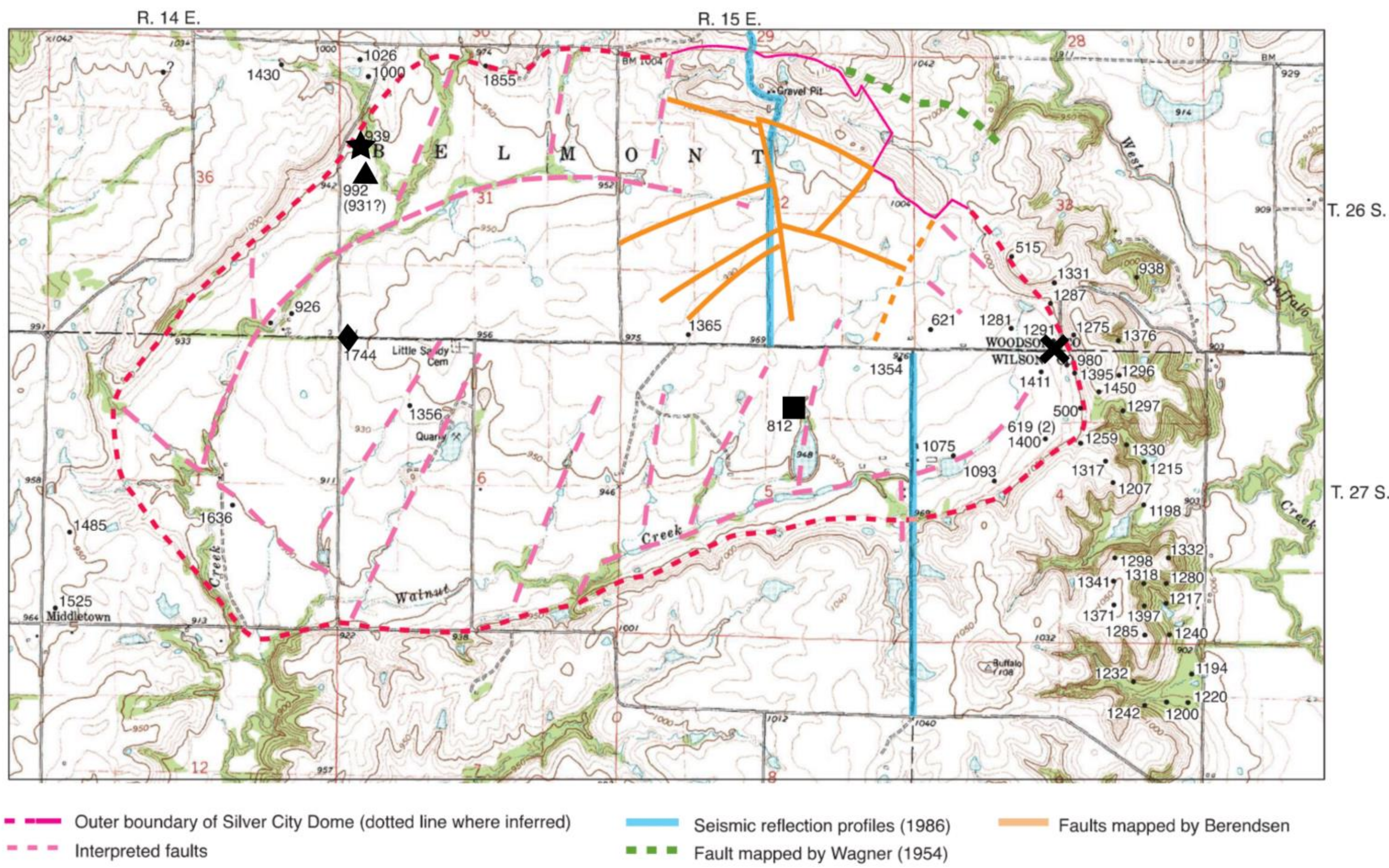

Figure 15. Map of the 1967 Cores Drilled at Hills Pond

Topographic map of the Silver City Dome showing the locations of drill holes and interpreted faults, modified from Berendsen (2011). The key drill holes mentioned in Table 1 are represented by different shapes while those not mentioned are represented as black dot with the total depth labeled beside it.

Table 1. 1967 Hills Pond Core Data

Lamproite sills in key commercial drill holes labeled in Fig. 15, modified from Berendsen (2011). Questions marks indicate information that may be more imprecise than the rest.

Drill Hole Name	Location	Depth (ft)	Approximate Thickness (ft)	T.D (ft)	Map Symbol
1 Ecco Ranch, Inc also called #1 ecco ranch	sec. 33, T. 26 S., R. 15 E. SE SE SW	374–400 428–432 458–484 520–531 602–616 755–786	26 4 26 11 14 31	1291	X
Guess No.1	sec. 31, T. 26 S., R. 15 E. S2 NW	884-992	100-108	992	Triangle
Guess No.2	sec. 31, T.26S., R.15E.	824–920 1000-1023	96-100 23	931 1023?	
Guess No.3	sec. 31, T. 26 S., R. 15 E. NW SW NW	870–939	30- 69	939	Star
Hase No. 1	sec. 6, T. 27 S., R. 15 E. NW NW NW	915–1105	190	1744	Diamond
Ecco Ranch #1	sec. 5, T. 27 S., R. 15 E. SW NW NE	49–70.5 255–256 313.5–317.5 408–408.5 577?–583? 691–692 734.5–743 744-745.5 758-758.5 771–778.5 781-790 798-812	21.5 1? 4 Trace 6 1 8.5 1.5 0.5 7.5 9 14	812	Square

Lamproite sills were identified at various depths within all 26 drill holes and sill thickness was observed to be variable, ranging from 0.3 to 32m (Berendsen, 2011). However, there exists some uncertainty on the number and thickness of the sills encountered in each core because (1) the lamproite was impossible to recognize on electric logs, (2) only a few geologists were trained to identify lamproite in the borehole cuttings, (3) the lamproites contained abundant xenoliths of the country rock, and (4) they were associated with a thick zone of contact metamorphism. From 1991-1998, KGS and Micro-Lite, LLC collaborated to better understand the origin, thickness, and continuity of the Hills Pond sills through the drilling and coring of 52 bore holes (Fig. 14) (Berendsen, 2011). Based on the data collected, it was determined that the variable thicknesses of the sills (0.3 - 58m) have no relation to depth and are frequently displaced by high angle normal or reverse faults, making correlation between sills difficult. Furthermore, no appreciable evidence was found to show whether the sills thin or swell, although all but one sill appear to dip (1.5˚-5.5˚) to the north; the anomalous sill dips 2˚ to the south. A project of similar extent was never completed at Rose Dome, as there were a limited number of oil exploration holes (Fig. 16) drilled and financial support was lacking. From 1964-2002 only seven drill holes (DHH1-5, and Eagle cores, see Table 7 from Cullers and Berendsen, 2011) on Rose Dome encountered lamproite sills, each with a thickness of at least 20m.

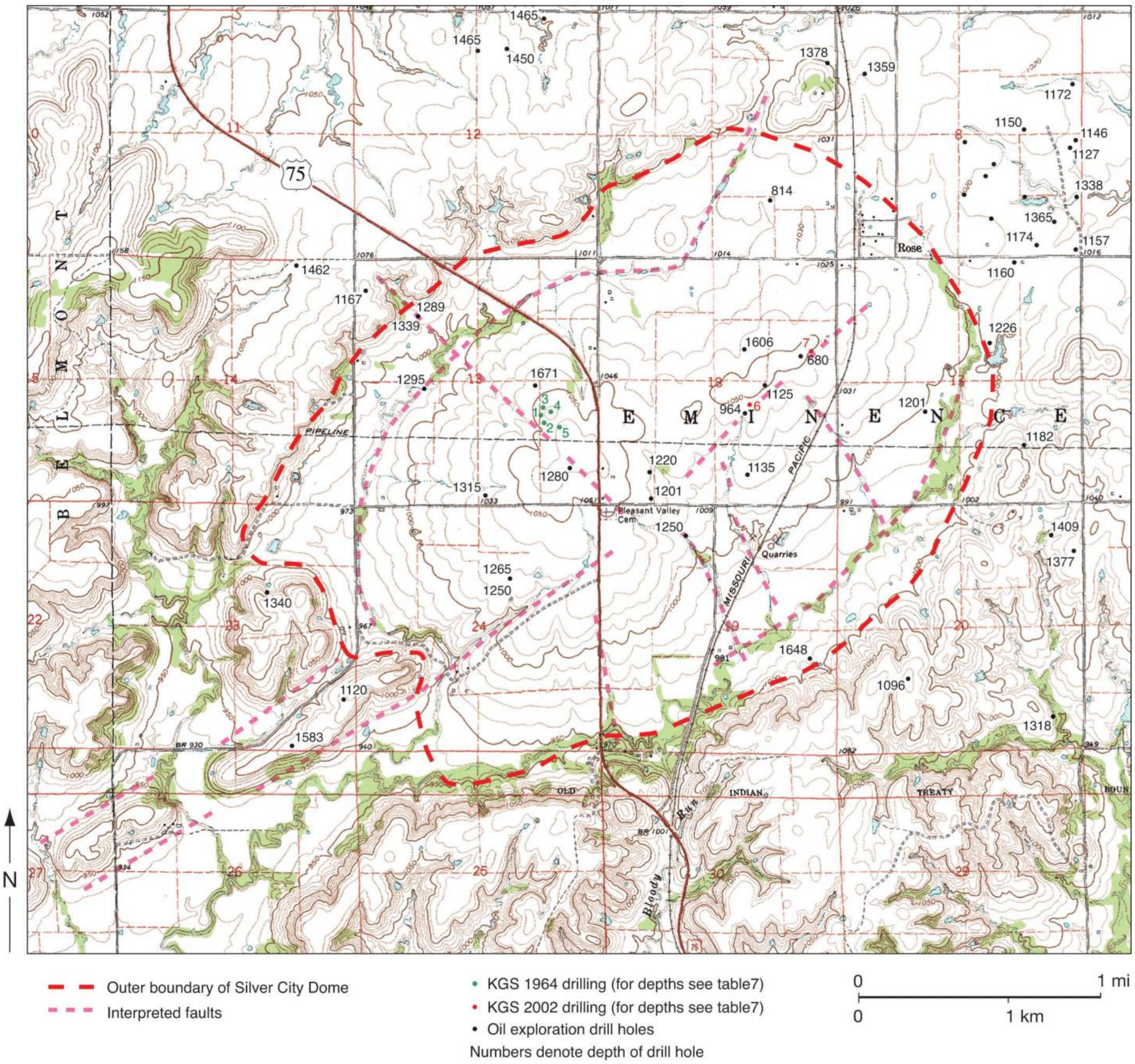

Figure 16. Locations of the Rose Dome Cores

Topographic map of the Rose Dome showing the locations of drill holes and interpreted faults, from Berendsen (2011). The DDH 1-5 cores are labeled in green, and the Eagle cores 4,5,6, and 7 in red.

2.5.2 Mineralogy and Petrology

The Hills Pond lamproite is porphyritic, consisting of the primary phases phlogopite, olivine (now totally serpentinized), diopside, K-richterite, K-Mg arfvedsonite, chrome spinel, sanidine, as well as the accessory phases perovskite, apatite, wadeite, magnetite, xenotime, shcherbakovite, pectolite, Ca-Si zeolite, titanite (sphene), rutile, and feldspar in a serpentinized groundmass (Cullers et al., 1985, 1996; Cullers and Berendsen, 2011) (Fig. 17). Primary mineral phases at Rose Dome include serpentinized olivine and phlogopite with accessory diopside, K-richterite, shcherbakovite, spinel, perovskite, apatite, wadeite, magnetite, ilmenite, (and garnet according to Coopersmith and Mitchell, 1986) in a serpentinized groundmass (Cullers et al., 1985; Cullers and Berendsen, 2011). Xenolithic material includes fragments of the country rock (sandstone, shale, and limestone) as well as Precambrian granite (Wagner, 1995). The granite xenoliths are larger and more abundant at Rose Dome. The only mention of granite from Hills Pond includes a report by Wagner (1995), who describes a granite-like material in a prospect pit, and a paper by Berendsen and Blair (1988), who describe centimeter-sized granite xenoliths within a core from the NW side of the Silver City dome. Many different sill cores have been given different compound names, following the scheme of Mitchell and Bergman (1991) (e.g., Table 2) due to the varying abundance of different minerals between and among sills. The Hills Pond lamproite had been referred to as a richterite-diopside-madupitic lamproite (Mitchell, 1985), madupitic-richterite-diopside-phlogopite-olivine lamproite (Cullers et al. 1985; Mitchell and Bergman, 1991), and olivine-phlogopite-richterite-diopside-madupitic lamproite (Mitchell and Bergman, 1991). Cullers et al. (1996) classified the Guess core as a sanidine lamproite and the Ecco Ranch Core as a richterite-sanidine or sanidine richterite lamproite. The Rose Dome lamproite has been referred to as a carbonated olivine-phlogopite (richterite-diopside?) lamproite (Mitchell and Bergman, 1991) as well as a madupitic lamproite (Bergman, 1987). For the purposes of this paper, we will refer to the Kansas lamproites as olivine-bearing madupitic lamproites, based primarily on the presence (and abundance) of poikilitic groundmass phlogopite (Mitchell, 1985; Bergman, 1987; Mitchell and Bergman, 1991).

Figure 17. Hills Pond Core Samples

Photo of the 92-5 Hills Pond core between a depth of 71'6" to 80'3" with a quarter for scale. Notice the serpentinized phenocrysts in a variably altered groundmass.

Table 2. Mineralogical-Genetic Classification Scheme

Mineralogical classification scheme for lamproites with their principal minerals listed to demonstrate how they are used to create a modern compound name. Table modified from Mitchell and Bergman (1991) and Mitchell (2020). Abbreviations as follows: opx, orthopyroxene; ol, olivine; amp, amphibole; cpx, clinopyroxene; phl, phlogopite; leu, leucite; san, sanidine.

	PRINCIPAL MINERALS									
HISTORICAL NAME	**opx**	**ol**	**amp**	**cpx**	**phl**	**leu**	**san**	**Occurrence**	**Originator**	**Compound Name**
WYOMINGITE				**X**	**X**	**X**		**Leucite Hills**	**Cross (1897)**	**Diopside Leucite Phlogopite Lamproite**
ORENDITE				**X**	**X**		**X**	**Leucite Hills**	**Cross (1897)**	**Diopside Sanidine Phlogopite Lamproite**
MADUPITE				**X**	**X**			**Leucite Hills**	**Cross (1897)**	**Diopside Madupitic Lamproite**
CEDRICITE				**X**		**X**		**West Kimberley**	**Wade and Prider (1940)**	**Diopside Leucite Lamproite**
MAMILITE			**X**			**X**		**West Kimberley**	**Wade and Prider (1940)**	**Leucite Richterite Lamproite**
WOLGIDITE			**X**	**X**	**X**	**X**		**West Kimberley**	**Wade and Prider (1940)**	**Diopside Leucite Richterite Madupitic Lamproite**
FITZROYITE				**X**	**X**	**X**		**West Kimberley**	**Wade and Prider (1940)**	**Leucite Phlogopite Lamproite**

In general, the Kansas kimberlites are porphyritic with phenocrysts of forsteritic olivine as well as smaller amounts of pyroxene, magnetite, ilmenite, pyrope garnet, phlogopite, perovskite, zircon, apatite, titanite, melilite, and chromite within a serpentine and calcite groundmass (Brookins, 1970; Blackburn et al., 2008; Kempton et al., 2019a,b). Most olivine and pyroxenes have been altered to serpentine and/or calcite (Brookins, 1970; Kempton et al., 2019a,b). Xenoliths of serpentinized peridotite, dunite, or kimberlite autoliths, as well as shale and limestone country rock, make up 60-70% of the material; other sedimentary or metasedimentary xenoliths are rare (Brookins, 1970; Cullers et al., 2012). The Tuttle kimberlite contains modally abundant xenoliths of all types (~70% of the mode), whereas the Bala kimberlite only contains moderate amounts of crustal xenoliths (≤ 20% of the mode) (Cullers et al., 2012, Rogers et al., in prep.) (Fig. 18). Brookins (1970) divided the Kansas kimberlites into two petrological groups: micaceous and non-micaceous (lamprophyric). One of each is represented in the two kimberlites selected for this study. The Tuttle kimberlite is classified as a micaceous kimberlite, whereas the Bala kimberlite is considered non-micaceous (Brookins, 1970; Cullers et al., 2012). The micaceous variety is characterized by an abundance of primary phlogopite, pyrope garnet, ilmenite, anhedral to subhedral olivine, xenoliths and calcite veins as well as rare pyroxenes. The non-micaceous variety is characterized by an abundance of euhedral olivine, pyroxene, and apatite, with fewer xenoliths and calcite veins, fewer and smaller ilmenite crystals, and fewer phlogopite grains most of which is limited to the groundmass (Brookins, 1970). Despite the petrologic complexity of the rocks—and the use of outdated, ambiguous naming conventions as described above—it has been demonstrated geochemically that all of the

Kansas kimberlites are archetypal kimberlites (Kempton et al., 2019a), i.e., those formerly referred to as Group I.

Figure 18. Kimberlite Core Samples

A) Bala core photo, sample 16/39, showing the macrocrysts of olivine pseudomorphs and the lack of crustal xenoliths. B) Photo of the Tuttle core at a depth of 297' 0", note the abundance of xenoliths and xenocrysts. Photos produced by KayLeigh Rogers.

2.5.3 Geochemistry

The Kansas lamproites are compositionally consistent with their intraplate tectonic setting, displaying low CaO (<10 %) and Al_2O_3 (< 11.5%) concentrations (Cullers and Berendsen, 2011) (Fig. 19). Typical of low degree partial melts, the Kansas lamproites (and kimberlites) are more enriched in light rare earth elements (LREE) relative to heavy rare earth elements (HREE) (Fig. 20). Figure 20 shows that the Kansas lamproites have small depletions in Ta and Nb, which in combination with a negative Ti anomaly, are attributed to fractionation of a Ti-rich mineral, e.g., perovskite. Enrichment in Ba is typical of lamproites (Pearson et al., 2019) and may be the result of its enrichment in the metasomatized lithospheric mantle source (Fig. 20).

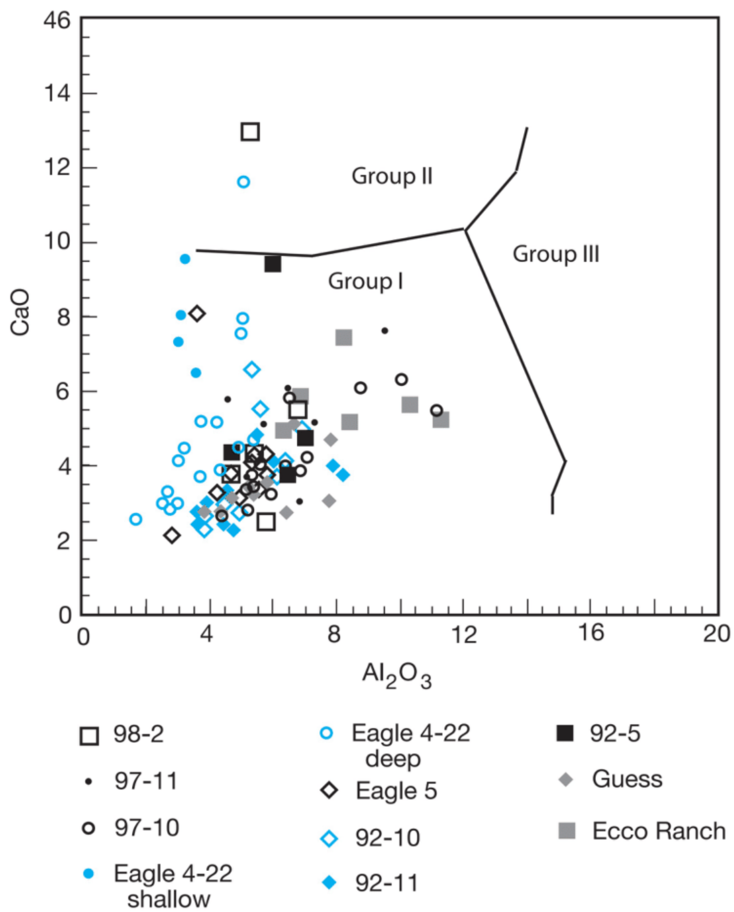

Figure 19. CaO vs Al_2O_3 Diagram

Whole rock compositions of Kansas lamproites in CaO vs Al_2O_3 space. The group 1 field corresponds to lamproites formed in continental settings, group 2 form in continental rift zones, and group 3 form in regions with active orogenies. Figure from Cullers and Berendsen (2011).

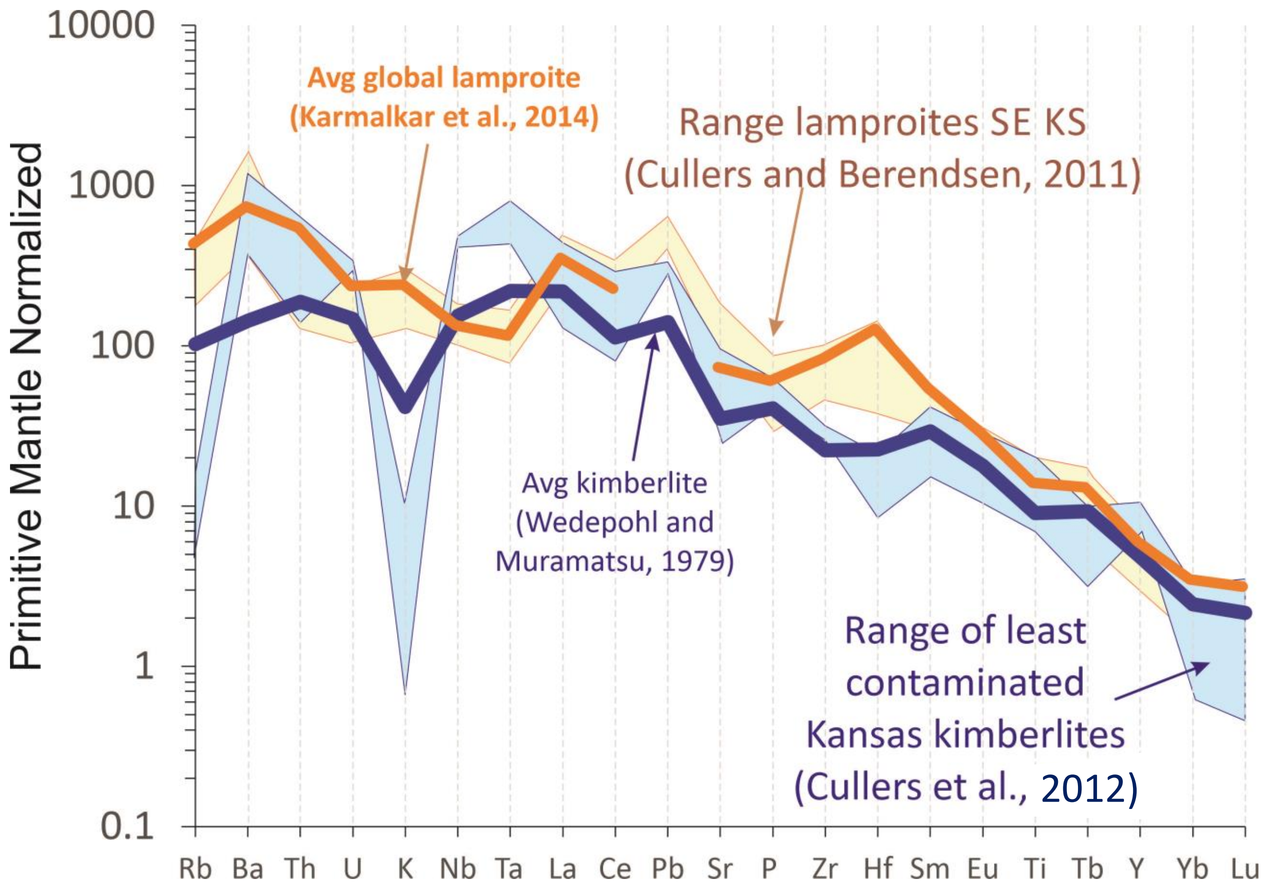

Figure 20. Comparison of Previously Published Trace Element Data for the Kansas

A primitive mantle normalized incompatible element plot (normalizing values from Sun and McDonough, 1989) displaying the difference between the range of compositions for least contaminated Kansas kimberlites (Cullers et al., 2012), the average kimberlite value proposed by Wedepohl and Muramatsu (1979), the average lamproite composition from Karlmalkar et al. (2014), and range of Kansas lamproites (Cullers and Berendsen, 2011).

Within each of the Hills Pond lamproite sills, vertical variations in composition and mineralogy are observed and interpreted as evidence for mineral gravity settling, flow differentiation, and/or volatile transport processes (Cullers et al., 1985; Cullers and Berendsen, 2011) (Fig. 21). The Rose Dome lamproites show an increase in carbonate content and a loss of primary minerals toward contacts with limestone, indicating chemical alteration has occurred. Due to this contamination, it is difficult to interpret vertical variation based on geochemistry alone, but processes mineralogically similar to those occurring at Silver City appear to have occurred (Cullers et al, 1985; Cullers and Berendsen, 2011). Whole rock analyses from shallow (T.D: 21-89.9 m) Hills Pond cores (series 92, 97, and 98) are compositionally similar to one another except for concentrations of Na_2O, Li, and Cs (see Table 4 from Cullers and Berendsen, 2011).

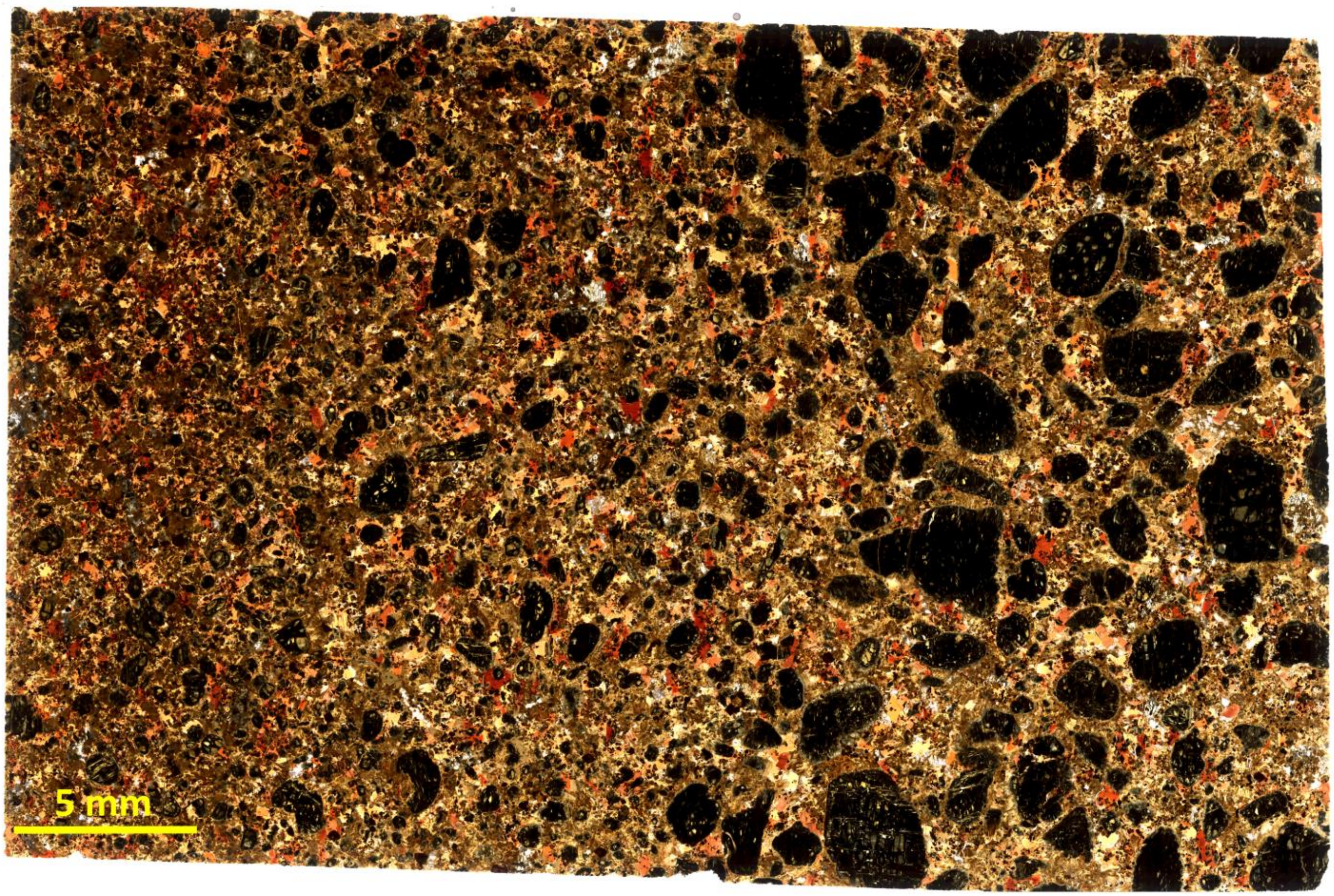

Figure 21. RDLE4-C442 Photomicrograph

Rose Dome Eagle 4 thin section (RDLE4-C442) photomicrograph in plane polarized light.

Samples from two deeper Hills Pond lamproite cores, referred to as the Guess (305-312 m) and Ecco Ranch (237.5-247.5 m) cores, have higher concentrations of K_2O, Rb, Hf, Zr, Y, and LREE and lower concentrations of MgO and lower Mg numbers than the shallower cores (see Table 5 from Cullers and Berendsen, 2011). Additionally, the Guess core material has higher TiO_2, total Fe_2O_3, and Th, whereas the Ecco Ranch core material has higher SiO_2 and Al_2O_3 concentrations than the shallower Hills Pond samples (see Table 5 from Cullers and Berendsen, 2011). Overall, the Hills Pond lamproites are considered SiO_2 rich and MgO poor compared to the Rose Dome lamproites, which is interpreted by Cullers and Berendsen (2011) as evidence for lower temperature melting of a higher proportion of vein material, enriched in Rb, Ba, Th, U, K, Ta, Nb, and the LREE, relative to lherzolite-harzburgite in the mantle source. Furthermore, the deeper Hills Pond cores generally have higher proportions of these trace elements than the Rose Dome cores (Fig. 22). However, the shallow Hills Pond cores do not display such a straightforward difference, as a few of these cores are lower in Th, U, Ta, Nb, and La than the Rose Dome cores, indicating that the metasomatized source may be compositionally heterogeneous and/or different magmatic processes affected the compositions (Cullers and Berendsen, 2011).

The Rose Dome lamproites are most similar to the shallow Hills Pond cores; but their concentrations in SiO_2, TiO_2, Al_2O_3, Na_2O, K_2O, Hf, and Li are lower and their concentrations in total Fe_2O_3, MgO, P_2O_5, Th, Co, Ni, Cr, U, Y, REE, Cu, and Cs are higher (see Tables 4 and 5 from Cullers and Berendsen, 2011). According to Cullers and Berendsen (2011), the higher concentrations of MgO and lower concentrations of Al_2O_3 and SiO_2 in the Rose Dome lamproites relative to those from Hills Pond are a result of a lower ratio of vein material to lherzolite-harzburgite melted to form this lamproite.

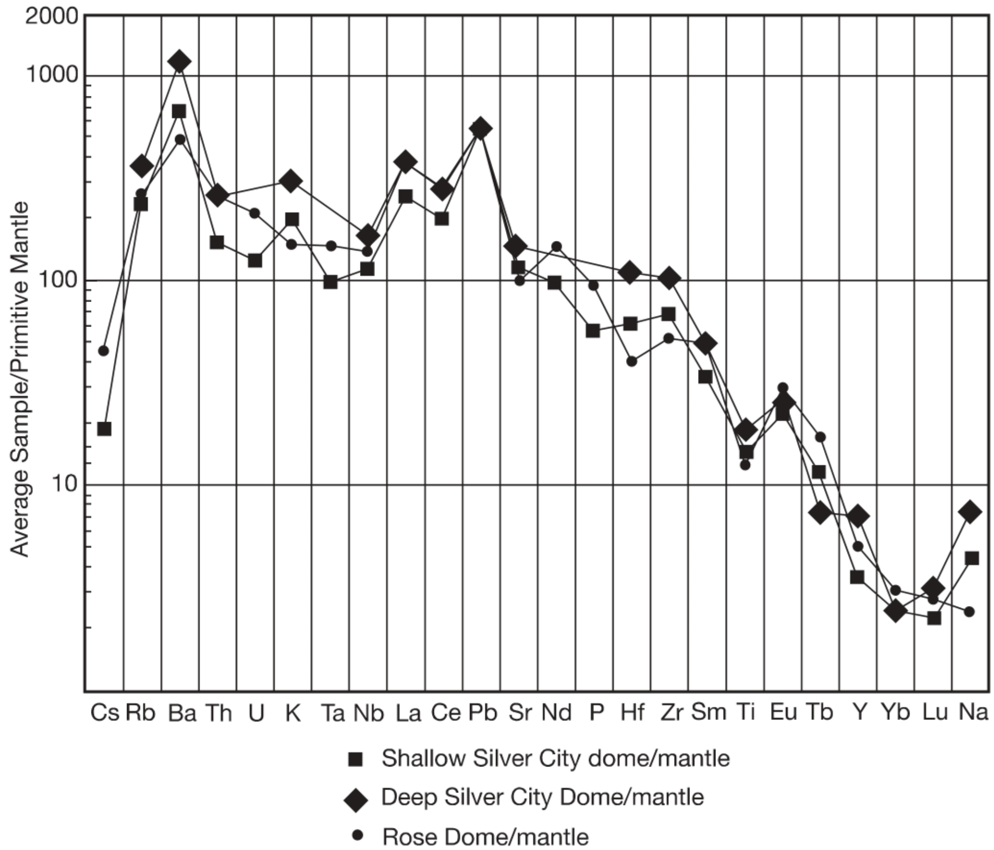

Figure 22. Kansas Lamproite Spider Diagram

A primitive mantle normalized multi-element plot of the average elemental values of the Silver City and Rose Dome lamproites from Cullers and Berendsen (2011). Normalizing values from McDonough et al. (1992).

Due to the extensive alteration of all the Kansas kimberlites, most studies focus on the geochemistry of specific constituent minerals rather than whole rock analyses. However, a few studies have analyzed and reviewed the whole rock geochemistry either through generalization or focusing on the least altered of the Kansas kimberlites (Brookins, 1970; Cullers et al.,1982; Cullers et al., 2012). Compared to average kimberlite (Wedepohl and Muramatsu, 1979), the Kansas kimberlites have higher concentrations of CaO and CO_2 and lower SiO_2, K_2O and Na_2O due to interaction with the surrounding calcareous country rocks (Brookins, 1970; Cullers et al., 1982). Figure 20 shows that the incompatible trace element patterns for the least altered of the

Kansas kimberlites are similar to the average global kimberlite composition. The concentrations of K and Rb are anonymously low, and this has been attributed to phlogopite, K-richterite and/or some other K-rich minerals mostly remaining in the source during melting (Mitchell, 1995; Cullers et al., 2012). In contrast, enrichments in Ba, Th, Nb, La, and Ce have been interpreted as evidence for there being no residual minerals retaining these elements during melting of the enriched source (Mitchell, 1995; Cullers et al., 2012).

As previously stated in Section 2.5.2, the Kansas kimberlites have previously been divided into two groups based on their abundance of primary phlogopite: micaceous which include the Stockdale, Leonardville, Wrinkler, Baldwin Creek, and Tuttle kimberlites; and non-micaceous which include the Bala, Antioch, Randolph No. 1 and 2 kimberlites (Brookins, 1970; Cullers et al., 1982; Cullers et al., 2012). Geochemically, micaceous and non-micaceous kimberlites differ in that the non-micaceous variety has higher REE, Ba, Th, Hf, Sc, and Ta concentrations, whereas micaceous kimberlites typically contain more CaO, CO_2, and K_2O. Contrary to expectations, given their abundance of phlogopite, the micaceous kimberlites also contain less H_2O (Brookins, 1970; Kempton et al., 2019a). Cullers et al. (1982) suggested that the difference in REE contents between the two kimberlite types is due to small variations in small degrees of partial melting. As incompatible elements tend to decrease in concentration with increased melting, non-micaceous kimberlites may represent smaller degrees of melting than micaceous kimberlites.

2.6 Previous Geochronology

Previous geochronological work on the Kansas kimberlites was conducted by Blackburn et al. (2008) who determined the emplacement ages of five of the twelve Kansas kimberlites (Tuttle, Stockdale, Baldwin Creek, Bala, and Leonardville) through the (U–Th)/He method on apatite, titanite, zircon, magnetite, and garnet (Table. 3). He also applied the Rb–Sr method to phlogopite and clinopyroxene for the Tuttle and Baldwin Creek kimberlites to verify the emplacement ages with a more traditional geochronological method.

Table 3. Previous Geochronology of the Kansas Kimberlites

Summary of the various isotope systems and phases utilized by Blackburn et al. (2008) to date the Kansas kimberlites.

	Method	Mineral	n	Mean Age (Ma)	Uncertainty
Tuttle					
	(U-Th)/He	Zircon	10	108.6	9.6
	(U-Th)/He	Apatite	9	67.2	5.1
	(U-Th)/He	Titanite	14	103.9	14.1
	(U-Th-[Sm])/He	Garnet	9	98.8	8.9
	Rb-Sr	Phlogopite/Clinopyroxene	5 and 1	106.6	1
Stockdale					
	(U-Th)/He	Titanite (not abraded)	5	102.9	11
	(U-Th)/He	Titanite (abraded)	4	106.4	3.1
	(U-Th)/He	Zircon	5	78.2	6.4
	(U-Th)/He	Apatite	9	73.4	4
Baldwin Creek					
	(U-Th)/He	Apatite	3	85.5	2.3
Bala					
	(U-Th)/He	Magnetite	11	97.1	8.7
	(U-Th)/He	Apatite	5	64.3	5.6
Leonardville					
	(U-Th)/He	Apatite	8	66.1	8

They found that emplacement occurred between 110-103 Ma for most of the kimberlites, although the Baldwin Creek and Leonardville kimberlites yielded ages of ~88-85 Ma based on (U-Th)/He on apatite and Rb–Sr on phlogopite. However, these younger ages may be unreliable, as the quality of apatite from both localities was suspect and the initial Sr isotope composition of the phlogopite from Baldwin Creek was very high ($^{87}Sr/^{86}Sr_{(i)}$ = 0.75), indicating crustal contamination (Blackburn et al., 2008; Kjarsgaard et al., 2017). Additionally, Blackburn et al.

(2008) found that many of the apatites, which have closure temperatures around ~70 ˚C, yielded younger ages (~65 Ma). Blackburn et al. (2008) interpreted this as evidence for a reheating event that reset the apatite (U–Th)/He radiogenic clock (Farley, 2000; Blackburn et al., 2008). A few titanite analyses from Tuttle and metamict zircons from Stockdale also yielded slightly younger ages at 67.2 ± 5.1 Ma and 78.2 ± 6.4 Ma, respectively, despite these minerals having slightly higher helium closure temperatures, i.e., titanite closing at ~200 ˚C and crystalline zircon at ~180 ˚C (Reiners and Farley, 1999; Reiners et al., 2002, 2004). Therefore, they too were interpreted as having been affected by the reheating event. The only kimberlite of the five to not show evidence of a reheating event is the Baldwin Creek kimberlite (Blackburn et al., 2008; Kjarsgaard et al., 2017).

Although the mineralogy, geochemistry, and stratigraphy of the lamproites have been explored (Cullers et al., 1985; Mitchell and Chakhmouradian, 1999; Berendsen, 2011; Cullers and Berendsen, 2011), considerably less research has been done on determining their ages, with most studies assuming emplacement ages similar to those of the Riley County kimberlites 200 km to the northwest. The only geochronological work on the Kansas lamproites was done over 50 years ago by Zartman et al. (1967), who included it as part of a broader study of alkaline intrusions from across the central and eastern United States, from Kansas to New Jersey. They reported K-Ar dates of 90-91 ± 5 and 88 ± 4 Ma for phlogopite from the Hills Pond and Rose Dome lamproites, respectively. However, after recalculation with updated decay constants following Dalrymple (1992) and Nebel et al. (2011), the Hills Pond lamproite yields an age of 92-93 ± 5 Ma while the Rose Dome yields an age of 90 ± 4 Ma (Table 4). Unlike the other micas Zartman et al. (1967) analyzed, they were unable to verify the K-Ar ages of the Kansas lamproites using Rb-Sr geochronology, because of their very high Sr contents and, hence, low

Rb/Sr ratios. This suggests that the mica analyzed was partially altered. Indeed, replacement of mica by chlorite is common in the Hills Pond lamproite (Berendsen, 2011; Cullers et al., 1985).

Table 4. Recalculated Zartman et al. (1967) Lamproite Ages

The conversion table, from Dalrymple used to recalculate the ages reported by Zartman et al. (1967) with updated decay constants. The multiplication factor used was 1.026.

Sample Number	Location	K_2O, %	Ar^{40}*, ppm	Ar^{40*}/K^{40}	Percent Radiogenic	Age, Ma	**Uncertainty, Ma**	**Recalculated Age, Ma**
556B	Hills Pond	8.06	0.0446	0.00546	97	91	5	93
557B	Hills Pond	8.52	0.0464	0.00538	95	90	5	92
703B	Rose Dome	7.85	0.0417	0.00527	83	88	4	90

The available K-Ar dates (Zartman et al., 1967) fall within the emplacement ages determined by Blackburn et al. (2008) for the Kansas kimberlites (110-85 Ma). However, given the uncertainties on the existing ages (Table 3), it is unclear whether the lamproites were emplaced near the start of kimberlite volcanism or toward its end. If the lamproites are younger, were they emplaced concurrently and through a similar mechanism to the emplacement of the younger kimberlites (i.e., Baldwin Creek and Leonardville)? Was lamproite emplacement related in any way to the reheating event seen in the Tuttle, Stockdale, Bala, and Leonardville kimberlites? Alternatively, do the lamproites truly occupy the time gap between the oldest and youngest kimberlites? Thus, more precise geochronology is an essential first step in answering these questions.

Chapter 3 - Methods

3.1 Sample Acquisition and Processing

The majority of the Hills Pond samples analyzed for this study were selected from Micro-Lite LLC's collection of 52 cores originally drilled between 1991-1998. At least one sample was collected from each of the drill holes that recovered fresh to semi-altered lamproite (i.e., lamproite that had not been altered significantly to clay minerals). Where whole rock geochemical data were available (Cullers et al., 1985, 1996; Cullers and Berendsen, 2011), samples were chosen from intervals with high Ti concentrations. Titanium is a major constituent of perovskite and, given that perovskite is the mineral of choice for this geochronological study, we used Ti concentration as a proxy for identifying core with a high probability of containing this phase. Where whole rock data were absent, samples were chosen based on how unaltered they appeared. The 'fresher' lamproite lacked abundant fractures and was durable. Additionally, it was darker and blacker (more purple according to the Micro-Lite LLC workers) as opposed to the varying colors observed in the more altered intervals, e.g., brown, lavender, blue, cream, and orange. The range of colors most likely reflects varying degrees of alteration of primary minerals to chlorite and other clay minerals. In a few cases multiple samples were selected from a single drill hole due to either multiple intervals having high Ti or an area of interest having a slightly different texture or color. Through this initial selection process, 61 samples were collected and cut with a water-cooled table saw into billets (a small section of rock cut in preparation of thin section creation), with a few samples crumbling beyond salvage for thin section creation. Only 22 billets were prioritized to be sent to Spectrum Petrographics, Inc, for preparation into thin sections, based on their dark color, durability and/or high TiO_2 content. There, the thin sections were set in clear epoxy and cut/polished using oil due to their fragility and high content of watersoluble minerals. In addition to the 22 samples collected during this project, two additional samples and their associated thin sections, (PK-LA-MI1, PK-LA-MI2, MML, and MML1) were provided by Dr. Pamela Kempton of KSU. These samples were collected from the recently excavated surface of the Micro-Lite, LLC, mine during a student field trip in 2019, so precise depth and locational data are lacking, aside from being accessible at the surface from within the mine area.

The Rose Dome core samples were provided by the Kansas Geological Survey (KGS). Samples were selected from the Eagle 4 (409-451 ft) and Eagle 5 (361-425 ft) drill holes, as they contained reasonably thick sections of 'fresh' lamproite (Pieter Berendsen, personal communication). A similar selection process as was done for the Hills Pond lamproite was utilized here, with five samples chosen based on durability and/or high TiO_2 content. Sample RDLE4-C442, from Eagle core 4, was chosen based on the gradient in olivine modal abundance observed in the core to see whether perovskite displayed a similar pattern. The five samples were cut into billets by KGS and sent to the Mineral Optics Laboratory for processing into thin sections via similar methods as Spectrum Petrographics, Inc. The locations of both the lamproites sampled can be found in Figure 23 and a description of their cores in Table 5. Photomicrographs and full petrographic descriptions can be found in Figures 21, Appendix A, respectively.

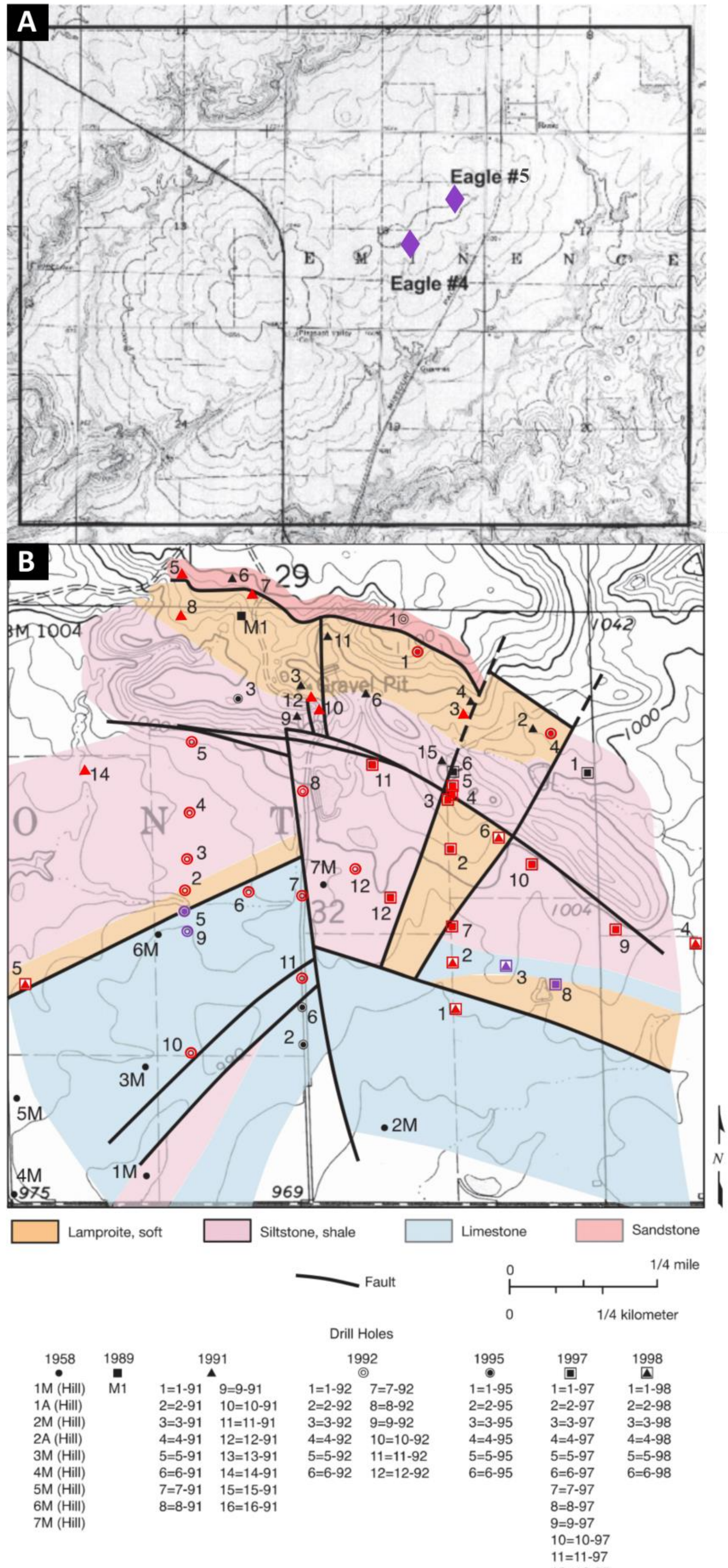
A
Eagle #5
Eagle #4
E M I N E N C E
B
29
32
Gravel Pit
Lamproite, soft
Siltstone, shale
Limestone
Sandstone
Fault
0 1/4 mile
0 1/4 kilometer
Drill Holes
1958
1M (Hill)
1A (Hill)
2M (Hill)
2A (Hill)
3M (Hill)
4M (Hill)
5M (Hill)
6M (Hill)
7M (Hill)
1989
M1
1991
1=1-91 9=9-91
2=2-91 10=10-91
3=3-91 11=11-91
4=4-91 12=12-91
5=5-91 13=13-91
6=6-91 14=14-91
7=7-91 15=15-91
8=8-91 16=16-91
1992
1=1-92 7=7-92
2=2-92 8=8-92
3=3-92 9=9-92
4=4-92 10=10-92
5=5-92 11=11-92
6=6-92 12=12-92
1995
1=1-95
2=2-95
3=3-95
4=4-95
5=5-95
6=6-95
1997
1=1-97
2=2-97
3=3-97
4=4-97
5=5-97
6=6-97
7=7-97
8=8-97
9=9-97
10=10-97
11=11-97
12=12-97
1998
1=1-98
2=2-98
3=3-98
4=4-98
5=5-98
6=6-98

Figure 23. Map of Sampled Lamproites

A) Topographic map of the Rose Dome with the locations of core analyzed in purple. B) Map of the NE portion of the Silver City Dome with the locations of the Hills Pond cores collected for this study in red and the locations of the cores geochemically analyzed and dated in purple. Figures modified from Cullers and Berendsen (2011).

Table 5. Sampled Lamproite Descriptions

A list of the core and hand samples collected or provided along with their depths and the number of thin sections created for each. Asterisks denote which core depth was made into a thin section.

Location	Sample Label (Core #/Name)	Sample type	# of Core Pieces/Billets /Samples	Depth (ft)	Rock Type	# of Thin Sections
Silver City Dome	C91-1	Half Core Piece	1	104’6”-105’1”	Madupitic Olivine bearing Lamproite	0
Silver City Dome	C91-2	Half Core Piece	1	43’5”-44’0”	Madupitic Olivine bearing Lamproite	0
Silver City Dome	C91-3	Half Core Piece	1	114’10”-115’5”	Madupitic Olivine bearing Lamproite	0
Silver City Dome	C91-5	Half Core Piece	1	64’6”-64’9”	Madupitic Olivine bearing Lamproite	1
Silver City Dome	C91-7	Half Core Piece	1	44’10”-45’2”	Madupitic Olivine bearing Lamproite	0
Silver City Dome	C91-8	Half Core Piece	1	3’2.5”-3’6.5”	Madupitic Olivine bearing Lamproite	1
Silver City Dome	C91-10	Half Core Piece	2	*22’2”-22’5” 32’1”-32’5”	Madupitic Olivine bearing Lamproite	1
Silver City Dome	C91-12	Half Core Piece	1	34’5”-38’6”	Madupitic Olivine bearing Lamproite	0
Silver City Dome	C91-13	Half Core Piece	1	41-7”-42’0”	Madupitic Olivine bearing Lamproite	0
Silver City Dome	C91-14	Half Core Piece	1	75’0”-75’4”	Madupitic Olivine bearing Lamproite	0
Silver City Dome	C92-2	Half Core Piece	1	38’4”-39’3”	Madupitic Olivine bearing Lamproite	0
Silver City Dome	C92-3	Half Core Piece	1	38’11”-39’7”	Madupitic Olivine bearing Lamproite	0
Silver City Dome	C92-4	Half Core Piece	1	66’5”-67’3”	Madupitic Olivine bearing Lamproite	0
Silver City Dome	C92-5	Half Core Piece	2	*78’5”-79’3” 97’7”-98’3”	Madupitic Olivine bearing Lamproite	1
Silver City Dome	C92-6	Half Core Piece	1	95’3”-45’10”	Madupitic Olivine bearing Lamproite	1
Silver City Dome	C92-7	Half Core Piece	1	60’6”-61’1”	Madupitic Olivine bearing Lamproite	0

Silver City Dome	C92-8	Half Core Piece	1	112’3”-112’10.5”	Madupitic Olivine bearing Lamproite	0
Silver City Dome	C92-9	Half Core Piece	1	51’6”-52’5”	Madupitic Olivine bearing Lamproite	1
Silver City Dome	C92-10	Half Core Piece	2	*37’8”-38’5” 64’8”-65’3”	Madupitic Olivine bearing Lamproite	1
Silver City Dome	C92-11	Half Core Piece	2	*63’10”-64’5” 83’10”-84’7”	Madupitic Olivine bearing Lamproite	1
Silver City Dome	C92-12	Half Core Piece	1	92’4”-92’11”	Madupitic Olivine bearing Lamproite	1
Silver City Dome	C95-1	Half Core Piece	2	64’7”-64’11” 74’1”-74’5”	Madupitic Olivine bearing Lamproite	0
Silver City Dome	C95-4	Half Core Piece	1	25’0”-25’5”	Madupitic Olivine bearing Lamproite	0
Silver City Dome	C95-5	Half Core Piece	1	41’3”-41’7”	Madupitic Olivine bearing Lamproite	1
Silver City Dome	C97-2	Half Core Piece	1	34’6”-34’9”	Madupitic Olivine bearing Lamproite	0
Silver City Dome	C97-3	Half Core Piece	1	58’5”-58’11”	Madupitic Olivine bearing Lamproite	0
Silver City Dome	C97-4	Half Core Piece	1	25’2”-25’4”	Madupitic Olivine bearing Lamproite	1
Silver City Dome	C97-5	Half Core Piece	1	71’3”-71’6”	Madupitic Olivine bearing Lamproite	0
Silver City Dome	C97-7	Half Core Piece	1	80’1”-80’5”	Madupitic Olivine bearing Lamproite	1
Silver City Dome	C97-8	Half Core Piece	1	51’5.5”-51’10.5”	Madupitic Olivine bearing Lamproite	1
Silver City Dome	C97-9	Half Core Piece	3	31’5”-31’10” 33’1”-33’6” *74’11”-75’4”	Madupitic Olivine bearing Lamproite	1
Silver City Dome	C97-10	Half Core Piece	2	*47’10”-48’3” 90’7”-96’7”	Madupitic Olivine bearing Lamproite	1
Silver City Dome	C97-11	Half Core Piece	2	80’5”-82’0” 145’10”-146’5”	Madupitic Olivine bearing Lamproite	2
Silver City Dome	C97-12	Half Core Piece	2	106’0”-106’5” *109’7”-109’11.5”	Madupitic Olivine bearing Lamproite	1
Silver City Dome	C98-1	Half Core Piece	1	97’4”-97’8”	Madupitic Olivine bearing Lamproite	0
Silver City Dome	C98-2	Half Core Piece	2	33’4”-33’8” 59’9”-60’2”	Madupitic Olivine bearing Lamproite	2
Silver City Dome	C98-3	Half Core Piece	2	35’5”-35’9” *68’7”-69’0”	Madupitic Olivine bearing Lamproite	1
Silver City Dome	C98-4	Half Core Piece	1	92’5”-92’8.5"	Madupitic Olivine bearing Lamproite	1
Silver City Dome	C98-5	Half Core Piece	1	25’8”-26’0”	Madupitic Olivine bearing Lamproite	0

Silver City Dome	C98-6	Half Core Piece	1	46’5”-46’10”	Madupitic Olivine bearing Lamproite	0
Silver City Dome	PK-LA-MI	Hand Sample	2	2019 Mine Surface	Madupitic Olivine bearing Lamproite	2
Silver City Dome	MML	Hand Sample	2	2019 Mine Surface	Madupitic Olivine bearing Lamproite	2
Rose Dome	Eagle 4	Billets	3	412’1” 418’8” 442’7”	Madupitic Olivine bearing Lamproite	3
Rose Dome	Eagle 5	Billets	2	384’6” 365’3”	Madupitic Olivine bearing Lamproite	2
Bala	Bala	Half Core/ Piece	1	N/A	Non-Micaceous Kimberlite	4
Tuttle	Tuttle	Half Core/ Piece	1	89’8”-297’0”	Micaceous Kimberlite	2

Core and thin sections for six (Antioch, Bala, Baldwin Creek, Tuttle, Winkler Crater, and Stockdale) of the twelve Kansas kimberlites were provided by the geology department at Kansas State University (KSU). Overall, the kimberlite samples are highly altered, containing 80-90% serpentine and calcite which occur as pseudomorphs, veins, and interstitially with only the Tuttle and Bala localities containing perovskite. Therefore, only thin sections from these two localities were utilized in this study. The locations of the kimberlites sampled can be found in Figure 9 and a description of their cores in Table 5. Photomicrographs and full petrographic descriptions can be found in Figures 24 and 25, and Appendix A, respectively.

3.2 Electron Microprobe

The thin sections chosen for electron microprobe analyses (EMPA) and backscattered electron (BSE) imaging are listed in Table 6. Each was chosen for its high abundance and large size of perovskite grains ($\geq$ 20 µm) and/or the occurrence of perovskite grains with different morphologies and colors. For example, sample MLA-C97-8 was chosen because it contains an unusual perovskite morphology (see Section 4.1 below describing perovskite petrography), but these perovskites tend to be smaller than those in other samples analyzed, which resulted in a smaller selection of perovskites large enough (≥ 20 µm) for analyzing by electron microprobe. This smaller sample size may also have affected the precision of the U-Pb age for this sample (see Section 4.3 below describing perovskite geochronology). EMPA were performed using the JEOL JXA-8230 located at the University of Colorado (CU) Boulder. Before EMPA, the thin sections were cleaned with isopropyl alcohol and coated with a 20 nm film of carbon, which was done in-house at CU Boulder for most samples. Samples from Hills Pond and some samples from Bala, Tuttle, MML1, and PK-LA-MI1 thin sections were coated at the University of Iowa when the CU Boulder carbon coater was not operational. Major and trace elements were measured by wavelength dispersive spectroscopy (WDS). The beam conditions for analysis were 15 keV and 20 nA, with a spot size of 1 µm. Element intensities were measured using analyzing crystals TAP for Si; TAPL for Na, Al and Mg; PETL for Th, Ca, Sr, Nb, U, and K; and LIFL for Fe, Ti, Mn, Ce, Cr, Ta, La, and Nd. Both the on- and off-peak counting times for the elements were 20 seconds. Calibration standards, from Astimex Minerals are Wilberforce apatite for Ca, celestite for Sr, chromite for Cr, hematite for Fe, monazite for Ce, Th, La, and Nd, olivine Fo93 for Mg, orthoclase for K, labradorite for Al, Na, and Si, rhodonite for Mn, and rutile for Ti. Ta, Nb, and U metals were used as standards for their associated elements.

Samples from Bala, Tuttle, MML1, and PK-LA-MI1 were analyzed over two separate sessions (September 2022 and March 2023). The first analytical session focused on collection of back-scatter electron images that were used to identify suitable analysis spots for the in situ U-Pb geochronology. During the second analytical session, perovskite compositional data were collected to complement the U-Pb geochronology. Ideally, EMPA were done prior to U-Pb geochronology, so that analysis spots could be located. However, due to time and instrument availability constraints, it was not always possible to do this. When U-Pb LA-ICP-MS was conducted before EMPA, despite being cleaned, probe spots were not collected on or within the laser debris halo of the LA-ICP-MS spot. Where sector zoning was observed, probe analyses were done on a variety of zones, where possible, and always included the zone within which laser ablation analyses were conducted. In large grains where sector zoning did not occur core, rim and/or mantle compositions were collected. For the purposes of this study, a 'core' refers to the centermost area of the grain; the 'rim' refers to the outermost section, and the 'mantle' is the area in between. Therefore, the names do not necessarily represent a petrogenic core, rim, or mantle. If the core and rim of a single crystal were analyzed for geochronology, a corresponding EMPA spot was collected close by.

Table 6. List of the Lamproites and Kimberlites Analyzed

List of the lamproite and kimberlite thin sections chosen for EMPA and geochronology along with the key characteristics that lead to their selection.

Thin Section name	Location	Core	Depth (ft)	Key Features
MLA-C92-9	Silver City Dome	C92-9	51’6”-52’5”	Anhedral to cubic, brown to red brown perovskite
MLA-C95-5	Silver City Dome	C95-5	41’3”-41’7”	Anhedral to cubic brown to red brown perovskite
MLA-C97-8	Silver City Dome	C97-8	51’5.5”-51’10.5”	Predominantly anhedral, brown to red brown perovskite
MLA-C98-3	Silver City Dome	C98-3	68’7”-69’0”	Predominantly anhedral red-brown perovskite
PK-LA-MI1	Silver City Dome	Hand Sample	2019 Mine Surface	Brown anhedral perovskite
MML1	Silver City Dome	Hand Sample	2019 Mine Surface	Brown anhedral perovskite
RDLE4-C412	Rose Dome	Eagle 4	412’1”	Large predominantly anhedral, golden brown to green-brown perovskite
RDLE4-C418	Rose Dome	Eagle 4	418’8”	Large cubic dark red-brown to golden brown perovskite
RDLE4-C442	Rose Dome	Eagle 4	442’7”	Large cubic dark red-brown to brown perovskite
RDLE5-C384	Rose Dome	Eagle 5	384’6”	Large predominantly anhedral, golden brown to green-brown perovskite
BA-62-39B	Bala	Bala	N/A	Cubo-octohedral to cubic perovskite, two petrologic textures
TU-1A-1D2	Tuttle	Tuttle	89’8”-297’0”	Cubic perovskite, magmaclasts

3.3 LA-ICP-MS

The U-Pb isotopes for geochronology and the trace elements of the perovskites were measured in situ via laser ablation inductively coupled plasma mass spectrometry (LA-ICP-MS) using a 193-nm wavelength, 5 ns pulse length ANALYTE.G2 excimer laser connected to a Thermo Finnigan Element2 sector-field mass-spectrometer at the University of Kansas. Both analyses were carried out with a laser beam size of 20 µm. For analyses done after EMPA, the carbon coat on the thin section was removed with isopropyl alcohol and/or acetone with some needing an additional fine polishing with 1 μm diamond slurry on a felt pad.

3.3.1 U-Pb Dating

Perovskites in the Kansas kimberlites and lamproites exhibit a range of petrographic characteristics (see Section 4.1 on petrography). Perovskites were selected for U-Pb isotope analysis to encompass as much of this variety as possible in order to determine whether certain perovskite characteristics, such as color or crystal morphology, reflected different melt generations. Within the Tuttle kimberlite, perovskites were sampled from within and outside of magmaclasts, fluidal-shaped bodies of kimberlite produced via magma disruption before solidification (Webb and Hetman, 2017; 2021) (see Section 4.1 on petrography). In the Bala kimberlite, analyses were collected within two texturally distinct zones: (a) pyroxene pseudomorph (replaced by calcite) dense areas, and (b) olivine pseudomorph (replaced by serpentine) dense areas (see Section 4.1 on petrography). For the samples that underwent EMPA and BSE imaging prior to dating (i.e., Bala, Tuttle, PK-LA-MI1, and MML1), U-Pb LA-ICP-MS spot analyses were placed based on the sector zoning observed. However, in general U-Pb spots were placed on areas of the grains that had smooth surfaces and were inclusion free, at least as far as could be determined from surface observation. Where possible, 80 spot analyses were collected for each thin section in order to measure the spread of U-Pb ratios present within the perovskite and maximize the chance to obtain precise results. However, due to limited time and the small number of perovskites ≥ 20 μm, the Bala (42 spots), Tuttle (45 spots), PK-LA-MI1 (53 spots), MML1 (13 spots), and MLA-C97-8 (31) thin sections had fewer analyses.

The U-Pb ratios were determined following methods similar to in situ analysis of zircon (e.g., Condit et al. 2018). At the beginning and end of every 10 'unknown' perovskite analyses, the U-Pb isotope ratios and elemental abundances were calibrated and validated using 3-4 reference materials. Downhole fractionation, Pb isotope fractionation, drift corrections and baseline subtraction were done in Iolite (Paton et al., 2010; Paton et al., 2011) using NIST612 glass as the reference material (Jochum et al., 2011). In a second step, Ice River-6 perovskite, which has a thermal ionization mass spectrometry (TIMS) $^{206}Pb/^{238}U$ age of 361.7 ± 1.0 Ma (Tappe and Simonetti, 2012) was used to calibrate the U-Pb fractionation correction. The reference perovskites Afrikanda-30, an 'in house' Afrikanda with a LA-ICP-MS age of 372 ± 6 Ma (2σ) (Reguir et al., 2010), 'in house' Magnet Cove perovskite with an LA-ICP-MS age of 85.71± 5.52 Ma were used to validate the U-Pb fractionation correction. Most analyses utilized all five reference materials, except for the initial runs done on Bala, Tuttle, MML1, and PK-LA-MI1, which only included the first three reference materials. The $^{206}Pb/^{238}U$ analytical uncertainties of the reference materials, as well as other sources of error, were propagated into the results of the unknown perovskite (e.g., Li et al., 2010).

Unlike most U-Pb analysis of zircon, analyses of perovskite need to account for common Pb, as it can make up to 80% of the total Pb within the mineral, which causes an offset from concordia (e.g., Wu et al., 2010; Abersteiner et al., 2019). This was done by plotting the measured values on Tera-Wasserburg diagrams in order to determine dates from discordia arrays between common Pb (upper intercept with concordia) and radiogenic Pb (lower intercept with concordia and interpreted age), similar to procedures for other minerals with higher common Pb content such as carbonate, titanite, apatite, or rutile (e.g., Cioffi et al., 2019; Roberts et al., 2020).

3.3.2 Trace Elements

The concentrations of select trace elements (Si^{29}, Ca^{44}, Sc^{45}, Ti^{49}, V^{51}, Cr^{53}, Co^{59}, Ni^{61}, Rb^{85}, Sr^{88}, Y^{89}, Zr^{90}, Nb^{93}, Cs^{133}, Ba^{137}, La^{139}, Ce^{140}, Pr^{141}, Nd^{146}, Sm^{147}, Eu^{153}, Gd^{157}, Tb^{159},

Dy^{163}, Ho^{165}, Er^{166}, Tb^{172}, Ta^{181}, Th^{232}, and U^{238}) were obtained in situ for perovskites in the Bala kimberlite (BA-62-39B) and lamproite samples MLA-C92-9, RDLE5-C384, and RDLE4-C418 using the same LA-ICP-MS system at KU as used for U-Pb isotope analysis. Two samples of Rose Dome were selected for trace element analysis, because few geochemical analyses of this lamproite have been published.

Where possible, trace element spot analyses were taken within the same area of the grains as analyzed for U-Pb geochronology and/or electron microprobe (EMP) major element analysis. Despite thin sections being cleaned after laser ablation, trace elements were never measured on or within the laser debris halo of a U-Pb LA-ICP-MS spot. Each thin section had around 50 spots measured. We used a combination of USGS basaltic (GSC-1G and GSD-1G) and NIST SRM high Si glass (NIST612) as the reference material for internal standard calibration with the Iolite software (Paton et al. 2010; 2011). Due to the unusually high variability in SiO_2 (up to 1.9 wt%; Mitchell and Chakhmouradian, 1999) observed within the perovskites of Kansas lamproites, we decided to use Ca^{43} as the internal standard. However, due to the ease of elemental substitution on the perovskite A site (see Section 2.3), even the Ca concentrations were variable. Therefore, in cases where precise overlap in spot locations for LA-ICP-MS and EMP was not possible, we assigned an individual Ca wt.% value based on the EMP analyses of other areas in the same crystal or in other crystals in the same thin section. Backscatter images of the grains analyzed via electron microbe were utilized to select areas most likely to be compositionally similar to the analyzed LA-ICP-MS spot. Matches were defined based on utilizing (i) a different portion of the same grain; (ii) a grain with a similar zone/color; and (iii) a similar core/mantle/rim position even if of a slightly different color or zone. Criteria were applied in the order of priority listed, i.e. where possible, the LA-ICP-MS spot was matched with an identically defined (i.e., same grain with same color zones and core/mantle/rim position) EMP analysis. As the perovskites are (1) small (5-800 µm; See Section 4.1); (2) complexly zoned (i.e., Hills Pond) (See Section 4.3); and (3) underwent U-Pb LA-ICP-MS analysis prior to trace element analysis, spot analysis could not always be collected within the same color zone or core/mantle/rim position as that collected during EMPA. Additionally, as detailed in Section 4.3.1, perovskite composition varies more by zone rather than core/mantle/rim position. Thus, if a match between grain and color zone could not be made, then an average of similarly colored zones within a matching thin section was utilized. In cases where no zoning was present (i.e., Bala), then a match would be made based on core/mantle/rim position either within an identical grain or an average of similarly positioned spots within a matching thin section. Unique to the Bala sample, where exact grain matches could not be made, an average of the composition from grains from the same age array (or between analyses that occurred between arrays) (see Section 4.2) was utilized. A match based on age array was prioritized over core/mantle/rim position for this sample. Only analysis 92-9G77 could not be matched with a corresponding-colored zone or rim position due to the small amount of EMP data deemed reliable available for this sample. As a result, an average of the thin sections mantle EMP spots was utilized instead.

Chapter 4 - Results

4.1 Petrology

4.1.1 Kimberlites

Typical of the Kansas kimberlites, both the Bala and Tuttle kimberlites are porphyritic with phenocrysts of olivine and pyroxene (extensively altered to serpentine and calcite) with minor to trace amounts of phlogopite, magnetite, ilmenite, pyrope garnet, perovskite, apatite, rutile, and zircon set in a fine-grained serpentine and calcite matrix (Cullers et al., 1982). The Bala kimberlite appears to be the densest and least brecciated of the Kansas kimberlites (Fig. 24). It contains abundant euhedral to subhedral olivine and pyroxene pseudomorphs (replaced by serpentine and calcite), <10% crustal xenoliths, few calcite veins, and trace amounts of phlogopite, predominantly in the groundmass, consistent with its classification as a non-micaceous kimberlite (Brookins, 1970; Cullers et al., 2012). Of the four Bala thin sections available, BA-62-39B was chosen for further analyses because it displays two petrologic textures (Fig. 24). Most of the thin section exhibits what we refer to here as texture A, which is characterized by densely packed, tabular, calcite pseudomorphs after pyroxene phenocrysts ranging in size from 200 μm to 1.5 mm. Only 3-5% of the phenocrysts in this texture are serpentinized olivine. The matrix is primarily serpentine and calcite with lesser magnetite and ilmenite. In contrast, texture B, which comprises ~30% of the thin section, is characterized by densely packed serpentinized olivine with <2% altered pyroxene phenocrysts within a slightly more calcite-rich matrix. Serpentinized olivine ranges in size from 100 μm to 1.5 mm, with the olivine within texture B falling on the smaller size of the range. The zones with texture B are amorphous in shape and generally elongated (Fig. 24). These petrographic observations suggests that flow differentiation may have occurred during transport, resulting in the different abundances of olivine phenocrysts observed.

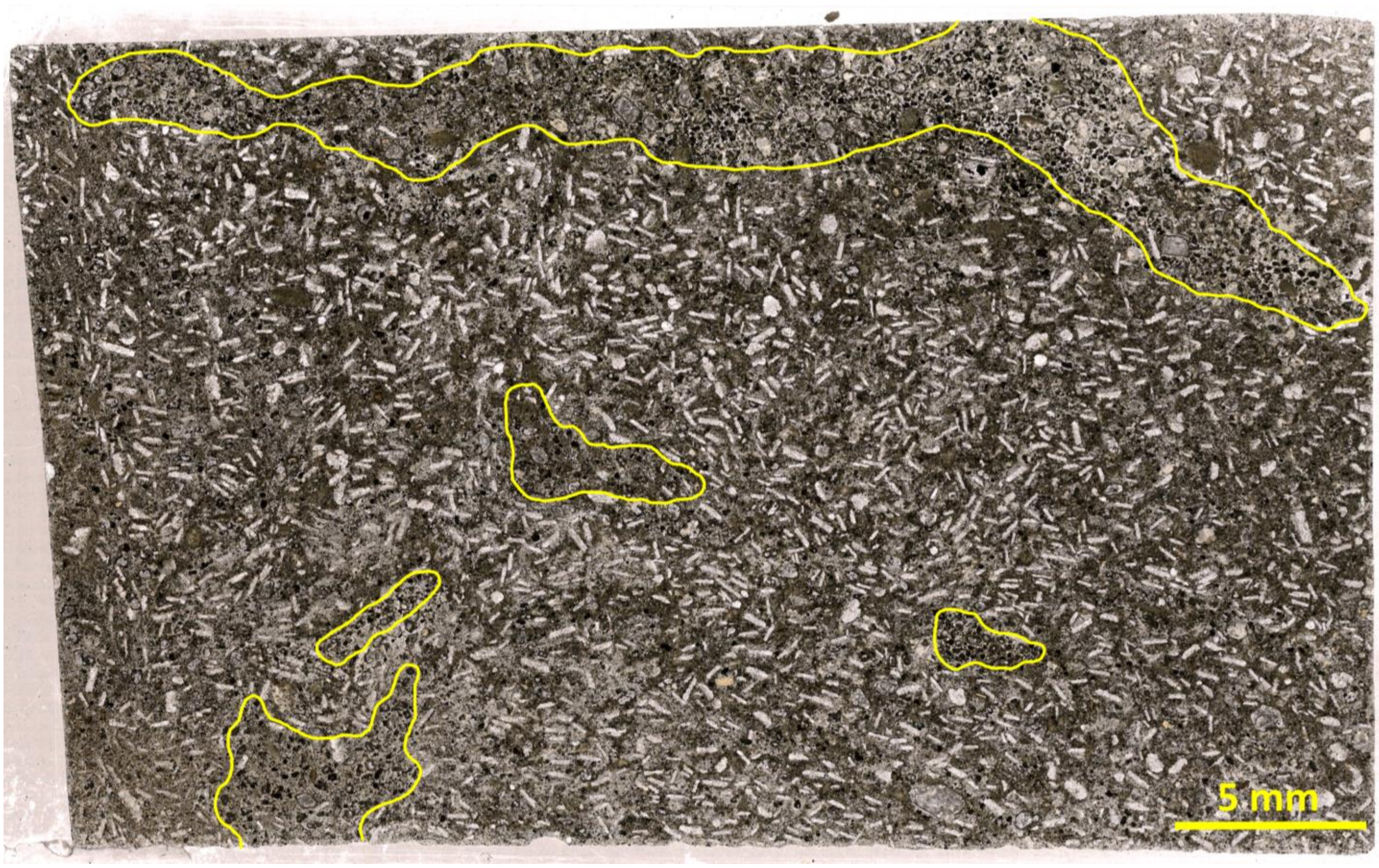

Figure 24. Photomicrograph of Bala's Two Petrologic Textures

Bala thin section (BA-62-39B) photomicrograph scanned in plane polarized light with areas with texture B circled in yellow.

In comparison, the Tuttle kimberlite is more brecciated and fragmental (Fig. 25). It consists of abundant anhedral olivine pseudomorphs (30-40%), phlogopite (5-8%), and pyrope garnet (2-5%), with minor to trace amounts of clinopyroxene (typically with alteration rims of serpentine and calcite), apatite, zircon, and opaque minerals. Xenoliths and autoliths occur in abundance of up to 70% of the mode and are predominantly comprised of partially altered country rock and kimberlitic material, respectively. Therefore, the mineralogy of the Tuttle kimberlite is consistent with its classification as a micaceous kimberlite (Brookins, 1970; Cullers et al., 2012). Autoliths make up 40-50% of the mode and range in size from 10 µm-1.3 cm.

Figure 25. Tuttle Photomicrograph

Tuttle thin section (TU-1A-1D2) photomicrograph in plane polarized light. Note that the thin section was polished thinner around the edges resulting in the edges of the photomicrograph being washed out.

Previously, classified as pelletal lapilli by Cullers et al. (2012), these autoliths are now considered magmaclasts. Magmaclasts are fluidal-shaped bodies of now solidified kimberlitic melt formed when the magma is disrupted via ductile deformation processes, prior to solidification (Moss and Russel, 2011; Webb and Hetman, 2021). It is considered an interim term utilized until further analysis of the magmaclast's characteristics allows it to be genetically classified as either (1) melt segregations, which form non-explosively via magmatic segregation within sub- to non-volcanic hypabyssal intrusions, or (2) melt-bearing pyroclasts, which form explosively during the fragmentation and rapid cooling of eruptions and occur within volcaniclastic rocks. Magmaclasts consist of entrained crystal or lithic solids and a matrix composed of melt solidification products ± exsolved solids. Their characteristic fluidal shape is due to low melt viscosity and surface tension processes during eruption (Webb and Hetman, 2021). Following the descriptive scheme for magmaclasts of Webb and Hetman (2021) shown in Figure 26, the magmaclasts within Tuttle are irregular to regular in shape, with relatively distinct margins ranging from ultra fine to very coarse (Fig. 27). Magmaclasts range from matrix to clast supported within a serpentine and calcite interclast matrix. Fine grained minerals such as perovskite and magnetite are found disseminated within both the magmaclast and interclast matrices. A majority of the magmaclasts are cored, possessing ultra-thin to thick complete and lesser incomplete, symmetrical to asymmetrical, single rims. A few multi-rimmed magmaclasts are also observed. The magmaclasts are non-vesicular with variable groundmass crystallinity and mineralogy. For example, some magmaclasts don't seem to include phlogopite while others, which tend to be crypto- to poorly crystalline, don't contain perovskite or magnetite. However, due to the extensive alteration of the kimberlite, it is difficult to distinguish cryptocrystalline magmaclasts from serpentinized olivine pseudomorphs and/or to determine whether olivine within the magmaclasts is of equivalent size inside and outside the magmaclast. Of the Kansas kimberlites only the Tuttle and Baldwin Creek localities have been observed to contain magmaclasts. Overall, based on the characteristics that are not obscured by alteration, the magmaclasts in the Kansas kimberlites can be classified as melt-bearing pyroclasts, which is consistent with the classification of the Tuttle kimberlite as VK by Blackburn et al. (2008).

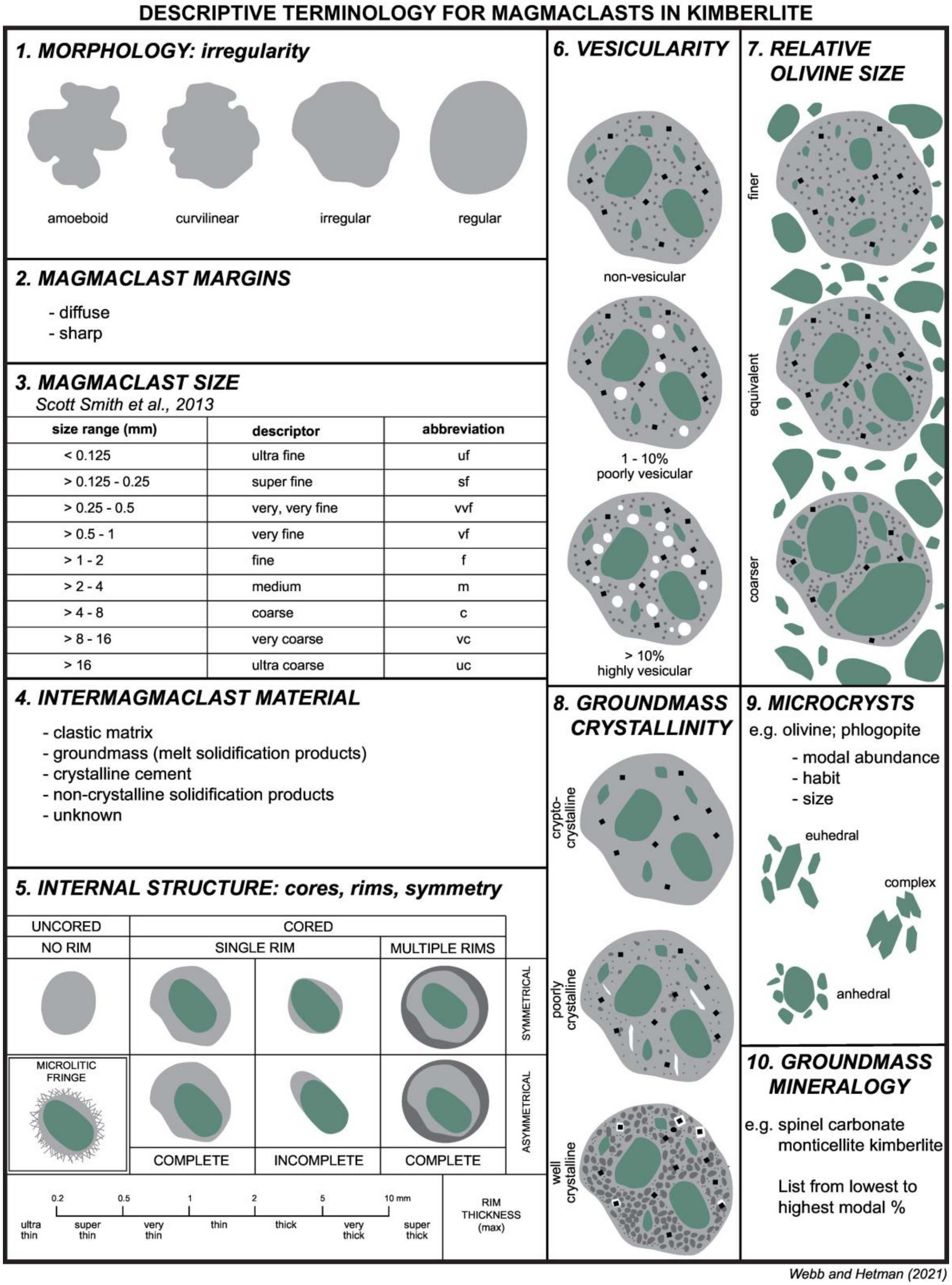

Figure 26. Magmaclast Description Scheme

Kimberlite magmaclast description scheme from Webb and Hetman (2021).

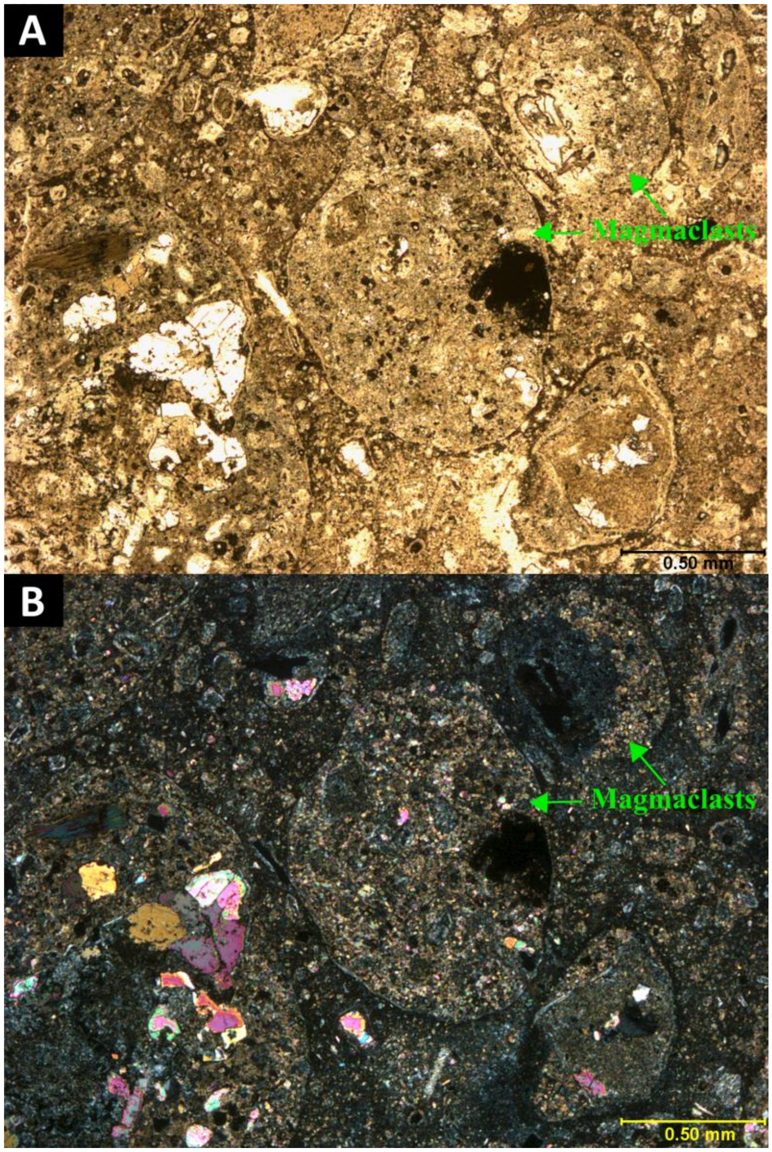

Figure 27. Tuttle Magmaclasts

Photomicrograph of magmaclasts within the Tuttle kimberlite (TU-1A-1D2) taken in plane polarized light (A) and cross polarized light (B).

Perovskite occurs within both the Bala (2-5%) and Tuttle (5-7%) thin sections as two distinct morphologies. One type, seen predominantly within the Bala kimberlite, occurs as larger (30-150 µm), brown, cubo-octohedral crystals (Fig. 28a). The second morphology occurs as smaller (5-25 µm), pale grey to light brown, cubic crystals (Fig.28b). This morphology is dominantly seen within the Tuttle kimberlite, with 55-90% of them occurring within melt-bearing pyroclasts. Where present, zoning within the Bala perovskites consists of a light, abraded core and a thin (up to 5 µm) dark rim, whereas zoning within the Tuttle perovskites consists of one to two concentric zones around a subhedral-anhedral core (Fig. 29). While they can be found within phlogopite, a majority of the grains occur in the interstices between phases, indicating it is predominantly a late-stage groundmass mineral.

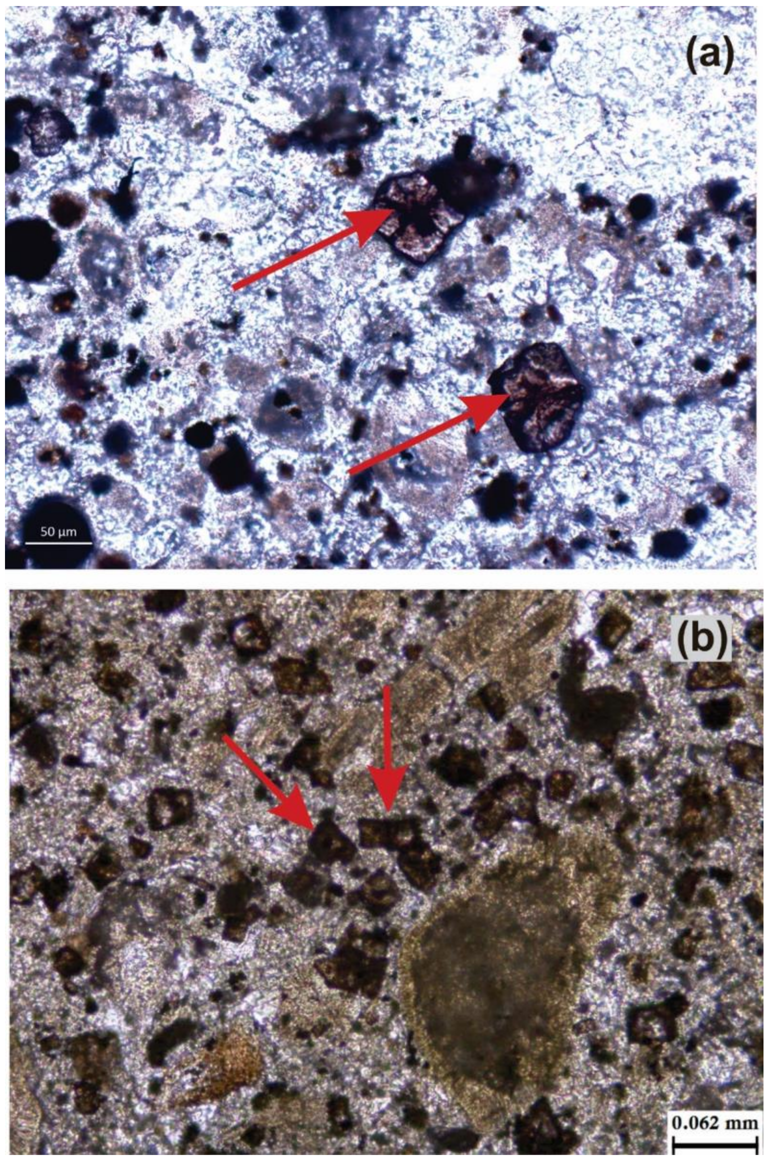

Figure 28. Perovskite Morphologies

Photomicrographs of the two perovskite (red arrows) morphologies, cubo-octohedral (a) and cubic (b), in plane polarized light from the Bala (a) and Tuttle (b) kimberlites. Photos from Rogers (in prep.)

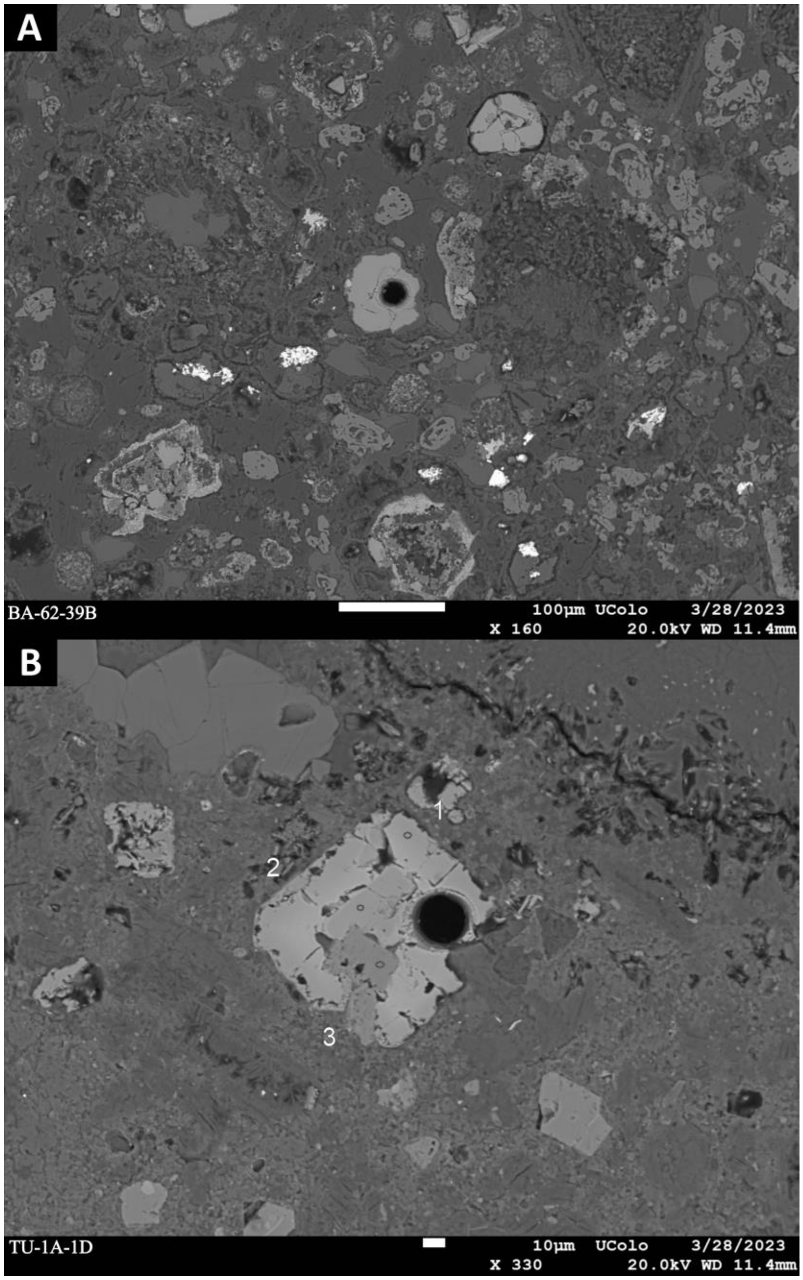

Figure 29. Kimberlitic Perovskite BSE Images

Kimberlite perovskite BSE images after LA-ICP-MS. The small grey open circles indicate EMP spot analyses, the 20 µm dark circles are the LA-ICP-MS ablation pits. a) Perovskite grain from BA-62-39B with a light core and a thin <5 µm dark rim. b) Perovskite grain from Tuttle with a dark euhedral core. The white numbers refer to the name of the EMPA spots (light grey circles). Note that spot 3 is within an inclusion.

4.1.2 Lamproites

The Hills Pond lamproite is porphyritic, consisting of phenocrysts of poikilitic phlogopite (4-60%), poikilitic and phenocrystic potassic richterite (5-7%), diopside (1-6%), serpentine and calcite pseudomorphs after olivine (25-55%), perovskite (1-6%), and magnetite (1-4%), with accessory apatite, wadeite, rutile, and titanite. Based on these general mineral abundances, the Hills Pond lamproite is considered an olivine-richterite-diopside-madupitic lamproite, which is consistent with the compound names previously assigned to it (Cullers et al. 1985; Mitchell, 1985; Mitchell and Bergman, 1991). Madupitic refers to the poikilitic texture of the groundmass phlogopite, which indicates that it, along with a portion of the richterite, were some of the last minerals to crystallize from the lamproitic melt (Fig. 30). Phlogopite occurs as anhedral to euhedral prismatic crystals up to 3.5 mm in length. The grains are commonly deformed, displaying undulatory extinction, kink bands, secondary mineral deposition between cleavage planes, and alteration into chlorite and serpentine. The significant range in modal abundance is most likely a result of alteration, as the lamproites with the lowest modal abundance of phlogopite are the samples collected from the 2019 mining surface (MML and MML1) and were the most heavily altered. Anhedral to subhedral, partially serpentinized diopside occurs in higher modal abundances than the partially altered pyroxenes observed in the kimberlites. Apatite and wadeite occur almost exclusively as inclusions within phlogopite and diopside. Serpentine pseudomorphs after olivine are anhedral to subhedral, 80 µm to 7 mm long and are composed of antigorite and/or lizardite with a few crosscut by veinlets of chrysotile. The groundmass comprises 40-70% of the modal abundance and is predominantly serpentine with lesser chlorite, phlogopite, and calcite.

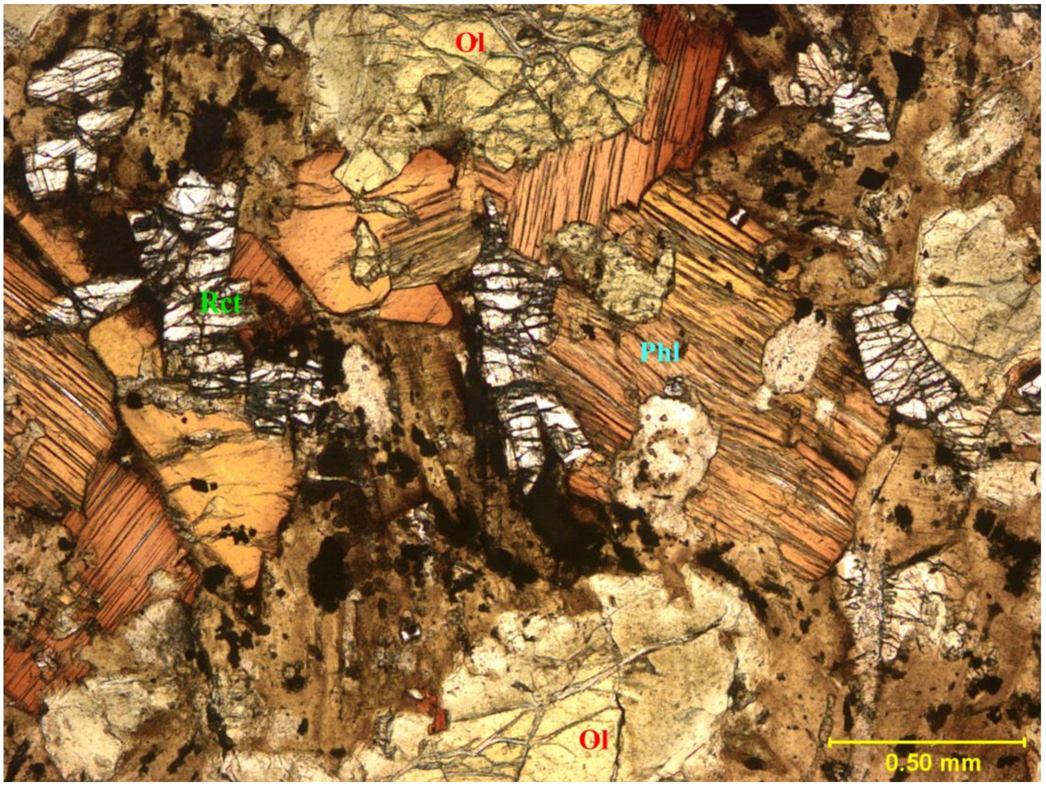

Figure 30. Phlogopite Texture

Photomicrograph of poikilitic phlogopite within the Hills Pond lamproite taken in plane polarized light. Abbreviations: Ol for serpentinized olivine, Phl for phlogopite, and Rct for richterite.

Similarly, the Rose Dome lamproite is porphyritic consisting of phenocrysts of poikilitic phlogopite (30-65%), diopside (1-9%), serpentine and calcite pseudomorphs after olivine (5-70%), perovskite (4-13%), and magnetite (1-8%) with accessory apatite, wadeite, and titanite. Based on these general mineral abundances, the Rose Dome lamproite is considered an olivine-diopside-madupitic lamproite, which is consistent with the compound names previously assigned to it (Bergman, 1987; Mitchell and Bergman, 1991). On average, the phlogopite is more anhedral, smaller (up to 2.5 mm), and shows less evidence of deformation than that of Hills Pond, i.e., an absence of kink bands and undulatory extinction. Additionally, at 412 ft within the Eagle 4 core, both poikilitic groundmass and phenocrystic phlogopite are observed. Lower abundances of partially altered diopside and apatite were also observed. Anhedral serpentinized olivine pseudomorphs are common. They are up to 4.5 mm in length and variable in abundance. Within the Eagle 4 core at 412 ft, the olivine and to a lesser extent diopside and phlogopite exhibit a gradient in grain size (Fig. 21), which has been previously interpreted to indicate mineral gravity settling occurred (Cullers and Berendsen, 2011). Similar to the Hills Pond, the Rose Dome groundmass comprises 55-60% of the modal abundance and is predominantly serpentine with lesser chlorite, phlogopite, and calcite.

Perovskite occurs within both lamproite localities with the Rose Dome containing a modal abundance of 4-13% while the Hills Pond contains 1-6%. Both morphologies seen within the Kansas kimberlites, i.e., cubic and cubo-octohedral, are also observed within both lamproites, except the grain size tends to be larger (5-800 μm) in the lamproites. However, a majority of the perovskites are anhedral. The Hills Pond perovskites range in color from cream to brown to red-brown and size from 5-300 μm, while the Rose Dome perovskites show a larger range in both color, grading from brown to red-brown to green-brown, and size with grain diameters up to 800 μm. The location of the majority of the perovskite between the silicate phases, similar to the Kansas kimberlites, indicates they are predominantly a late-stage groundmass mineral.

Two patterns of zonation were observed within the perovskites: concentric and sector zoning. Perovskites within the Rose Dome lamproite are strongly zoned with multiple oscillatory zones typically starting with a dark core. A majority of the cores and concentric zones are euhedral to subhedral (54%) while the remaining 46% have anhedral cores with euhedral to subhedral concentric zones (Fig. 31a,b). Only two Rose Dome grains from core E4-442 were found to change their overall habit from core to rim. BSE imaging also shows subtle alteration rims, especially in cores E4-442 and E4-418, that were found to be significantly richer in TiO_2 ($\geq$ 83 wt.%) (Fig. 31c). Concentric zoning is also present within the perovskites of both kimberlites;

however, it is rarer and subtler in comparison to that observed within the Rose Dome. The Hills Pond perovskites are strongly sectorally zoned, typically consisting of two to three zones. The cores have been previously described as petal or star shaped, which Mitchell and Chakhmouradian (1999) attributed to a change in habit from cubic to cubo-octahedral, and the different rates of growth and capacity to absorb LREE on {100} and {111}. We were unable to observe a fully star shaped zonation pattern as described by Mitchell and Chakhmouradian (1999), perhaps due to how the perovskites were cut or due to their anhedral and fractured nature (Fig. 32). However, it is evident from their zonation pattern they had a complex crystallization history.

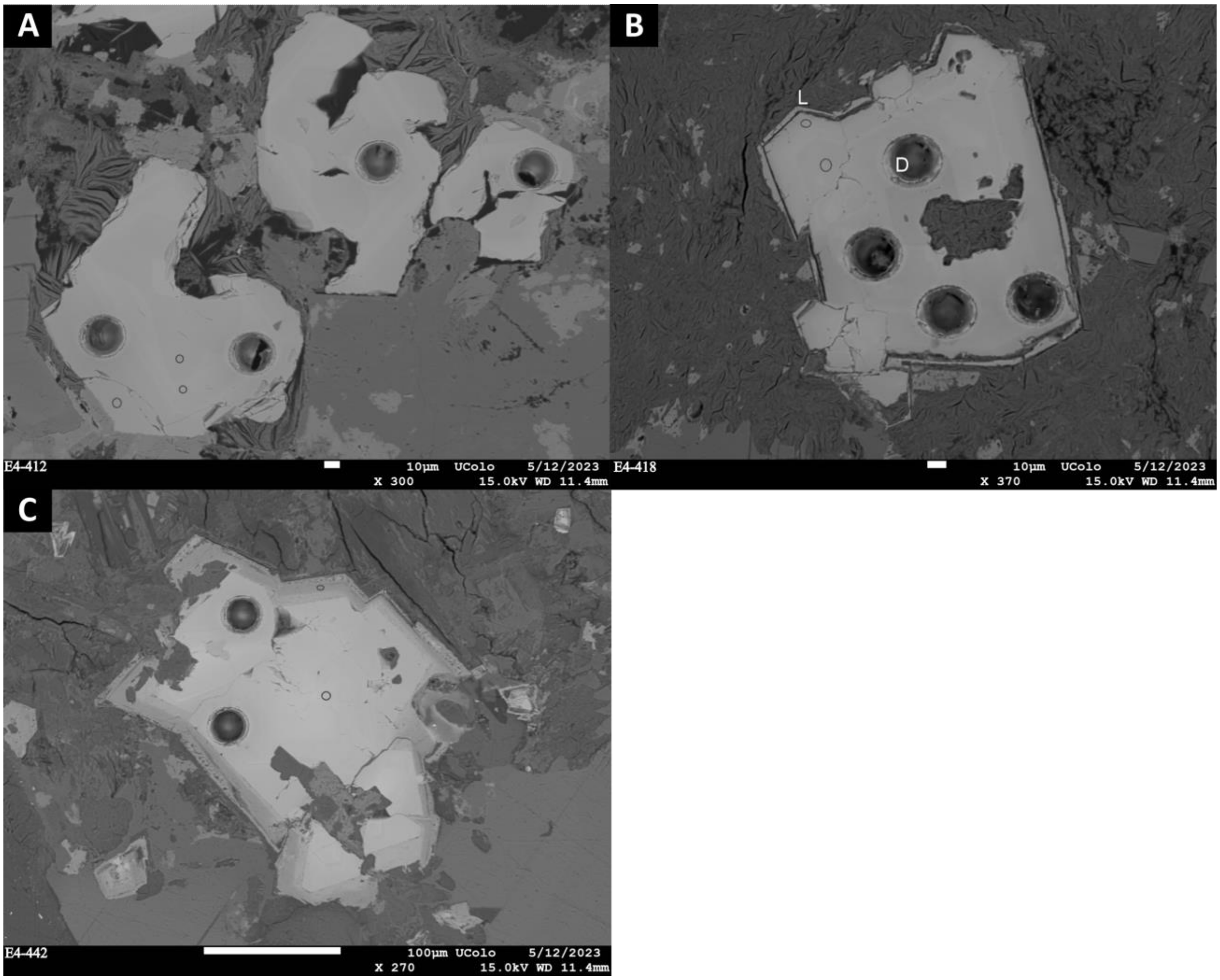

Figure 31. Rose Dome Perovskite BSE Images

Dome perovskite BSE images after LA-ICP-MS. The small grey open circles indicate EMP spot analyses, the 20 µm dark circles are the LA-ICP-MS ablation pits. a) Perovskite grains from E4-412 with a dark anhedral core and euhedral-subhedral concentric zones. b) Perovskite grain from E4-418 with a dark euhedral core and euhedral-subhedral concentric zones. Note the dark ring of alteration near the rim and inclusion near the core. The white L and D refer to the shade of the zone the EMPA spots are on. c) Perovskite grain from E4-442 with 15 µm dark rim of alteration or overgrowth of a TiO_2 rich phase.

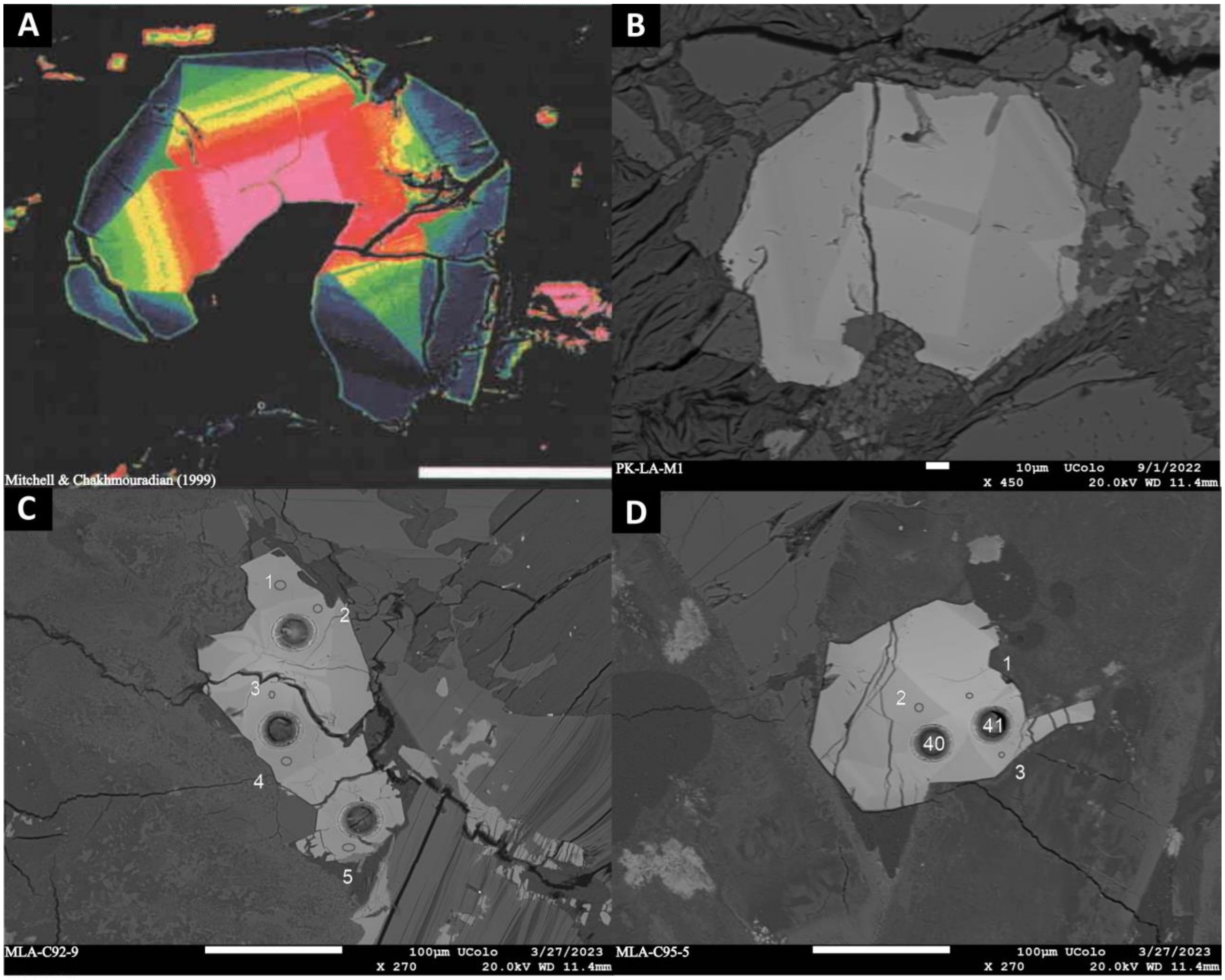

Figure 32. Hills Pond Perovskite BSE Images

Sector zoning within the Hills Pond perovskite BSE images a) False colored BSE image of a perovskite with a petal/star shaped core from Mitchell and Chakhmouradian (1999). Scale bar is 100 µm. b) Perovskite grain from PK-LA-M1 taken before LA-ICP-MS analyses. c) Perovskite grain from core 92-9. d) Perovskite grain from core 95-5. The small grey open circles indicate EMP spot analyses, the 20 µm dark circles are the LA-ICP-MS ablation pits. The white numbers refer to the name of the EMPA (1-5) and LA-ICP-MS spots (40-41).

4.2 Geochronology

For the Tuttle kimberlite, 45 spots were analyzed on 38 individual grains. A majority of the spot analyses were done on perovskites within melt-bearing pyroclasts, where the perovskites are predominantly located (Fig. 33). We were able to obtain the precise age of 105.6 ± 2.0 Ma (MSWD=1.5, n=30), which is in agreement with the phlogopite Rb-Sr age of 106.6 ± 1.0 Ma reported by Blackburn et al. (2008) (Fig. 34c). A total of 15 spot analyses represented outliers and were excluded. Many of these analyses have U and Th concentrations that indicate they are not perovskite (see Supplementary Table 1), while others may represent open system behavior or recrystallization. The Tuttle perovskites have a common lead $^{207}Pb/^{206}Pb$ ratio of 0.86.

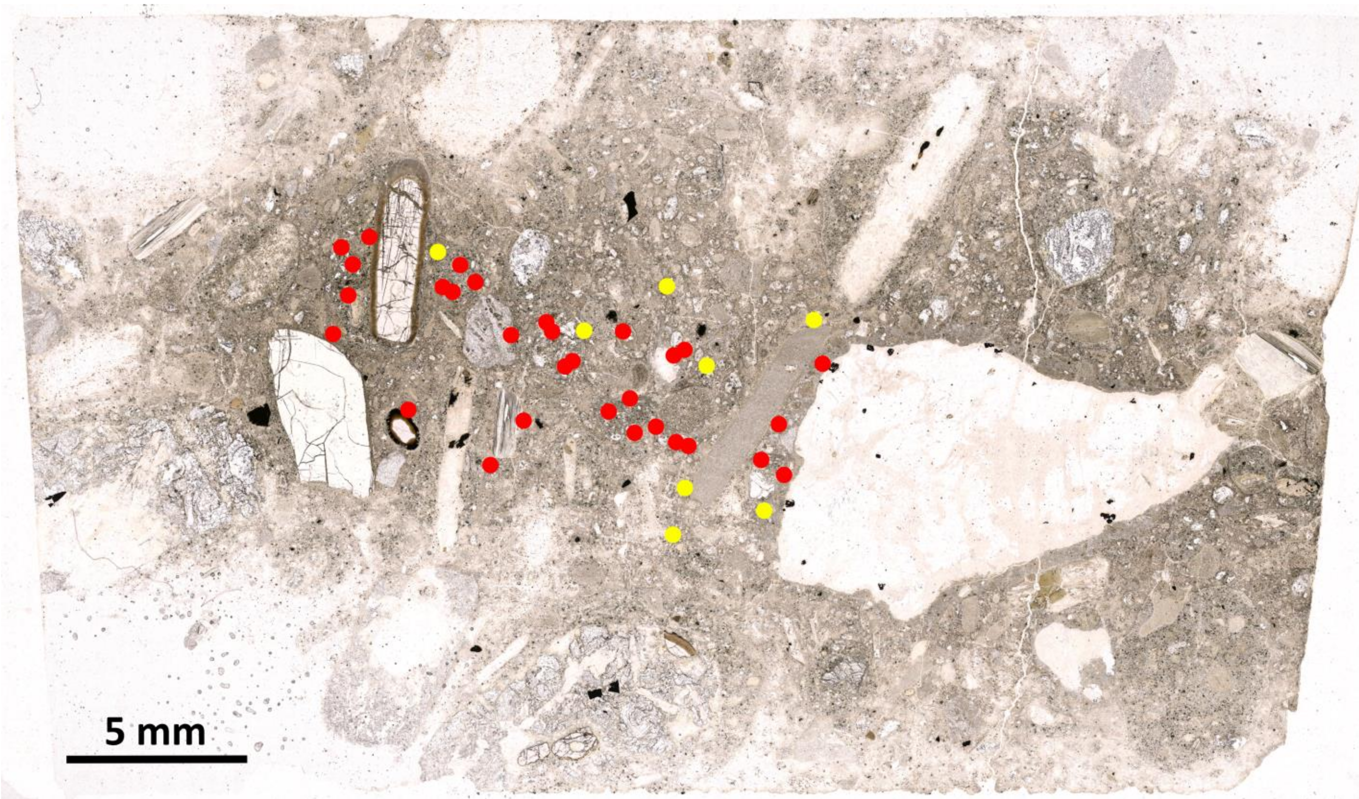

Figure 33. Locations of the Tuttle LA-ICP-MS Spot Analyses

Thin section photomicrograph of TU-1A-1D2, from the Tuttle kimberlite, showing the locations of the LA-ICP-MS spot analyses taken for U-Pb geochronology. The yellow spots represent analyses of perovskites between melt-bearing pyroclasts, while the red spots represent analyses taken within melt-bearing pyroclasts.

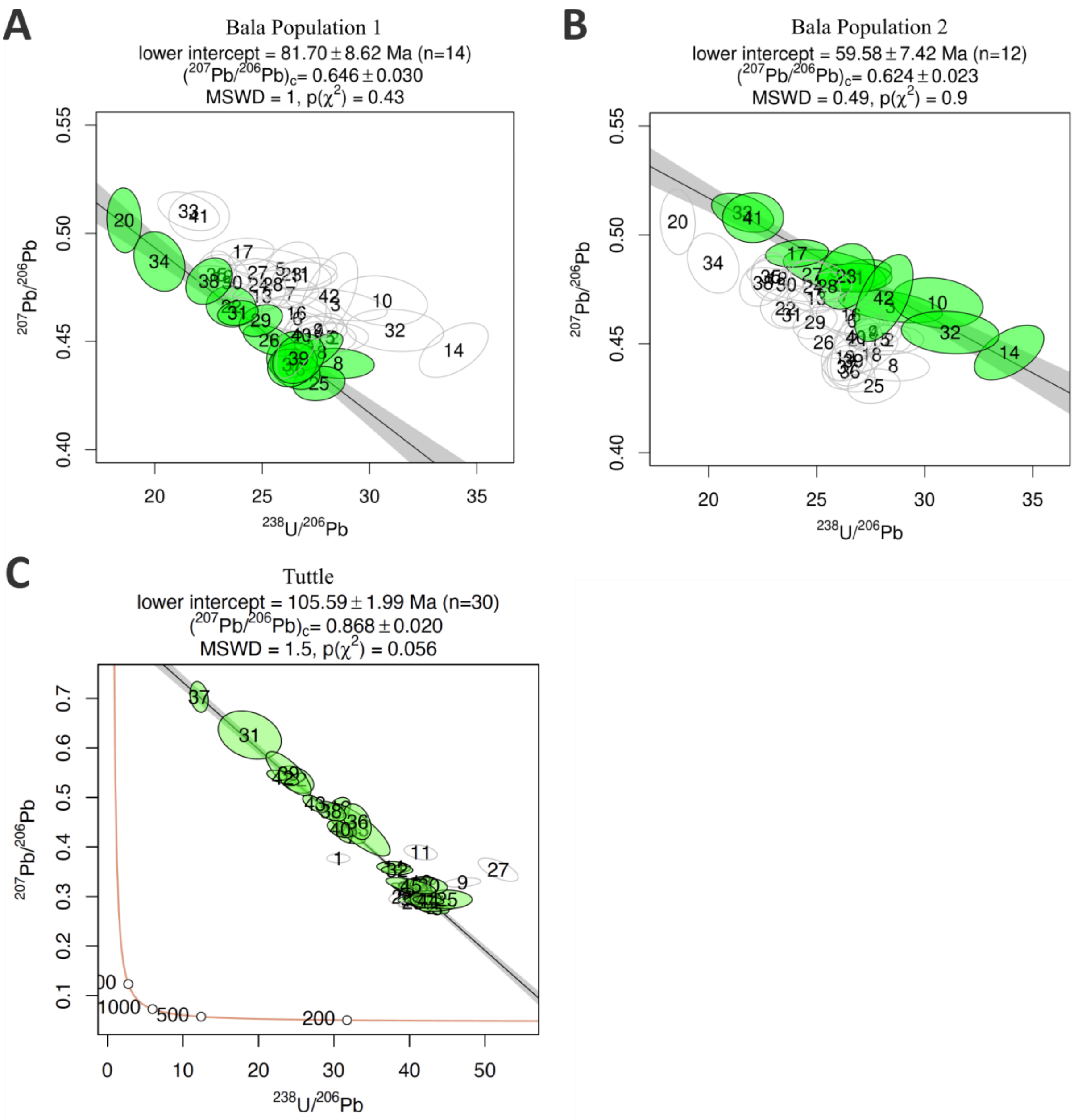

Figure 34. Kansas Kimberlite Concordia Diagrams

Tera-Wasserburg plots showing the U-Pb LA-ICP-MS data from kimberlite perovskites. The greyed-out ellipses represent outliers that were excluded from the age calculation. Note that analyses not determined to be perovskite were not labeled on the diagrams. Error ellipses are 2σ.

For the Bala kimberlite, a total of 42 spots were analyzed on 42 unique perovskite grains with a majority of the analyses done within or near the edges of texture B (i.e., areas dense with olivine). Figure 35 shows the spot locations and divides the analyses into two populations based on their concordia age (i.e., age determined via the Tera-Wasserburg diagram): perovskites from population 1 yield an age of 81.7 ± 8.6 Ma (MSWD = 1, n=14) (Fig. 34a), whereas perovskites from population 2 yield an age of 59.6 ± 7.4 Ma (MSWD=0.49, n=12) (Fig. 34b). The perovskite analyses that plot between the two age arrays (Fig. 34a,b) occur throughout the thin section (Fig. 35). While it is unclear if the different petrologic textures (A and B) indicate distinct kimberlite melt batches (Fig. 24), it is evident that this kimberlite contains two separate generations of perovskite. The age of the older perovskite population falls within error of the 110-88 Ma age range previously reported for the Kansas kimberlites, while the age of the younger perovskite population falls within uncertainty of the reheating event at 65 Ma proposed by Blackburn et al. (2008). Overall, the Bala perovskites have a $^{207}Pb/^{206}Pb$ ratio of ~0.6.

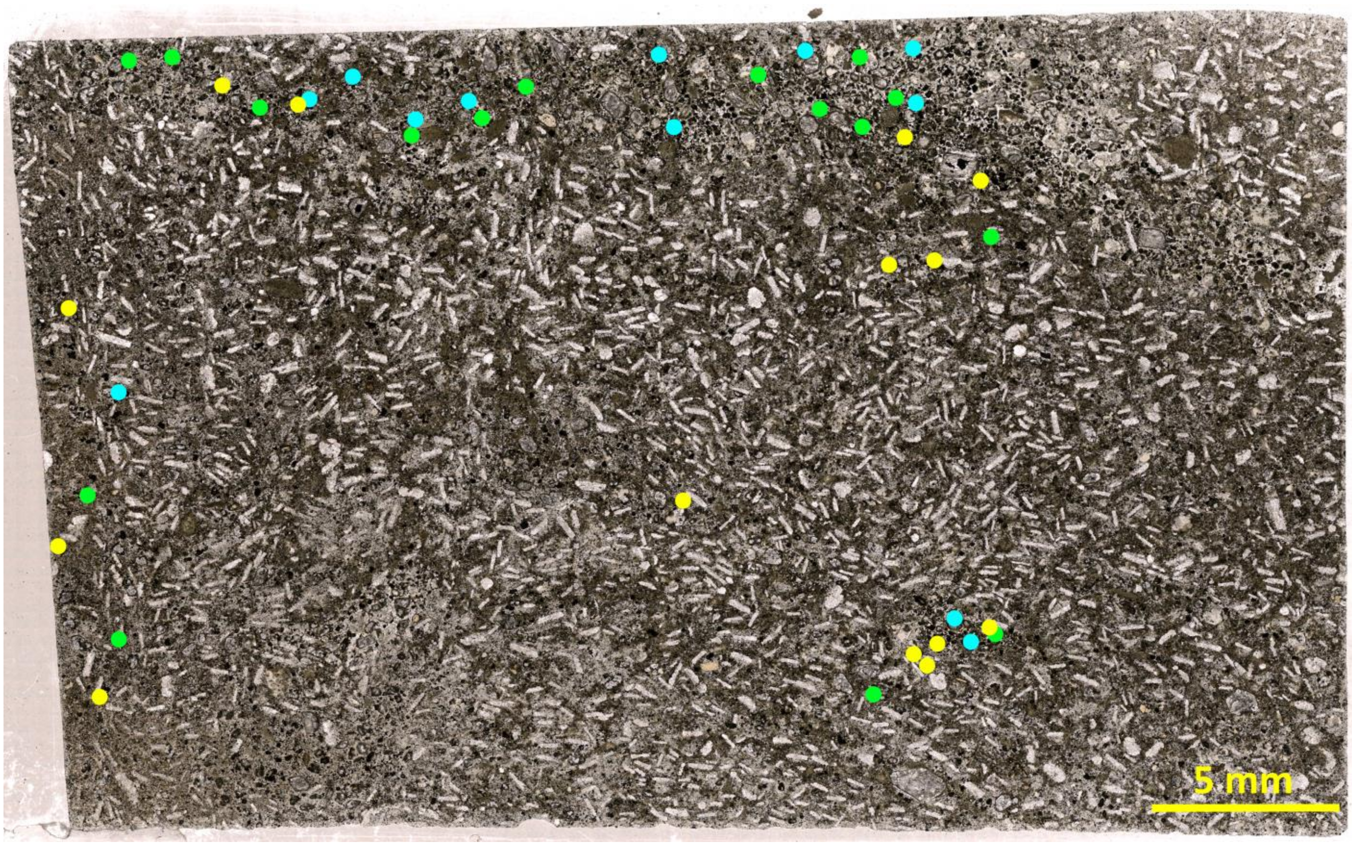

Figure 35. LA-ICP-MS Spot Locations of the Bala Perovskite Populations

Thin section photomicrograph of BA-62-39B, from the Bala kimberlite, in plane polarized light showing the locations of the two perovskite age populations. The yellow spots making up population 1 represent analyses that reported an age of 81.7 ± 8.6 Ma (MSWD = 1, n=14) while the blue spots making up the population 2 represent analyses that reported an age of 59.6 ± 7.4 Ma (MSWD=0.49, n=12). The green spots indicate grains that fall between the two age arrays in Figure 34.

Compared to the kimberlite perovskites, those found at both lamproite localities have a higher uncertainty due to their smaller spread in $^{207}Pb/^{206}Pb$ and $^{238}U/^{206}Pb$ ratios as well as their higher proportions of common Pb (Figs. 36 and 37). Despite the different morphologies, sizes, and colors of perovskite present throughout the lamproite thin sections, different age populations could not be distinguished on the basis of the data we collected. For the Hills Pond lamproite we obtained the following five ages: 87.0 ± 8.6 Ma (MSWD=1.2, n=83) from MLA-C92-9; 84.0 ± 7.1 Ma (MSWD=1.1, n=82) from MLA- C95-5; 75.3 ± 15.1 Ma (MSWD=1.1, n=31) from MLA- C97-8; 89.7 ± 4.8 Ma (MSWD=1.1, n=78) from MLA-C98-3; and 77.7 ± 13.2 Ma (MSWD=0.78, n=52) from PK-LA-M1 (Fig. 36). There were too few perovskites (n=13) suitable for LA-ICP-MS analysis within sample MML1; therefore, an accurate age could not be obtained for this sample. Combining all the U-Pb LA-ICP-MS analyses for each analytical session (i.e., September 2022 and February 2023), yielded more precise ages, with MSWD values consistent with them representing single age populations. Perovskite analyses from the first analytical session, which includes samples PK-LA-M1 and MML1 (the latter of which did not yield a precise age on its own), yield an age of 74.5 ± 11.9 Ma (MSWD=0.9, n=65) (Fig. 38a). Analyses from the second analytical session, which includes samples MLA-C92-9, MLA- C95-5, MLA-C97-8, and MLA-C98-3, yield an age of 86.9 ± 3.5 Ma (MSWD=1.1, n=274) (Fig. 38b). All of the Hills Pond samples yield a $^{207}Pb/^{206}Pb$ ratio around 0.9 (Fig. 36 and 38a,b).

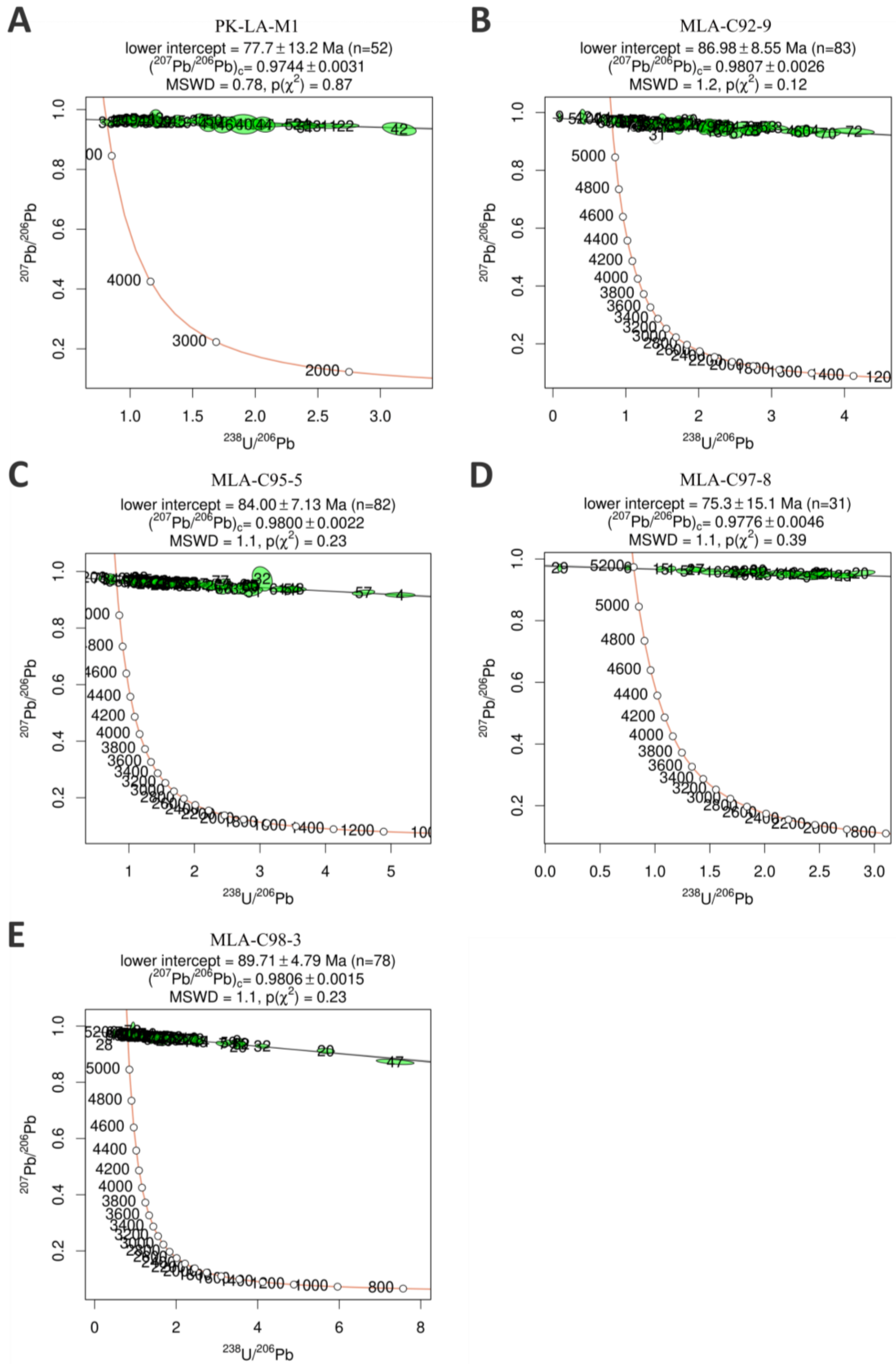

Figure 36. Hills Pond Concordia Diagrams

Tera-Wasserburg plots showing the U-Pb LA-ICP-MS data from the Hills Pond perovskites. The greyed-out ellipses represent outliers that were excluded from the age calculation. Error ellipses are 2σ.

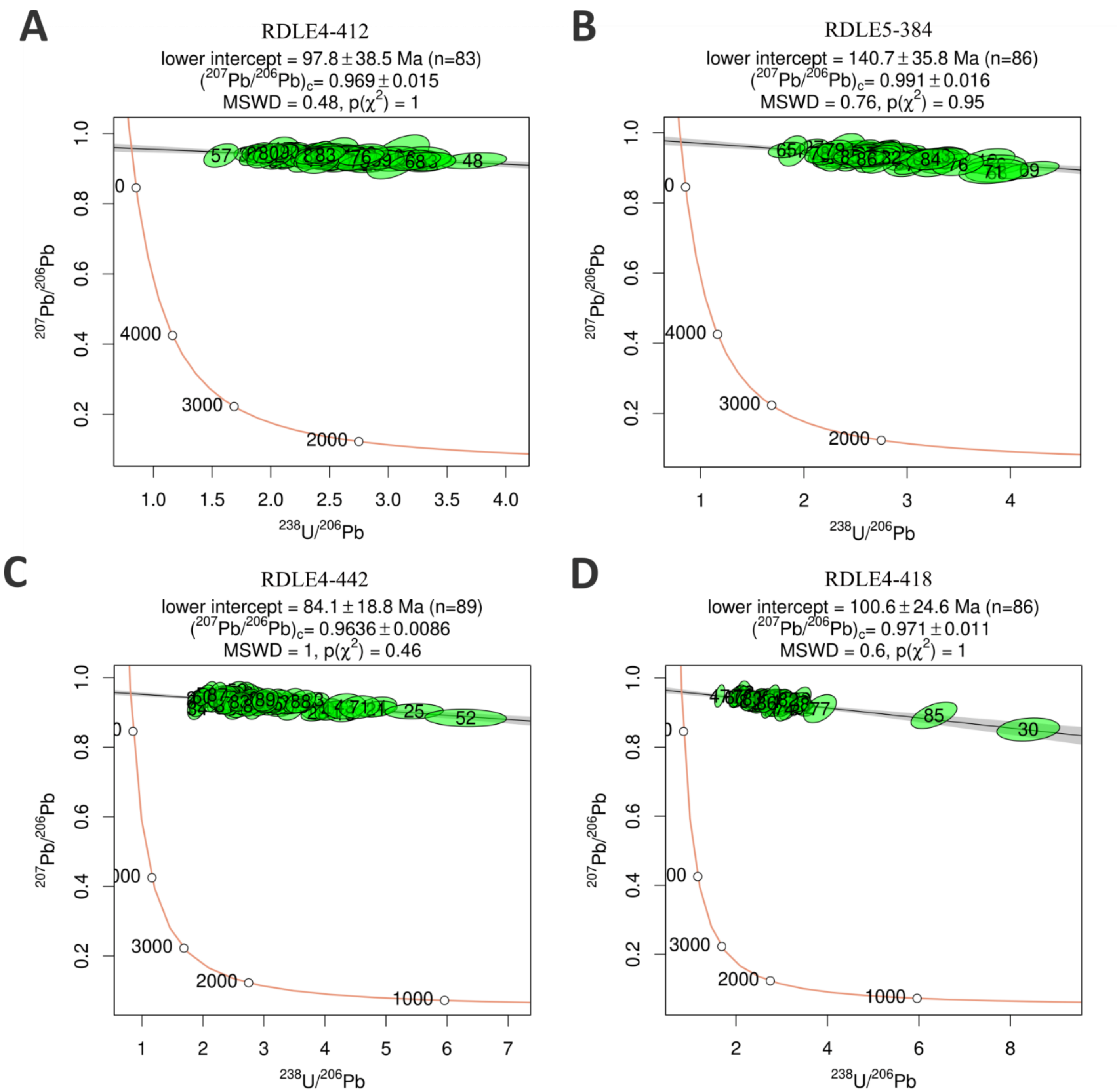

Figure 37. Rose Dome Concordia Diagrams

Tera-Wasserburg plots showing the U-Pb LA-ICP-MS data from the Rose Dome perovskites. Error ellipses are 2σ.

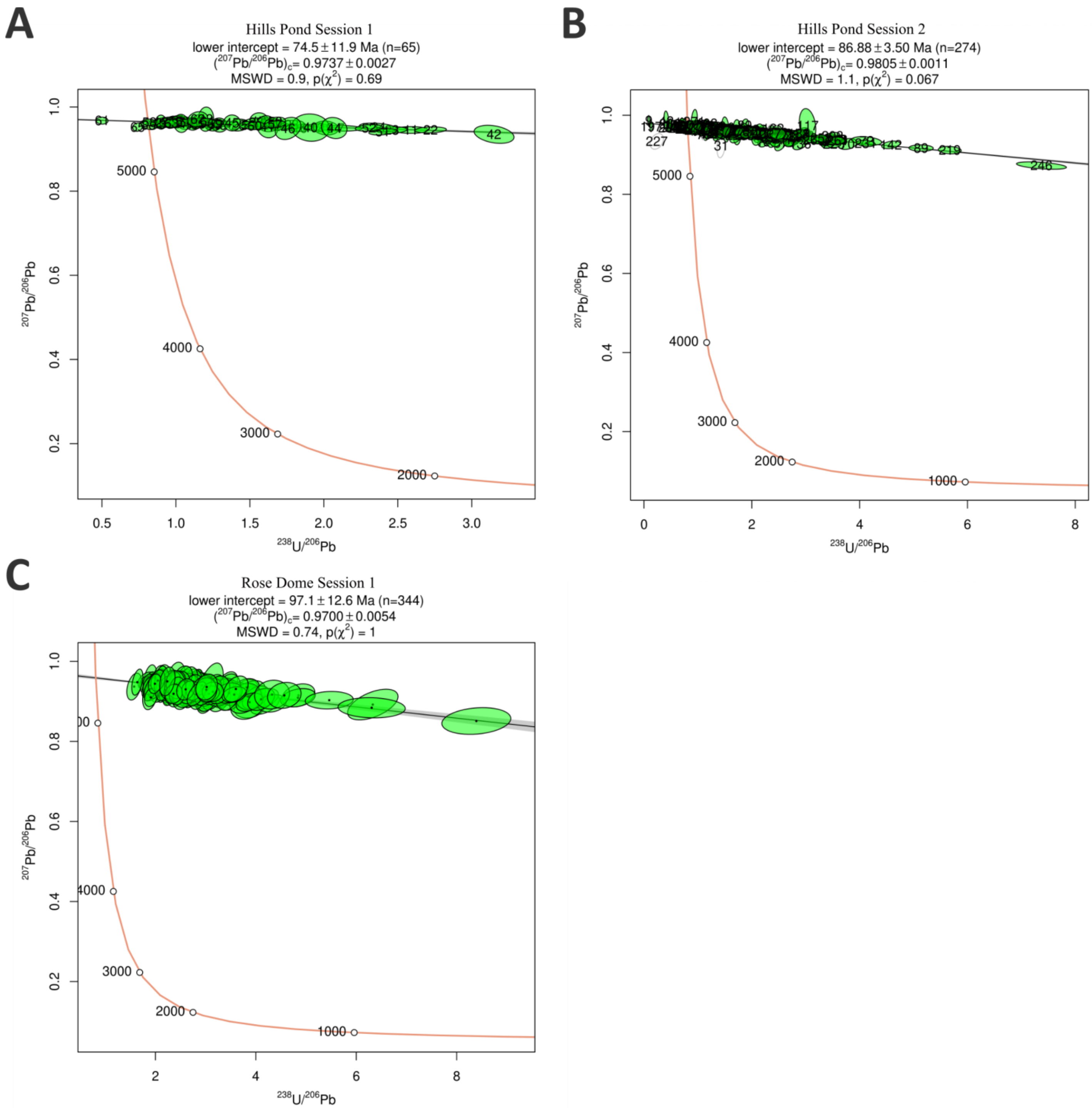

Figure 38. Combined Lamproite Concordia Diagrams

Tera-Wasserburg plots showing the U-Pb LA-ICP-MS data showing the combined session analyses for the Kanas lamproites. A) Hills Pond perovskite analyses from the first analytical session, September 2022, includes samples PK-LA-M1 and MML1. B) Hills Pond perovskite analyses from the February 2023 analytical session, includes samples MLA-C92-9; MLA- C95-5; MLA- C97-8; and MLA-C98-3. C) Rose Dome perovskites include samples RDLE4-442; RDLE4-418; RDLE5-384; and RDLE4-412. The greyed-out ellipses represent outliers that were excluded from the age calculation. Error ellipses are 2σ.

An even smaller spread in $^{207}Pb/^{206}Pb$ and $^{238}U/^{206}Pb$ ratios is observed for the Rose Dome perovskites, resulting in higher uncertainties in the calculated dates. The most precise date obtained from an individual sample, 84.1 ± 18.8 Ma (MSWD=1, n=89) was acquired from RDLE4-442 followed by 100.6 ± 24.6 (MSWD= 0.6, n=86) from RDLE4-418; 140.7 ± 35.8 Ma (MSWD= 0.76, n=86) from RDLE5-384; and 97.8 ± 38.5 Ma (MSWD= 0.48, n=83) from RDLE4-412 (Fig. 37). Since all the Rose Dome U-Pb perovskite data were analyzed during the same session, we were able to combine them to yield a more precise age of 97.1 ± 12.6 Ma (MSWD= 0.74, n=344) (Fig. 38c). Similar to the Hills Pond, the $^{207}Pb/^{206}Pb$ ratios for all the Rose Dome samples is ca. 0.9 (Fig. 37 and 38c). Both of the most precise, combined ages from the Hills Pond and Rose Dome lamproites fall within error of the updated age range of 92-93 ± 5 Ma for Hills Pond and 90 ± 4 Ma for Rose Dome (Zartman et al., 1967) (Table 4).

4.3 Geochemistry

4.3.1 Major Elements (EMPA)

A total of 224 perovskite EMP analyses were done on 102 distinct crystals. The data are presented in Supplementary Table 2. BSE imagery shows that some of the perovskites have titanosilicate and iron-rich inclusions (Figs. 30b,c and 31b), and while an attempt was made to avoid them, those below the grain surface may have contaminated a few analyses. As a result, 15% of the analyses were determined to be unreliable based on the following criteria: (i) totals < 95 wt.% or > 102 wt.%, (ii) $SiO_2 \geq 2$ wt.%, (iii) anomalously low CaO and TiO_2 wt.% (i.e., < 5 wt. %), and (iv) a cation total > 2.09%. See Locock and Mitchell (2018) for detailed mineralogical justification for these criteria. Analyses with SiO_2 >1 wt.% were not initially excluded from the dataset, even though such high SiO_2 concentrations are rare. This is because previous studies (Mitchell and Chakhmouradian, 1999; Cullers and Berendsen, 2011) have reported SiO_2 concentrations in the perovskites from the Hills Pond lamproites of up to 1.9 wt.% SiO_2 and the authors of these studies concluded they had no reason to exclude these analyses. Nevertheless, we are not as confident as these authors that the analyses with high SiO_2 are free from the effects of contamination from titanosilicate inclusions. Therefore, when reporting the EMP data, analyses with SiO_2 >1 wt.% are distinguished from those with lower SiO_2 concentrations by using different symbols (Figs. 39 and 40). In addition, the EMP data were collected over three analytical sessions (See Section 3.2) with the last two sessions (March 2023 and May 2023) occurring after LA-ICP-MS analysis. Despite attempts to polish off the thin film of ablated material produced by LA-ICP-MS analyses, there appears to be a slight systematic difference in Ti concentrations and analytical totals for analyses done during the March and May sessions (i.e., BA-62-39B, TU-1A-1D, MML1, and PK-LA-MI1). Therefore, the scaling of diagrams involving major element data, particularly TiO_2, has been set conservatively so that compositional variations attributable to these analytical issues are not artificially emphasized.

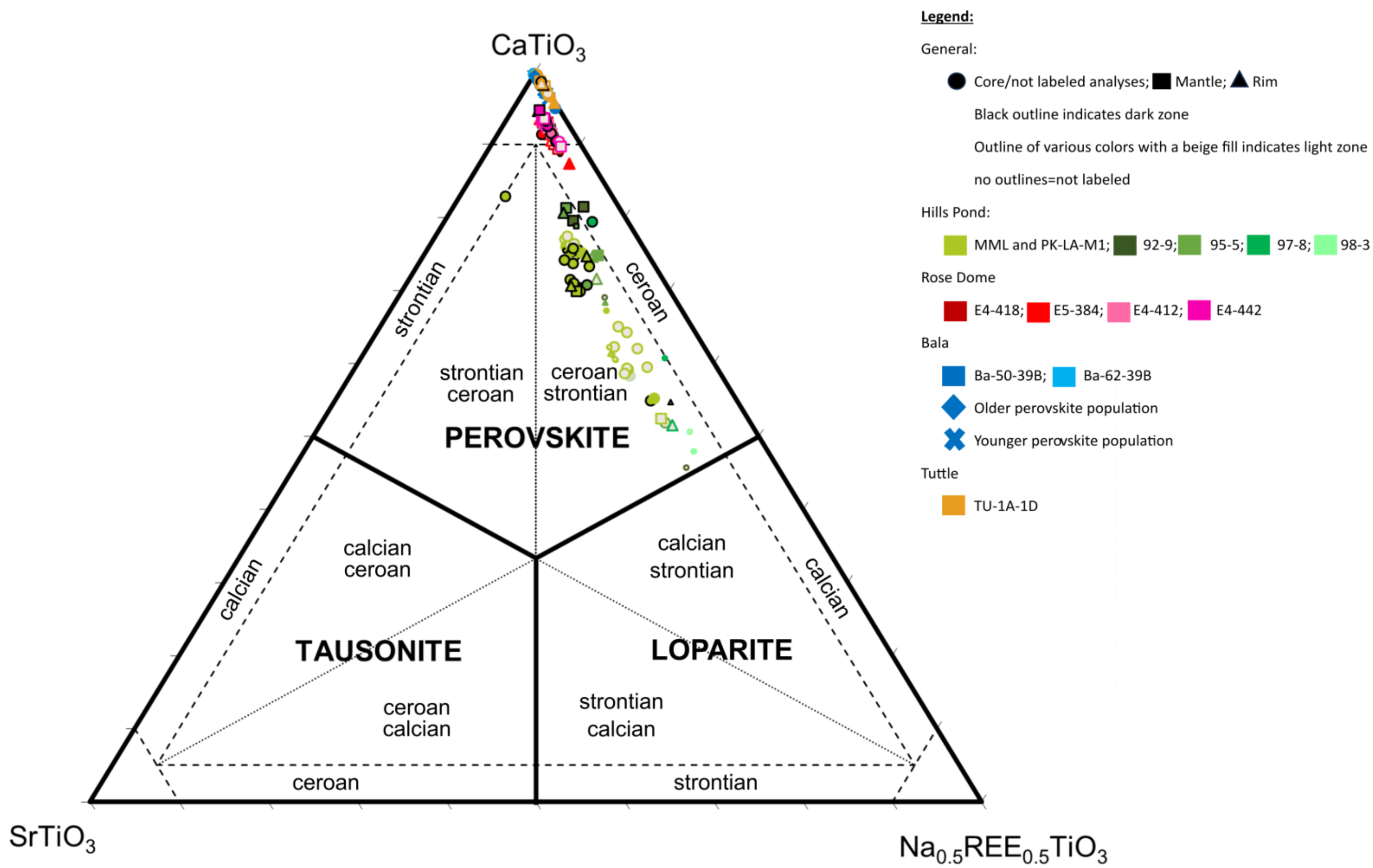

Figure 39. Kansas Perovskite Ternary Diagram

Compositional variation (mol. %) perovskite in the ternary system $CaTiO_3$ (perovskite) – $Na_{0.5}REE_{0.5}TiO_3$ (loparite) - $SrTiO_3$ (tausonite). Note that the analyses with SiO_2 > 1 wt. % are represented with smaller symbols.

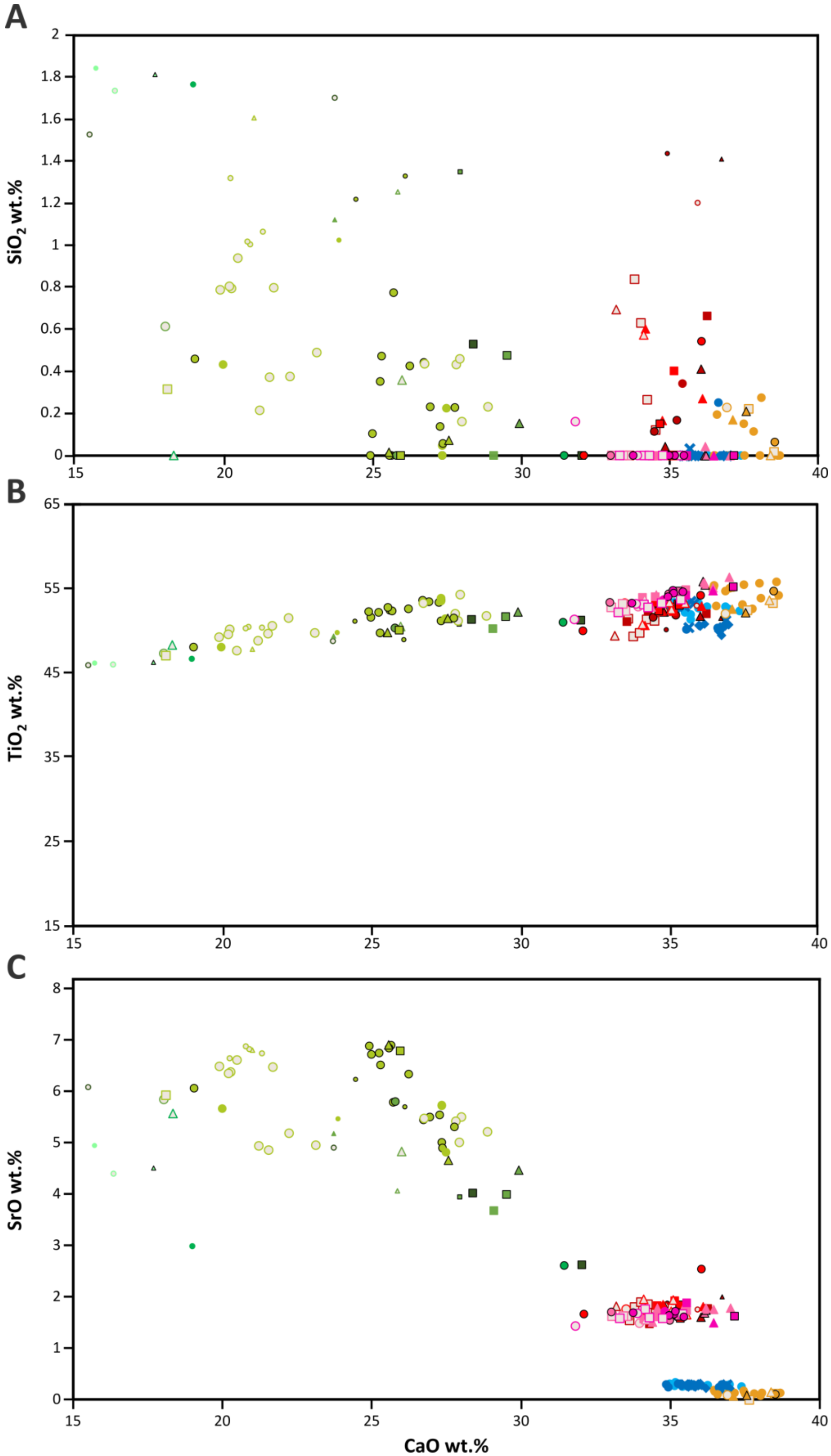
A
B
C
SiO2 wt.%
TiO2 wt.%
SrO wt.%
CaO wt.%
15
20
25
30
35
40
0
0.2
0.4
0.6
0.8
1
1.2
1.4
1.6
1.8
2
45
55
65
0
1
2
3
4
5
6
7
8

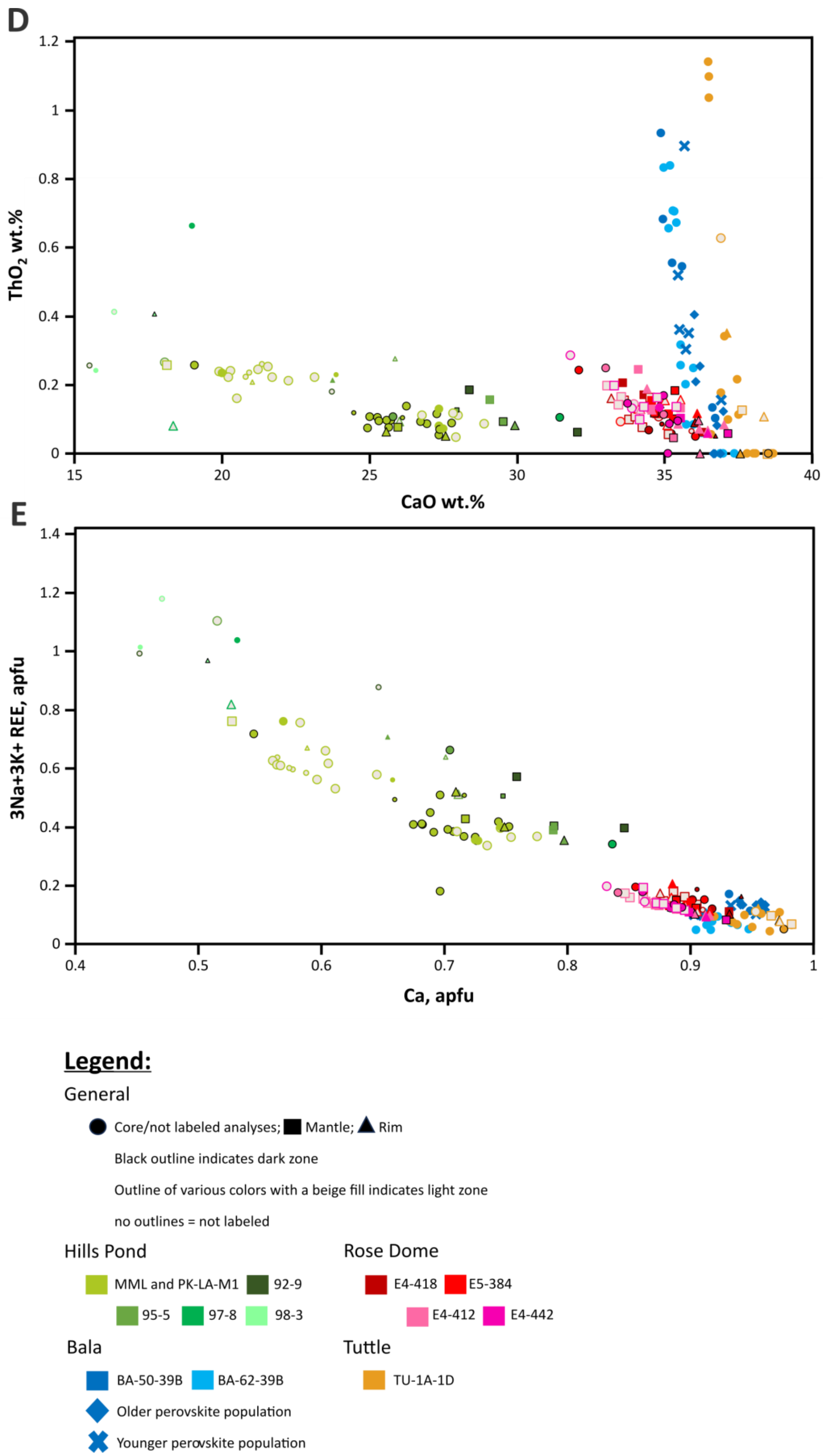
D
1.2
1
0.8
0.6
0.4
0.2
0
ThO_2 wt.%
15
20
25
30
35
40
CaO wt.%
E
1.4
1.2
1
0.8
0.6
0.4
0.2
0
3Na+3K+ REE, apfu
0.4
0.5
0.6
0.7
0.8
0.9
1
Ca, apfu
Legend:
General
Core/not labeled analyses; Mantle; Rim
Black outline indicates dark zone
Outline of various colors with a beige fill indicates light zone
no outlines = not labeled
Hills Pond
MML and PK-LA-M1
92-9
95-5
97-8
98-3
Rose Dome
E4-418
E5-384
E4-412
E4-442
Bala
BA-50-39B
BA-62-39B
Older perovskite population
Younger perovskite population
Tuttle
TU-1A-1D

Figure 40. Perovskite Bivariate Plots

Perovskite compositional plots. A) TiO_2 vs CaO B) SiO_2 vs CaO C) SrO vs CaO D) ThO_2 vs CaO E) 3Na+3K+REE vs CaO.

Mitchell (1996) demonstrated that a majority of the compositional variation of most naturally occurring perovskites (ABO_3) can be expressed in terms of the following endmembers: $CaTiO_3$ (perovskite), $Na_{0.5}REE_{0.5}TiO_3$ (loparite), $NaNbO_3$ (lueshite), and $SrTiO_3$ (tausonite) (Fig. 6). Major element data were recalculated into these endmembers (as well as a few lesser abundant end members) from the perovskite and vapnikite subgroups [$REEFeO_3$, $REETiO_{3.5}$, $CaSnO_3$ (megawite); $CaZrO_3$ (lakargiite); $Ca_{1.5}U_{0.5}O_3$ (vapnikite); $Th_{0.25}NbO_3$, $CaNb_{0.5}Fe_{0.5}O_3$ (latrappite); $CaNbO_{3.5}$, $Th_{0.5}TiO_3$, $PbTiO_3$ (macedonite); and $BaTiO_3$ (barioperovskite)] using the Excel spreadsheet from Locock and Mitchell (2018) (Supplementary Table 3).The kimberlite perovskites of this study are closest to the ideal $CaTiO_3$ endmember composition (>90 mol%) with minor amounts of Na and LREE (Ce, La, and Nd) substituting on the A site, resulting in the loparite component constituting only a maximum of 4.5 mol% of the mineral (Table 7 and Fig. 39). These minor differences in element abundances and substitutions are also reflected in the trends shown in Fig. 40. Variations in the proportions of cations substituting on the B site are generally less significant than on the A site for most perovskites (Chakhmouradian et al., 2007). Bala perovskites exhibit slightly more substitution (of Nb and Fe^{3+}) on the B site than those from Tuttle, as they contain 0 -2.3 mol% lueshite ($NaNbO_3$) and 2.8-5.0 mol% $REEFeO_3$, whereas Tuttle perovskites contain 0.8-1.7 mol% and 0-2.1 mol% of each, respectively (Table 7 and Fig. 39). Between the two Bala samples, there is a slight difference in the dominant cation substitutions observed (Table 7), as sample BA-50-39B is slightly richer in perovskite endmember, whereas sample BA-62-39B contains more loparite and lueshite, based on their median values. Although most of the BA-62-39B analyses were done during a separate session from BA-50-39B, we believe this slight difference is not an analytical artifact as the same pattern is observed on analyses from both samples taken during the same session. As detailed in Section 4.2, the BA-62-39B sample contains two perovskite age populations. However, comparison of the data in Table 7 shows that there is little compositional difference between the two age populations (Table 7). Overall, the older population (81.7 ± 8.6 Ma) is higher in loparite and lueshite, whereas the younger population (59.6 ± 7.4 Ma) has higher perovskite and $REEFeO_3$, but the differences are relatively small.

Similar to the Kansas kimberlite perovskites, those from the Rose Dome lamproite are also close to the perovskite endmember composition (84.9-93.8 mol%) (Fig. 39). However, the Rose Dome perovskites are more enriched in Na, LREE, K, and Sr (Fig. 40c,e) resulting in higher proportions of the loparite (2.9-9.9 mol%) and tausonite (2.0-3.6 mol%) endmembers (Table 7). The Na, LREE, and K enrichments, in addition to high Fe^{3+} concentrations (Fig. 40c), are responsible for the wider range of $REEFeO_3$ proportions (0-5.7 mol%) relative to the kimberlites (Table 7). Among the different Rose Dome cores, E5-384 generally has the highest level of substituent cations, as it has the highest concentrations of loparite, tausonite, and $REEFeO_3$ (Table 7, Fig. 39). The lowest proportions of loparite and tausonite are from core E4-412, whereas the lowest for $REEFeO_3$ are from E4-418 (Table 7, Fig. 39). While the SiO_2 concentration is not as high as that observed within the Hills Pond, perovskite from cores E5-384 and E4-418 do contain a significant amount, up to 1.4 wt.% (Fig. 40b). The remaining cores contain perovskite with low concentrations of SiO_2, similar to the kimberlites (≤ 0.3 wt.%).

Table 7. Perovskite Endmember Proportions

Comparison of the mol % endmembers of the perovskite group minerals from the Kansas lamproites and kimberlites.

	Perovskite			Loparite			Tausonite			Lueshite			$REEFeO_3$			$REE_2Ti_2O_7$		
	Min	Median	Max	Min	Median	Max	Min	Median	Max	Min	Median	Max	Min	Median	Max	Min	Median	Max
MML1 & PK-LA-M1 (n=45)	51.4%	69.8%	78.3%	4.9%	19.3%	37.1%	7.0%	9.0%	11.3%	0.5%	0.8%	1.2%	0.0%	0.0%	1.4%	0.0%	0.0%	3.2%
MLA-C92-9 (n=4)	45.3%	73.4%	81.1%	14.2%	18.9%	43.7%	3.9%	6.8%	10.1%	0.4%	0.8%	1.2%	0.0%	0.0%	0.0%	0.0%	0.0%	0.0%
MLA-C95-5 (n=9)	51.5%	73.5%	80.3%	12.7%	19.5%	38.4%	5.6%	6.5%	9.5%	0.4%	0.9%	1.2%	0.0%	0.0%	0.1%	0.0%	0.0%	0.0%
MLA-C97-8 (n=3)	50.9%	57.8%	79.0%	16.7%	32.6%	39.1%	3.9%	4.9%	8.8%	0.4%	1.2%	3.8%	0.0%	0.0%	0.0%	0.0%	0.0%	0.0%
MLA-C98-3 (n=3)	47.5%	49.9%	53.7%	37.1%	41.6%	43.5%	7.3%	7.4%	8.2%	0.9%	1.1%	1.4%	0.0%	0.0%	0.0%	0.0%	0.0%	0.0%
Total Hills Pond (n=64)	45.3%	69.9%	81.1%	4.9%	19.5%	43.7%	3.9%	8.3%	11.3%	0.4%	0.8%	3.8%	0.0%	0.0%	1.4%	0.0%	0.0%	3.2%
BA-50-39B (n=16)	91.1%	93.4%	95.0%	0.0%	0.0%	2.4%	0.3%	0.4%	0.5%	0.0%	1.5%	2.0%	2.8%	3.8%	5.0%	0.0%	0.0%	0.9%
BA-62 old array (n=8)	91.2%	91.9%	92.8%	2.0%	2.5%	3.3%	0.2%	0.4%	0.5%	1.5%	1.9%	2.3%	2.8%	3.2%	3.6%	0.0%	0.0%	0.0%
BA-62 young array (n=6)	91.5%	92.6%	93.3%	0.2%	0.9%	2.7%	0.4%	0.4%	0.4%	1.4%	1.6%	1.8%	3.7%	4.1%	4.6%	0.0%	0.0%	0.0%
Total BA-62-39B (n=20)	90.3%	92.0%	93.3%	0.2%	1.8%	4.5%	0.2%	0.4%	0.5%	1.4%	1.8%	2.3%	2.8%	3.7%	4.6%	0.0%	0.0%	0.0%
Total Bala (n=36)	90.3%	92.5%	95.0%	0.0%	0.9%	4.5%	0.2%	0.4%	0.5%	0.0%	1.7%	2.3%	2.8%	3.7%	5.0%	0.0%	0.0%	0.9%
TU-1A-1D2 (n=21)	93.3%	95.3%	97.8%	0.3%	2.0%	4.2%	0.0%	0.2%	0.2%	0.8%	1.3%	1.7%	0.0%	1.3%	2.1%	0.0%	0.0%	0.0%
RDLE4-C418 (n=20)	86.6%	89.3%	93.8%	2.9%	4.7%	8.5%	2.1%	2.5%	3.0%	0.2%	0.3%	0.6%	0.0%	2.5%	4.7%	0.0%	0.0%	0.0%
RDLE5-C384 (n=15)	85.0%	89.3%	90.9%	3.6%	5.0%	9.9%	2.2%	2.6%	3.6%	0.2%	0.3%	0.4%	0.0%	2.9%	5.7%	0.0%	0.0%	0.0%
RDLE4-C412 (n=19)	85.9%	89.1%	91.9%	3.7%	4.4%	5.7%	2.1%	2.3%	2.5%	0.2%	0.3%	0.4%	1.4%	3.6%	5.5%	0.0%	0.0%	0.1%
RDLE4-C442 (n=16)	84.9%	89.4%	93.0%	3.1%	4.4%	7.7%	2.0%	2.3%	2.6%	0.2%	0.3%	0.4%	1.3%	3.6%	5.4%	0.0%	0.0%	0.0%
Total Rose Dome (n=70)	84.9%	89.3%	93.8%	2.9%	4.5%	9.9%	2.0%	2.4%	3.6%	0.2%	0.3%	0.6%	0.0%	3.1%	5.7%	0.0%	0.0%	0.1%

Of the four localities studied, the Hills Pond perovskites are the most compositionally diverse, as the mol% $CaTiO_3$ ranges from 45.3 – 81.1% (Table 7 and Fig. 39). They are the most enriched in Na, LREE, K, and Sr and thus have the highest proportions of loparite (4.9- 43.7 mol%) and tausonite (3.9 – 11.3 mol%) (Table 7 and Fig. 39). Nb is the dominant substituent on the B site, as very little Fe^{3+} is present (Table 7, Supplementary Table 2 and 3). Most of the perovskites have similarly low lueshite component of ~0.4 – 1.4 mol% except for core 97-8, which ranges up to 3.8 mol% (Table 7). Likewise, all the perovskites have little to no $REEFeO_3$, except for those from the samples collected in 2019 from the mine surface (MML and PK-LA-M1), which have up to 1.4 mol% of this component (Table 7). Core 98-3 has the highest loparite content and a consistently high tausonite content, although samples MML and PK-LA-M1 are highest in the tausonite component (Table 7). The samples with the lowest loparite component are MML and PK-LA-M1; core 97-8 is lowest in tausonite component (Table 7, Fig. 39). Although all Hills Pond perovskites have a high SiO_2 content, core 98-3 has the highest SiO_2 concentrations we measured, i.e., 1.7-1.8 wt.% (Fig. 40b). Figure 40e shows a strong negative correlation between Ca and 3Na +3K + REE between all perovskites except for sample PK-LA-M1perov2d, which is an outlier due to it containing 3.2 mol% $REE_2TiO_2O_7$, a non-stoichiometric perovskite (Table 7).

As detailed in Section 4.1, two types of zonation are observed within the perovskites: concentric zoning within the Rose Dome (and to a lesser extent Tuttle and Bala) localities; and sector zoning within the Hills Pond lamproite. The compositions of light and dark zones are relatively similar for the different localities. Due to the limited zoning present, no compositional data for dark vs light zones were collected for Bala, and few data were collected for Tuttle. Overall, the dark zones tend to have higher proportions of the perovskite endmember and are, therefore, more enriched in Ca and Ti, whereas the lighter zones have higher proportions of loparite, $REEFeO_3$, lueshite, (and tausonite for the Hills Pond perovskites) and are therefore enriched in Na, K, LREE, Nb, Fe3+ (and Sr) (Table 8 and Fig. 39). The Hills Pond perovskites show the most significant compositional distinction between light and dark sector zones due to their overall high compositional variability. There is less of a compositional distinction between core, mantle, rim analyses than that observed between light and dark zones within every locality (Table 9). The perovskites from the Tuttle kimberlite and both the Kansas lamproites become depleted in Na, K, and LREE (loparite) and enriched in Ca and Ti (perovskite) from core to rim (Table 9), whereas the proportion of tausonite (Sr) remains relatively constant (Fig. 39). This is consistent with the observations made by Mitchell and Chakhmouradian (1999) on the Hills Pond perovskites.

Table 8. Compositional Variation between Perovskite Zones

Comparison of the compositional variation (mol. %) of perovskite group minerals from the light and dark zones within the Kansas kimberlites and lamproites. Note perovskites from Bala are not listed as little to no zonation is present.

			Perovskite			Loparite			Tausonite			Lueshite			$REEFeO_3$			$REE_2Ti_2O_7$		
	Zone	n#	Min	Median	Max	Min	Median	Max	Min	Median	Max	Min	Median	Max	Min	Median	Max	Min	Median	Max
MML1 & PK-LA-M1	dark	20	53.8%	72.7%	78.3%	4.9%	18.1%	34.8%	7.0%	9.6%	11.3%	0.6%	0.9%	1.2%	0.0%	0.0%	1.1%	0.0%	0.0%	3.2%
	light	20	51.4%	60.9%	76.8%	14.7%	27.9%	37.1%	7.4%	9.7%	10.9%	0.5%	0.7%	0.9%	0.0%	0.0%	1.4%	0.0%	0.0%	0.3%
MLA-C92-9	dark	2	78.3%	79.7%	81.1%	14.2%	14.4%	14.6%	3.9%	5.0%	6.0%	0.4%	0.8%	1.2%	0.0%	0.0%	0.0%	0.0%	0.0%	0.0%
	light	2	45.3%	56.9%	68.5%	23.2%	33.4%	43.7%	7.7%	8.9%	10.1%	0.7%	0.8%	0.8%	0.0%	0.0%	0.0%	0.0%	0.0%	0.0%
MLA-C95-5	dark	4	70.0%	78.9%	80.3%	12.7%	13.9%	20.2%	5.9%	6.3%	8.8%	0.9%	1.0%	1.1%	0.0%	0.0%	0.0%	0.0%	0.0%	0.0%
	light	3	51.5%	70.9%	73.5%	18.8%	20.8%	38.4%	6.2%	7.3%	9.5%	0.6%	1.0%	1.2%	0.0%	0.0%	0.0%	0.0%	0.0%	0.0%
MLA-C97-8	dark	1	79.0%	79.0%	79.0%	16.7%	16.7%	16.7%	3.9%	3.9%	3.9%	0.4%	0.4%	0.4%	0.0%	0.0%	0.0%	0.0%	0.0%	0.0%
	light	1	50.9%	50.9%	50.9%	39.1%	39.1%	39.1%	8.8%	8.8%	8.8%	1.2%	1.2%	1.2%	0.0%	0.0%	0.0%	0.0%	0.0%	0.0%
MLA-C98-3	dark	1	53.7%	53.7%	53.7%	37.1%	37.1%	37.1%	7.4%	7.4%	7.4%	1.4%	1.4%	1.4%	0.0%	0.0%	0.0%	0.0%	0.0%	0.0%
	light	1	49.9%	49.9%	49.9%	41.6%	41.6%	41.6%	7.3%	7.3%	7.3%	1.1%	1.1%	1.1%	0.0%	0.0%	0.0%	0.0%	0.0%	0.0%
Total Hills Pond	dark	28	53.7%	73.7%	81.1%	4.9%	17.0%	37.1%	3.9%	8.5%	11.3%	0.4%	0.9%	1.4%	0.0%	0.0%	1.1%	0.0%	0.0%	3.2%
	light	27	45.3%	60.9%	76.8%	14.7%	28.0%	43.7%	6.2%	8.8%	10.9%	0.5%	0.8%	1.2%	0.0%	0.0%	1.4%	0.0%	0.0%	0.3%
TU-1A-1D2	dark	2	95.8%	96.7%	97.6%	1.4%	1.5%	1.7%	0.1%	0.1%	0.1%	0.8%	1.1%	1.3%	0.0%	0.5%	1.0%	0.0%	0.0%	0.0%
	light	4	94.2%	95.3%	96.2%	1.2%	1.7%	2.8%	0.0%	0.2%	0.2%	1.2%	1.4%	1.6%	1.2%	1.4%	1.5%	0.0%	0.0%	0.0%
RDLE4-C418	dark	6	88.3%	90.2%	93.8%	2.9%	4.4%	8.5%	2.3%	2.5%	3.0%	0.3%	0.3%	0.5%	0.0%	1.9%	2.9%	0.0%	0.0%	0.0%
	light	9	86.6%	88.5%	92.9%	3.9%	5.1%	7.6%	2.2%	2.6%	2.9%	0.2%	0.4%	0.6%	0.0%	2.7%	4.7%	0.0%	0.0%	0.0%
RDLE5-C384	dark	5	85.0%	89.9%	90.9%	4.0%	5.1%	6.6%	2.2%	2.4%	3.6%	0.2%	0.4%	0.4%	0.0%	3.4%	5.7%	0.0%	0.0%	0.0%
	light	5	86.7%	89.6%	90.6%	3.6%	5.6%	6.9%	2.4%	2.6%	2.9%	0.2%	0.4%	0.4%	2.6%	3.1%	3.5%	0.0%	0.0%	0.0%
RDLE4-C412	dark	5	85.9%	89.7%	91.6%	3.9%	4.2%	5.6%	2.1%	2.3%	2.4%	0.2%	0.3%	0.4%	1.4%	3.6%	5.3%	0.0%	0.0%	0.1%
	light	5	86.0%	87.1%	88.2%	4.5%	5.0%	5.7%	2.1%	2.3%	2.3%	0.2%	0.2%	0.3%	4.7%	5.3%	5.5%	0.0%	0.0%	0.0%
RDLE4-C442	dark	6	86.8%	90.0%	93.0%	3.1%	4.4%	6.9%	2.2%	2.3%	2.4%	0.2%	0.3%	0.4%	1.3%	2.9%	3.6%	0.0%	0.0%	0.0%
	light	7	84.9%	88.4%	90.0%	3.9%	4.7%	7.7%	2.1%	2.2%	2.5%	0.2%	0.2%	0.3%	3.6%	4.0%	5.4%	0.0%	0.0%	0.0%
Total Rose Dome	dark	22	85.0%	89.9%	93.8%	2.9%	4.4%	8.5%	2.1%	2.4%	3.6%	0.2%	0.3%	0.5%	0.0%	2.8%	5.7%	0.0%	0.0%	0.1%
	light	26	84.9%	88.1%	92.9%	3.6%	4.9%	7.7%	2.1%	2.4%	2.9%	0.2%	0.3%	0.6%	0.0%	3.6%	5.5%	0.0%	0.0%	0.0%

Table 9. Compositional Variation between Core/Mantle/Rim Analyses

Comparison of the compositional variation (mol. %) of perovskite group minerals from the core, mantle, and rim within the Kansas kimberlites and lamproites. Note perovskites from Bala are not listed as this data was not collected.

			Perovskite			Loparite			Tausonite			Lueshite			$REEFeO_3$			$REE_2Ti_2O_7$		
	Zone	n#	Min	Median	Max	Min	Median	Max	Min	Median	Max	Min	Median	Max	Min	Median	Max	Min	Median	Max
MML1 & PK-LA-M1	core	9	53.8%	63.8%	75.1%	15.5%	28.0%	35.4%	7.3%	8.9%	10.6%	0.5%	0.7%	0.9%	0.0%	0.0%	1.0%	0.0%	0.0%	0.0%
	mantle	2	51.4%	60.3%	69.2%	19.5%	28.3%	37.1%	9.5%	9.9%	10.4%	0.7%	0.8%	0.9%	0.0%	0.7%	1.4%	0.0%	0.0%	0.0%
	rim	3	60.9%	70.0%	74.2%	18.3%	18.5%	27.5%	7.0%	10.6%	10.9%	0.6%	0.7%	0.9%	0.0%	0.0%	0.0%	0.0%	0.0%	0.0%
MLA-C92-9	core	2	45.3%	56.9%	68.5%	23.2%	33.4%	43.7%	7.7%	8.9%	10.1%	0.7%	0.8%	0.8%	0.0%	0.0%	0.0%	0.0%	0.0%	0.0%
	mantle	2	78.3%	79.7%	81.1%	14.2%	14.4%	14.6%	3.9%	5.0%	6.0%	0.4%	0.8%	1.2%	0.0%	0.0%	0.0%	0.0%	0.0%	0.0%
	rim	1	65.8%	65.8%	65.8%	23.5%	23.5%	23.5%	5.8%	5.8%	5.8%	4.2%	4.2%	4.2%	0.0%	0.0%	0.0%	0.0%	0.0%	0.0%
MLA-C95-5	core	2	51.5%	60.7%	70.0%	20.2%	29.3%	38.4%	8.8%	9.1%	9.5%	0.6%	0.8%	1.0%	0.0%	0.0%	0.0%	0.0%	0.0%	0.0%
	mantle	3	74.3%	77.9%	80.3%	12.7%	15.1%	19.5%	5.6%	5.9%	6.0%	0.4%	0.9%	1.1%	0.0%	0.0%	0.1%	0.0%	0.0%	0.0%
	rim	4	67.9%	72.2%	79.9%	12.7%	19.8%	23.4%	6.2%	6.9%	8.0%	0.7%	0.9%	1.2%	0.0%	0.0%	0.0%	0.0%	0.0%	0.0%
MLA-C97-8	core	1	79.0%	79.0%	79.0%	16.7%	16.7%	16.7%	3.9%	3.9%	3.9%	0.4%	0.4%	0.4%	0.0%	0.0%	0.0%	0.0%	0.0%	0.0%
	rim	1	50.9%	50.9%	50.9%	39.1%	39.1%	39.1%	8.8%	8.8%	8.8%	1.2%	1.2%	1.2%	0.0%	0.0%	0.0%	0.0%	0.0%	0.0%
MLA-C98-3	core	1	49.9%	49.9%	49.9%	41.6%	41.6%	41.6%	7.3%	7.3%	7.3%	1.1%	1.1%	1.1%	0.0%	0.0%	0.0%	0.0%	0.0%	0.0%
	rim	1	53.7%	53.7%	53.7%	37.1%	37.1%	37.1%	7.4%	7.4%	7.4%	1.4%	1.4%	1.4%	0.0%	0.0%	0.0%	0.0%	0.0%	0.0%
Total Hills Pond	core	15	79.0%	63.8%	79.0%	41.6%	28.0%	43.7%	8.8%	8.8%	10.6%	1.1%	0.7%	1.1%	0.0%	0.0%	1.0%	0.0%	0.0%	0.0%
	mantle	6	78.3%	76.1%	80.3%	19.5%	17.3%	37.1%	9.5%	6.0%	10.4%	1.2%	0.9%	1.2%	0.0%	0.0%	1.4%	0.0%	0.0%	0.0%
	rim	9	67.9%	70.0%	79.9%	39.1%	20.8%	39.1%	8.8%	7.4%	10.9%	1.4%	0.9%	1.4%	0.0%	0.0%	0.0%	0.0%	0.0%	0.0%
TU-1A-1D2	core	2	94.2%	95.9%	97.6%	1.4%	2.1%	2.8%	0.1%	0.1%	0.1%	0.8%	1.2%	1.5%	0.0%	0.7%	1.3%	0.0%	0.0%	0.0%
	mantle	2	95.0%	95.6%	96.2%	1.2%	1.6%	2.0%	0.0%	0.1%	0.2%	1.2%	1.4%	1.6%	1.2%	1.4%	1.5%	0.0%	0.0%	0.0%
	rim	3	94.0%	95.6%	95.8%	1.4%	1.7%	4.2%	0.1%	0.1%	0.2%	1.3%	1.3%	1.3%	0.4%	1.0%	1.5%	0.0%	0.0%	0.0%
RDLE4-C418	core	5	88.3%	89.9%	92.9%	4.1%	4.6%	8.5%	2.3%	2.6%	2.9%	0.2%	0.3%	0.5%	0.0%	2.0%	3.0%	0.0%	0.0%	0.0%
	mantle	9	86.6%	88.6%	91.3%	3.9%	5.1%	7.6%	2.1%	2.5%	2.9%	0.2%	0.3%	0.6%	0.6%	2.7%	4.7%	0.0%	0.0%	0.0%
	rim	4	86.7%	90.7%	93.8%	2.9%	4.2%	6.9%	2.4%	2.7%	3.0%	0.3%	0.4%	0.5%	0.0%	2.3%	3.2%	0.0%	0.0%	0.0%
RDLE5-C384	core	3	85.0%	86.7%	90.9%	5.1%	6.6%	6.9%	2.4%	2.5%	3.6%	0.2%	0.2%	0.4%	0.0%	3.5%	5.7%	0.0%	0.0%	0.0%
	mantle	5	88.6%	89.1%	90.0%	4.0%	4.4%	5.7%	2.2%	2.5%	2.8%	0.3%	0.3%	0.4%	2.2%	3.4%	3.5%	0.0%	0.0%	0.0%
	rim	7	85.9%	89.6%	90.6%	3.6%	4.8%	9.9%	2.3%	2.6%	2.9%	0.3%	0.4%	0.4%	1.2%	2.9%	3.1%	0.0%	0.0%	0.0%
RDLE4-C412	core	3	85.9%	88.2%	89.7%	4.2%	4.6%	5.6%	2.1%	2.1%	2.4%	0.2%	0.3%	0.4%	3.6%	4.7%	5.3%	0.0%	0.0%	0.1%
	mantle	7	86.0%	88.0%	90.2%	3.9%	4.8%	5.7%	2.2%	2.3%	2.4%	0.2%	0.3%	0.4%	2.9%	4.5%	5.5%	0.0%	0.0%	0.0%
	rim	9	88.1%	91.0%	91.9%	3.7%	4.3%	4.9%	2.1%	2.4%	2.5%	0.2%	0.4%	0.4%	1.4%	2.0%	4.8%	0.0%	0.0%	0.0%
RDLE4-C442	core	7	84.9%	89.3%	90.2%	4.1%	4.4%	7.0%	2.1%	2.3%	2.4%	0.2%	0.3%	0.4%	2.7%	3.1%	5.4%	0.0%	0.0%	0.0%
	mantle	7	86.2%	89.6%	93.0%	3.1%	4.1%	7.7%	2.2%	2.2%	2.6%	0.2%	0.2%	0.3%	1.3%	3.6%	4.5%	0.0%	0.0%	0.0%
	rim	1	92.0%	92.0%	92.0%	3.2%	3.2%	3.2%	2.0%	2.0%	2.0%	0.3%	0.3%	0.3%	2.4%	2.4%	2.4%	0.0%	0.0%	0.0%
Total Rose Dome	core	18	88.3%	89.3%	92.9%	5.1%	4.8%	8.5%	2.4%	2.4%	3.6%	0.2%	0.3%	0.5%	3.6%	3.1%	5.7%	0.0%	0.0%	0.1%
	mantle	28	88.6%	88.8%	93.0%	4.0%	4.7%	7.7%	2.2%	2.3%	2.9%	0.3%	0.3%	0.6%	2.9%	3.5%	5.5%	0.0%	0.0%	0.0%
	rim	21	92.0%	90.2%	93.8%	3.7%	4.2%	9.9%	2.4%	2.4%	3.0%	0.3%	0.4%	0.5%	2.4%	2.6%	4.8%	0.0%	0.0%	0.0%

4.3.2 Trace Elements (LA-ICP-MS)

Perovskite trace element analyses from the Hills Pond (MLA-C92-9), Rose Dome (RDLE5-C384 and RDLE4-C418), and Bala (BA-62-39B) localities are presented in Supplementary Table 4. As mentioned in Section 4.3.1, many of the perovskites contain inclusions that may have contaminated the analyses. Therefore, a similar filtering system to that utilized for the major elements was implemented for the trace elements. Approximately 9% of the 194 trace element spot analyses were excluded based on the following criteria: (i) Si ≥ 9,350 ppm, (ii) Ca ≤ 35,730 ppm, (iii) Ti ≤ 30,000 ppm, and (iv) anonymously high Ba (i.e., > 2,400 ppm). Additionally, analyses with Si ≥ 4,670 ppm were regarded with caution.

The perovskites from all three localities display trace element concentrations that encompass over seven orders of magnitude, with all elements occurring in concentrations greater than that of primitive mantle except for Rb (Fig.41). Note that some of the elements (i.e., Sr, Nb, La, Ce, Pr, Nd, Th, and Ta) represented within the spider diagrams occur in concentrations above 1000 ppm and are, therefore, technically not trace elements. However, many occur in concentrations close to or below the detection limits of the EMP; therefore, they are discussed both here and in Section 4.3.1 on major elements. Perovskites from both age populations observed in the Bala kimberlite (see Section 4.2) display similar trace element patterns (Fig. 42a). They are characterized by (1) an enrichment in light rare earth elements (LREE) relative to the heavy rare earth elements (HREE); (2) depletions in the large-ion-lithophile elements (LILE) Cs, Rb, Ba, and Sr relative to adjacent elements on multi-element diagrams; and (3) similar relative depletion in the high-field-strength elements (HFSE) Zr and Y. Note, however, that the kimberlite perovskites do not show the same relative depletions for the HFSE Nb and Ta. Th/U ratios are high in the Bala perovskites, i.e., typically >1. Despite the similar trace element patterns between Bala's two age arrays, there are a few elements that show slight variations when comparing the median values for the two perovskite populations. The grains that make up the older array have a higher concentration of Rb and display a wider spread in Cs, Rb, and Th; by comparison, the younger perovskite population exhibits a wider spread in Ba (Fig.42b).

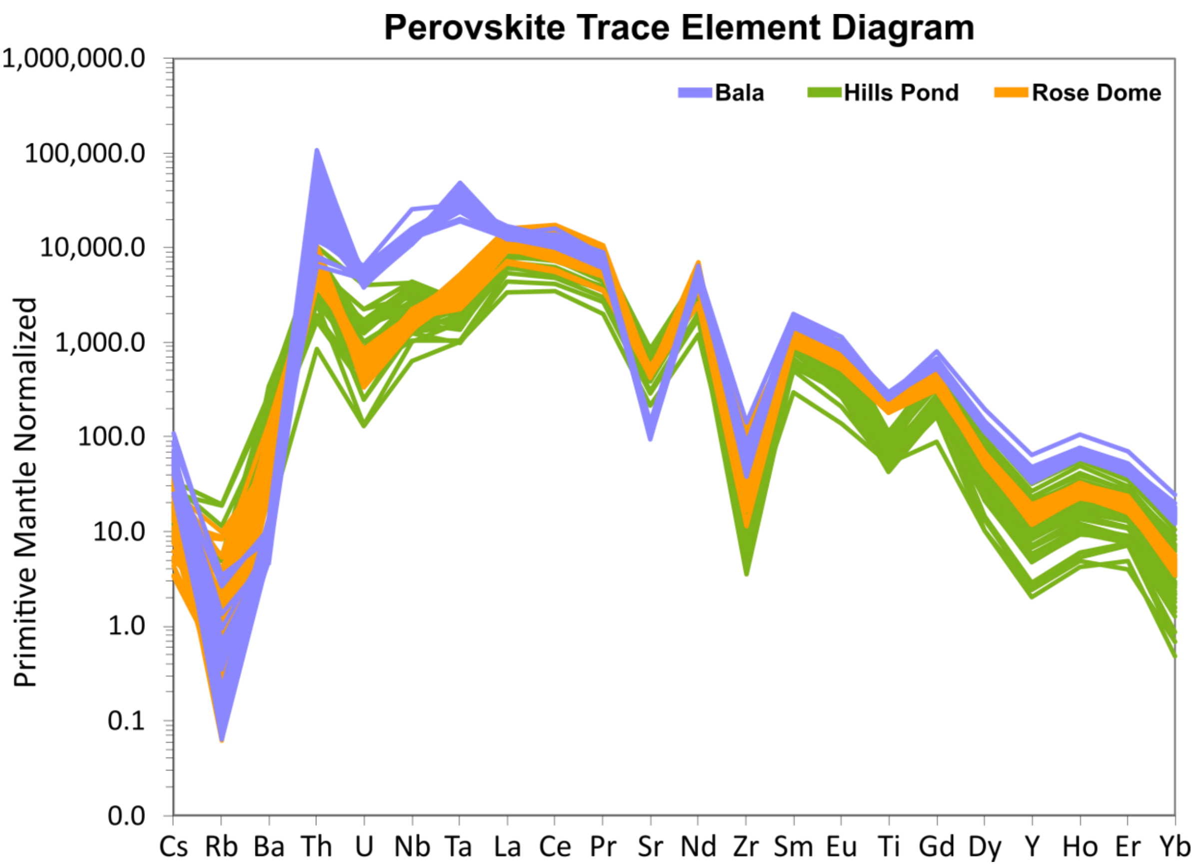

Figure 41. Spider Diagram Comparing the Kansas Lamproites and Kimberlites

Trace element data for perovskites from Bala kimberlite (purple), Hills Pond lamproites (green), and Rose Dome lamproite (orange) normalized to the primitive mantle values of Sun and McDonough (1989).

When the trace element LA-ICP-MS analyses were collected, nine analyses from the Bala kimberlite (see Supplementary Table 4) were included that did not have any major element or geochronologic data associated with them.

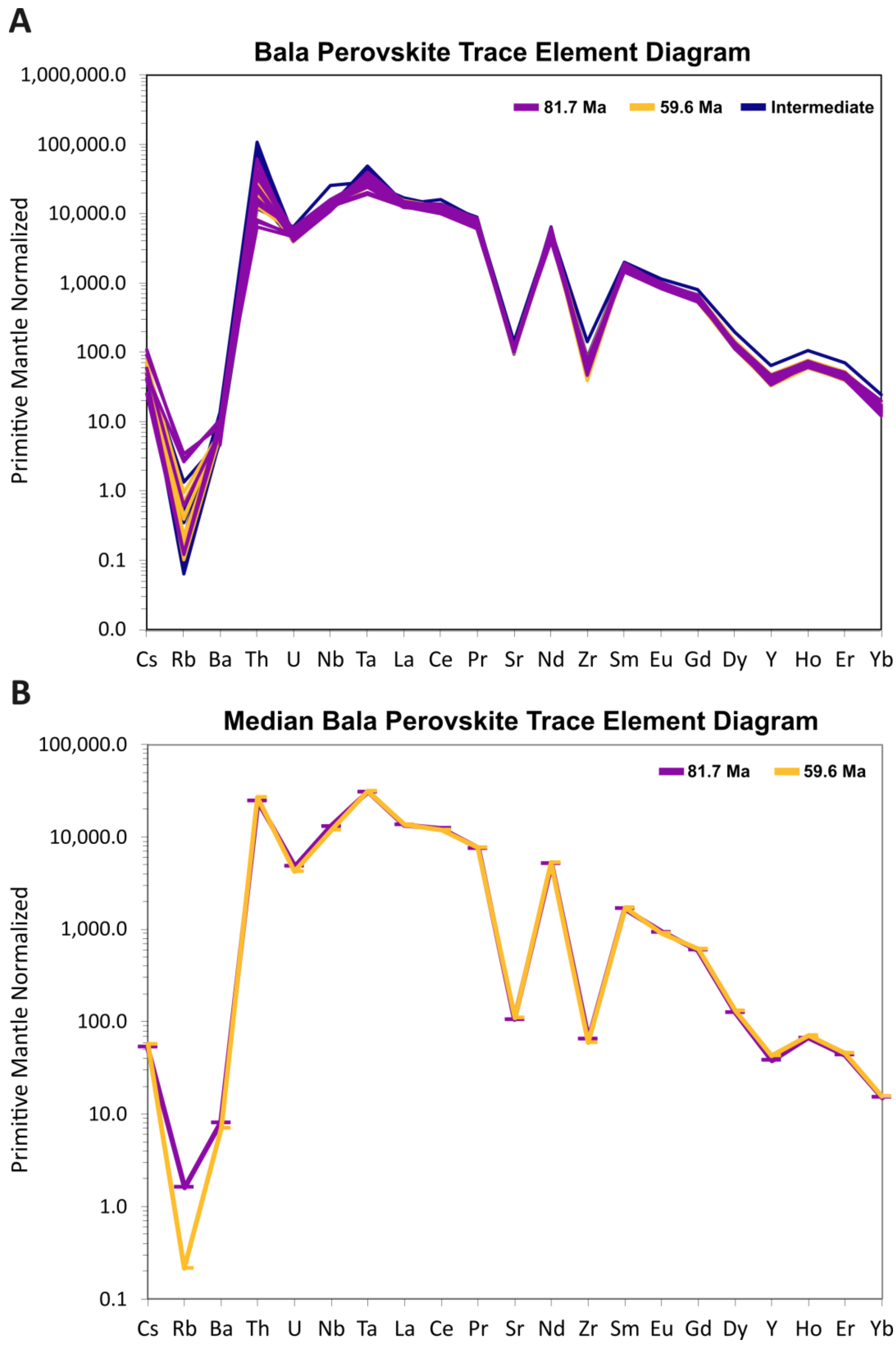

Figure 42. Bala Perovskite Spider Diagrams

A) A comparison of the trace element data of the older (purple) and younger (orange) perovskite populations. Those analyses that fall in between the two age arrays are labeled in blue. B) A comparison of the median values of the older (purple) and younger (orange) perovskite populations within Bala. All analyses are normalized to the primitive mantle values of Sun and McDonough (1989).

Due to the correlation observed between petrologic texture and perovskite population (see detailed discussion in Section 5.1), these extra spots were collected from textures A and B in order to determine whether they could be assigned to a specific population based solely on their trace element pattern. However, as both perovskite populations (as well as the perovskites that make up the analyses between the two age arrays) exhibit very similar trace element patterns, no such correlation can be made.

We were unable to provide trace element data for the Tuttle perovskites as, due to their small size (5-150 μm) relative to the size of the laser beam (20 μm), no grains remained large enough for analysis after U-Pb geochronology. Trace element data for some of the Tuttle perovskites from Rogers (in prep.) show similar patterns to those from Bala. However, the data also show consistently high Si concentrations (≥ 389,000 ppm), suggesting contamination of the analyses from surrounding phases. We have therefore excluded these data from further discussion.

The perovskites from the Hills Pond and Rose Dome lamproites show similar trace element patterns to those from Bala; however, the Bala perovskites show more significant enrichment in Th, Ta (and Nb) and are slightly more depleted in Sr (Fig. 41). In general, the concentrations of most trace elements in the Bala perovskites are similar to the most enriched analyses from Hills Pond and Rose Dome, with the exception of LILEs, Rb, Ba, and Sr, which are lower. Perovskites from the Hills Pond lamproite show significantly more variation in trace element concentrations than Rose Dome, consistent with the indication that the Hills Pond perovskites are more compositionally diverse (See Section 4.3.1 on perovskite major elements)

(Fig. 43). The Rose Dome perovskites only show a greater range of concentrations for Cs and Zr. Although the two Rose Dome samples have similar perovskite trace element patterns the perovskites from RDLE4-C418 have higher median concentrations for the LILEs Cs, Rb, Ba, and Sr; as well as the HFSEs Nb, Ta, and Zr (see Supplementary Table 4). Conversely, the perovskites from RDLE5-C384 have higher median concentrations for the HFSEs Th, U, and REEs. When comparing the median values between the Hills Pond and Rosse Dome perovskites, perovskites from the former locality have higher concentrations of Rb, Ba, U, Nb, and Sr whereas the latter have higher concentrations of Cs, Th, Ta, Zr, and REEs (Fig. 43, Supplementary Table 4).

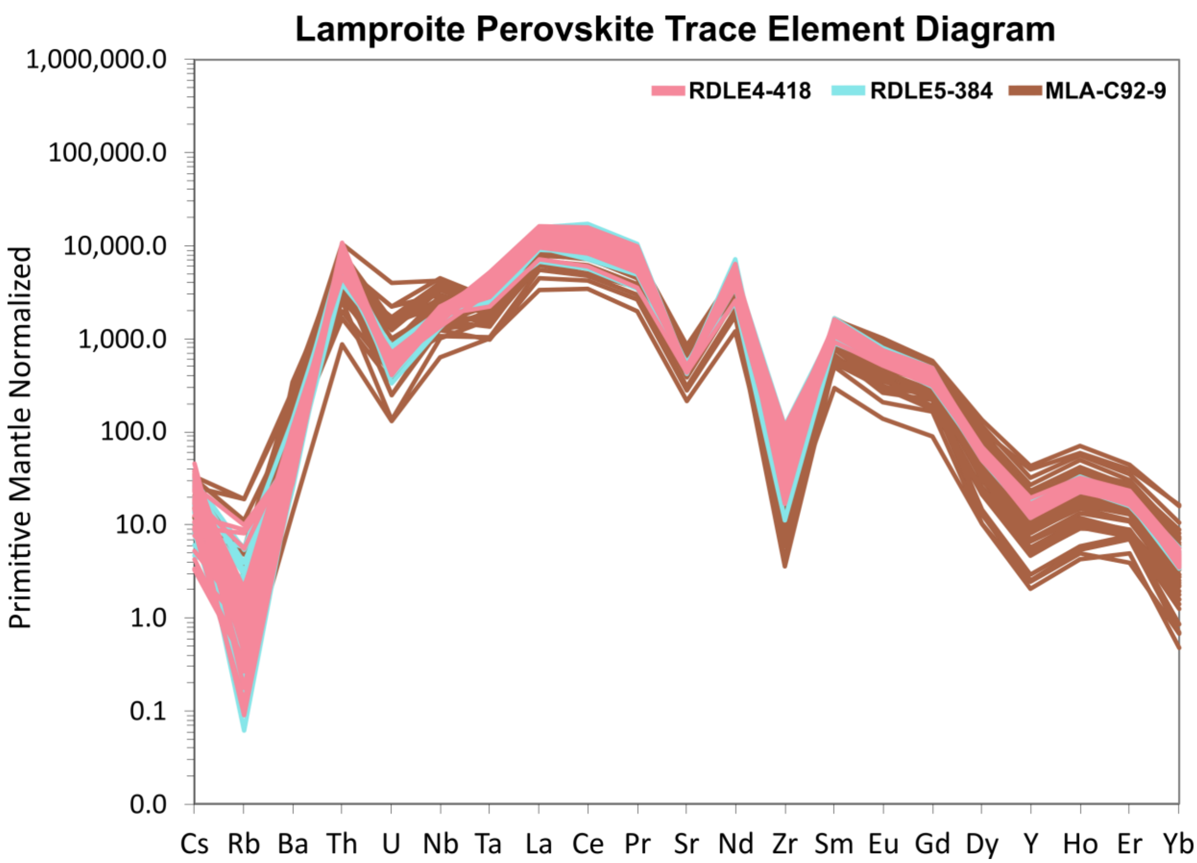

Figure 43. Lamproite Perovskite Spider Diagram

A comparison of the trace element data of the Hills Pond (brown) and Rose Dome (pink and blue) perovskites normalized to the primitive mantle values of Sun and McDonough (1989).

Chapter 5 - Discussion

As stated in Sections 1 and 2.6 the overall goal of this study is to better constrain the geochronology of the Kansas kimberlites and lamproites to not only evaluate their relationship to each other, but the geodynamic setting responsible for their origin. Due to the pervasive alteration, we have concentrated on U-Pb geochronology of perovskite, despite the tendency for this mineral to have high common Pb contents in some cases. We evaluate the effectiveness of perovskite as a U-Pb geochronometer in these rocks in Section 5.1. The original melt composition of the Kansas kimberlites and lamproites are modeled in Section 5.2 based on the perovskite trace element data. A revised magmatic history for the Kansas kimberlites and lamproites is presented in Section 5.3, and the tectonic mechanisms responsible for their protracted history are examined in Section 5.4.

5.1 Perovskite U-Pb Geochronology

In the absence of more well-established U-Pb geochronometers, such as zircon and monazite, perovskite is considered a popular alternative to date undersaturated alkaline rocks such as carbonatites, kimberlites, and lamproites (Wu et al., 2010; Tappe and Simonetti, 2012; Heaman et al., 2019; Sun et al., 2022). This is because perovskite (1) is a relatively abundant, early crystallizing primary phase; (2) contains high abundances of U (20–200 ppm) and Th (>500 ppm); and (3) is highly unlikely to represent entrained crustal material (Wu et al., 2010; Tappe and Simomnetti, 2012; Heaman et al., 2019) (See Section 2.3). In terms of this study, it is one of the only shared phases present in both the kimberlites and lamproites that has survived the pervasive alteration characteristics of both rock types. However, as detailed in Section 2.3, analysis of perovskite is not without challenges. For the Kansas kimberlites, many perovskite crystals are not large enough to analyze reliably (many < 20 μm), given the beam size used for laser ablation (20 µm) (See Section 4.3 on the discussion of the filtering criteria applied to the perovskite EMP geochemistry). Moreover, the presence of inclusions and/or adjacent phases (sometimes just below the grain surface) must be considered and criteria for screening out such analyses based on anonymously low U and Th concentrations (< 20 ppm) were described in Section 4.3. Fortunately, the size of the perovskite crystals was only a significant issue for the Tuttle kimberlite (< 25 µm) (see Section 4.1). Despite this impediment, analysis of the Tuttle perovskites provided a wide spread in $^{207}Pb/^{206}Pb$ and $^{238}U/^{206}Pb$ space and the most radiogenic ratios (Fig. 34c) and therefore yields the most precise age of the localities analyzed as part of this study (105.6 ± 2.0 Ma). The perovskites in the Bala kimberlite also yield a moderate spread in U-Pb ratios, but the results are complicated by the discovery of two age arrays (81.7 ± 8.6 Ma and 59.6 ± 7.4 Ma, Fig. 34a, b). We interpret the significance of these two age arrays in Section 5.3. Interestingly, the $^{207}Pb/^{206}Pb$ ratios for the Bala perovskites are significantly lower (~0.6) while the $^{207}Pb/^{206}Pb$ ratios for the Tuttle, Rose Dome, and Hills Pond perovskites are higher (~0.9) than one would expect for common lead, i.e., common lead at the time of eruption, as inferred from the Stacey and Kramers (1975) (i.e., ~0.84). However, a discussion of the mechanisms responsible for this discrepancy is beyond the scope of this thesis.

While geochronology of the kimberlites was only moderately adversely affected by the presence of common lead, the high common lead contents of the Kansas lamproites significantly decreased the spread in the U-Pb ratios of the perovskites analyzed, causing the data to plot close to the upper concordia intercept, especially those from Rose Dome. As a result, a majority of the individual sample ages have high uncertainties on the age-defining lower concordia intercept (Fig. 36 and 37). However, by combining all of the perovskite analyses per locality and analytical session, we were able to obtain more reasonably precise ages (i.e., Hills Pond: 86.9 ±

3.5 Ma and Rose Dome: 97.1 ± 12.6 Ma) (Fig. 38). Overall, provided sufficient analyses were collected, perovskite proved to be nearly as effective a U-Pb chronometer for the Kansas lamproites as they were for the kimberlites. Moreover, the ages produced are overall consistent with the recalculated K-Ar ages from Zartman et al. (1967) (92-93 ± 5 Ma for Hills Pond and 90 ± 4 Ma for Rose Dome). The results add support to the idea that the kimberlite and lamproite magmatism overlapped in time in Kansas, with the kimberlites starting earlier and continuing longer (see Section 5.3)

We noted in Section 4.1 that the perovskites studied exhibit a range of morphologies, colors, and sizes. Despite this morphological variability none of these physical attributes were observed to correlate with age. This is of interest, particularly for the Bala kimberlite, where two distinct age populations were observed (81.7 ± 8.6 Ma and 59.6 ± 7.4 Ma). Yet, these two age populations do not appear to correlate with any obvious physical or significant chemical differences. Figure 44 indicates that there may be a correlation between petrographic texture and age, as a majority of the younger perovskite population occurs within texture B, i.e., elongated zones with abundant serpentinized olivine within a slightly more calcite-rich matrix. In contrast, most of the older perovskite population occurs within or near the edges of texture A, i.e., regions with abundant tabular, pyroxene pseudomorphs (replaced by calcite) within a matrix of primarily serpentine and calcite. However, it is difficult to say whether there is an unambiguous correlation between age and petrographic texture, as most of the analyses collected are located around the edges of each texture. Therefore, additional U-Pb geochronology on perovskites further within texture A is needed to clarify the relationship between the age populations and textures.

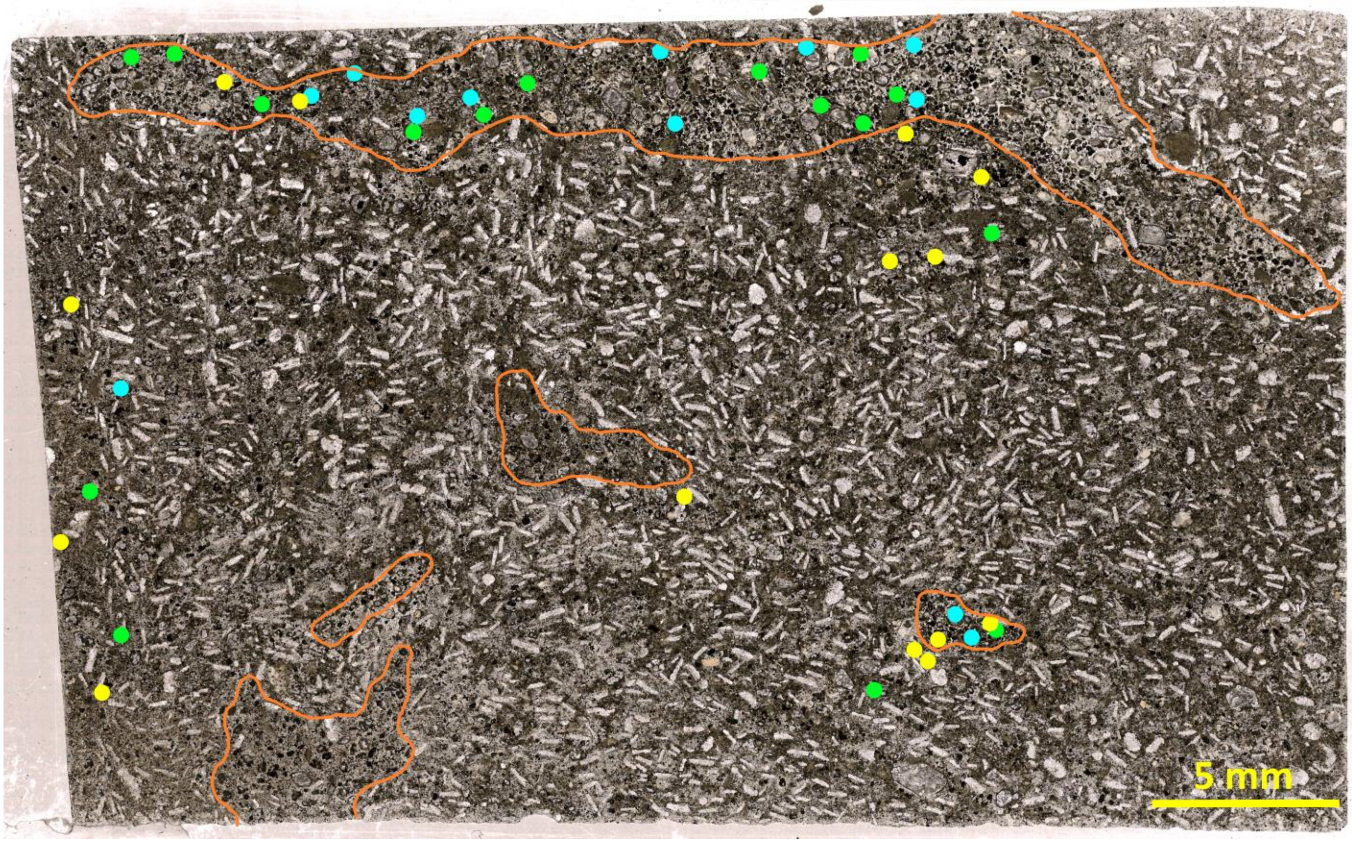

Figure 44. Relationship Between Texture and Perovskite Population within the Bala

Thin section photomicrograph of BA-62-39B in plane polarized light showing the locations of the two perovskite age populations (shown in Figure 35) compared with the two petrologic textures shown in Figure 24. The yellow spots making up population 1 represent analyses that reported an age of 81.7 ± 8.6 Ma (MSWD = 1, n=14) while the blue spots making up the population 2 represent analyses that reported an age of 59.6 ± 7.4 Ma (MSWD=0.49, n=12). The green spots indicate grains that fall between the two age arrays in Figure 34. Texture B is outlined in orange.

5.2 Modeling Melt Composition

Due to their hybrid nature and propensity for alteration, characterizing the original melt compositions of kimberlites and lamproites via traditional whole rock methods is impractical (Pearson et al., 2019). However, as detailed in Section 2.3, perovskite is a common primary microphenocryst to early groundmass phase and, thus, can be used to estimate the geochemistry of the primary melt with which it was in equilibrium (Wu et al., 2010; Sarkar et al., 2014).

Additionally, due to perovskite's flexibility toward cation substitution and ionic defects, it is regarded as a sensitive indicator of magmatic differentiation (Mitchell et al., 2017). Therefore, perovskite trace element analyses can be utilized to calculate parental melt composition at the time of perovskite crystallization, i.e., prior to crustal contamination and alteration.

In our pursuit of sampling and analyzing all potential perovskite age fractions, we obtained detailed trace element data for the perovskites within the Kansas kimberlites and lamproites, which we utilized to evaluate the compositions of the parental magmas. Inverse modeling was conducted using the perovskite/kimberlite partition coefficients (Di) provided by Chakhmouradian et al. (2013). These coefficients were found to be consistent with those obtained experimentally by Beyer et al. (2013). There are currently no perovskite/lamproite partition coefficients reported in the literature, thus the kimberlite partition coefficients (D_i) were used instead. Concentrations in the melt in equilibrium with the analyzed perovskites were calculated using the equation for the partition coefficient, shown in Equation 1:

Equation 1

$$D_i = \frac{C_i, solid}{C_i, melt}$$

Where:

i = trace element,

D_i = partition coefficient for the trace element (i),

C_i, solid = measured concentration of trace element (i) in the mineral,

C_i, melt = concentration of trace element (i) in the melt.

The calculated melts for the Bala kimberlite are 10x to 1000x more enriched than those of primitive mantle, showing greater enrichment in the most incompatible elements (i.e., those on the left of the diagram) (Fig. 45). Th, and to a lesser degree U, are depleted relative to adjacent elements Ba and Nb. Considering Th is significantly more compatible within perovskite than U (i.e., D_{Th} = 164 and D_U = 18), the low Th/U ratio suggests that the kimberlitic melt may have fractionated perovskite or another early crystallizing mineral that prefers Th over U (e.g., apatite), prior to the crystallization of the perovskite population analyzed. Melt compositions from both perovskite generations observed in the Bala kimberlite (detailed in Section 4.3) exhibit similar trace element patterns. As expected from the trace element data, the median melt composition of the older perovskite population is more enriched in Rb (see Section 4.3).

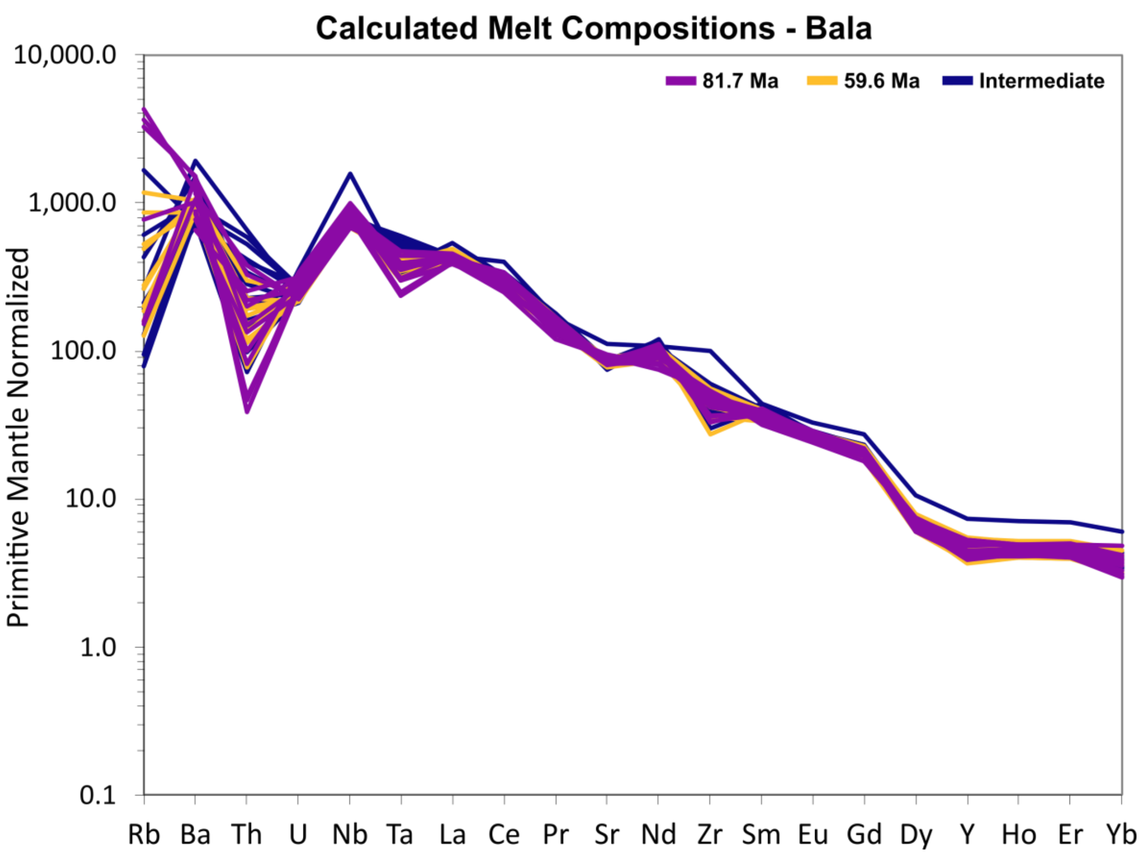

Figure 45. Bala Perovskite Calculated Melt Compositions

Kimberlite parental melt composition calculated from Bala perovskites. Purple analyses indicate perovskites from the older perovskite population (81.7 ± 8.6 Ma) while orange analyses represent perovskites from the younger perovskite population (59.6 ± 7.4 Ma). Blue analyses that fall between the two age arrays. Data normalized to primitive mantle (Sun and McDonough, 1989).

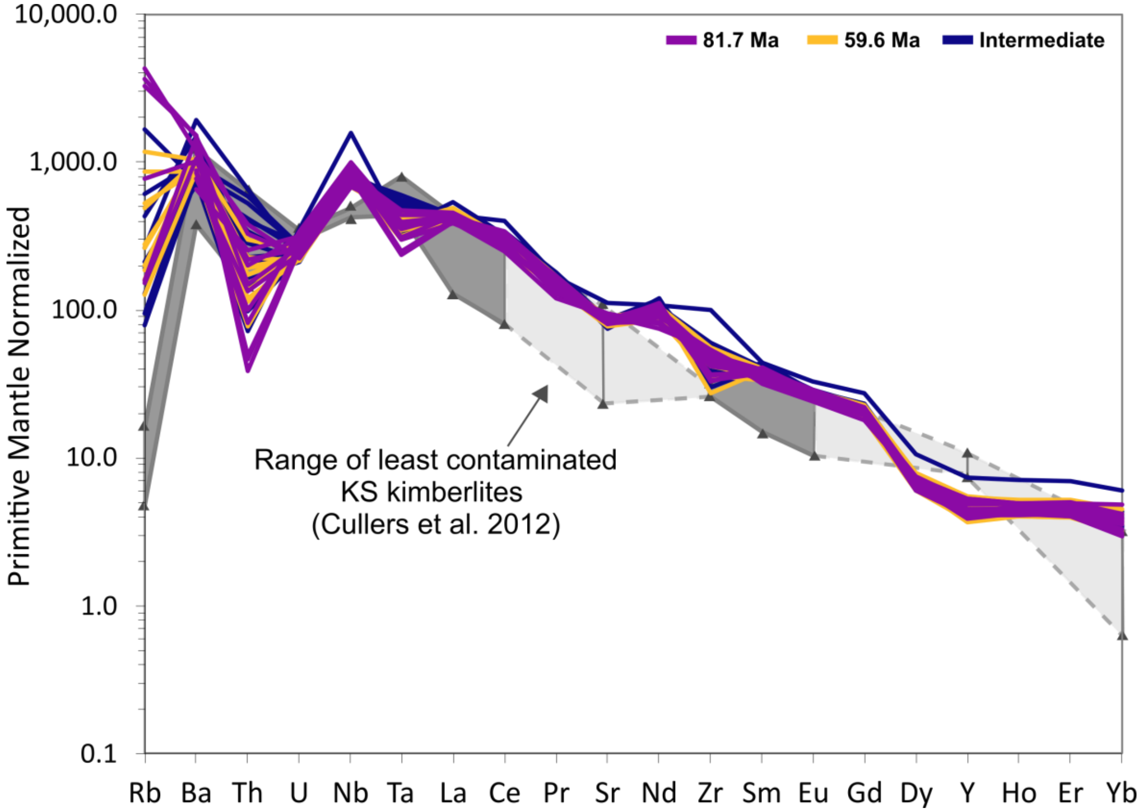

Figure 46. Bala Perovskite Estimated Melt Compositions vs Least Contaminated Whole Rock Data

Primitive mantle normalized trace element diagram for Bala perovskite calculated melt compositions compared to the range of the 'least contaminated' whole rock compositions for the Kansas kimberlites from Cullers et al. (2012) in grey. The solid grey segments are based on reported data, while the dotted segments are extrapolations between existing data. Colors for melt compositions calculated from the old, young, and intermediate perovskite populations are the same as Figure 45.

In Figure 47, we compare our calculated Bala kimberlite melt compositions to the whole rock composition estimated from the least contaminated samples from Cullers et al. (2012). Despite the limited range of trace elements reported by Cullers et al. (2012), the two melt compositions display similar patterns. Both melt compositions show enrichment in the most incompatible elements that is as much as three orders of magnitude greater than that of the least incompatible elements. In general, our calculated kimberlite melt compositions are slightly more enriched relative to that estimated from the whole rock data for most elements. The major differences between the two estimates occur for Rb, Th, Nb, and to a lesser degree Ta and Y. The perovskite compositions estimate Rb concentrations that are up to three orders of magnitude greater than those estimated via whole rock data. Factors that may contribute to this discrepancy include one or more of the following. (1) Rb concentrations within whole rock calculations may be underestimated as a result of its high mobility during hydrothermal alteration. However, other fluid mobile elements such as Ba and Sr don't show such a disparity. (2) The Rb partition coefficient (0.0008 ± 0.0005) reported by Chakhmouradian et al. (2013) may be too high. However, despite the uncertainty associated with the D value, variations within the perovskite/melt partition coefficient cannot account for the low Rb concentrations estimated based on whole rock data (Fig. 47). (3) The high Rb concentrations in the melts calculated from perovskite compositions may be an artefact caused by partial ablation of phlogopite, despite attempts to filter out such mixed analyses (see Section 3.3.2).

In Figure 49 we compare the estimated kimberlite melt composition from the Bala kimberlites to the average whole rock compositions of kimberlites published by Wedepohl and Muramatsu (1979) and Chakhmouradian et al. (2013). The trends observed for the two average kimberlite compositions are similar to those calculated from the Kansas perovskites, with the latter being more enriched for most elements. The only differences between the two average kimberlite compositions occur in the most incompatible elements (Rb, Ba, and Nb). However, we have also calculated the melts in equilibrium with the perovskites analyzed by Chakhmouradian et al. (2013) (Fig. 49) from the Chicken Park (Colorado), Iron Mountain

(Wyoming), and Udachnaya East (Russia) kimberlites, and these calculated melt compositions show similar differences relative to the proposed average (i.e., 'typical') kimberlite compositions (Wedepohl and Muramatsu, 1979; Chakhmouradian et al., 2013). Therefore, the differences we observe in Rb, Ba, and Nb concentrations are not unique to perovskites and kimberlites in Kansas.

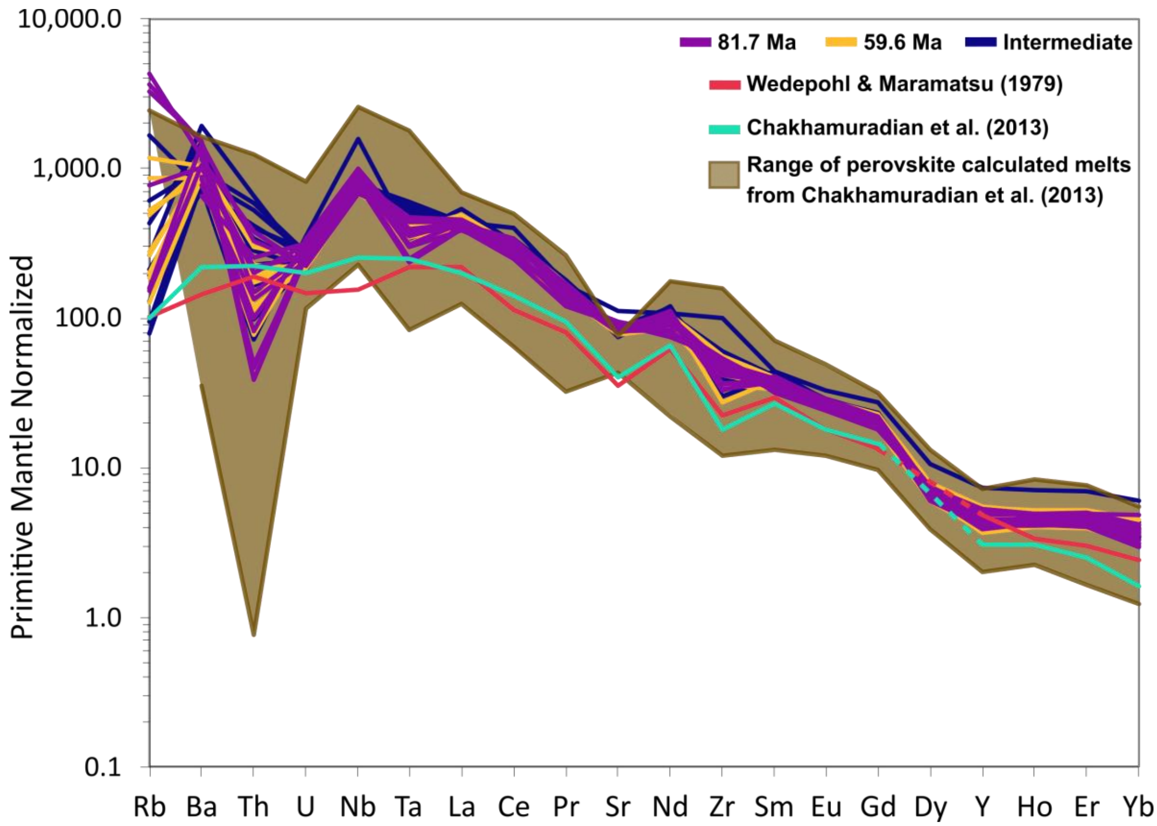

Figure 47. Bala Perovskite Estimated Melt Compositions vs Average Kimberlite

Primitive mantle normalized trace element diagram for Bala perovskite calculated melt compositions compared to the average whole rock composition of kimberlites from Wedepohl and Muramatsu (1979), shown in red, and Chakhmouradian et al. (2013), shown in green. Additionally, the range in kimberlite melt composition estimated from the perovskites analyzed in Chakhmouradian et al. (2013) are shown in brown. Colors for melt compositions calculated from the old, young, and intermediate perovskite populations are the same as Figure 45.

Similar to the calculated melt composition for the Bala kimberlite, the calculated lamproite melts generally show greater enrichment in the most incompatible elements (Fig. 48).

Additionally, in common with the perovskite trace element data (Fig. 41), the calculated melt compositions for the kimberlites exhibit greater enrichment in Th, Nb, and Ta, than the lamproites, whereas the lamproites are more enriched in Rb, Ba, and Sr than the kimberlites.

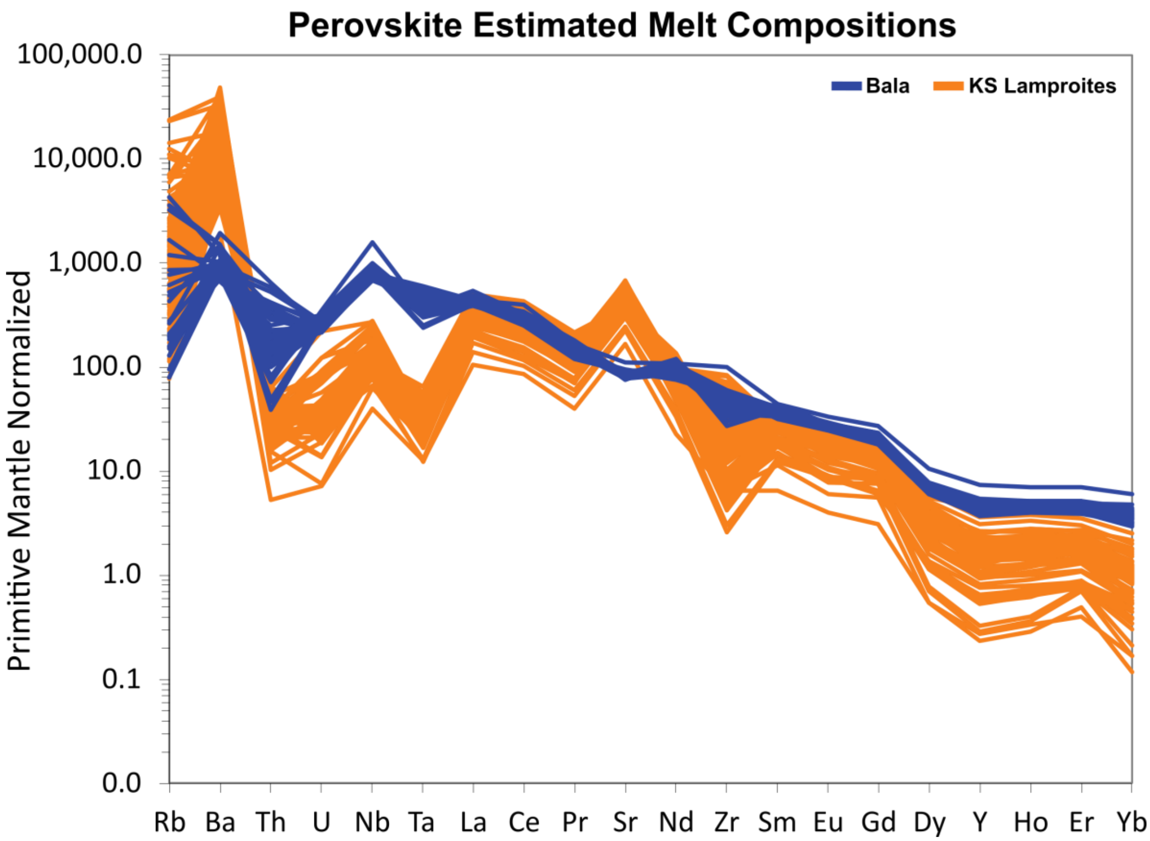

Figure 48. Comparison of the Kansas Rocks Estimated Melt Compositions

Primitive mantle normalized trace element diagram comparing the perovskite calculated melt compositions for the Bala kimberlite (blue) and Kansas lamproites (orange).

The contrast between the depletion in Sr in the calculated kimberlitic melt and enrichment in the calculated lamproitic melt is likely a result of their differing mineralogy (Fig. 48). Calcite, a common primary phase observed within the kimberlites, but largely absent from the lamproites, has significantly higher D values for Sr in kimberlites compared to perovskite (Chen and Simonetti, 2013). Hence, Bala's depletion in Sr may reflect fractionation of primary calcite.

Future study on the trace element partition behavior between perovskites and lamproitic melts is needed to clarify whether the difference in enrichment, specifically HFSE enrichment, observed between the estimated melts is a result of differing compatibilities as found to occur between kimberlitic and carbonatitic melts (Beyer et al., 2013) or different source mineral modes.

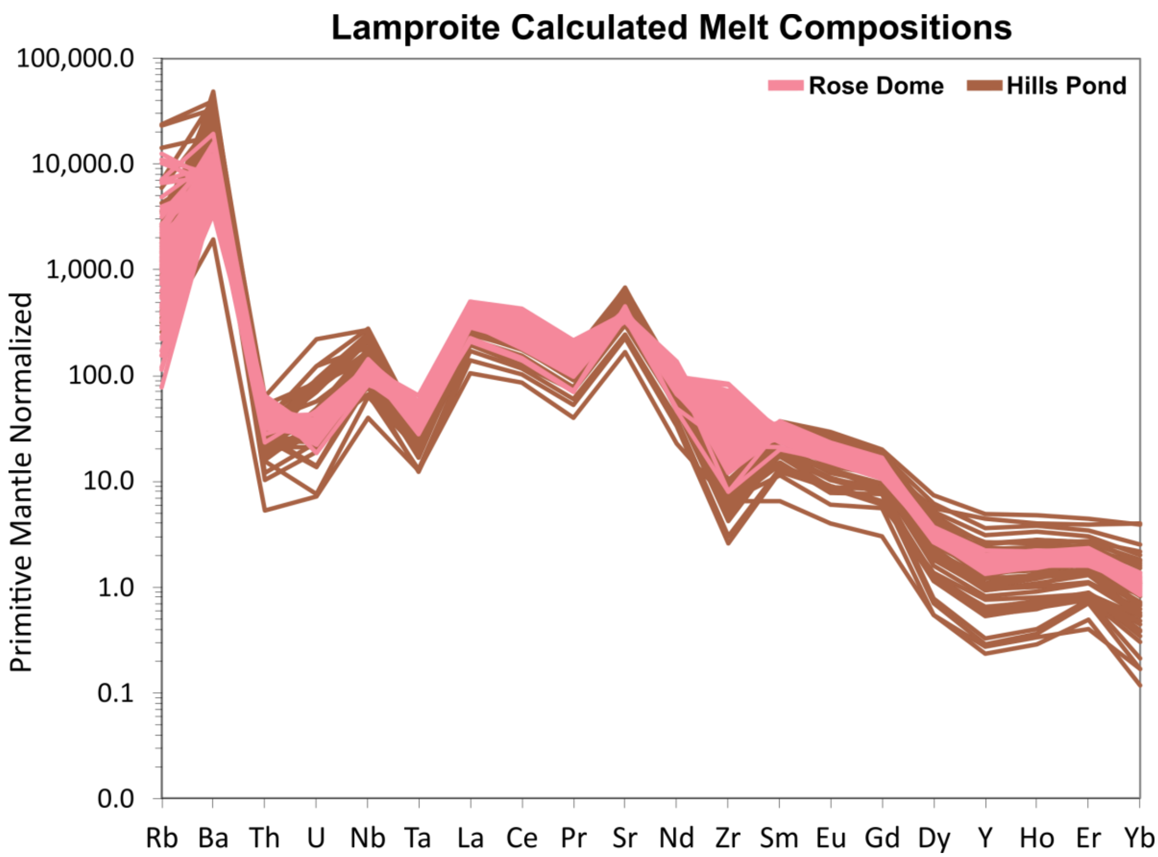

Figure 49. Perovskite Calculated Melt Compositions for the Kansas Lamproites

Comparison of the parent melt compositions for the Hills Pond (brown) and Rose Dome lamproites (pink) normalized to primitive mantle (Sun and McDonough, 1989).

When comparing the calculated melt compositions of the Hills Pond and Rose Dome lamproites, besides the overall wider range in trace element contents for Hills Pond, the only significant differences are between their Th-U ratio and Zr variability (Fig. 49). The Hills Pond melt compositions have lower Th-U ratios than those observed for the Rose Dome, suggesting that the perovskites analyzed from Hills Pond were in equilibrium with a melt that had previously undergone fractionation of perovskite or another early crystallizing mineral that prefers Th over U (e.g., apatite). Given that our age data suggest that the Rose Dome lamproite could be slightly older than the Hills Pond, the calculated melt composition for the Rose Dome may represent that initial phase of perovskite fractionation. Despite the overall wide range in trace element concentrations observed for the Hills Pond melt composition, the Rose Dome melts display higher variability for Zr (Fig. 49). The perovskite/kimberlite partition coefficient for Zr is near 1 (1.4 ± 0.6) (Chakhmouradian et al., 2013) and shown to be sensitive to changes in melt composition (Beyer et al., 2013), so the higher variation in Zr within the Rose Dome may reflect small changes in its compatibility over the course of crystallization. Most of the calculated melt compositions for Hills Pond illustrate a negative Zr anomaly, which may be attributed to the fractionation of a Zr-bearing phases such as wadeite (Fig. 49). Around half of the Hills Pond perovskite melt compositions exhibit HREE concentrations below primitive mantle (i.e., <1) suggesting that garnet, which has a high affinity for HREEs, was in the source. This is interesting given that garnet has not been observed within the Hills Pond lamproites but has been observed within the Kansas kimberlites (see Section 4.1.1) and potentially within the Rose Dome lamproite (Coopersmith and Mitchell, 1986). It has also been hypothesized that the Kansas lamproites were derived from a garnet-rich source (Merrill et al., 1977; Cullers et al., 1985).

Figure 50 compares the melt composition estimated from the lamproite perovskites with the whole rock composition from Cullers and Berendsen (2011). In general, the melt compositions calculated from the perovskites are more variable than those determined from the whole rock data. Both the estimated melt and whole rock compositions display similar trends for elements less incompatible than La. The two trends differ in terms of the elements between Rb and U, as well as for Ta, Sr, and Zr. Similar to the perovskite melt composition estimated for Bala, the enrichment in Rb and Ba within the lamproites could be the result of composite analyses of phlogopite and Ba-Ti rich inclusions in the perovskites. Alternatively, the enrichment in Rb and Ba could be a real reflection of the lamproite melt composition (see below).

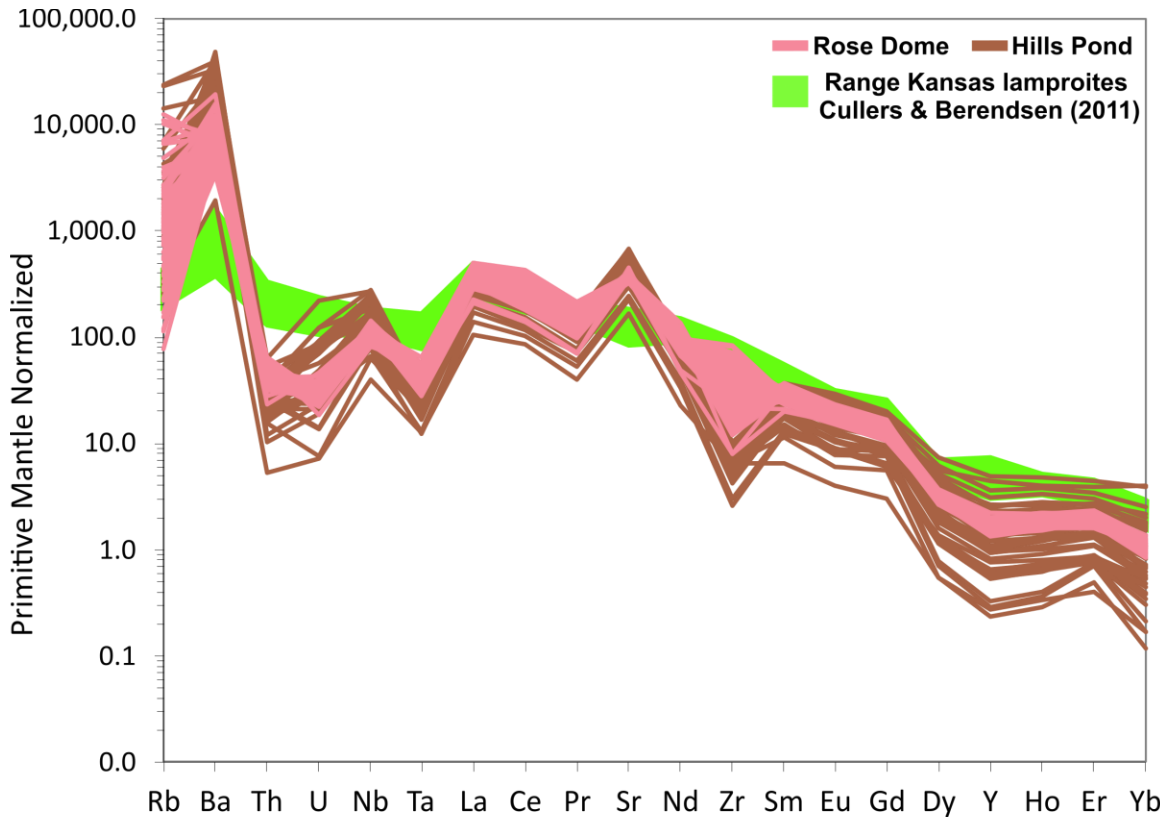

Figure 50. Perovskite Estimated Lamproite Melt Compositions vs Whole Rock Data

Primitive mantle normalized trace element diagram for perovskite calculated melt compositions compared to the range of whole rock compositions for the Kansas lamproites from Cullers and Berendsen (2011) (green). The Rose Dome melt compositions are shown in pink, while the Hills Pond are shown in brown.

Figure 51 illustrates the melt compositions estimated from the Hills Pond and Rose Dome perovskites relative to the average lamproite whole rock composition from Karmalker et al. (2014). A more limited range of elements is available for the average lamproite whole rock composition than for our study; yet, many similarities between the two estimates can be observed. The general shape of the trace element patterns is similar, with the whole rock compositions typically being more enriched relative to the melt compositions estimated from perovskite. The principal exceptions being Rb, Ba, and Sr, the overall enrichment of which could be the result of hydrothermal alteration, as previously mentioned. When we compare the compositions of melts calculated from perovskites from western Australian lamproites (Jaques, 2016) to our Kansas perovskite estimate, they show as similar significant enrichment in Rb, Ba, and Sr. This suggests element mobility is likely not responsible for the difference between melt compositions. Indeed, lamproites are characteristically enriched in Ba, Rb, K, and other incompatible elements as a result of their derivation from compositionally heterogeneous metasomes in the lithospheric mantle (Mitchell and Bergman, 1991; Mitchell, 2020; Ezad and Foley, 2022; Sarkar et al., 2022). The particularly high concentrations of Ba (as well as the coupled behavior of F and K_2O) indicate the presence of phlogopite within the source region (Ezad and Foley, 2022). As a result, the following metasome lithologies have been previously proposed: (1) mica-amphibole-rutile-ilmenite-diopside (MARID), (2) phlogopite harzburgite, and (3) phlogopite pyroxenite (Mitchell, 2020; Ezad and Foley, 2022; Sarkar et al., 2022). Therefore, the relative abundance of Rb and Ba and depletion in Th and U observed within the estimated Kansas lamproite melt compositions may be due to the abundance of phlogopite within the metasomes as phlogopite's partition coefficients of Rb and Ba (~1.3 and ~1.61) within lamproitic melts are higher than those of Th and U (0-0.0002 and 0.0001-0.0002) (Schmidt et al., 1999; Ezad and Foley, 2022). However, it is difficult to unambiguously determine the cause of the differences in Rb (and to a lesser extent Ba and Sr) observed between the whole rock and perovskite estimated melts for both the lamproites and kimberlites without further clarification of trace element partition behavior between perovskites and lamproitic melts.

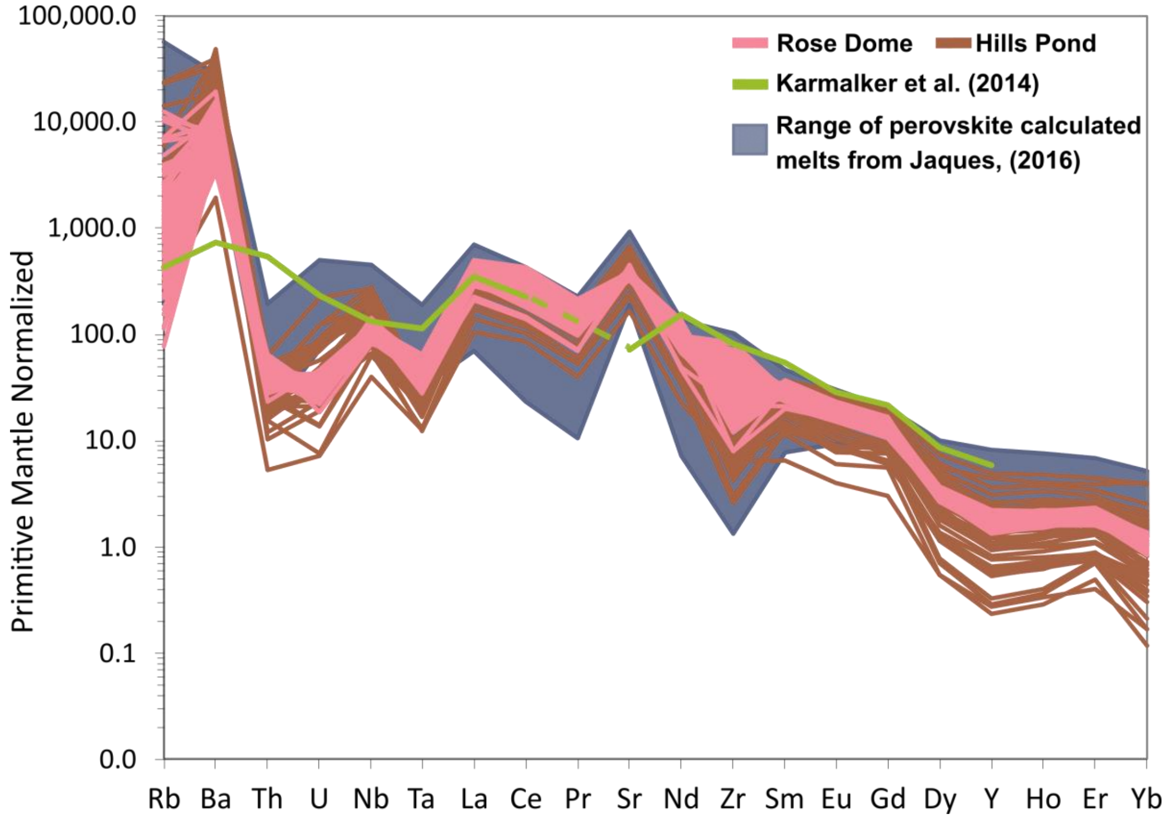

Figure 51. Perovskite Estimated Lamproite Melt Compositions vs Average Lamproite

Primitive mantle normalized trace element diagram for Hills Pond and Rose Dome perovskite calculated melt compositions compared to the average whole rock composition of lamproites from Karmalker et al. (2014) (green). The solid green segments are based on reported data, while the dotted segments are extrapolations between existing data. Additionally, the range in lamproite melt composition estimated from the perovskites analyzed in Jaques (2016) are shown in grey. Colors for melt compositions calculated from the Kansas perovskites are the same as Figure 50.

5.3 A Revised Magmatic History for the Kimberlites and Lamproites of Kansas

As previously stated in Section 2.6, the emplacement ages of the Kansas kimberlites and lamproites were previously reported to range from 110-85 Ma (Blackburn et al., 2008) and 91-88 Ma (Zartman et al., 1967), respectively. The U-Pb and petrologic data presented here expand those ranges and offer new insights into their magmatic history.

For the Tuttle kimberlite we observe a singular precise age of 105.6 ± 2.0 Ma, which is consistent with the emplacement age Blackburn et al. (2008) determined on the basis of U-Th/(He) in zircon (108.6 ± 9.6 ma), titanite (103 ± 14.1 Ma), and garnet (98.8 ± 8.9 Ma); and phlogopite/clinopyroxene Rb-Sr (106.6 ± 1.0 Ma).

(U-Th)/He apatite analyses and Rb-Sr phlogopite analyses (Blackburn et al., 2008) record a magmatic event around 88-85 Ma for the Baldwin Creek and Leonardville kimberlites, but these authors attribute younger ages of around 65 Ma for some apatites, titanites, and zircons from the Tuttle, Bala, Stockdale, and Leonardville kimberlites to a hydrothermal 'reheating' event. However, our new data suggest that this interpretation is in error. Instead, it is more likely that the kimberlites contain multiple mineral populations representing magmatic events younger than 85 Ma. In particular, our data on the perovskites from the Bala kimberlite include two age groups, one at ~81 Ma and the other at ~60 Ma. Both values are near to or within error of those reported for Bala (Blackburn et al., 2008) (i.e., 103 ± 7.5 Ma and 64.3 ± 7.5 Ma). Blackburn et al. (2008), interpreted the emplacement age (i.e., 103 ± 7.5 Ma) of the Bala kimberlite via (U-Th)/He analyses of magnetite sampled from crosscutting calcite veins. These veins most likely represent the latest stages of kimberlitic cooling and therefore would be slightly younger than the kimberlite. However, the magnetite yields the *oldest* age for the Bala kimberlite suggesting that the magnetite may be xenocrystic, although it remains unclear based on the data provided. In contrast to Blackburn et al. (2008), our analyses were conducted in situ, and our petrologic observations suggest that there may be a connection between petrographic textures, i.e., A and B (Fig. 44), and the two perovskite age populations within Bala. The younger perovskite fraction occurs almost exclusively within two ovate zones of texture B, included within and crossing texture A. This suggests that texture B may represent a separate kimberlitic melt intruding into the previous magmatic texture A. Those perovskite analyses that fall in between the two age arrays and show no correlation with texture may represent mixtures of the two perovskite crystallization episodes. However due to the abundance of U-Pb analyses near the edges of the two petrologic textures, further U-Pb geochronology is needed to clarify the relationship between the petrologic textures and perovskite generations.

Our results are consistent with numerous recent studies that show kimberlite magmatism can be protracted, spanning between 13 and 55 m.y. within a single field, and up to 20 m.y. within a single pipe (Heaman and Kjarsgaard, 2000; Zurevinski et al., 2008; Sarkar et al., 2015; Heaman et al., 2015; Kjarsgaard et al., 2017; Ranger et al., 2018). Our new data show that kimberlite magmatism in Kansas spanned at least ~46 m.y., with a few individual kimberlites (Tuttle, Bala, Stockdale, and Leonardville) sustaining reoccurring magmatism for 22-40 m.y. U-Pb perovskite analyses and (U-Th)/He titanite xenolith analyses (Blackburn et al., 2008) record the earliest known magmatic event at around 105 Ma for the Tuttle and Stockdale kimberlites. Our data then indicate at least two further magmatic events followed at around 82 Ma and 60 Ma within the Bala kimberlite. (U-Th)/He titanite xenolith and apatite analyses (Blackburn et al., 2008) suggest that the older magmatic pulse recorded by the Bala kimberlite includes the Baldwin Creek and Leonardville localities (85-88 Ma). Additionally, if we assume that the younger, 65-Ma ages reported by Blackburn et al. (2008) are the product of subsequent intrusions of kimberlitic melt, as seen at Bala, then the youngest magmatic pulse additionally affected the Tuttle, Stockdale, and Leonardville kimberlites. A more detailed in situ muti-phased geochronological approach is needed to determine whether each of these kimberlite localities contains autoliths (i.e., inclusions of pre-existing kimberlite)/intrusions or if the various ages reported are the result of different closure temperatures.

Through the combination of all the U-Pb analyses per analytical session, we were able to obtain a singular precise age of 86.9 ± 3.5 Ma for the Hills Pond lamproite, which nominally is ~7 Ma younger than the recalculated age range Zartman et al. (1967) determined on the basis of phlogopite (92-93 ± 5), but within uncertainty, and falls within the age range of the second period of kimberlite magmatic activity (~82-88 Ma). Despite being unable to provide more precise emplacement ages for the Rose Dome lamproite, our combined age of 97.1 ± 12.6 Ma from all samples may imply that the Hills Pond lamproite is younger than the Rose Dome, contrary to that reported by Zartman et al. (1967). However, due to the high uncertainty on the age, this remains unclear, as the date obtained for the Hills Pond (86.9 ± 3.5 Ma) falls within the Rose Dome uncertainty range. Additionally, it is difficult to assess whether the Rose Dome falls within the first (~105 Ma) or second (~82-88 Ma) period of kimberlite magmatism. Based on the U-Pb perovskite ages obtained for the Kansas kimberlites and lamproites, we suggest that the timing of lamproite and kimberlite emplacement overlaps, beginning around 8 m.y after the initiation of kimberlite magmatism.

5.4 Geodynamic Models

One of the main objectives of this study is to utilize newly acquired temporal data to evaluate the geodynamic mechanisms responsible for alkaline magmatism within the southern portion of the North American Mid-Cretaceous corridor. Our new data provide significant new constraints in this context, particularly our observation that the Kansas kimberlite and lamproite fields were magmatically active for at least 46 m.y. Each of the four main models proposed to explain the formation of the Kansas alkaline magmatism, i.e., mantle plumes (Heaman and Kjarsgaard, 2000; Heaman et al., 2003, 2004; Chu et al., 2013), subduction-related processes (Currie and Beaumont, 2011; Duke et al., 2014), large low shear velocity provinces (LLSVP) (Torsvik et al., 2010,2014; Giuliani et al., 2021), and edge-driven mantle-convection cells (EDC) (Kjarsgaard et al., 2017; Kempton et al., 2019a,b) will be reviewed below in the context of our new geochronological and geochemical data.

5.4.1 Mantle Plumes

Many studies have hypothesized a connection between alkaline magmatism and mantle hotspots in a variety of locations (e.g., Le Roex, 1986; Sleep, 1990; Heaman et al., 2000, 2003, 2004). However, Crough et al. (1980) was the first to test their genetic relationship by backtracking the positions of fourteen post-Triassic kimberlite and alkaline igneous fields relative to the Great Meteor, Tristan da Cunha, and Trindade volcanic chains. They found that a majority of the alkaline igneous rocks backtracked positions were within 5˚ of a mantle plume. In relation to the North American Mid-Cretaceous corridor, the mantle plume theory has been rejected by many, as global tomography data show the underlying region is too cold and exhibits seismic velocities that are too high to be consistent with an upwelling mantle plume (Torsvik et al., 2016; Kjarsgaard et al., 2017; Kempton et al., 2019a,b). Additionally, kimberlites and lamproites within the corridor do not display a spatial temporal relationship consistent with the direction of plate movement (Duke et al., 2014; Kempton et al., 2019a,b). Indeed, our data indicates that not only did alkaline magmatism span 46 million years within the kimberlite and lamproite fields but over 22 m.y. within a few individual kimberlites (e.g., Tuttle, Bala, Stockdale, and Leonardville). Such a protracted period of magmatism in one location is inconsistent with a plume model for the origin of the Kansas kimberlites and lamproites.

5.4.2 Subduction Processes

Models involving subduction-related processes (McCandless, 1999; Currie and Beaumont, 2011; Duke et al., 2014) emphasize the parallel spatial relationship between the Mid-Cretaceous corridor and the convergent western margin of the North American and Farallon plates. Both McCandless (1999) and Currie and Beaumont (2011) suggested that the Farallon plate's release of slab-derived fluids facilitated melt generation in the upper asthenospheric mantle. Yet, if the Kansas kimberlites and lamproites are subduction related, then their magmas should exhibit a strong negative Nb-Ta trace element signature diagnostic of subduction zone processes. While no such anomaly is observed in previously published whole rock data (Fig. 20, 22) (Kjarsgaard et al., 2017; Kempton et al., 2019a,b), our perovskite-calculated melt compositions for the Kansas lamproites exhibit a trough from Th to Ta compared to the adjacent elements Ba and La (Fig. 48). In contrast, the perovskite-calculated melt compositions for the Kansas kimberlites do not show a depletion in Nb and Ta relative to the adjacent elements U and La (Fig. 48). We argue that for subduction-derived fluids from Farallon slab subduction to be the stimulus for alkaline magmatism in Kansas, a subduction signature should be observed in both the kimberlites and lamproites. Duke et al. (2014) proposed that tears in the Farallon slab orthogonal to the direction of subduction facilitated upwelling of asthenospheric mantle from the mantle transition zone explains the absence of a subduction signature in the trace element patterns. Regardless of whether this model would generate alkaline melt unmodified by subduction, reconstruction of the position of the Farallon plate in Mid-Cretaceous times shows that the eastern edge of the plate is too far west (~1200 km) of Kansas to provide slab-derived fluids into the mantle source region for the kimberlites and lamproites during the roughly 50 m.y. time span we have determined for the alkaline magmatism of the region (Fig. 3 and 52) (Liu et al., 2008; Spasojevic et al., 2009; Kjarsgaard et al., 2017; Kempton et al., 2019a,b). Instead, the apparent subduction signature in the lamproite trace element patterns may be the result of an ancient subduction event that affected the lithospheric mantle, an interpretation that is consistent with most models that attribute lamproite generation from a lithospheric mantle source based on their radiogenic isotope compositions (Fig. 4).

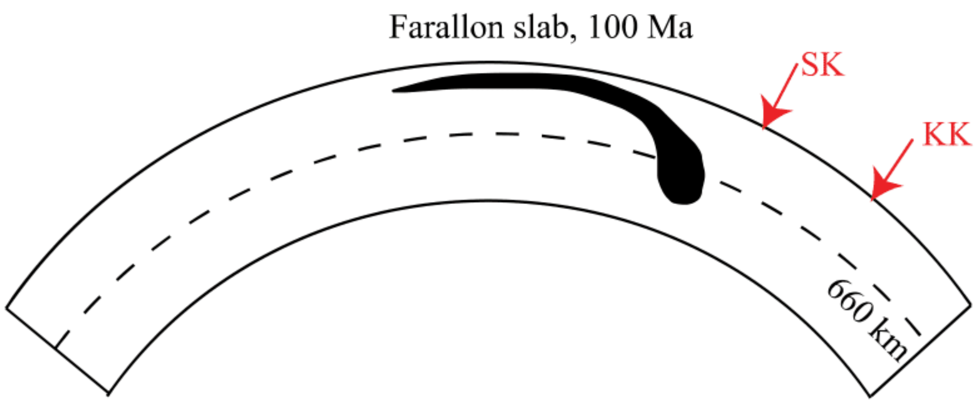

Figure 52. Reconstructed Farallon Slab Position, 100 Ma

Cross section of the Farallon slab around 100 Ma (41 ˚N) from Kjarsgaard et al. (2017), showing the spatial relationship between the slab and the Kansas and Saskatchewan kimberlite (KK, SK) fields. The backtracked location of the Farallon slab is based on modeling from Liu et al. (2008) and Spasojevic et al. (2009).

5.4.3 Large Low Shear Velocity Provinces (LLSVP)

LLSVPs are areas of slow shear wave velocities at the core-mantle boundary separated by regions of fast velocities (Fig. 53) (Davaille and Romanowicz, 2020). There are two main LLSVPs: (1) the African LLSVP (also known as the Atlantic LLSVP and Tuzo) located beneath the Atlantic and southern Africa and (2) the Pacific LLSVP (also known as Jason) located beneath the south-central Pacific (Fig. 53 and 54) (Torsvik et al., 2016; Davaille and Romanowicz, 2020). It is currently debated whether their seismic signature is due to purely thermal heterogeneity (Davies et al., 2015) or if the LLSVPs have an additional dense (primitive/recycled) compositional component (see review by Garnero and McNamara 2008; Deschamps et al. 2015; Kreielkamp et al., 2022).

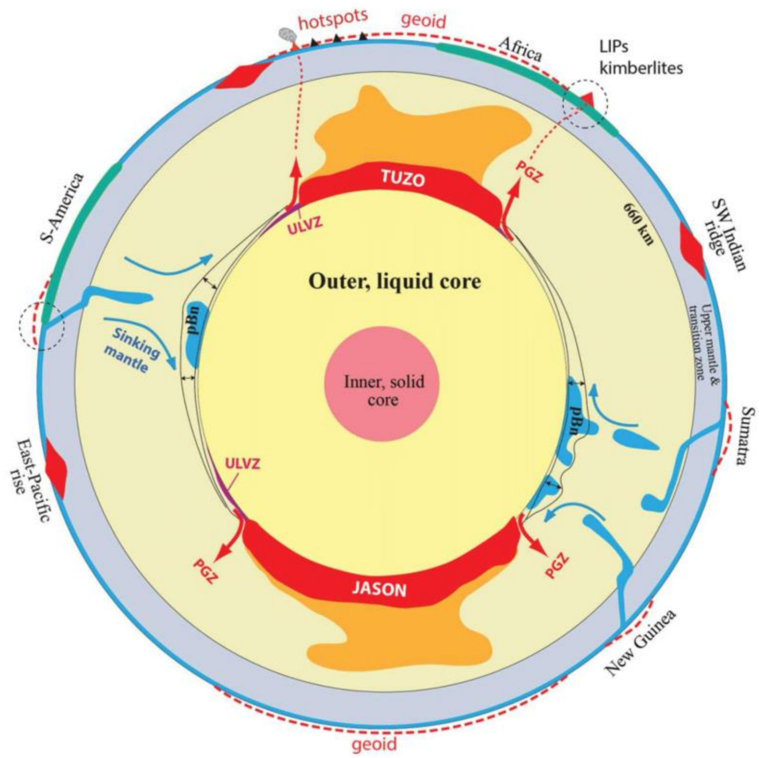

Figure 53. Cross Sectional Model of LLSVPs

Conceptual cross-section of the Earth from the South Pole illustrating the locations of the African (Tuzo) and Pacific (Jason) LLSVPs from Torsvik et al. (2016). The margins of the LLVPS, termed the plume generation zones (PGZs), are theorized to be the source regions for a majority of large igneous provinces, hotspots, and kimberlites (Torsvik et al., 2010). The red arrows above the LLSVPs indicate that the elevated regions of the residual geoid (dashed red lines) are due to hot buoyant upwellings (Steinberger and Torsvik, 2010). The region labeled "pPV" with thin black lines at the core mantle boundary refers to the lenses of postperovskite (Trønnes, 2010).

However, many studies agree that there is a clear correlation between the margins of LLSVPs and the reconstructed locations of a majority of hotspots, large igneous provinces (LIP) and some kimberlites (Torsvik et al., 2010; 2014; Davies et al., 2015; Giuliani et al., 2021). Guliani (2021) showed that kimberlites and ultramafic lamprophyres that were spatio-temporally correlated with LLSVPs have Sr, Nd, and Hf isotope compositions typical of prevalent mantle (PREMA) (Fig. 54). However, their reconstructions were based on circular reasoning, as the kinematic model (Torsvik et al., 2014) used to backtrack the locations of the kimberlites was based on the hypothesis that kimberlites, hotspots, and LIPs erupt along LLSVP margins (Adam et al., 2023).

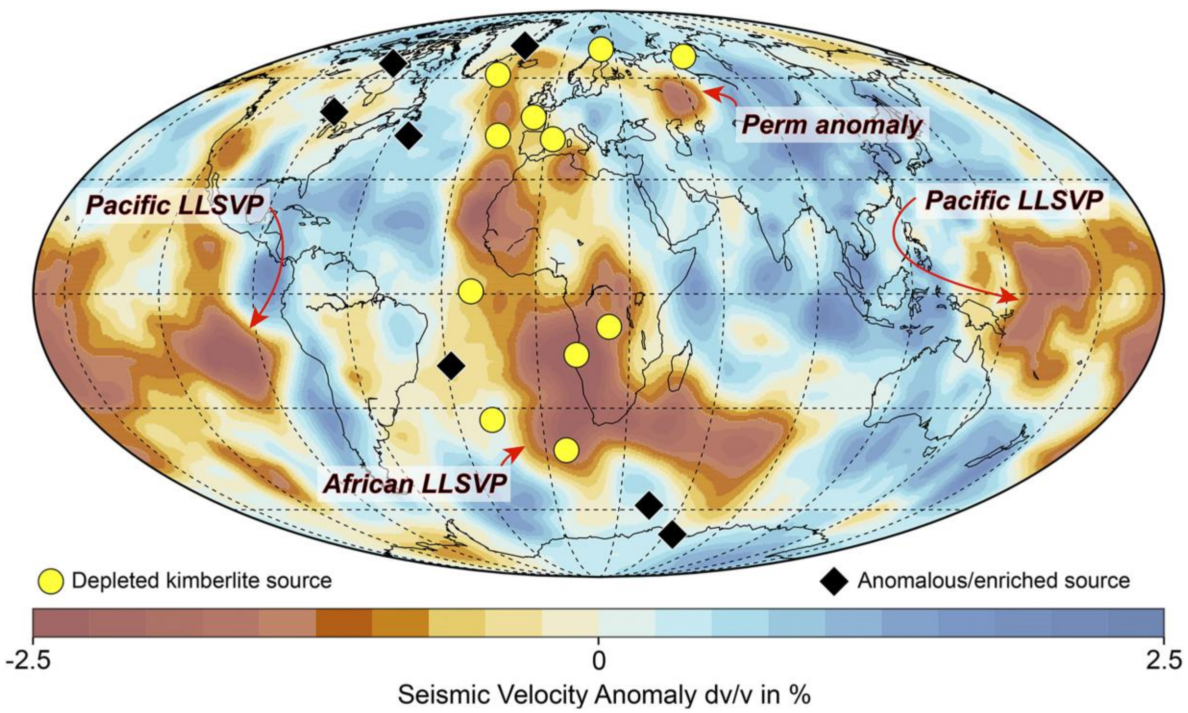

Figure 54. LLSVPs Relative the Backtracked Locations of Kimberlites and Lamprophyres

Seismic tomography model from Giuliani et al. (2021) illustrating the backtracked locations of kimberlites and ultramafic lamprophyre provinces within the last 270 m.y. relative to the African and Pacific LLSVPs. The reconstructions are based on Torsvik et al. (2014)'s continent rotation model. Kimberlites and ultramafic lamprophyres with a PREMA component are geographically associated with LLVSPS (except the Siberian Jurassic kimberlites), while those without a PREMA component (black diamonds) are not. Red indicates areas with the lowest seismic velocities (LLSVPs) while blue indicates areas with the highest.

Based on the Merdith et al. (2021) kinematic model, Lee (2023) showed that the North American kimberlites that erupted between 110-660 Ma can be backtracked to the margins of LLSVPs, whereas those younger than 110 Ma cannot. Therefore, LLSVPs cannot explain the occurrence of all kimberlites. Using similar methods and models as described in Lee (2023), we backtracked the locations of the Kansas kimberlites and lamproites to the oldest (~105 Ma) and youngest (~60 Ma) ages, based on our new perovskite U-Pb geochronology, and similarly found that they cannot be correlated with the location of an LLSVP (Fig. 55). Thus, some other mechanism must be responsible for mid to late Cretaceous alkaline magmatism in North America.

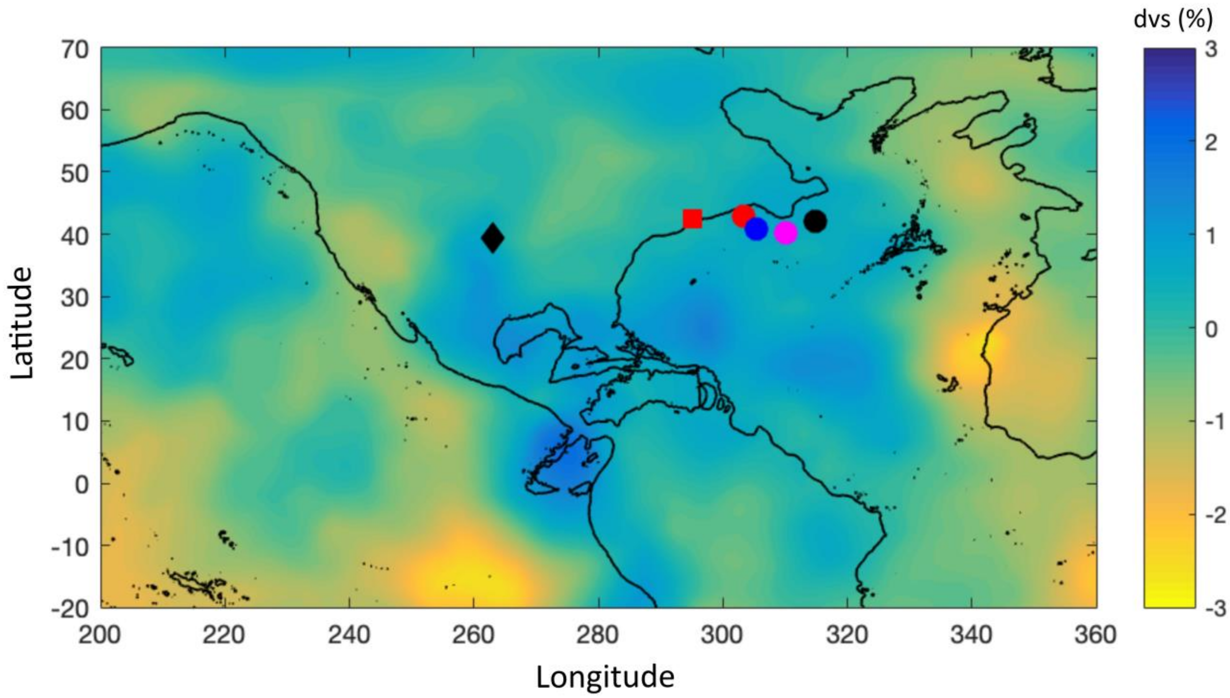

Figure 55. Seismic Tomography Model of the Backtracked Locations of the Kansas

Seismic tomography model, SEMUCB-WM1, (French and Romanowicz, 2014) illustrating the locations of the Kansas kimberlites and lamproites today (black diamond) and during their emplacement. The red symbols represent Bala at 60 Ma (square) and 82 Ma (circle). Tuttle (magenta) is backtracked to 106 Ma, while the Hills Pond (blue) and Rose Dome lamproites are backtracked to 87 and 97 Ma, respectively. The locations were backtracked via the rotation poles from Merdith et al. (2021). The color map displays the lateral seismic velocity anomaly, dvs, at a depth of ~2,800 km.

5.4.4 Edge Driven Convection

Edge Driven Convection (EDC) is a type of small-scale convection triggered by significant changes in lithospheric thickness (e.g., craton edges) (King and Anderson, 1998; Dockman, 2016; Kaislaniemi and van Hunen, 2014; Manjón-Cabeza Córdoba and Ballmer, 2021). There are two situations in which EDC may be generated. One is referred to as EDC *sensu stricto* (EDC s.s), the other is EDC with shear (EDC w.s) (Fig. 56) (Kaislaniemi and van Hunen, 2014). EDC s.s is caused when the cold lithosphere at the cratonic edge cools the adjacent mantle, inducing downwelling. EDC w.s is due to the horizontal thermal gradient between the mantle beneath the thicker, more insulating lithosphere and the thinner lithosphere. The resulting longwave length convection cell produces secondary convection cells on the lee side of the cratonic edge (Kaislaniemi and van Hunen, 2014; Dockman, 2016). Both types of EDC facilitate decompression melting (Kaislaniemi and van Hunen, 2014).

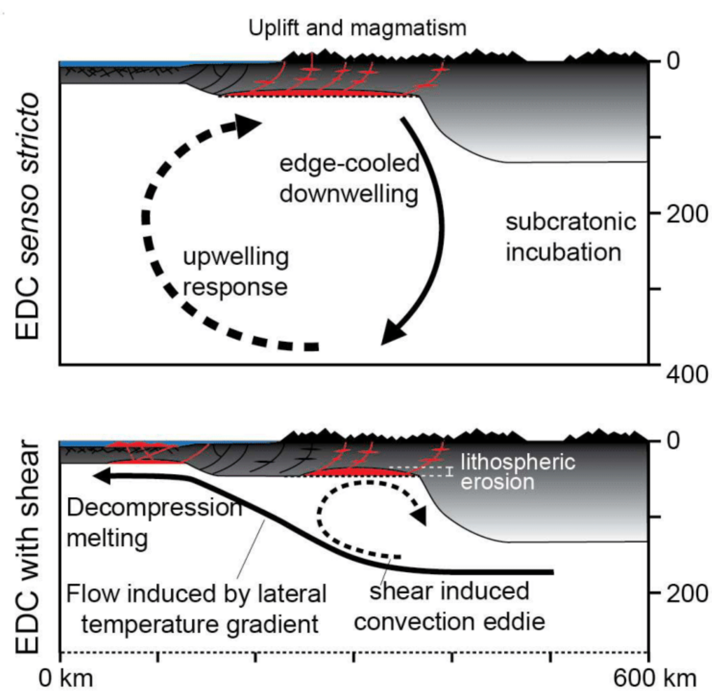

Figure 56. Two Edge Driven Convection Style Models

Simplistic diagram of the two styles of edge-driven convection (EDC) from Dockman, (2016) (modified from Kaislaniemi and van Hunen, 2014). Top) EDC senso stricto: the boundary of the cold thick lithosphere cools the adjacent mantle inducing downwelling. The resulting upwelling facilitates decompression melting. Bottom) EDC with shear: A long wavelength convection cell produced by the lateral temperature gradient beneath the lithospheric step produces secondary convection cells (eddies) which erode the lithosphere.

Several studies have recently hypothesized that EDC processes are responsible for the intense pulse of alkaline igneous magmatism observed in the Mid-Cretaceous (Matton and Jebrak, 2009; Kjardsgard et al., 2017; Walker, 2021). Kjardsgard et al. (2017) noted that many of the kimberlite fields within the Mid-Cretaceous corridor occurr in close proximity to the North American cratonic margin in areas where the lithosphere significantly thins toward western Mesozoic basins (Fig. 3). In the southern portion of the corridor, USArray data depict a north-trending transition at 98-95 W longitude from a strong and deep (200-240 km) lithosphere-asthenosphere boundary (LAB) to the east and a weak and shallow (150-190 km) LAB to the west (Fig. 3, 57) (Foster et al., 2014). This north-trending lithospheric gradient was termed the American Midwest Transition (AMT) by Foster et al. (2014); based on seismic models proposed by Schaeffer and Lebedev (2014) the AMT can be extended toward Arkansas. Based on the CAM2016 model of LAB gradients, the Kansas kimberlites and lamproites occur in the middle of this transition—a position well suited for initiation of EDC (Fig. 57a) (Priestley et al., 2018). Additionally, Fig. 57b illustrates that the Kansas lamproites are associated with shallower LAB depths than the kimberlites, consistent with the geochemical data that suggest kimberlites originate from a deeper source (Fig. 2).

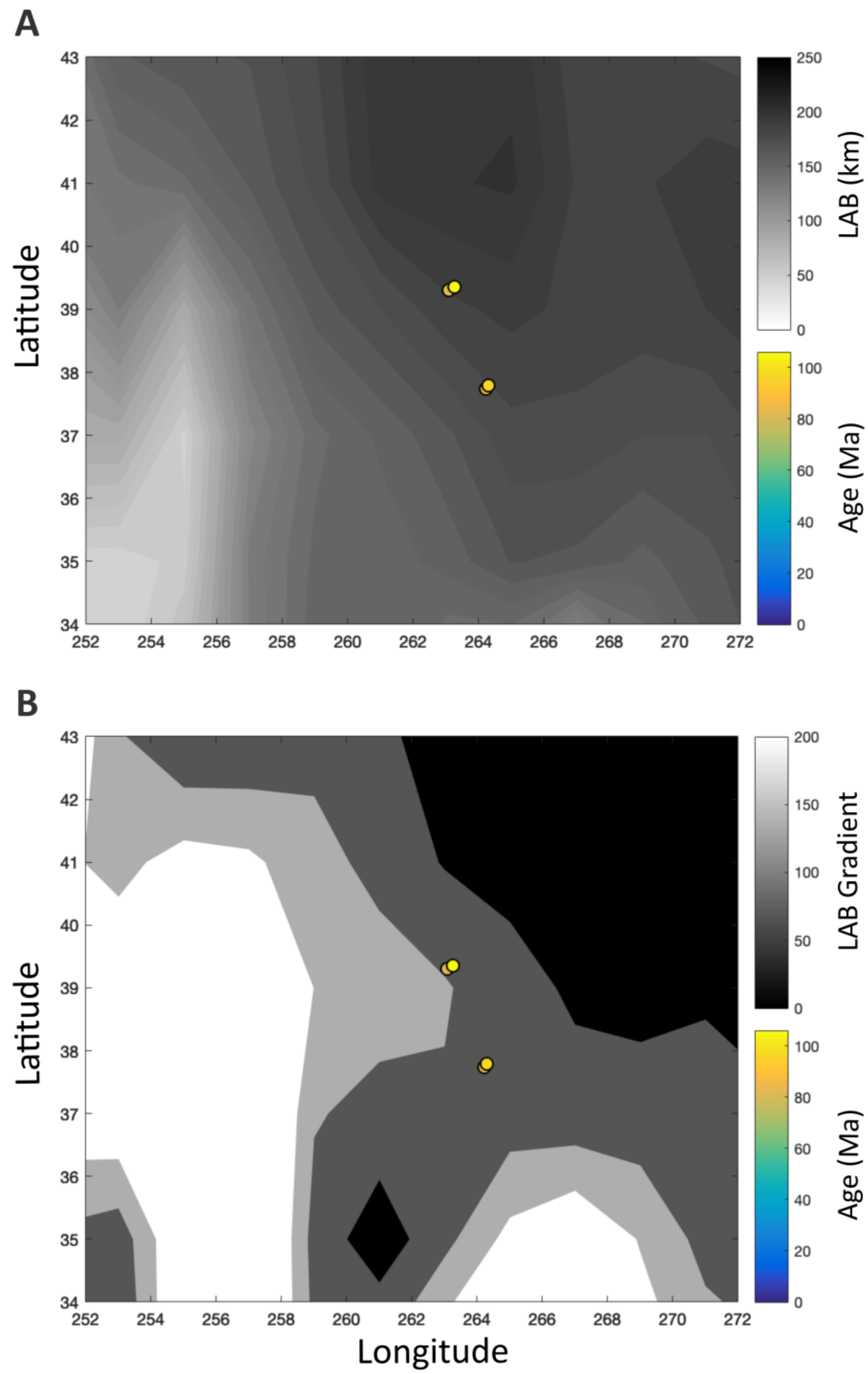

Figure 57. Lithosphere Asthenosphere Boundary Below the Kansas Kimberlites and Lamproites

Models illustrating the lithosphere asthenosphere boundary (LAB) beneath the present-day locations of the Kansas kimberlites (northern most circles) and lamproites (southernmost circles) according to the CAM2016 model (Priestley et al., 2018). A) Depicts the depth to the LAB. B) Depicts the LAB gradient. The LAB gradient is the derivative of the depths to the LAB relative to the longitudinal axis. The colors of the symbols of the kimberlites and lamproites correspond to their ages.

In addition, Walker (2021) and Matton and Jebrak (2009) noted that the emplacement ages of alkali rocks within Arkansas and Kansas correlate with major phases associated with opening and tectonic evolution of the Atlantic Ocean basin. According to simulations run by King and Anderson (1998), EDC reaches peak velocity after ~80-100 Ma. Assuming sufficient contrast between the continental and oceanic plate was established between 200 and 180Ma, peak EDC convection would have occurred in the vicinity of the AMT between 120 and 80 Ma (Matton and Jebrak, 2009). This time period correlates well with two of the three magmatic events recorded via the perovskite (~105 Ma and 82-88 Ma). The youngest age, (~60 Ma) recorded by the Bala kimberlite could be caused by a lag in upwelling of the asthenosphere as the North American plate moved westward, as modelled by Shahnas and Pysklywec (2004) and Walker (2021). Alternatively, Walker (2021) proposed that EDC could also be related to the opening of the Gulf of Mexico, as the Northern Gulf Anomaly, an area with extremely low asthenospheric velocities, may represent past or present edge driven connective upwelling (Krauss and Menke, 2020). If the Northern Gulf Anomaly represents past EDC initiated during the opening of the Gulf of Mexico, ~180 Ma, peak EDC velocity would have occurred at ~100 or 80 Ma, a range similar to that predicted via the opening of the Atlantic.

The transition in seismic structure, in combination with the thermal blanketing effect of the large North American craton, could lead to the generation of a combination of EDC s.s and EDC w.s., which would enable decompression melting to facilitate the ascent of kimberlitic magma from the mantle (Kjardsgard et al., 2017) (Fig. 58). Despite EDC processes generally producing basaltic to alkali basaltic melt, Kaislaniemi and van Hunen (2014) demonstrated that less intense mantle upwelling is also initiated 200-300 km behind the attenuated lithosphere edge, potentially inducing small degrees of partial melting (i.e., kimberlitic/lamproitic) (Kjardsgard et al., 2017).

In summary, current geochronological data appear to be most consistent with an edge-driven convection model for the origin of kimberlite and lamproite magmatism in Kansas and may similarly explain the occurrence of other alkaline magmatism of a similar age, such as Prairie Creek and Magnet Cove in Arkansas (Zartman et al., 1967; Eby and Vasconcelos, 2009; Möller and Pell, 2023) and Elliot Co, Kentucky (Heaman 1989; Faure, 2010).

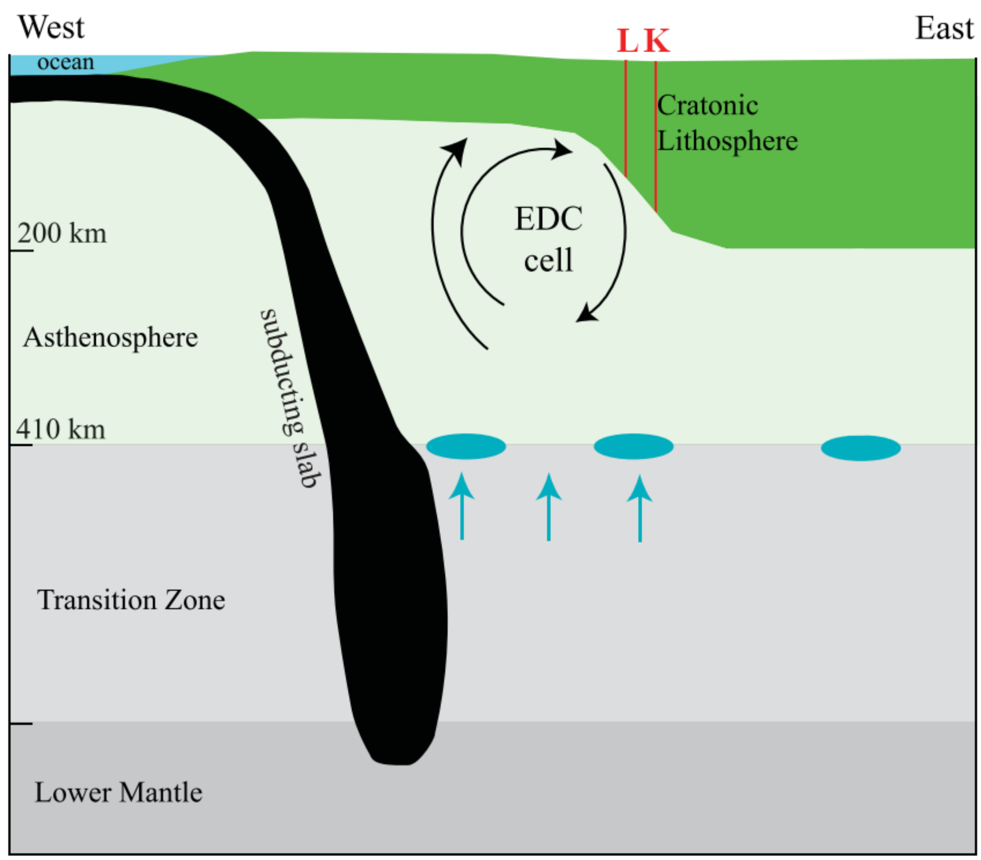

Figure 58. Kansas Kimberlite and Lamproite Geodynamic Model

Interpreted cross section, modified from Kjarsgaard et al. (2017) depicting edge-driven convection cells (EDC's) forming near the attenuated lithosphere margin. The EDC generates and transports (red line) melt to the Kansas kimberlite and lamproite fields. Blue ovals represent water-rich zones within the transition zone.

Chapter 6 - Conclusions

U-Pb analysis on perovskite can produce ages for alkaline rocks such as lamproites and kimberlites. However, the accuracy of this method depends on the proportion of common Pb present within the mineral. We have shown that accurate emplacement ages for the Kansas kimberlites and lamproites can be achieved via this method. The U-Pb perovskite age achieved for the Tuttle kimberlite, 105.6 ± 1.9 Ma, is consistent with the 106.6 ± 1.0 Ma age determined by Blackburn et al. (2008) using Rb-Sr on phlogopite and clinopyroxene. Additionally, we were able to confirm that the Bala kimberlite yields two separate ages (59.6 ± 7.4 Ma and 81.7 ± 8.6 Ma). However, given our in-situ analytical approach, we are able to show a correlation between the petrologic texture and two perovskite generations present within Bala, indicating that the younger ages are not the result of a hydrothermal 'reheating' event as suggested by Blackburn et al. (2008). Given Bala's classification as hypabyssal, it's likely that it was subject to multiple intrusive events of subsequent kimberlite melts over 22 m.y. Additionally, if we are to assume all the younger ages reported for the Kansas kimberlites by Blackburn et al. (2008) are the result of separate magma intrusions, the Kansas kimberlite field experienced at least three magmatic pulses over ~47 m.y. The earliest recorded intrusive event around 105 Ma produced the Tuttle and Stockdale kimberlites. Around 82-88 Ma another pulse is recorded in the Bala, Creek, and Leonardville localities. The youngest pulse at ~60 Ma is observed within the Bala, Tuttle, Stockdale, and Leonardville localities.

By combining all the U-Pb analyses per analytical session, we were able to overcome the high common Pb component and limited spread in U-Pb ratios in the perovskites from the Kansas lamproites. We were able to produce the precise age of 86.9 ± 3.5 Ma for the Hills Pond lamproite, which is ~7 Ma younger than the updated age range reported by Zartman et al. (1967)

(92-93 ± 5) from K-Ar analyses, which we interpret as possible K-loss due to alteration, or excess Ar. Although we were unable to provide a more precise age for the Rose Dome lamproite, our age of 97.1 ± 12.6 Ma implies that the lamproite sampled at Rose Dome may be older than the Hills Pond, contrary to the ages reported by Zartman et al. (1967). The lower Th/U ratios obtained for the Hills Pond relative to the Rose Dome additionally support this order of emplacement.

Based on U-Pb geochronology, we are able to show that magmatism with the Kansas kimberlites and lamproites is protracted, spanning at least 46 and 11 m.y., respectively. The emplacement of both rock types overlaps, with the kimberlites preceding the lamproites by approximately 8 m.y. Given the significant time span over which magmatism occurred, not only within Kansas but within individual localities, edge-driven convection is the most plausible formation model.

References

Abersteiner, A., Kamenetsky, V. S., Goemann, K., Giuliani, A., Howarth, G. H., Castillo-Oliver, M., Thompson, J., Kamenetsky, M., and Cherry, A. (2019). Composition and emplacement of the Benfontein kimberlite sill complex (Kimberley, South Africa): Textural, petrographic and melt inclusion constraints. *Lithos*, *324–325*, 297–314. https://doi.org/10.1016/j.lithos.2018.11.017

Adam, C., Lee, E., and Kempton, P.D. (2023). Backtracking the Kimberlites Emplaced over the North American Continent. *Geological Society of America Abstracts with Programs*. v. 55, Fort Collins, Colorado, May 23-25.

Benedictus, A., Berendsen, P., and Hagni, A. M. (2008). Quantitative characterisation of processed phlogopite ore from Silver City Dome District, Kansas, USA, by automated mineralogy. *Minerals Engineering*, *21*(15), 1083–1093. https://doi.org/10.1016/j.mineng.2008.01.012

Berendsen, P. (1997). Tectonic evolution of the Midcontinent Rift System in Kansas. In R. W. Ojakangas, A. B. Dickas, and J. C. Green (Eds.), *Middle Proterozoic to Cambrian Rifting, Central North America* (pp. 235–241). Geological Society of America Special Paper 312. https://doi.org/10.1130/0-8137-2312-4.235

Berendsen, P., and Blair, K. P. (1986). Subsurface structural maps over the Central North American rift system (CNARS), central Kansas, with discussion. *Kansas Geological Survey*, 1–16.

Berendsen, P., and Blair, K. P. (1988). The lamproites of Woodson and Wilson Counties, SE Kansas. In P. Berendsen and R. Knapp (Eds.), *Cretaceous Lamproites of the Silver City and Rose Domes, Woodson and Wilson counties, Kansas: Geol. Soc. Amer. Guidebook for Field Trip No. 2* (Open File Rept. 88-49, pp. 2–10). Kansas Geological Survey.

Berendsen, P., Wilson, F. W., Yarger, H., and Steeples, D. W. (1978). New Data on Major Basement Fractures in the Tectonic Development of Eastern Kansas. In D. W. O'Leary and J. L. Earle (Eds.), *Proceedings of the Third International Conference on the New Basement Tectonics*. (pp. 227–240). Basement Tectonics Committee.

Berendsen, P. (2011). Structural Setting and Stratigraphy of Lamproite Occurrences in Woodson and Wilson Counties, Southeast Kansas, USA. *Kansas Geological Survey, Open File Report 2011-5*, 1-77.

Bergman, S. C. (1987). Lamproites and other potassium-rich igneous rocks: A review of their occurrence, mineralogy and geochemistry. *Geological Society, London, Special Publications*, *30*(1), 103–190. https://doi.org/10.1144/GSL.SP.1987.030.01.08

Beyer, C., Berndt, J., Tappe, S., and Klemme, S. (2013). Trace element partitioning between perovskite and kimberlite to carbonatite melt: New experimental constraints. *Chemical Geology*, *353*, 132–139. https://doi.org/10.1016/j.chemgeo.2012.03.025

Bickford, M. E., Harrower, K. L., Nusbaum, R. L., Thomas, J. J., and Nelson, G. E. (1979). *Preliminary geologic map of the Precambrian basement rocks of Kansas (with text material) M-9* [Map]. Kansas Geological Survey.

Blackburn, T. J., Stockli, D. F., Carlson, R. W., and Berendsen, P. (2008). (U–Th)/He dating of kimberlites—A case study from north-eastern Kansas. *Earth and Planetary Science Letters, 275*(1–2), 111–120. https://doi.org/10.1016/j.epsl.2008.08.006

Brookins, D. G. (1970). The Kimberlites of Riley County, Kansas. *Bulletin - Kansas Geological Survey, 200*, 1–32.

Bunker, B. J., Witzke, B. J., Watney, W. L., and Ludvigson, G. A. (1988). Phanerozoic history of the central midcontinent, United States. In L. L. Sloss (Ed.), *Sedimentary Cover—North American Craton: Vol. D-2.* Geological Society of America. https://doi.org/10.1130/DNAG-GNA-D2.243

Casalini, M., Avanzinelli, R., Tommasini, S., Natali, C., Bianchini, G., Prelevic, D., Mattei, M., and Conticelli, S. (2022). Petrogenesis of Mediterranean lamproites and associated rocks; the role of overprinted metasomatic events in the post-collisional lithospheric upper mantle. *Geological Society Special Publication, 513*(1), 271–296. https://doi.org/10.1144/SP513-2021-36

Cas, R. and Wright, J.V. (1987). Volcanic Succession: Modern and Ancient. Allen and Unwin, London

Chakhmouradian, A. R., Halden, N. M., Mitchell, R. H., and Horvath, L. (2007). Rb-Cs-rich rasvumite and sector-zoned "loparite-(Ce)" from Mont Saint-Hilaire (Quebec, Canada) and their petrologic significance. *European Journal of Mineralogy (Stuttgart), 19*(4), 533–546. https://doi.org/10.1127/0935-1221/2007/0019-1739

Chakhmouradian, A. R., and Mitchell, R. H. (2000). Occurrence, alteration patterns and compositional variation of perovskite in kimberlites. *Canadian Mineralogist, 38*(4), 975–994. https://doi.org/10.2113/gscanmin.38.4.975

Chakhmouradian, A. R., Reguir, E. P., Kamenetsky, V. S., Sharygin, V. V., and Golovin, A. V. (2013). Trace-element partitioning in perovskite: Implications for the geochemistry of kimberlites and other mantle-derived undersaturated rocks. *Chemical Geology, 353*, 112–131. https://doi.org/10.1016/j.chemgeo.2013.01.007

Chen, W., and Simonetti, A. (2013). In-situ determination of major and trace elements in calcite and apatite, and U–Pb ages of apatite from the Oka carbonatite complex: Insights into a complex crystallization history. *Chemical Geology, 353*, 151–172. https://doi.org/10.1016/j.chemgeo.2012.04.022

Chu, R., Leng, W., Helmberger, D. V., and Gurnis, M. (2013). Hidden hotspot track beneath the eastern United States. *Nature Geoscience, 6(11)*, 963–966. https://doi.org/10.1038/ngeo1949

Cioffi, C.R., Campos Neto, M.C., Möller, A., and Rocha, B.C. (2019). Titanite petrochronology of the southern Brasília Orogen basement: Effects of retrograde net-transfer reactions on titanite trace element compositions. *Lithos, 344-345*, 393-408. doi.org/10.1016/j.lithos.2019.06

Clement, C.R. and Skinner, E.M. (1979). A textural-genetic classification of kimberlite rocks. Kimberlite symp. II, Cambridge, Extended Abstract.

Clement, C.R. and Skinner, E.M. (1985). A textural-genetic classification of kimberlites. *Trans. Geol. Soc. S. Afr. 88*, 403-409

Clement, C. R. (1982). A comparative geological study of some major kimberlite pipes in the Northern Cape and Orange Free State. Ph.D. thesis (2 vols), University of Cape Town, South Africa

Condit, C. B., Mahan, K. H., Curtis, K. C., and Möller, A. (2018). Dating Metasomatism: Monazite and Zircon Growth during Amphibolite Facies Albitization. *Minerals*, *8*(5), 1-30. https://doi.org/10.3390/min8050187

Cook, K. L. (1955). Magnetic surveys over serpentine masses, Riley County, Kansas. *Mining Engineering*, *7(5)*, 481-488.

Coopersmith, H. G., and Mitchell, R. H. (1986). Geology and exploration of the Rose lamproite. South East Kansas, USA. *International Kimberlite Conference: Extended Abstracts*, *4*, 446–447. https://doi.org/10.29173/ikc1197

Cross, C. W. (1897). Igneous rocks of the Leucite Hills and Pilot Butte, Wyoming. *American Journal of Science (1880)*, *4*(20), 115–141. https://doi.org/10.2475/ajs.s4-4.20.115

Crough, S. T., Morgan, W. J., and Hargraves, R. B. (1980). Kimberlites: Their relation to mantle hotspots. *Earth and Planetary Science Letters*, *50*(1), 260–274. https://doi.org/10.1016/0012-821X(80)90137-5

Cullers, R. L., and Berendsen, P. (2011). Mineralogical and Chemical Evolution of Lamproites in Woodson and Wilson Counties, Southeastern Kansas. *Kansas State Geological Survey*, Technical Series 22, 1-38.

Cullers, R. L., Dorais, M. J., Berendsen, P., and Chaudhuri, S. (1996). Mineralogy and petrology of Cretaceous subsurface lamproite sills, southeastern Kansas, USA. *Lithos*, *38(3)*, 185–206. https://doi.org/10.1016/0024-4937(96)00010-2

Cullers, R. L., Pieter, B., and Andrzej, B. (2012). The Geology, Petrology, and Elemental Composition of Kimberlites from Riley and Marshall Counties, Kansas, USA. *Kansas State Geological Survey, KGS Open File Report, 2012-17 (Written in 2006)*, 1–41.

Cullers, R.L., Mullenax, J., Dimarco, M.J., and Nordeng, S. (1982). The trace element content and petrogenesis of kimberlites in Riley County, Kansas, U. S. A. *American Mineralogist*, *67*(3-4), 223-233.

Cullers, R. L., Ramakrishnan, S., Berendsen, P., and Griffin, T. (1985). Geochemistry and petrogenesis of lamproites, late cretaceous age, Woodson County, Kansas, U.S.A. *Geochimica et Cosmochimica Acta*, *49*(6), 1383–1402. https://doi.org/10.1016/0016-7037(85)90289-3

Currie, C. A., and Beaumont, C. (2011). Are diamond-bearing Cretaceous kimberlites related to low-angle subduction beneath western North America? *Earth and Planetary Science Letters*, *303*(1–2), 59–70. https://doi.org/10.1016/j.epsl.2010.12.036

Dalrymple, G. B. (1992). Critical tables for conversion of K-Ar ages from old to new constants. *Isochron/West*, *58*, 22–24.

Davaille, A., and Romanowicz, B. (2020). Deflating the LLSVPs: Bundles of Mantle Thermochemical Plumes Rather Than Thick Stagnant "Piles." *Tectonics, 39*(10), 1-21. https://doi.org/10.1029/2020TC006265

Davies, D. R., Goes, S., and Lau, H. C. P. (2015). Thermally Dominated Deep Mantle LLSVPs: A Review. In A. Khan and F. Deschamps (Eds.), *The Earth's Heterogeneous Mantle: A Geophysical, Geodynamical, and Geochemical Perspective* (pp. 441–477). Springer International Publishing. https://doi.org/10.1007/978-3-319-15627-9_14

Dawson, J. B. (1980). Kimberlites and their xenoliths. Springer-Verlag; Berlin; Heidelberg; New York, 1-5.

Deschamps, F., Li, Y., and Tackley, P. J. (2015). Large-Scale Thermo-chemical Structure of the Deep Mantle: Observations and Models. In A. Khan and F. Deschamps (Eds.), *The Earth's Heterogeneous Mantle: A Geophysical, Geodynamical, and Geochemical Perspective* (pp. 479–515). Springer International Publishing. https://doi.org/10.1007/978-3-319-15627-9_15

Dockman, D. M. (2016). *U-Pb geochronology and REE geochemistry of the pulsed Cretaceous magmatism in High Arctic Canada: Implications for lithospheric evolution and magma genesis* [MSc Thesis]. University of Alberta.

Dowell, A.R. (1964). *A magnetic investigation of northern Riley County, Kansas.* [Unpublished MSc thesis]. Kansas State University.

Dreyer, R. M. (1947). Magnetic survey of the Bala intrusive, Riley County, Kansas. *Kansas Geological Survey, Bulletin 70*, 21–28.

Duke, G. I., Carlson, R. W., Frost, C. D., Hearn, B. C., and Eby, G. N. (2014). Continent-scale linearity of kimberlite–carbonatite magmatism, mid-continent North America. *Earth and Planetary Science Letters, 403*, 1–14. https://doi.org/10.1016/j.epsl.2014.06.023

Eby, G. N., and Vasconcelos, P. (2009). Geochronology of the Arkansas alkaline province, southeastern United States. *The Journal of Geology*, *117*(6), 615–626. https://doi.org/10.1086/605779

Ezad, I. S., and Foley, S. F. (2022). Experimental partitioning of fluorine and barium in lamproites. *American Mineralogist, 107*(11), 2008–2019. https://doi.org/10.2138/am-2022-8289

Farley, K. A. (2000). Helium diffusion from apatite: General behavior as illustrated by Durango fluorapatite. *Journal of Geophysical Research: Solid Earth, 105*(B2), 2903–2914. https://doi.org/10.1029/1999JB900348

Faure, S. (2010). World kimberlites CONSOREM database. Université du Québec à Montréal. http://www.consorem.ca.

Foley, S. F., Yaxley, G. M., Rosenthal, A., Buhre, S., Kiseeva, E. S., Rapp, R. P., and Jacob, D. E. (2009). The composition of near-solidus melts of peridotite in the presence of CO_2 and H_2O between 40 and 60 kbar. *Lithos*, *112*, 274–283. https://doi.org/10.1016/j.lithos.2009.03.020

Foley, S. F. (2011). A Reappraisal of Redox Melting in the Earth's Mantle as a Function of Tectonic Setting and Time. *Journal of Petrology*, *52*(7–8), 1363–1391. https://doi.org/10.1093/petrology/egq061

Foster, K., Dueker, K., Schmandt, B., and Yuan, H. (2014). A sharp cratonic lithosphere–asthenosphere boundary beneath the American Midwest and its relation to mantle flow. *Earth and Planetary Science Letters, 402*, 82–89. https://doi.org/10.1016/j.epsl.2013.11.018

French, S. W., and Romanowicz, B. A. (2014). Whole-mantle radially anisotropic shear velocity structure from spectral-element waveform tomography. *Geophysical Journal International, 199*(3), 1303–1327. https://doi.org/10.1093/gji/ggu334

Fritschle, T., Prelević, D., Foley, S. F., and Jacob, D. E. (2013). Petrological characterization of the mantle source of Mediterranean lamproites: Indications from major and trace elements of phlogopite. *Chemical Geology*, *353*, 267–279. https://doi.org/10.1016/j.chemgeo.2012.09.006

Gaetani, G. A., and Grove, T. L. (1998). The influence of water on melting of mantle peridotite. *Contributions to Mineralogy and Petrology, 131*(4), 323–346. https://doi.org/10.1007/s004100050396

Garnero, E. J., and McNamara, A. K. (2008). Structure and Dynamics of Earth's Lower Mantle. *Science, 320*(5876), 626–628. https://doi.org/10.1126/science.1148028

Giuliani, A., Jackson, M. G., Fitzpayne, A., and Dalton, H. (2021). Remnants of early Earth differentiation in the deepest mantle-derived lavas. *Proceedings of the National Academy of Sciences*, *118*(1). https://doi.org/10.1073/pnas.2015211118

Green, D. H. and Falloon, T. J. (1998). Pyrolite: a Ringwood concept and its current expression. In: Jackson, I. (ed.) The Earth's Mantle: Composition, Structure, and Evolution (pp. 311-378). Cambridge University Press.

Heaman, L. M. (1989). The nature of the subcontinental mantle from Sr Nd Pb isotopic studies on kimberlitic perovskite. *Earth and Planetary Science Letters, 92*(3), 323–334. https://doi.org/10.1016/0012-821X(89)90057-5

Heaman, L. M., and Kjarsgaard, B. A. (2000). Timing of eastern North American kimberlite magmatism: Continental extension of the Great Meteor hotspot track? *Earth and Planetary Science Letters, 178*(3), 253–268. https://doi.org/10.1016/S0012-821X(00)00079-0

Heaman, L. M., Kjarsgaard, B. A., and Creaser, R. A. (2003). The timing of kimberlite magmatism in North America: Implications for global kimberlite genesis and diamond exploration. *Lithos, 71*(2–4), 153–184. https://doi.org/10.1016/j.lithos.2003.07.005

Heaman, L. M., Kjarsgaard, B. A., and Creaser, R. A. (2004). The temporal evolution of North American kimberlites. *Lithos*, *76*(1–4), 377–397. https://doi.org/10.1016/j.lithos.2004.03.047

Heaman, L. M., Pell, J., Grütter, H. S., and Creaser, R. A. (2015). U–Pb geochronology and Sr/Nd isotope compositions of groundmass perovskite from the newly discovered Jurassic Chidliak kimberlite field, Baffin Island, Canada. *Earth and Planetary Science Letters, 415*, 183–199. https://doi.org/10.1016/j.epsl.2014.12.056

Heaman, L. M., Phillips, D., and Pearson, G. (2019). Dating Kimberlites: Methods and Emplacement Patterns Through Time. *Elements (Quebec)*, *15*(6), 399–404. https://doi.org/10.2138/gselements.15.6.399

Jaques, A. L. (2016). Major and trace element variations in oxide and titanate minerals in the West Kimberley lamproites, Western Australia. *Mineralogy and Petrology, 110*(2), 159–197. https://doi.org/10.1007/s00710-015-0420-4

Jochum, K. P., Weis, U., Stoll, B., Kuzmin, D., Yang, Q., Raczek, I., Jacob, D. E., Stracke, A., Birbaum, K., Frick, D. A., Günther, D., and Enzweiler, J. (2011). Determination of Reference Values for NIST SRM 610–617 Glasses Following ISO Guidelines. *Geostandards and Geoanalytical Research*, *35*(4), 397–429. https://doi.org/10.1111/j.1751-908X.2011.00120.x

Kaislaniemi, L., and van Hunen, J. (2014). Dynamics of lithospheric thinning and mantle melting by edge-driven convection: Application to Moroccan Atlas mountains. *Geochemistry*, *Geophysics*, *Geosystems*, *15*(8), 3175–3189. https://doi.org/10.1002/2014GC005414

Karmalkar, N. R., Duraiswami, R. A., Jonnalagadda, M. K., and Griffin, W. L. (2014). Mid-Cretaceous lamproite from the Kutch region, Gujarat, India: Genesis and tectonic implications. *Gondwana Research*, *26*(3), 942–956. https://doi.org/10.1016/j.gr.2013.09.012

Kempton, P.D., Brueseke, M.E., Rogers, K., Adam, C. (2019a). The Mystery of Kimberlites in Kansas: Geological Society of America Abstracts with Programs, v. 51, Phoenix, Arizona, September 22-25.

Kempton, P. D., Rogers, K., and Brueseke, M. E. (2019b). Windows into the Cretaceous mantle of the North American midcontinent—Kimberlites of Riley County, Kansas. In M. K. Schulmeister and J. S. Aber (Eds.), *Exploring Extreme and Unusual Geology in the Stable Midcontinent: Field Excursions for the 2019 GSA South-Central, North-Central, and Rocky Mountain Sections Joint Meeting* (Vol.52). Geological Society of America. https://doi.org/10.1130/2019.0052(03)

King, S. D., and Anderson, D. L. (1998). Edge-driven convection. *Earth and Planetary Science Letters*, *160*(3), 289–296. https://doi.org/10.1016/S0012-821X(98)00089-2

Kjarsgaard, B. A. (2007). Kimberlite Pipe models: Significance for exploration. *Proceedings of Exploration*, *7*, 667–677.

Kjarsgaard, B. A., Heaman, L. M., Sarkar, C., and Pearson, D. G. (2017). The North America mid-Cretaceous kimberlite corridor: Wet, edge-driven decompression melting of an OIB-type deep mantle source: Mid-Cretaceous North America Kimberlites. *Geochemistry, Geophysics, Geosystems*, *18*(7), 2727–2747. https://doi.org/10.1002/2016GC006761

Kjarsgaard, B. A., and Levinson, A. A. (2002). Diamonds in Canada. *Gems and Gemology*, *38*(3), 208–238. https://doi.org/10.5741/GEMS.38.3.208

Kononova, V. A., Bogatikov, O. A., and Kondrashov, I. A. (2011). Kimberlites and lamproites: Criteria for similarity and differences. *Petrology*, *19*(1), 34–54. https://doi.org/10.1134/S0869591111010024

Kopylova, M. G., and Caro, G. (2004). Mantle Xenoliths from the Southeastern Slave Craton: Evidence for Chemical Zonation in a Thick, Cold Lithosphere. *Journal of Petrology*, *45*(5), 1045–1067. https://doi.org/10.1093/petrology/egh003

Krauss, Z., and Menke, W. (2020). The Northern Gulf Anomaly: P- and S-wave travel time delays illuminate a strong thermal feature beneath the Northern Gulf of Mexico. *Earth and Planetary Science Letters*, *534*. https://doi.org/10.1016/j.epsl.2020.116102

Kreielkamp, P., Stein, C., and Hansen, U. (2022). LLSVPs of primordial origin: Implications for the evolution of plate tectonics. *Earth and Planetary Science Letters*, *579*. https://doi.org/10.1016/j.epsl.2021.117357

Lee, E. (2023). *Backtracking potential mantle sources of North American kimberlites through kinematic models to constrain their origin* [MSc Thesis, Kansas State University]. https://krex.k-state.edu/handle/2097/42890

Lee, J., Bazilian, M., Sovacool, B., Hund, K., Jowitt, S. M., Nguyen, T. P., Månberger, A., Kah, M., Greene, S., Galeazzi, C., Awuah-Offei, K., Moats, M., Tilton, J., and Kukoda, S. (2020). Reviewing the material and metal security of low-carbon energy transitions. *Renewable and Sustainable Energy Reviews*, *124*, 109789-. Science (American Association for the Advancement of Science)https://doi.org/10.1016/j.rser.2020.109789

Le Roex, and P, A. (1986). Geochemical correlation between southern African kimberlites and South Atlantic hotspots. *Nature*, *324*(6094), Article 6094. https://doi.org/10.1038/324243a0

Li, Q.-L., Li, X.-H., Liu, Y., Wu, F.-Y., Yang, J.-H., and Mitchell, R. H. (2010). Precise U–Pb and Th–Pb age determination of kimberlitic perovskites by secondary ion mass spectrometry. *Chemical Geology*, *269*(3), 396–405. https://doi.org/10.1016/j.chemgeo.2009.10.014

Liu, J., Brin, L. E., Graham Pearson, D., Bretschneider, L., Luguet, A., van Acken, D., Kjarsgaard, B., Riches, A., and Mišković, A. (2018). Diamondiferous Paleoproterozoic mantle roots beneath Arctic Canada: A study of mantle xenoliths from Parry Peninsula and Central Victoria Island. *Geochimica et Cosmochimica Acta*, *239*, 284–311. https://doi.org/10.1016/j.gca.2018.08.010

Liu, L., Spasojevic, S., and Gurnis, M. (2008). Reconstructing Farallon plate subduction beneath North America back to the Late Cretaceous. *Science, 322*(5903), 934–938. https://doi.org/10.1126/science.1162921.

Locock, A. J., and Mitchell, R. H. (2018). Perovskite classification: an Excel spreadsheet to determine and depict end-member proportions for the perovskite- and vapnikite-subgroups of the perovskite supergroup. *Computers and Geosciences, 113*, 106–114. https://doi.org/10.1016/j.cageo.2018.01.012

Lustrino, M., Agostini, S., Chalal, Y., Fedele, L., Stagno, V., Colombi, F., and Bouguerra, A. (2016). Exotic lamproites or normal ultrapotassic rocks? The Late Miocene volcanic rocks from Kef Hahouner, NE Algeria, in the frame of the circum-Mediterranean lamproites. *Journal of Volcanology and Geothermal Research, 327*, 539–553. https://doi.org/10.1016/j.jvolgeores.2016.09.021

Manjón-Cabeza Córdoba, A., and Ballmer, M. D. (2021). The role of edge-driven convection in the generation of volcanism – Part 1: A 2D systematic study. *Solid Earth, 12*(3), 613–632. https://doi.org/10.5194/se-12-613-2021

Mansker, W.L., Richards, B.D., and Cole, G.P. (1987). A note on newly discovered kimberlites in Riley County, Kansas. In *Morris, E. Metasomatism and Alkaline Magmatism* (Vol. 215, pp. 197-204). Geological Society of America Special Paper.

Matton, G., and Jébrak, M. (2009). The Cretaceous Peri-Atlantic Alkaline Pulse (PAAP): Deep mantle plume origin or shallow lithospheric break-up? *Tectonophysics, 469*(1), 1–12. https://doi.org/10.1016/j.tecto.2009.01.001

McCandless, T. E. (1999). Mantle expressions of deep-seated subduction. In J. J. Gurney (Ed.), *Proceedings of the 7th International Kimberlite Conference* (Vol. 2, pp. 545–549). Red Roof.

McDonough, W. F., Sun, S.-S., Ringwood, A. E., Jagoutz, E., and Hofmann, A. W. (1992). Potassium, rubidium, and cesium in the Earth and Moon and the evolution of the mantle of the Earth. *Geochimica et Cosmochimica Acta, 56*(3), 1001–1012. https://doi.org/10.1016/0016-7037(92)90043-I

Merdith, A. S., Williams, S. E., Collins, A. S., Tetley, M. G., Mulder, J. A., Blades, M. L., Young, A., Armistead, S. E., Cannon, J., Zahirovic, S., and Müller, R. D. (2021). Extending full-plate tectonic models into deep time: Linking the Neoproterozoic and the Phanerozoic. *Earth-Science Reviews, 214*(103477). https://doi.org/10.1016/j.earscirev.2020.103477

Merrill, R. B., Bickford, M. E., and Irving, A. J. (1977). The Hills Pond peridotite, Woodson County, Kansas: A richterite-bearing Cretaceous intrusive with kimberlitic affinities. *International Kimberlite Conference: Extended Abstracts, 2*, 220–222. https://doi.org/10.29173/ikc999

Mitchell, R. (1985). A review of the mineralogy of lamproites. *South African Journal of Geology, 88*, 411-437.

Mitchell, R.H. (1986) *Kimberlites: Mineralogy, Geochemistry, and Petrology*. Plenum Press, New York, 1-104.

Mitchell, R. H. (1995). *Kimberlites, orangeites, and related rocks.* Plenum Press. pages

Mitchell, R. H. (1996). Perovskites: a revised classification scheme for an important rare earth element host in alkaline rocks. *Mineralogical Society Series, 7,* 41–76.

Mitchell, R. H. (1997). Preliminary studies of the solubility and stability of perovskite group compounds in the synthetic carbonatite system calcite-portlandite. *Journal of African Earth Sciences*, *25*(1), 147–158. https://doi.org/10.1016/S0899-5362(97)00067-5

Mitchell, R. H. (2008). Advances in Kimberlite Geology and Petrology. *Golden Jubilee Memoir of the Geological Society of India, 66,* 423-461.

Mitchell, R. H. (2020). Igneous Rock Associations 26. Lamproites, Exotic Potassic Alkaline Rocks: A Review of their Nomenclature, Characterization and Origins. *Geoscience Canada, 47*(3). https://doi.org/10.12789/geocanj.2020.47.162

Mitchell, R. H., and Chakhmouradian, A. R. (1999). Sr-bearing perovskite and loparite from lamproite and agpaitic nepheline syenite pegmatites. *The Canadian Mineralogist*, *37(1)*, 99–112.

Mitchell, R. H., and Bergman, S. C. (1991). *Petrology of lamproites*. Plenum Press. pages

Mitchell, R. H., Giuliani, A., and O'Brien, H. (2019). What is a Kimberlite? Petrology and Mineralogy of Hypabyssal Kimberlites. *Elements, 15*(6), 381–386. https://doi.org/10.2138/gselements.15.6.381

Mitchell, R., and Reed, S. J. B. (1988). Ion Microprobe Determination of Rare Earth Elements in Perovskite from Kimberlites and Alnöites. *Mineralogical Magazine, 52*, 331–339. https://doi.org/10.1180/minmag.1988.052.366.04

Mitchell, R. H., and Vladykin, N. V. (1993). Rare earth element-bearing tausonite and potassium barium titanates from the Little Murun potassic alkaline complex, Yakutia, Russia. *Mineralogical Magazine, 57*(389), 651–664. https://doi.org/10.1180/minmag.1993.057.389.09

Mitchell, R. H., Welch, M. D., and Chakhmouradian, A. R. (2017). Nomenclature of the perovskite supergroup; a hierarchical system of classification based on crystal structure and composition. *Mineralogical Magazine, 81*(3), 411–461. https://doi.org/10.1180/minmag.2016.080.156

Möller, A., and Pell, D. (2023) Precise LA-ICP-MS U-Pb schorlomite garnet and perovskite ages: new constraints on emplacement of the Magnet Cove Igneous Complex, AR. Geological Society of America Abstracts with Programs, v. 55(6), Pittsburgh, Pennsylvania, October 15-18, doi: 10.1130/abs/2023AM-394821

Mulyukova, E., Steinberger, B., Dabrowski, M., and Sobolev, S. V. (2015). Survival of LLSVPs for billions of years in a vigorously convecting mantle: Replenishment and destruction of chemical anomaly. *Journal of Geophysical Research: Solid Earth*, *120*(5), 3824–3847. https://doi.org/10.1002/2014JB011688

Moss, S., and Russell, J. K. (2011). Fragmentation in kimberlite: Products and intensity of explosive eruption. *Bulletin of Volcanology*, *73*(8), 983–1003. https://doi.org/10.1007/s00445-011-0504-x

Nebel, O., Scherer, E. E., and Mezger, K. (2011). Evaluation of the 87Rb decay constant by age comparison against the U–Pb system. *Earth and Planetary Science Letters*, *301*(1–2), 1–8. https://doi.org/10.1016/j.epsl.2010.11.004

Niggli, P. (1923). Gesteins und Mineralprovinzen: Verlag Gebrüder Borntraegar, Berlin, 586 p

Paton, C., Hellstrom, J., Paul, B., Woodhead, J., and Hergt, J. (2011). Iolite: Freeware for the visualisation and processing of mass spectrometric data. *Journal of Analytical Atomic Spectrometry*, *26*(12), 2508–2518. https://doi.org/10.1039/C1JA10172B

Paton, C., Woodhead, J. D., Hellstrom, J. C., Hergt, J. M., Greig, A., and Maas, R. (2010). Improved laser ablation U-Pb zircon geochronology through robust downhole fractionation correction. *Geochemistry, Geophysics, Geosystems*, *11*(3). https://doi.org/10.1029/2009GC002618

Pearson, D. G., Woodhead, J., and Janney, P. E. (2019). Kimberlites as Geochemical Probes of Earth's Mantle. *Elements (Quebec)*, *15*(6), 387–392. https://doi.org/10.2138/gselements.15.6.387

Priestley, K., McKenzie, D., and Debayle, E. (2006). The state of the upper mantle beneath southern Africa. *Tectonophysics*, *416*(1), 101–112. https://doi.org/10.1016/j.tecto.2005.11.024

Priestley, K., McKenzie, D., and Ho, T. (2018). A Lithosphere–Asthenosphere Boundary—A Global Model Derived from Multimode Surface-Wave Tomography and Petrology. In *Lithospheric Discontinuities* (pp. 111–123). American Geophysical Union (AGU). https://doi.org/10.1002/9781119249740.ch6

Ranger, I. M., Heaman, L. M., Pearson, D. G., Muntener, C., and Zhuk, V. (2018). Punctuated, long-lived emplacement history of the Renard 2 kimberlite, Canada, revealed by new high precision U-Pb groundmass perovskite dating. *Mineralogy and Petrology*, *112*(2), 639–651. https://doi.org/10.1007/s00710-018-0629-0

Reguir, E. P., Camacho, A., Yang, P., Chakhmouradian, A. R., Kamenetsky, V. S., and Halden, N. M. (2010). Trace-element study and uranium-lead dating of perovskite from the Afrikanda plutonic complex, Kola Peninsula (Russia) using LA-ICP-MS. *Mineralogy and Petrology*, *100*(3), 95–103. https://doi.org/10.1007/s00710-010-0131-9

Reiners, P. W., and Farley, K. A. (1999). Helium diffusion and (U-Th)/He thermochronometry of titanite. *Geochmica et Cosmochimica Acta*, *63*(22), 3845–3859. https://doi.org/10.1016/S0016-7037(99)00170-2

Reiners, P. W., Farley, K. A., and Hickes, H. J. (2002). He diffusion and (U-Th)/He thermochronometry of zircon: Initial results from Fish Canyon Tuff and Gold Butte. *Tectonophysics*, *349*(1–4), 297–308. https://doi.org/10.1016/S0040-1951(02)00058-6

Reiners, P. W., Spell, T. L., Nicolescu, S., and Zanetti, K. A. (2004). Zircon (U-Th)/He thermochronometry: He diffusion and comparisons with 40Ar/39Ar dating. *Geochmica et Cosmochimica Acta*, *68*(8), 1857–1887. https://doi.org/10.1016/j.gca.2003.10.021

Roberts, N. M. W., Drost, K., Horstwood, M. S. A., Condon, D. J., Chew, D., Drake, H., Milodowski, A. E., McLean, N. M., Smye, A. J., Walker, R. J., Haslam, R., Hodson, K., Imber, J., Beaudoin, N., and Lee, J. K. (2020). Laser ablation inductively coupled plasma mass spectrometry (LA-ICP-MS) U–Pb carbonate geochronology: Strategies, progress, and limitations. *Geochronology, 2*(1), 33–61. https://doi.org/10.5194/gchron-2-33-2020

Rogers, K.A. (in prep.). *Constraining the origin and emplacement of off-craton kimberlites in Riley and Marshall County, Kansas: A petrological, geochemical and geophysical study* [MSc Thesis]. Kansas State University.

Sarkar, C., Heaman, L. M., and Pearson, D. G. (2015). Duration and periodicity of kimberlite volcanic activity in the Lac de Gras kimberlite field, Canada and some recommendations for kimberlite geochronology. *Lithos, 218–219*, 155–166. https://doi.org/10.1016/j.lithos.2015.01.017

Sarkar, S., Giuliani, A., Phillips, D., Howarth, G. H., Ghosh, S., and Dalton, H. (2022). Sublithospheric melt input in cratonic lamproites. *Geology, 50*(11), 1296–1300. https://doi.org/10.1130/G50384.1

Sarkar, C., Storey, C. D., and Hawkesworth, C. J. (2014). Using perovskite to determine the pre-shallow level contamination magma characteristics of kimberlite. *Chemical Geology, 363*, 76–90. https://doi.org/10.1016/j.chemgeo.2013.10.032

Schaeffer, A. J., and Lebedev, S. (2014). Imaging the North American continent using waveform inversion of global and USArray data. *Earth and Planetary Science Letters*, *402*, 26–41. https://doi.org/10.1016/j.epsl.2014.05.014

Schmidt, K. H., Bottazzi, P., Vannucci, R., and Mengel, K. (1999). Trace element partitioning between phlogopite, clinopyroxene and leucite lamproite melt. *Earth and Planetary Science Letters*, *168*(3–4), 287–299. https://doi.org/10.1016/S0012-821X(99)00056-4

Scott, R. W. (1966). New Precambrian(?) Formation in Kansas. *Bulletin of the American Association of Petroleum Geologists*, *50*(2), 380–384.

Scott Smith, B. H., and Skinner, E. M. W. (1984). Diamondiferous Lamproites. *The Journal of Geology*, *92*(4), 433–438. https://doi.org/10.1086/628877

Scott Smith, B., Nowicki, T., Russell, J., Webb, K., Hetman, C., Hetman, C., and Robey, J. (2018). *A Glossary of Kimberlite and Related Terms Part 1*. Scott-Smith Petrology Inc.

Shahnas, M. H., and Pysklywec, R. N. (2004). Anomalous topography in the western Atlantic caused by edge-driven convection. *Geophysical Research Letters*, *31*(18). https://doi.org/10.1029/2004GL020882

Sims, P. K., Isvarsanyi, E. B. K., and Morey, G. B. (1987). Geology and metallogeny of Archean and Proterozoic basement terranes in the northern midcontinent, U.S.A.; an overview. In *Bulletin* (1815). U.S. G.P.O. https://doi.org/10.3133/b1815

Sleep, N. H. (1990). Monteregian hotspot track: A long-lived mantle plume. *Journal of Geophysical Research: Solid Earth*, *95*(B13), 21983–21990. https://doi.org/10.1029/JB095iB13p21983

Spasojevic, S., Liu, L., and Gurnis, M. (2009). Adjoint models of mantle convection with seismic, plate motion, and stratigraphic constraints: North America since the Late Cretaceous. *Geochemistry, Geophysics, Geosystems*, *10*(5). https://doi.org/10.1029/2008GC002345.

Sparks, R. S. J. (2013). Kimberlite Volcanism. *Annual Review of Earth and Planetary Sciences, 41*(1), 497–528. https://doi.org/10.1146/annurev-earth-042711-105252

Stacey, J. S., and Kramers, J. D. (1975). Approximation of terrestrial lead isotope evolution by a two-stage model. *Earth and Planetary Science Letters*, *26*(2), 207–221. https://doi.org/10.1016/0012-821X(75)90088-6

Stamm, N., Schmidt, M. W., Szymanowski, D., von Quadt, A., Mohapi, T., and Fourie, A. (2018). Primary petrology, mineralogy and age of the Letseng-la-Terae Kimberlite (Lesotho, Southern Africa) and parental magmas of group I kimberlites. *Contributions to Mineralogy and Petrology, 173*(9), 1–25. https://doi.org/10.1007/s00410-018-1502-1

Steeples, D.W., and Brozius, L., 2014, Earthquakes: Kansas Geological Survey, Public Information Circular, 5 p

Sun, S. -s., and McDonough, W. F. (1989). Chemical and isotopic systematics of oceanic basalts: Implications for mantle composition and processes. *Geological Society, London, Special Publication*, *42*, 313–345. https://doi.org/10.1144/GSL.SP.1989.042.01.19

Sun, J., Wu, F.-Y., Sklyarov, E., Sarkar, C., Liu, C.-Z., Pearson, G. D., Cheng, Z., and Mitchell, R. N. (2022). Matrix effects during in situ U-Pb dating of perovskite with variable crystal structure: Evidence from the Tazheran Massif, Russia. *Chemical Geology*, *589*(120685). https://doi.org/10.1016/j.chemgeo.2021.120685

Tappe, S., Foley, S. F., Jenner, G. A., and Kjarsgaard, B. A. (2005). Integrating Ultramafic Lamprophyres into the IUGS Classification of Igneous Rocks: Rationale and Implications. *Journal of Petrology*, *46*(9), 1893–1900. https://doi.org/10.1093/petrology/egi039

Tappe, S., and Simonetti, A. (2012). Combined U–Pb geochronology and Sr–Nd isotope analysis of the Ice River perovskite standard, with implications for kimberlite and alkaline rock petrogenesis. *Chemical Geology*, *304–305*, 10–17. https://doi.org/10.1016/j.chemgeo.2012.01.030

Tappe, S., Smart, K., Torsvik, T., Massuyeau, M., and de Wit, M. (2018). Geodynamics of kimberlites on a cooling Earth: Clues to plate tectonic evolution and deep volatile cycles. *Earth and Planetary Science Letters*, *484*, 1–14. https://doi.org/10.1016/j.epsl.2017.12.013

Taylor, W. R., and Green, D. H. (1988). Measurement of reduced peridotite-C-O-H solidus and implications for redox melting of the mantle. *Nature (London), 332*(6162), 349–352. https://doi.org/10.1038/332349a0

Torsvik, T. H., Burke, K., Steinberger, B., Webb, S. J., and Ashwal, L. D. (2010). Diamonds sampled by plumes from the core-mantle boundary. *Nature (London), 466*(7304), 352–355. https://doi.org/10.1038/nature09216

Torsvik, T. H., Steinberger, B., Ashwal, L. D., Doubrovine, P. V., and Tronnes, R. G. (2016). Earth evolution and dynamics; a tribute to Kevin Burke. *Canadian Journal of Earth Sciences, 53*(11), 1073–1087. https://doi.org/10.1139/cjes-2015-0228

Torsvik, T. H., van der Voo, R., Doubrovine, P. V., Burke, K., Steinberger, B., Ashwal, L. D., Trønnes, R. G., Webb, S. J., and Bull, A. L. (2014). Deep mantle structure as a reference frame for movements in and on the Earth. *Proceedings of the National Academy of Sciences, 111*(24), 8735–8740. https://doi.org/10.1073/pnas.1318135111

Wade, A., and Prider, R. T. (1940). The leucite-bearing rocks of the West Kimberley area, Western Australia. *Quarterly Journal of the Geological Society of London, 96*(1–4), 39–98. https://doi.org/10.1144/GSL.JGS.1940.096.01-04.04

Wagner, H. C. (1954). *Geology of the Fredonia Quadrangle, Kansas: U.S. Geological Survey, Map GQ 49* [Map]. U. S. Geological Survey.

Wagner, H. C. (1995). *Wilson County, Southeastern Kansas, U.S.A. Its geologic environment, cyclic sedimentation, basic intrusive rocks, and mineral and petroleum resources.* [PhD Thesis]. University of Leicester.

Walker, S. (2021). *Geochemistry, Thermochronometry, Petrogenesis, and Geometry of Igneous Dikes in Central Arkansas: Implications for Mississippi Embayment Evolution* [MSc Thesis, University of Alabama]. http://ir.ua.edu/handle/123456789/8191

Wall, F., Rollat, A., and Pell, R. S. (2017). Responsible sourcing of critical metals. *Elements*, *13*(5), 313–318. https://doi.org/10.2138/gselements.13.5.313

Webb, K. J., and Hetman, C. M. (2017). Magmaclasts in kimberlite. *International Kimberlite Conference: Extended Abstracts*, *11*. https://doi.org/10.29173/ikc3997

Webb, K., and Hetman, C. (2021). Magmaclasts in kimberlite. *Lithos*, *396–397*, 106197-. https://doi.org/10.1016/j.lithos.2021.106197

Wedepohl, K. H., and Muramatsu, Y. (1979). The chemical composition of kimberlites compared with the average composition of three basaltic magma types. In F. R. Boyd and H. O. A. Meyer, *Kimberlites, Diatremes, and Diamonds: Their Geology, Petrology, and Geochemistry* (Vol. 1, pp. 300–312). American Geophysical Union, Proceedings of the International Kimberlite Conference. https://doi.org/10.1029/SP015p0300

Wilson, F. W. (1979). *Study of the regional tectonics and seismicity of eastern Kansas: Summary of project activities and results to the end of the second year, or September 30, 1979. [Nemaha Uplift and related structures]* (NUREG/CR-0666). Kansas Geological Survey, Lawrence (USA). https://www.osti.gov/biblio/6311497

Woolley, R. A., Bergman, C. S., Edgar, D. A., Le Bas, J., Michael, Mitchell, H. R., Rock, H. N., and Scott Smith, H. B. (1996). Classification of Lamprophyres, Lamproites, Kimberlites, and the Kalsilitic, Melilitic, and Leucitic Rocks. *The Canadian Mineralogist*, *34*, 175–186.

Wu, F.-Y., Yang, Y.-H., Mitchell, R. H., Li, Q.-L., Yang, J.-H., and Zhang, Y.-B. (2010). In situ U–Pb age determination and Nd isotopic analysis of perovskites from kimberlites in southern Africa and Somerset Island, Canada. *Lithos*, *115*(1–4), 205–222. https://doi.org/10.1016/j.lithos.2009.12.010

Zartman, R. E., Brock, M. R., Heyl, A. V., and Thomas, H. H. (1967). K-Ar and Rb-Sr ages of some alkalic intrusive rocks from central and eastern United States. *American Journal of Science*, *265(10)*, 848–870.

Zurevinski, S. E., Heaman, L. M., Creaser, R. A., and Strand, P. (2008). The Churchill kimberlite field, Nunavut, Canada; petrography, mineral chemistry, and geochronology. *Canadian Journal of Earth Sciences*, *45*(9), 1039–1059. https://doi.org/10.1139/E08-052

Appendix A - Petrographic Descriptions

Kimberlite, Bala: BA-62-39B

Analyses available: U-Pb geochronology, EMP, and LA-ICP-MS trace elements.

In this thin section the kimberlite is relatively homogeneous and densely packed with pseudomorphs of olivine and pyroxene, replaced by serpentine and calcite (Fig. 24, 35, 44). It is a fined grained porphyritic rock consisting of 40% phenocrysts/macrocrysts of olivine and pyroxene, as well as accessory ilmenite, magnetite, phlogopite, and perovskite. There are two textures observed (Fig. 24). Texture A comprises a majority (~70%) of the thin section and is characterized by subhedral, tabular, carbonatized pyroxene phenocrysts ranging in size from 200 μm-1.5 mm. Only 3-5% of the phenocrysts in this texture are serpentinized olivine, the remaining ~95% of phenocrysts consist of pyroxene. The groundmass is primarily serpentine and calcite with lesser amounts perovskite and opaque minerals such as magnetite and ilmenite. Texture B constitutes 30% of the kimberlite and is characterized by serpentinized olivine with <2% altered pyroxene phenocrysts within a slightly more calcite-rich matrix. Subhedral to euhedral olivine pseudomorphs, replaced by serpentine, range in size from 100 μm to 1.5mm with the altered olivine within texture B tending to fall on the smaller side. All the olivine has altered into serpentine, calcite, and magnetite. Phlogopite and partially fresh pyroxene are rare, with only a few altered crystals observed. No country rock xenoliths are observed. Some of the phenocrysts have a fine-grained alteration rim of chlorite, fine-grained serpentine, and/or a secondary amphibole. Perovskites constitute ~5% of the modal abundance and tend to cubo-octohedral, although cubic and anhedral grains occur. They are light tan to brown and range in size from 30-200 μm.

Kimberlite, Bala: BA-50-39B

Analyses available: EMP.

The kimberlite in this interval is porphyritic with medium grained phenocrysts of altered olivine and pyroxene. Pseudomorphs of olivine and pyroxene; replaced by serpentine, calcite, and magnetite; are euhedral to anhedral, equant to prismatic, ranging in size from 150 μm to 1 cm. Phenocrysts comprise 30% of the modal abundance and tend to have a fine-grained rim of chlorite, fine-grained serpentine, and/or a secondary amphibole. No phlogopite or xenoliths are observed. The groundmass is primarily serpentine and calcite with lesser amounts of opaque minerals such as magnetite and ilmenite. Calcite is present in a slightly higher abundance in the matrix here than in BA-62-39B, and calcite veins are present. Perovskites constitute ~2% of the modal abundance and tend to cubo-octohedral although cubic and anhedral grains occur. They are light brown to brown pink and range in size from 30-150 μm.

Kimberlite, Bala: BA-36-39B

The kimberlite in this interval is porphyritic with phenocrysts of olivine and pyroxene. Pseudomorphs of olivine and pyroxene; replaced by serpentine, calcite, and magnetite are euhedral to anhedral, equant to prismatic, ranging in size from 100 μm to 4 mm. Phenocrysts comprise ~20% of the modal abundance and to have a fine-grained rim of chlorite, fine-grained serpentine, and/or a secondary amphibole. The groundmass is calcite with lesser serpentine and opaque minerals such as magnetite and ilmenite. Similar to BA-62-39B there are a few subhedral, tabular pyroxene phenocrysts pseudomorphs that are up 1mm in length. They only occur in the bottom corner of the thin section in an area where the groundmass is more serpentine as opposed to calcite dominant. Within this portion, the calcite after pyroxene phenocrysts comprises ~10% of the modal abundance. A few calcite veins and country rock xenoliths are observed. Perovskites consist of ~2% of the modal abundance and tend to be cubo-octohedral, although cubic and anhedral grains occur. They are dark brown to brown pink and range in size from 30-150 μm.

Kimberlite, Bala: BA-59-39B

The kimberlite is porphyritic with phenocrysts of olivine and pyroxene. Pseudomorphs of olivine and pyroxene; replaced by serpentine, calcite, and magnetite are euhedral to anhedral, equant to prismatic, ranging in size from 100 μm to 2.5 mm. All the olivine and pyroxene have altered into serpentine, calcite, and magnetite. Phenocrysts comprise 20% of the modal abundance and tend to have a fine-grained rim of serpentine. The groundmass is calcite with lesser serpentine, chlorite, and opaque minerals such as magnetite and ilmenite. There are zones that are more calcite rich that have lesser altered olivine/pyroxene phenocrysts and opaque minerals. An oxide rich vein runs down the middle of the thin section and has oxidized the surrounding minerals. There is a trace number of xenoliths and no phlogopite. Perovskites consist of 2% of the modal abundance and tend to cubo-octohedral although cubic and anhedral grains occur. They are dark brown to brown pink and range in size from 30-150 μm.

Kimberlite, Tuttle: TU-1A-1D and TU-1A-1D2

Analyses available for TU-1A-1D2: U-Pb geochronology and EMP.

In comparison to the Bala kimberlite, Tuttle is more brecciated and fragmental. It is porphyritic containing serpentinized olivine, fully to partially altered clinopyroxene, and phlogopite with minor to trace amounts of garnet, rutile, apatite, zircon, and opaque minerals such as magnetite and ilmenite. The phlogopite is anhedral to subhedral and shows evidence of deformation such as undulatory extinction and comprises ~5% of the mode. Many of the grains have sections that are discolored in plane polarized light, indicating they have altered into Mg-chlorite or serpentine. Apatite occurs almost exclusively as inclusions within the phlogopite and altered pyroxene. The pyrope garnets are anhedral, fractured grains that typically have kelyphite rims. They comprise ~3% of the mode and range in size from 900 µm to 5 mm. The serpentinized olivine and clinopyroxene are anhedral with 99% of the clinopyroxene altered into calcite and serpentine. Overall, there are fewer opaque minerals within this thin section of the Tuttle kimberlite than observed within the Bala kimberlite. The matrix consists of predominantly serpentine with lesser calcite, oxides, and chlorite within thin section TU-1A-1D2. Whereas the matrix within thin section TU-1A-1D contains slightly more chlorite. Magmaclasts comprise 40-50% of the modal abundance and range in size from 100 µm - 1.3 cm (Fig. 25 and 27). They are irregular to regular shaped with relatively distinct margins, non-vesicular, and range from matrix to clast supported. A majority of the magmaclasts are cored with ultra-thin to thick rims (0.2-3 mm) (Fig. 26). While a few multi-cored magmaclasts were observed, most only exhibit a single rim. The rims were variable in terms of how much of the core they encompassed as well as their symmetry. Cores range from primary minerals such as olivine or garnet to country rock xenoliths. The magmaclasts show a range in groundmass crystallinity and mineralogy, with some containing phlogopite while in others phlogopite is absent. Due to high degree of alteration, it is difficult to distinguish between serpentine matrix and serpentinized olivine phenocrysts /macrocrysts. Additionally, phenocrysts of serpentinized olivine pseudomorphs can be difficult to distinguish from olivine magmaclasts with ultra-thin rims (≤ 0.2 mm). Perovskites comprise ~7% of the modal abundance and are predominantly cubic. They are pale grey to light brown in color and range from 10-60 μm (although most are under 20 μm). They occur chiefly within magmaclasts (80-90%) but can be found in the interclast matrix.

Kimberlite, Tuttle: TU-1A-3B

The Tuttle kimberlite in this thin section exhibits a brecciated and fragmental texture similar to other thin sections from this kimberlite. It is porphyritic containing phenocrysts of serpentinized olivine, fully to partially altered clinopyroxene, and phlogopite, with minor to trace amounts of garnet, apatite, and opaque minerals such as magnetite and ilmenite. The phlogopite is anhedral to subhedral and shows evidence of deformation such as undulatory extinction and comprises ~7-8% of the mode. Many of the grains have sections that are discolored in plane polarized light, indicating they have altered into Mg-chlorite or serpentine. Apatite occurs almost exclusively as inclusions within phenocrysts. There is a single anhedral pyrope garnet grain. It has fractures, a kelyphite rim, and is 1 mm in length. The olivine (replaced by serpentine) and clinopyroxene (99% altered to calcite and serpentine) are anhedral to subhedral. Both the fully and partially altered grains have calcite/serpentine alteration rims. Overall, there are fewer opaque minerals within this Tuttle thin section than observed within the Bala kimberlite. The matrix consists of predominantly serpentine and chlorite with lesser calcite and oxides. Magmaclasts comprise ~40% of the modal abundance and range in size from 10 μm – 6mm.

They are irregular to regular shaped with relatively distinct margins, non-vesicular, and range from matrix to clast supported (Fig. 25 and 27). A majority of the magmaclasts are cored with a singular ultra-thin to thick rim (0.2-3 mm) (Fig. 26). The rims were variable in terms of how much of the core they encompassed as well as their symmetry. Cores range from primary minerals such as olivine or garnet to country rock xenoliths. The magmaclasts show a range in groundmass crystallinity and mineralogy. Due to the degree of alteration, it is difficult to distinguish between serpentine matrix and serpentinized olivine phenocrysts/macrocrysts. Additionally, phenocrysts of olivine pseudomorphs can be difficult to distinguish from olivine magmaclasts with ultra-thin rims. Perovskites comprise ~7% of the modal abundance and are predominantly cubic. They are pale grey to light brown in color and range from 10-60 μm (although most are under 20 μm). They occur chiefly within magmaclasts (~55%) but can also be found in the interclast matrix.

Lamproite, Hills Pond, MicroLite Mine surface exposure: PK-LA-MI1

Analyses available: U-Pb geochronology and EMP.

This lamproite sample is porphyritic, containing poikilitic phlogopite (~30%), serpentinized olivine (~45%), richterite (~6%), and diopside (~4%) with minor amounts of apatite, perovskite (~2%), and opaque minerals such as magnetite (~3%). The phlogopite is anhedral to subhedral, up to 3.5 mm in length, and shows evidence of deformation such as undulatory extinction and kink bands. A few phlogopite grains show simple twinning while others are partially altered into serpentine/chlorite. Apatite occurs almost exclusively as inclusions within the phlogopite. Anhedral grains of serpentinized olivine make up ~45% of the modal abundance and range in size from 100 μm to 5 mm. Richterite is faintly pleochroic in pale pink, subhedral-euhedral, partially altered to chlorite/serpentine and occurs as blades or bladed aggregates. It typically shows undulatory extinction. There is more abundant fresh pyroxene (diopside) than within the kimberlites. It occurs as anhedral grains that are partially to fully serpentinized. Magnetite is scattered throughout the groundmass and within the phlogopite and serpentinized olivine pseudomorphs. The perovskite tends to be larger than those found in the kimberlites (50-200 µm). They are brown, anhedral grains that occur both within and outside of phlogopite, but most occur in the matrix rather than as inclusions in other phases. The groundmass consists of serpentine, phlogopite, and chlorite and accounts for ~40% of the thin section.

Figure 59. PK-LA-MI Photomicrograph

Photomicrograph of the Hills Pond lamproite sample PK-LA-MI

Lamproite, Hills Pond, MicroLite Mine surface exposure: PK-LA-MI2

This sample of the Hills Pond lamproite is porphyritic, containing poikilitic phlogopite (~30%), serpentinized olivine (~50%), richterite (~5%), and diopside (~4%) with minor to trace amounts of apatite, titanite, perovskite (~2%), and opaque minerals such as magnetite (~3%). The phlogopite is anhedral to subhedral, up to 3 mm in length, and shows evidence of deformation such as undulatory extinction, kink bands, and low interference colors (with some showing low interference colors only along rims). A couple of phlogopite grains show simple twinning, while others are partially altered into serpentine/chlorite. Apatite occurs almost exclusively as inclusions within the phlogopite. Anhedral to subhedral grains of serpentinized olivine make up ~50% of the modal abundance and range in size from 80 μm to 4 mm. Richterite is faintly pleochroic in pale pink, subhedral-euhedral, partially altered to chlorite/serpentine and occurs as blades or bladed aggregates. It typically shows undulatory extinction. Unaltered to only partially pyroxene (diopside) is more abundant than within the kimberlites. It occurs as anhedral, partially to fully serpentinized grains. Magnetite is scattered throughout the groundmass and within the phlogopite and olivine pseudomorphs. The perovskite tends to be larger than those found in the kimberlites (12-200 μm). They are cream to brown anhedral grains that occur both within and outside of phlogopite, but most occur in the matrix rather than as inclusions in other phases. The groundmass consists of phlogopite, serpentine, chlorite and accounts for ~50% of the thin section.

Figure 60. PK-LA-MI2 Photomicrograph

Photomicrograph of the Hills Pond lamproite sample PK-LA-MI-2

Lamproite, Hills Pond, MicroLite Mine surface exposure: MML

Analyses available: U-Pb geochronology and EMP.

This lamproite sample is significantly more altered than others in this study; so much so that it is difficult to distinguish phenocryst from matrix. Most phenocrysts have been altered to serpentine and to a lesser degree calcite. Nonetheless, the lamproite is clearly porphyritic, containing poikilitic phlogopite (~4%) and diopside (~6%) with minor to trace amounts of apatite, rutile, perovskite (<1%), and opaque minerals (~1%). The phlogopite is anhedral to subhedral, up to 2.5 mm in length, and shows evidence of deformation such as undulatory extinction and kink bands. It is partially to fully altered to serpentine/chlorite. Apatite occurs almost exclusively as inclusions within the phlogopite. The subhedral to anhedral partially altered diopside is, on average, larger than that in other examples of the lamproite from Hills Pond (up to 3.5mm). The opaque minerals mostly occur within serpentine. The perovskite tends to be larger than those found in the kimberlites (30-210 μm). They are brown, anhedral grains that occur both within and outside of phlogopite, but most occur in the matrix rather than as inclusions in other phases. The groundmass consists of serpentine, chlorite, and calcite.

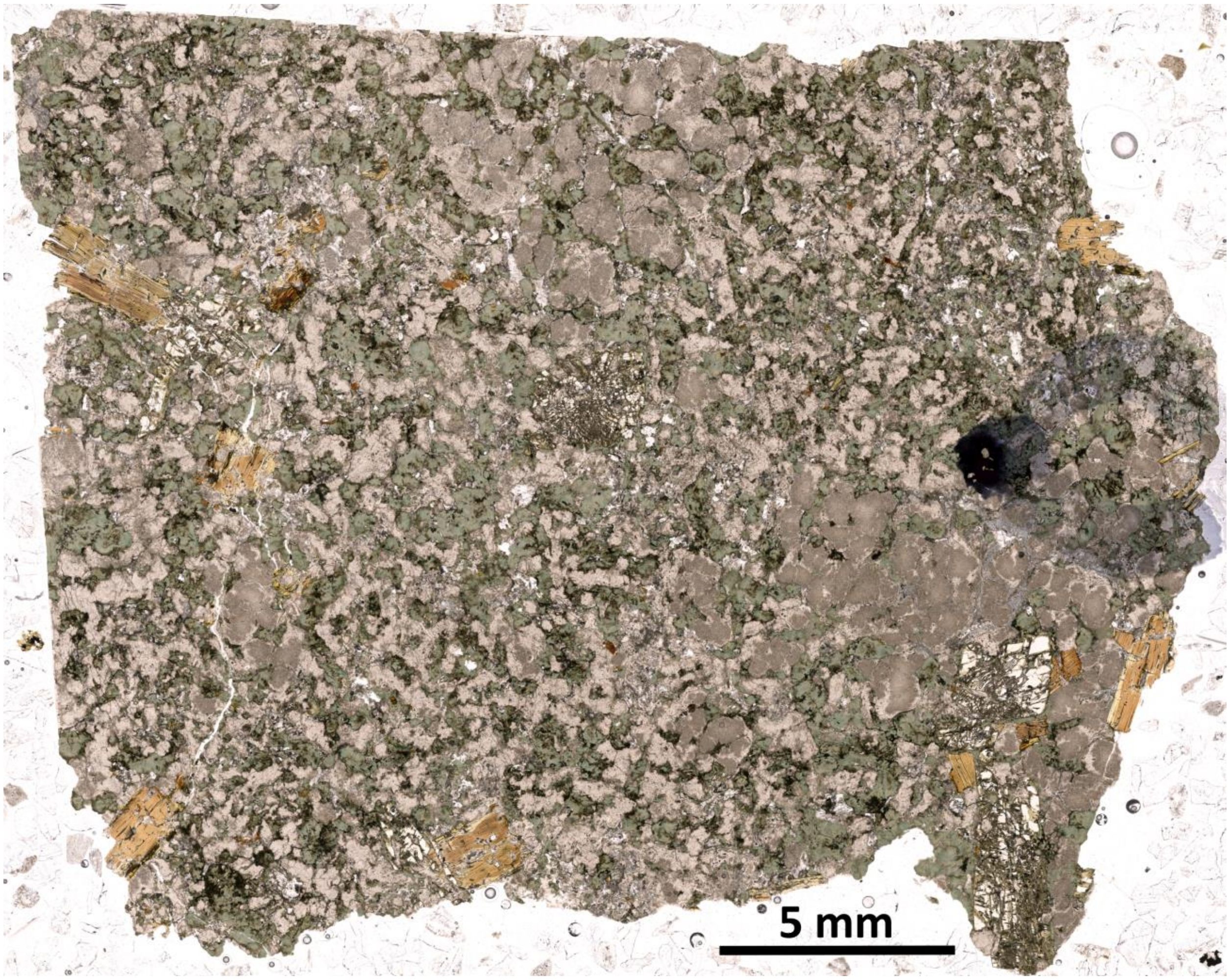

Figure 61. MML Photomicrograph

Photomicrograph of the Hills Pond lamproite sample MML. Note that the black circle on the right side of the image is sharpie.

Lamproite, Hills Pond, MicroLite Mine surface exposure: MML1 (glass covered)

This lamproite sample is significantly altered, similar to the previous sample, MML. As with that sample, it is difficult to distinguish phenocryst from matrix. A majority of the phenocrysts have been altered to serpentine and to a lesser degree calcite. The lamproite is porphyritic, containing poikilitic phlogopite (~15%) and diopside (~1-2%) with minor to trace amounts of apatite, rutile, perovskite (<1%), and opaque minerals. The phlogopite is anhedral to subhedral, up to 3 mm in length, and shows evidence of deformation such as undulatory extinction and kink bands. Additionally, many of the phlogopite show anomalously low interference colors potentially due to alteration. It is partially to fully altered to serpentine/chlorite, with serpentine found between its cleavage planes. Apatite occurs almost exclusively as inclusions within the phlogopite. The subhedral to anhedral, partially altered diopside is, on average, larger than most of the lamproites at Hills Pond, but smaller than MML (up to 2 mm). The perovskite tends to be larger than those found in the kimberlites (50-180 µm). They are brown, anhedral grains that occur both within and outside of phlogopite, but most occur in the matrix rather than as inclusions in other phases. The groundmass consists of serpentine, chlorite, and calcite.

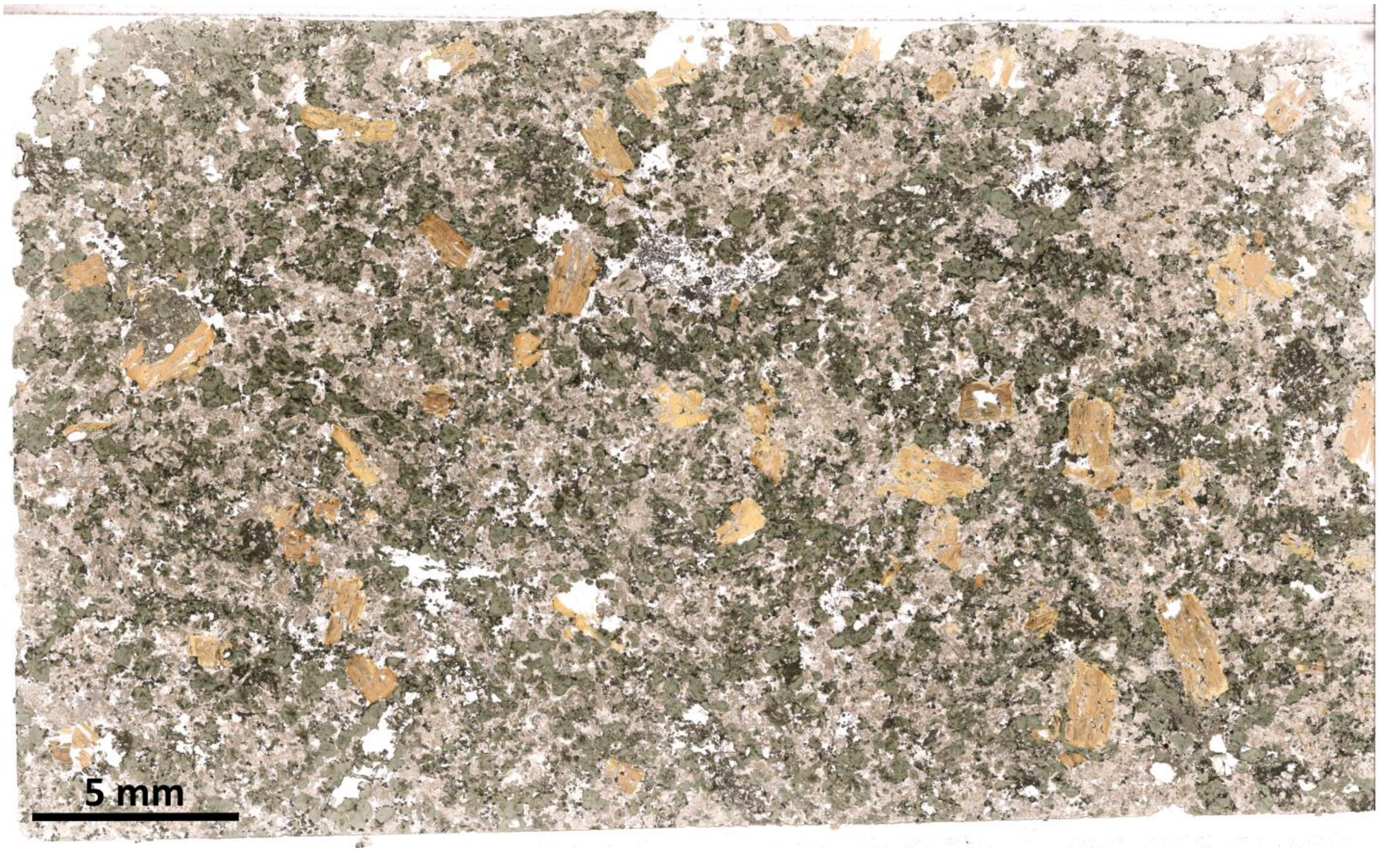

Figure 62. MML1 Photomicrograph

Photomicrograph of the Hills Pond lamproite sample MML1.

Lamproite, Hills Pond, Core 98-3

Analyses available: U-Pb geochronology and EMP.

The sample is porphyritic, containing poikilitic phlogopite (~45%), serpentinized olivine (~35%), richterite (~7%), and diopside (~6%) with minor to trace amounts of apatite, wadeite, perovskite (~5-6%), and opaque minerals such as magnetite (~1%). The phlogopite is anhedral to euhedral, up to 3.2 mm in length, and displays bird's eye extinction. Some of the grains show evidence of deformation such as undulatory extinction. A couple phlogopite grains show simple twinning, while others are partially altered to serpentine/chlorite with some serpentine found between cleavage planes. Apatite and wadeite occur almost exclusively as inclusions within the phlogopite. Anhedral to subhedral grains of serpentinized olivine make up ~40% of the modal abundance and are up to 2.7mm long. Richterite phenocrysts are poikilitic, enclosing apatite and olivine. It is faintly pleochroic in pale pink, anhedral, and partially altered to chlorite/serpentine. It typically shows undulatory extinction. Pyroxene (diopside) is less altered than in most kimberlite samples in this study and the MML and MML1 lamproites. It occurs as anhedral-euhedral, partially to fully serpentinized grains. Magnetite is scattered throughout the groundmass and within the phlogopite and olivine pseudomorphs. The perovskite tends to be larger than those found in the kimberlites (6-230 µm). They occur in a variety of morphologies (cubic and cubo-octohedral) but are predominantly anhedral, brown to red-brown grains. The groundmass consists of serpentine and chlorite and accounts for about ~60% of the thin section.

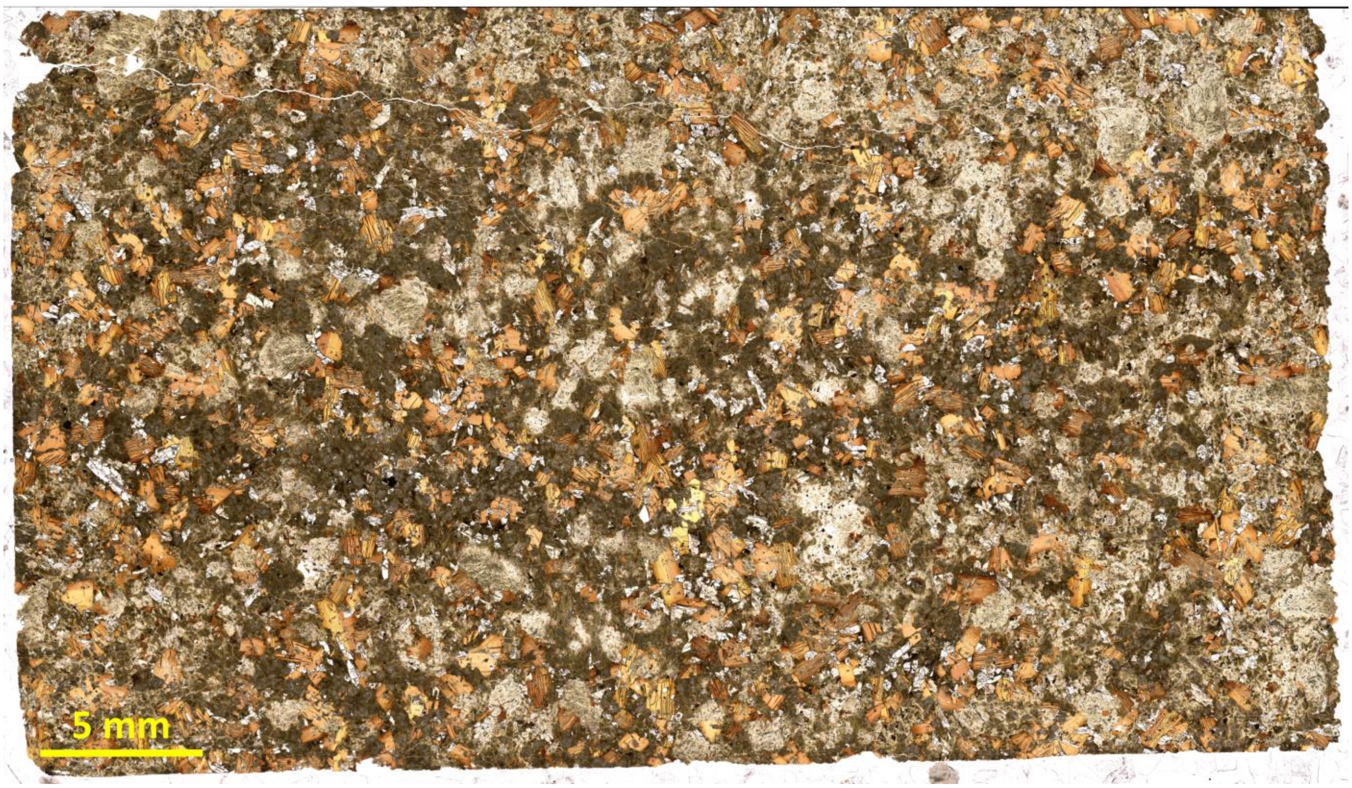

Figure 63. MLA-C98-3 Photomicrograph

Photomicrograph of the Hills Pond lamproite sample MLA-C98-3.

Lamproite, Hills Pond, Core 92-9

Analyses available: U-Pb geochronology, EMP, and LA-ICP-MS trace elements.

This sample of lamproite is porphyritic, containing poikilitic phlogopite (~50%), serpentinized olivine (~35%), richterite (~7%), and diopside (~5%) with minor to trace amounts of apatite, wadeite, perovskite (~5-6%), and opaque minerals such as magnetite (~2%). The phlogopite is anhedral to euhedral, up to 2.2 mm in length, and displays bird's eye extinction. Some of the grains show evidence of deformation such as undulatory extinction, and kink bands. Additionally, many of the phlogopite show anomalously low interference colors potentially due to alteration. It is partially to fully altered to serpentine, with serpentine/chlorite found between its cleavage planes. Apatite and wadeite occur almost exclusively as inclusions within the phlogopite and diopside. Anhedral to subhedral grains of serpentinized olivine make up ~40% of the modal abundance and are up to 4 mm long. Richterite phenocrysts are poikilitic, enclosing apatite and olivine. It is faintly pleochroic in pale pink, anhedral, and partially altered to chlorite/serpentine. It typically shows undulatory extinction. There is more abundant fresh pyroxene (diopside) than within the kimberlites and the MML and MML1 lamproites. It occurs as anhedral-subhedral partially to fully serpentinized grains. Magnetite is scattered throughout the groundmass and within the phlogopite and olivine pseudomorphs. The perovskite tends to be larger than those found in the kimberlites (15-250 μm). They are anhedral (with a few showing cubic morphologies) and light pink to brown to red brown in color. The groundmass consists of serpentine, chlorite, and phlogopite and accounts for about ~50% of the thin section.

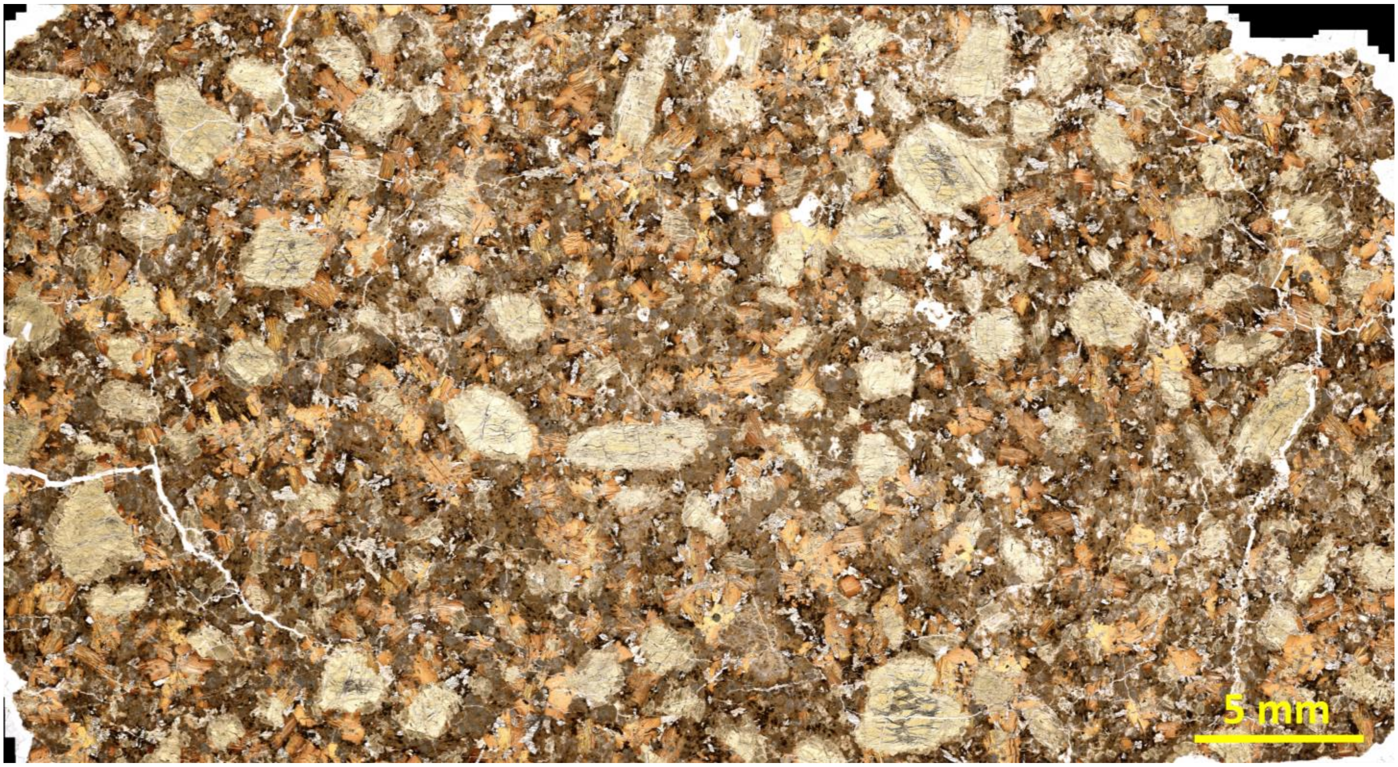

Figure 64. MLA-C92-9 Photomicrograph

Photomicrograph of the Hills Pond lamproite sample MLA-C92-9.

Lamproite, Hills Pond, Core 97-8

Analyses available: U-Pb geochronology and EMP.

The lamproite in this core is porphyritic, containing poikilitic phlogopite (~55%), serpentinized olivine (~30%), richterite (~6-7%), and diopside (~1-2%) with minor to trace amounts of apatite, wadeite, perovskite (~3-4%), and opaque minerals such as magnetite (~2%). The phlogopite is anhedral to euhedral, up to 2 mm in length, and displays bird's eye extinction. Some of the grains show evidence of deformation such as undulatory extinction. A couple of phlogopite grains show simple twinning, while others are partially altered into serpentine/chlorite with some serpentine found between its cleavage planes. Additionally, many of the phlogopite show anomalously low interference colors potentially due to alteration. Apatite and wadeite occur almost exclusively as inclusions within the phlogopite and diopside. Anhedral grains of serpentinized olivine make up ~25% of the modal abundance and are up to 3.5 mm long. Richterite phenocrysts are poikilitic, enclosing apatite and olivine. It is faintly pleochroic in pale pink, anhedral, and partially altered to chlorite/serpentine. A few crystals are bladed or form bladed aggregates. It typically shows undulatory extinction. The pyroxene (diopside) is less altered overall than within the kimberlites. It occurs as anhedral, partially to fully serpentinized grains. Magnetite is scattered throughout the groundmass and within the phlogopite and olivine pseudomorphs. The perovskite tends to be larger (9-150 µm) than those found in the kimberlites in this study. They occur in a variety of morphologies (cubic and cubo-octohedral) but are predominantly anhedral, brown to red-brown grains. The groundmass consists of mostly serpentine with lesser chlorite, and phlogopite and accounts for ~ 70% of the thin section.

Figure 65. MLA-C97-8 Photomicrograph

Photomicrograph of the Hills Pond lamproite sample MLA-C97-8.

Lamproite, Hills Pond, Core 95-5

Analyses available: U-Pb geochronology and EMP.

The lamproite in this interval is porphyritic, containing poikilitic phlogopite (~33%), serpentinized olivine (~48%), richterite (~6%), and diopside (~5%) with minor to trace amounts of apatite, wadeite, perovskite (~5%), and opaque minerals such as magnetite (~3%). The phlogopite is anhedral to subhedral, up to 2 mm in length, and displays bird's eye extinction. Some of the grains show evidence of deformation such as undulatory extinction. A couple of phlogopite grains show simple twinning, while others are partially altered into serpentine/chlorite with some serpentine found between its cleavage planes. Additionally, many of the phlogopite show anomalously low interference colors potentially due to alteration. Apatite and wadeite occur almost exclusively as inclusions within the phlogopite and diopside. Anhedral grains of serpentinized olivine make up ~55% of the modal abundance and are up to 7 mm long. Richterite phenocrysts are poikilitic, enclosing apatite and olivine. It is faintly pleochroic in pale pink, anhedral, and partially altered to chlorite/serpentine. A few crystals are bladed and/or form bladed aggregates. It typically shows undulatory extinction. There is more abundant fresh pyroxene (diopside) than within the kimberlites. It occurs as anhedral-euhedral partially to fully serpentinized grains. Magnetite is scattered throughout the groundmass and within the phlogopite and olivine pseudomorphs. The perovskite tends to be larger than those found in the kimberlites (5-300 μm). They are anhedral (with a few showing cubic morphologies) and brown to red brown in color. The groundmass consists of mostly serpentine with lesser chlorite, and phlogopite and accounts for about ~55% of the thin section.

Figure 66. MLA-C95-5 Photomicrograph

Photomicrograph of the Hills Pond lamproite sample MLA-C95-5.

Lamproite, Rose Dome, Core Eagle 5, 384 ft depth

Analyses available: U-Pb geochronology, EMP, and LA-ICP-MS trace elements.

This example of the Rose Dome lamproite is porphyritic, containing poikilitic phlogopite (~65%) and serpentinized olivine (~25%) with minor to trace amounts of diopside, apatite, wadeite, perovskite (~8%), and opaque minerals such as magnetite (~1-2%). The phlogopite is anhedral, up to 2.5 mm in length, and displays bird's eye extinction. Some of the grains show evidence of deformation such as undulatory extinction while others are partially altered into serpentine/chlorite. Overall, the phlogopite contains significantly more inclusions and is more anhedral than those in the Hills Pond lamproites. Apatite and wadeite occur almost exclusively as inclusions within the phlogopite. Anhedral grains of serpentinized olivine make up ~25% of the modal abundance and are up to 3.4 mm long. The olivine pseudomorphs tend to have alteration rims that are lighter in color than the core. There are trace amounts of anhedral diopside that has been fully to partially altered to serpentine and calcite. Magnetite is scattered throughout the groundmass and within the phlogopite and olivine pseudomorphs. The perovskite tends to be larger than those found in the kimberlites (15-350 µm). They are anhedral (with some showing cubic morphologies) and golden brown to brownish green in color. The groundmass consists of serpentine and phlogopite.

Figure 67. RDE5-384 Photomicrograph

Photomicrograph of the Rose Dome lamproite sample RDLE5-384.

Lamproite, Rose Dome, Core Eagle 4, 442 ft depth

Analyses available: U-Pb geochronology and EMP.

The lamproite in this core is porphyritic, containing poikilitic phlogopite (~36%), serpentinized olivine (~50%), and diopside (~3%) with minor to trace amounts of apatite, wadeite, perovskite (~4%), and opaque minerals such as magnetite (~7%). Olivine (replaced by serpentine) and to a lesser extent diopside and phlogopite exhibit a gradient in grain size (Fig. 21). The phlogopite is anhedral to subhedral, up to 2 mm in length, and displays bird's eye extinction. A couple are zoned, while others are partially altered into serpentine/chlorite. Apatite is rare and where it does occur is exclusively as inclusions within the phlogopite. Anhedral grains of serpentinized olivine make up ~30-50% of the modal abundance and are up to 4 mm long. The olivine pseudomorphs tend to have chlorite alteration rims. The diopside occurs as anhedral-subhedral, partially to fully serpentinized grains. Magnetite is scattered throughout the groundmass and within the phlogopite and olivine pseudomorphs. The perovskite tends to be larger than those found in the kimberlites and in the Hills Pond lamproites (70-800 μm). They are mostly cubic (with some anhedral) and red brown to brown in color. The groundmass consists of serpentine and chlorite and accounts for about ~50% of the thin section.

Lamproite, Rose Dome, Core Eagle 4, 418 ft depth

Analyses available: U-Pb geochronology, EMP, and LA-ICP-MS trace elements.

This interval of Rose Dome lamproite is porphyritic, containing poikilitic phlogopite (~40%), serpentinized olivine (~33%), and diopside (~9%) with minor to trace amounts of apatite, wadeite?, titanite, perovskite (~11%), and opaque minerals such as magnetite (~7%). The phlogopite is anhedral to subhedral, up to 1.7 mm in length, and displays bird's eye extinction.

Some of the grains show evidence of deformation such as undulatory extinction while others are partially altered into serpentine/chlorite especially in between cleavage planes. Apatite and wadeite? are rare and where they do occur it is exclusively as inclusions within the phlogopite. Anhedral grains of serpentinized olivine make up ~35% of the modal abundance and are up to 5 mm long. There is more abundant fresh pyroxene (diopside) than within the kimberlites. It occurs as anhedral-euhedral, partially to fully serpentinized grains. Magnetite is scattered throughout the groundmass and within the phlogopite and olivine pseudomorphs. The perovskite tends to be larger than those found in the kimberlites and the Hills Pond lamproites (20-500 µm). They are mostly cubic (with some anhedral) and red brown to golden brown in color. The groundmass consists of serpentine and chlorite and accounts for about ~60% of the thin section.

Figure 68. RDE4-418 Photomicrograph

Photomicrograph of the Rose Dome lamproite sample RDLE4-418.

Lamproite, Rose Dome, Core Eagle 4, 412 ft depth

Analyses available: U-Pb geochronology, EMP.

This sample of Rose Dome lamproite is more homogeneous and finer grained than others in this study. Similar to Hills Pond samples MML and MML1, RDLE4, C412 is significantly altered, making it difficult to distinguish altered phenocrysts from matrix. The lamproite is porphyritic, containing poikilitic phlogopite (~33%), olivine pseudomorphs, replaced by serpentine and calcite (~60%), and diopside (~1%) with minor to trace amounts of apatite, perovskite (~4%), titanite, and opaque minerals such as magnetite (~2%). The phlogopite is anhedral to subhedral, up to 1.2 mm in length, and displays bird's eye extinction. Some of the grains show evidence of deformation such as undulatory extinction while others are partially altered into serpentine/chlorite especially in between cleavage planes. There is a 1.6cm long zone within the thin section that contains larger, more euhedral phenocrystic phlogopite set in a matrix richer in calcite and chrysotile. Some of the phlogopite crystals in this area are zoned with darker rims. Apatite occurs exclusively as inclusions within the phlogopite. Anhedral olivine (replaced by serpentine and calcite) make up ~60-70% of the modal abundance. The diopside occurs as anhedral-subhedral, partially to fully serpentinized grains. Magnetite is scattered throughout the groundmass and within the phlogopite and olivine pseudomorphs. The perovskite tends to be larger than those found in the kimberlites (20-300 µm). They are anhedral and brown to greenish brown in color. The groundmass consists of serpentine, calcite, and chlorite.

Figure 69. RDE4-412 Photomicrograph

Photomicrograph of the Rose Dome lamproite sample RDLE4-412.

Lamproite, Rose Dome, Core Eagle 4, 365 ft depth

Similar to RDLE4-C412, this lamproite is homogeneous and fine grained. It is porphyritic, containing poikilitic phlogopite (~70%) and olivine pseudomorphs that have been replaced by serpentine and calcite (~20%), with minor to trace amounts of apatite (~5%) and opaque minerals (~5%). The phlogopite is anhedral to euhedral, up to 1.2 mm in length, and displays bird's eye extinction. Some of the grains show evidence of deformation such as undulatory extinction. Additionally, many of the phlogopite show anomalously low interference colors potentially due to alteration. A couple of phlogopite grains show simple twinning, while others are partially altered into serpentine/chlorite with some serpentine found between its cleavage planes. Apatite is rare and occurs exclusively as inclusions within the phlogopite.

Anhedral olivine pseudomorphs make up ~5% of the modal abundance and are up to 3.5mm long. Opaque minerals mostly occur as an alteration production with the serpentine. The groundmass consists of serpentine, calcite, and phlogopite and accounts for about ~50% of the thin section.